CHAPTER 1

Introduction

Chapter Outline

1.1 Background and Problem Statement 1
1.2 Motivations 3
1.3 Organization of the Book 3
References 3

1.1 Background and Problem Statement

The difference between a flexible and a rigid manipulator can be explained both physically and mathematically. In terms of physics, a rigid manipulator has theoretically only one fundamental frequency of vibration with an infinite value, and thus can move at any desired speed without significant tip deflection and body deformation, leading to a large link mass and a correspondingly low energy efficiency; a flexible manipulator, on the other hand, has many fundamental frequencies of vibration with finite values and thus can experience significant tip deflection under normal operating conditions. The oscillation becomes severe when its speed approaches one of its fundamental frequencies, so it is of low mass but is very difficult to operate. In mathematical terms, a rigid manipulator can only have a finite number of degrees of freedom (DOF), described by ordinary differential equations. A flexible manipulator will have an infinite number of DOF, and thus has to be specified by partial differential equations, so-called distributed parameter systems.

Compared with rigid robotic manipulators, flexible ones are more efficient and safer to operate due to their lightness, good damping behavior, and less pronounced interconnections between different segments of multiple arm links. However, they are much more difficult to control and operate than their rigid counterparts due to their flexibility. Examples of flexible manipulators can be found in space exploration, such as the NASA Remote Manipulator System; in mining operations, such as robotic excavators; in construction applications, such as robotic crane systems, and so on. In those situations, size, mass, payload, speed, environmental or task constraint factors make the flexibility of a robotic manipulator an important issue with respect to its design, modeling, analysis, control, and operation.

Flexible Manipulators. DOI: 10.1016/B978-0-12-397036-7.00001-5
Copyright © 2012 Elsevier Inc. All rights reserved.

For example, the NASA Remote Manipulator System has very low natural frequencies ranging from 0.04 to 0.35 Hz and consequently it has to move slowly at a speed of 0.5°/s to avoid vibrations due to its large mass (450 kg) and heavy payload (27,200 kg) [1]. Other operational problems in flexible manipulators can be found in the literature [2].

The objective of this book is to provide a unified approach that simultaneously considers all factors in mechanical, electrical, sensing, and control components to address modeling, analysis, optimization, and control of flexible manipulators. Specifically, we will investigate the following problems:

1. **Modeling of flexible manipulators**
   Modeling is the first step in the design, analysis, and control of flexible manipulators. Many and various models, from linear to nonlinear, from numerical to analytical, have been proposed in the literature. However, their accuracy, complexity, and overall efficiency have not been investigated systematically up to now. In this book, we will carry out a systematic study of these models and compare their pros and cons with respect to specific design and control problems, especially trade-offs between benefits and costs.
2. **Analysis of flexible manipulators**
   Various model-specific analytical papers have been published, but no thorough comparative investigation of these analyses has ever been conducted. In addition, very few studies with quantitative results have been reported in the literature on the effect of size, shape, mass distribution, tip load, and other factors on the dynamics and operational performance of flexible manipulators. However, such analyses are critical to the effectiveness of any model for optimization and control purposes. Here, we will address these issues with systematic but specific numerical investigations based on the currently available dynamic models.
3. **Optimization of flexible manipulators**
   Two conventional dual optimal design problems have been well studied in our previous research: (a) Given a fixed mass for the link, find a shape that maximizes its speed; and (b) given a fixed speed for the link, find a shape that minimizes its mass. However, the formulations used for optimization in the previous studies are too simple for real-world applications. To make those designs useful, we must include complicated constraints that are encountered in reality. In most of these cases, analytical procedures developed previously would no longer be applicable. We must look into new methods for optimal design problems with meaningful constraints.
4. **Mechatronic design of flexible manipulators**
   The complexity of a manipulator system is due to the interrelation and interdependency of its subsystems, for example its kinematic system (mainly the beam or link structure), control system, driver system (mainly the actuation mechanism), and measuring or sensing system. In traditional design, a manipulator's link structure is designed first, followed by its driver system, then a measuring system, and finally its control system. This leads to a sequential design process and a locally optimal solution, and therefore the potential of

a flexible manipulator is rarely fully realized. To overcome such problems, a concurrent design procedure that integrates all subsystems must be undertaken, namely a mechatronic approach must be considered in the design of flexible manipulators.

1.2 Motivations

First of all, this book presents a unified and systematic approach that deals with the modeling, analysis, optimization, and mechatronic design of flexible manipulators. This approach will enable us to deal with various issues in the design and operation of flexible manipulators so that both analytical and numerical procedures, especially new methods in optimization in the field of computational intelligence, can be applied.

Secondly, with this unified approach we have developed a different methodology for the design of flexible manipulators that deals with their mechanical, electrical, sensing, and control components concurrently instead of sequentially from the very beginning of the design process. Theoretically, this method is capable of finding the global optimal design solution, resulting in a better design outcome.

Thirdly, our approach has opened a new direction in the research of flexible manipulators. Currently, most researchers try to simplify beam model complexity by neglecting some less significant factors, such as shear deformation, rotary inertia, viscous and Coulomb friction, or linearizing the model at some particular operating points, in their effort to make real-time control feasible. In the new direction we have proposed here, the focus is to design a better manipulator system so its control problem and the accuracy of the dynamic model will be less critical in its performance. In other words, the result from our proposed mechatronic design is better than that obtained from previous model-intensive or control-intensive designs.

1.3 Organization of the Book

The previous work on related issues of flexible manipulators will be addressed in Chapter 2, while Chapters 3, 4, 5, and 6 discuss modeling, analysis, optimization, and mechatronic design of flexible manipulators respectively. Finally, Chapter 7 summarizes this book and looks into critical efforts that are needed for future research.

References

[1] W.J. Book, Structural flexibility of motion systems in the space environment, IEEE Transactions on Robotics and Automation 9 (5) (1993) 524–538.

[2] P.K. Nguyen, R. Ravindran, R. Carr, D.M. Gossain, K.H. Doetsch, Structural Flexibility of the Shuttle Remote Manipulator System Mechanical Arm, SPAR AeroSpace Ltd., Tech. Info. AIAA, 1982.

CHAPTER 2

Past and Recent Works

Chapter Outline

2.1 Earlier Research on Flexible Manipulators 5
2.2 Recent Work on Flexible Manipulators 6
References 11

2.1 Earlier Research on Flexible Manipulators

Interest in the utilization of flexible manipulators for space exploration and automation started in the early 1980s. For example, Nguyen et al. [1] investigated the dynamics and control of the space shuttle manipulator arm. In 1984, Cannon and Schmitz published one of the first papers on the control of flexible manipulators [2]. Book [3] investigated the dynamics of flexible manipulators using a recursive Lagrangian formulation. In 1985, Sakawa et al. [4] considered the feedback control problem inherent in flexible arms. Yang and Donath [5] formulated a dynamic model of a flexible arm that also included the flexibility of the joints.

From the late 1980s to 1990s, there have been a multitude of papers published on control models for flexible manipulators. In 1990, Belvin and Park [6] were one of the first teams to attempt a comprehensive optimization scheme that included both structure and control optimization using cost functions. Khorrami and Özgöner [7] presented a set of integro-partial equations and used a perturbation method for control purposes. A complete study of different dynamic equations under various boundary conditions for flexible manipulators was conducted by Bellezze et al. [8]. Kim and Junkins [9] developed cost functions of total mass, stability, and eigenvalue sensitivity for optimum flexible structures. Park and Asada [10] developed an optimal control design based on a variable point of torque transmission to a flexible link. Asada et al. [11] have addressed the optimal design problem using a finite-element computational model. As part of their effort toward a control-configured flexible arm, they tried to increase the fundamental frequency of vibration through optimum tapering of a beam of varying rectangular cross-section. A theoretical increment of 43% in the fundamental frequency of the manipulator was obtained. De Luca and Siciliano [12] considered the additional factor of gravity in their control model.

Flexible Manipulators. DOI: 10.1016/B978-0-12-397036-7.00002-7
Copyright © 2012 Elsevier Inc. All rights reserved.

The majority of research up to the early 1990s concentrated on the optimization of flexible manipulators from a control perspective. Practically no work was being done on the problem of structural or shape optimization, although some researchers such as Asada, Park, and Rai included shape design as an integral part of an overall control scheme, but with no analytical analysis. In 1991, Wang [13] reexamined the earlier work of Karihaloo and Niordson [14] and found that the Lagrange multiplier in the optimality equations could be removed completely, thus simplifying the iteration scheme considerably. At around the same time, Wang et al. [15] also developed an optimization model for a flexible manipulator and, using the modified iteration scheme, produced the first optimum shapes and frequencies for flexible manipulators. They found that an increase of over 600% in the fundamental frequency of vibration was possible for flexible links of geometrically similar cross-sections.

Wang and Guan [16] in 1994 produced an excellent paper on different models of flexible manipulators and examined the effect of tip loads on the fundamental frequency of vibration using modal frequencies and vibration modes. They showed that both rotary inertia and shear deformation have very little effect upon the fundamental frequency of vibration. Wang and Russell [17], concentrating on the Euler–Bernoulli model of flexible manipulators with tip loads, produced numerous examples for various tip load design vectors. They then investigated the minimum-weight design of a flexible manipulator with no tip load [18], and also applied previous work in optimum shape design to a closed-loop control formulation called the mechatronic approach [19]. Wang and Russell [18] extended their previous work to include constrained designs by expanding the displacement function in a base set of modal shape functions derived for uniform links. In 1995, Wang and Russell [19] presented an innovative new segmentized model of a flexible manipulator that opened up the problem of optimum design to numerous mathematical programming techniques.

2.2 Recent Work on Flexible Manipulators

Numerous papers have addressed the control of flexible manipulators. Initial studies concentrated on the state space model. Cannon and Schmitz [2] first investigated the linear quadratic Gaussian (LQG) controller assuming that the states were available. However, the states were not available and they had to be reconstructed by optimal estimators. In 1993, Lin and Lewis [20] studied the Kalman filter for the estimation of the rigid and flexible modes for control purposes. Sakawa et al. [4] applied a linear quadratic (LQ) control to track the hub reference by damping the flexible modes. The states were obtained by means of an observer. Geniele et al. [21] used an inner loop to stabilize the flexible system and an outer loop to track the joint angle and one point along the arm respectively, using input–output inversion. The same approach was used by Madhavan and Singh in their study [22]. They also used a sliding

mode control to design a controller that could tolerate a wide range of uncertainties, thus enhancing its robustness [23].

Other studies used the transfer function approach. Wang and Vidyasagar [24] used tip deflection as output and devised an output feedback based on the passivity of the model's transfer function. Siciliano and Book decomposed the flexible manipulator dynamics into two subsystems, a fast and a slow system, by applying singular perturbation theory. They showed that the fast system was linear, but that the slow system was nonlinear. Furthermore, a linear state controller and a nonlinear controller were designed for the two systems respectively to track the hub angle. Similar research was carried out by Aoustin et al. [25]. Corrected slow and fast subsystems were used in (1997) by Moallem et al. [26].

A computational intelligence approach has also been used in the control of flexible manipulators. Gutierrez et al. [27] proposed one scheme based on this approach using a neural network (NN) tracking controller. The outer NN proportional deviator (PD) tracking loop was used to stabilize the fast mode, while the inner feedback loop was used to liberalize the slow mode dynamics. The results were compared between PD and the proportional integral derivative (PID). Lenz et al. [28] derived the robust control for a flexible beam subjected to perturbations and delay by using H_∞ theory. In 1997, Tchernychev et al. [29] developed a constrained H_∞ controller in which time-domain constraints are treated directly without translation to the frequency domain. In the same year, Zhu et al. [30] investigated a backstepping approach for tip tracking by lumping the beam to a spring-mass system to develop a robust controller in the presence of system disturbances/uncertainties. Also in 1997, Jnifene and Fahim [31] dealt with nonminimum phase characteristics by introducing active damping into the system, and proposed a computed torque/delayed deflection approach. The torque was calculated from the joint angle and a delayed deflection, while the delay time depended on the point where the deflection was measured.

Ghanekar et al. [32] examined the large robotic manipulator scaling laws for linear controllers by nondimensional groups, thus allowing a small-scale prototype to be used to perform the design work. Liang et al. [33], in 1998, discussed the problem of a free-floating space manipulator and mapped it to a conventional, fixed-base manipulator. This allowed well-understood methods to be used to build the manipulator system. Simulation work was also presented, for example by Tang and Lu [34] using a video system to estimate model shapes and vibration states. Strain gages were used by Fukuda [35] and by Hastings and Book [36] to measure the deflection. Photosensors were also used for detecting the displacement [2,15,37]. Chalhoub et al. [38] used an accelerometer to measure the beam vibration. The state of vibration could be obtained indirectly by combining some strain gages and/or displacement Sundararajan et al. [39].

A port-based modeling of a flexible link has also been proposed, which is a simple way to model flexible robotic links [40]. This is different from classical approaches and from

Euler–Bernoulli or Timoshenko theory, in that the proposed model is able to describe large deflections in 3D space and does not rely on any finite-dimensional approximation (e.g. modal approximation). The model has been formulated within the port-Hamiltonian formalism because intuitive considerations of the geometric behavior of the elastic link naturally define a Stokes–Dirac structure, the kernel of a port-Hamiltonian system. Moreover, port-Hamiltonian systems can be easily interconnected, thus allowing the description of complex systems as a composition of parts in an object-oriented way. By combining rigid bodies, springs, dampers, joints and, finally, flexible links, it is possible to model and mathematically describe whatever complex mechanical structure is formed by the beams. In order to demonstrate the dynamical properties of the model and how complex mechanisms can be obtained by port interconnection, simulations of one and two degrees of freedom (DOF) serial manipulators and of a two-DOF flexible closed kinematic chain are presented.

These studies did control-intensive work to improve beam performance, but they ignored the impact arising from the beam mechanic shape. The couplings between the controller and structure of flexible manipulators were not considered in the design and optimization. Therefore, the resulting system and performance was only locally optimal.

Xu and Ritz [41] proposed a vision-based flexible beam tip point control where a two-time-scale controller has been presented to track a desired tip point signal and at the same time mitigate the tip point vibration. In their approach, a camera was used to provide visual feedback in which the delayed vision signal was compensated by the state estimator and predictor. The controller has been experimentally verified and shown to exceed the performance of other tested controllers. A similar study on two-time-scale visual serving of eye-in-hand flexible manipulators [42] has also been reported. In this work, the dynamic effects of both the rigid and the flexible motion of the manipulator are fully taken into account in a control solution where the two-time-scale nature of the problem is exploited. The visual information is used in the "slow" subsystem for a task-space-oriented control law, where computationally expensive operations, such as the inverse and time derivative of the Jacobian, are avoided. A constructive proof of the stability of this control scheme, based on Lyapunov theory, is also presented. The effectiveness of the proposed controller is shown by means of a numerical simulation concerning a trajectory tracking problem. Some experimental results finally demonstrate the precision enhancement achieved by the proposed algorithm on a single-link flexible manipulator.

Becedas et al. [43] constructed an adaptive controller for single-link flexible manipulators. They designed a fast online closed-loop identification method combined with an output-feedback controller of the generalized proportional integral (GPI) type for the control of an uncertain flexible robotic arm with unknown mass at the tip, including a Coulomb friction term in the motor dynamics. Barczyk and Lynch [44] developed a flatness-based estimated state feedback control for a rotating flexible beam and verified the design with experimental results,

where a so-called flat output is introduced in order to parameterize the system's variables in power series. These series lead to open- and closed-loop controls, which can solve finite-time motion planning problems. Vibration control of a flexible arm by a multiple observer structure is discussed in Ref. [45]. This paper proposes vibration control of the flexible arm by acceleration feedback, and disturbance rejection by a multiple-observer structure using the acceleration of the arm. The validity of the proposed method is shown by simulations and experiments.

Chatterjee et al. [46] proposed an augmented stable fuzzy control for a flexible robotic arm using an LMI approach and neuro-fuzzy state space modeling. In this method, the controller is designed on the basis of a neuro-fuzzy state-space model that is successfully trained using the experimental data acquired from a real robotic arm. The complex problem of solving stability conditions is taken care of by recasting them in the form of linear matrix inequalities and then solving them using a popular interior-point-based method. This asymptotically stable fuzzy controller is further augmented to provide enhanced transient performance along with maintaining the excellent steady-state performance shown by the stable control strategy. The controller thus designed has been successfully implemented for a real robotic arm to operate over a long angular range of 180° with several payload conditions and, for situations where the system is operated over a long range and with a large variation in payload conditions, it successfully outperformed the proposed proportional derivative and strain controller.

Dogan and Istefanopulos [47] addressed the issues of optimal nonlinear controller design for flexible robot manipulators with an adaptive internal model. In this paper, the dynamic state feedback controller is used to achieve robust regulation of the rigid modes as well as suppression of elastic vibrations. However, the control of highly nonlinear multilink flexible arms is subject to uncertainties caused by backlash, payload changes, and external disturbances. The internal model approach is adaptively tuned up for unknown disturbances, in parallel with a robust stabilizer. The stabilizer part of the controller is optimized with a new evolutionary algorithm.

Another new development is the work on tip position control of a lightweight flexible manipulator using a fractional order controller [48]. One of the interesting features of this design method is that the overshoot of the controlled system is independent of the tip mass. This allows a constant safety zone to be delimited for any given placement task of the arm, independent of the load being carried, thereby making it easier to plan collision avoidance. Other considerations about noise and motor saturation issues are also presented in that paper. The overall control scheme proposed consists of three nested control loops. Once the friction and other nonlinear effects have been compensated for, the inner loop is designed to give a fast motor response. The middle loop simplifies the dynamics of the system and reduces its transfer function to a double integrator. A fractional derivative controller is used to shape the outer loop into the form of a fractional order integrator. The result is a constant phase system with, in the

time domain, step responses exhibiting constant overshoot, independent of variations in the load and robust, in a stability sense, to spillover effects. Experimental results are included, when controlling the flexible manipulator with this fractional order derivator, that prove the good performance of the system.

Wave-based analysis and control of lump-modeled flexible robots is also very interesting [49]. In that paper, the authors provide a foundation for wave-based control applications by exploring the validity and nature of wave concepts in lumped flexible robotic systems. A new wave-based model of uniform mass-spring systems is proposed and verified. The model is exact but not unique. Useful simplifications and approximations are also presented. The model leads to control strategies for flexible robotic systems that are simple, powerful, robust, and generic. The wave approach also provides a new analytical tool and conceptual framework for lumped dynamic systems.

Output tracking control of a one-link flexible manipulator via causal inversion [50] is a new design procedure for output tracking control of nonminimum phase systems, where flexible manipulators are a typical example. This new controller achieves stable tracking of a reference profile given in real time via a causal inversion approach. In this approach, the nonminimum phase system is first stably inverted online to obtain both desired (and stable) state and input trajectories. Then an H_∞ optimal controller is used to stabilize the closed-loop system. In contrast to stable inversion, the causal inversion approach does not require pre-calculation. In contrast to nonlinear regulation, the causal inversion approach avoids the numerical intractability of solving nonlinear PDEs. As an example of the application, a causal inversion-based controller is designed for tip trajectory tracking of a one-link flexible manipulator. Simulation results demonstrate its effectiveness in output tracking.

Gomes et al. studied the active control of flexible manipulators [51] using a nonlinear conventional motor with gear actuators. Due to the existence of a dead zone in the torque caused by the nonlinear friction inside the actuator, this has been a problem without an acceptable solution backed up by experimental evidence, until now. The torque needed to attenuate the vibrations, although calculated by the control law, is consumed by the friction and does not arrive at the flexible structure. This paper proposes a control strategy with friction compensation using neural networks to solve this problem. Experimental results obtained with a flexible manipulator attest to the excellent performance of the proposed control law.

For optimal structures of flexible manipulators, very little progress has been made after the extensive initial studies in optimal shape design conducted by Wang's group [13,17−19,52−54]. A new computing method for optimum mass and rigidity distributions has been formulated by Wang et al. [15] for a flexible manipulator with a tip load so that the robustness with respect to design specification and known constraints can be considered. Based on this new formulation, other practical issues can also be addressed.

However, these studies were still focused on open-loop design. They only concerned the beam's mechanical construction. From these studies, a proper design of a flexible beam shape can make it suffer less vibration. But in reality, all manipulators must be in a closed loop to achieve high performance. How to design a flexible beam shape from the control perspective still remains a challenge.

References

[1] P.K. Nguyen, R. Ravindran, R. Carr, D.M. Gossain, K.H. Doetsch, Structural Flexibility of the Shuttle Remote Manipulator System Mechanical Arm, SPAR AeroSpace Ltd., Tech. Info. AIAA, 1982.

[2] R.H. Cannon Jr., E. Schmitz, Precise control of flexible manipulators, in: Robotics Research: First International Symposium, MIT Press, Cambridge, MA, 1984, pp. 841–861.

[3] W.J. Book, Structural flexibility of motion systems in the space environment, IEEE Transactions on Robotics and Automation 9 (5) (1993) 524–538.

[4] T. Sakawa, F. Matsuno, S. Fukushima, Modeling and feedback control of a flexible arm, Journal of Robotic Systems 2 (1985) 453–472.

[5] G.B. Yang, M. Donath, Dynamic model of a one link manipulator with both structural and joint flexibility, IEEE International Conference on Robotics and Automation 6 (3) (1988) 454–461.

[6] W.K. Belvin, K.C. Park, Structural tailoring and feedback control synthesis: An interdisciplinary approach, Journal of Guidance and Control 13 (3) (1990) 424–429.

[7] F. Khorrami, U. Özgöner, Perturbation method in control of flexible link manipulators, IEEE International Conference on Robotics and Automation 1 (1988) 310–315.

[8] F. Bellezze, L. Lanari, G. Ulivi, Exact modeling of the flexible slewing link, IEEE 1990 International Conference on Robotics and Automation 2 (1990) 734–739.

[9] K.B. Kim, J.L. Junkins, Robustness optimization of structural and controller parameters, Journal of Guidance and Control 12 (1) (1989) 89–96.

[10] J.-H. Park, H. Asada, Design and control of minimum-phase flexible arms with torque transmission mechanisms, IEEE 1990 International Conference on Robotics and Automation 3 (1990) 1790–1795.

[11] H. Asada, J.-H. Park, S. Rai, A control-configured flexible arm: Integrated structure/control design, IEEE Conference on Robotics and Automation, Sacramento, CA 3 (1991) 2356–2362.

[12] A. De Luca, B. Siciliano, Trajectory control of non-linear one link flexible arm, International Journal of Control 50 (1989) 1699–1715.

[13] F.Y. Wang, Optimum design of vibrating cantilevers: A classical problem revisited, Journal of Optimization Theory and Applications 84 (3) (1995) 635–652.

[14] B.L. Karihaloo, F.I. Niordson, Optimum design of vibrating cantilevers, Journal of Optimization Theory and Applications 11 (1973) 638–654.

[15] F.-Y. Wang, P.X. Zhou, P. Lever, Dynamic effects of rotary inertia and shear deformation on flexible manipulators, in: Proceedings of IEEE International Conference on Systems, Man, and Cybernetics, Beijing, China (1996) 2315–2320.

[16] F.Y. Wang, G.G. Guan, Influences of rotary inertia, shear deformation and tip load on vibrations of flexible manipulators, Journal of Sound and Vibrations 171 (4) (1994) 433–452.

[17] F.-Y. Wang, J.L. Russell, Optimum shape construction of flexible manipulators with tip loads, in: Proceedings of IEEE International Conference on Decision and Control, Tucson, AZ 1 (1992) 311–316.

[18] F.Y. Wang, J.L. Russell, Optimum shape construction of flexible manipulators with total weight constraint, IEEE Transactions on Systems, Man, and Cybernetics, 25 (4) (1995) 605–614.

[19] F.-Y. Wang, J.L. Russell, A new approach to optimum flexible link design, in: Proceedings of IEEE International Conference on Robotics and Automation, Nagoya, Japan (1995) 931–936.

[20] J. Lin, F.L. Lewis, Improvement measurement/estimation technique for flexible link robot arm control, Proceedings of 32nd Conference on Decision and Control, San Antonio, TX (1993) 627–632.
[21] H. Geniele, R.V. Patel, K. Khorasani, End-point control of a flexible-link manipulator: Theory and experiments, IEEE Transactions on Control System Technology 5 (6) (1997) 556–570.
[22] S.K. Madhavan, S.N. Singh, Inverse trajectory control and zero dynamic sensitivity of an elastic manipulator, International Journal of Robotics and Automation 6 (4) (1991) 179–192.
[23] S.K. Madhavan, S.N. Singh, Sliding mode end point trajectory control of a two link elastic manipulator, in: Proceedings of 31th Conference on Decision and Control, Tucson, AZ (1992) 305–310.
[24] D. Wang, M. Vidyasagar, Modelling a class of multi-link manipulators with the last link flexible, IEEE Transactions on Robotics and Automation 8 (1) (1992) 33–41.
[25] Y. Aoustin, C. Chevallereau, The singular perturbation control of a two-flexible link robot, IEEE Conference on Robotics and Automation, Atlanta, GA (1993) 737–742.
[26] M. Moallem, K. Khorasani, R. Patel, An integral manifold approach for tip-position tracking of flexible multi-link manipulators, IEEE Transactions on Robotics and Automation 13 (6) (1997) 825–837.
[27] L.B. Gutierrez, F.L. Lewis, J.A. Lowe, Implementation of a neural network tracking controller for a single flexible link: Comparison with PD and PID controller, IEEE Transactions on Industrial Electronics 45 (2) (1998) 307–318.
[28] K. Lenz, H. Ozbay, A. Tannenbaum, J. Turi, B. Morton, Frequency domain analysis and robust control design for an ideal flexible beam, Automatica 27 (1991) 947–961.
[29] A. Tchernychev, A. Sideris, J. Yu, Constrained H_∞ control of an experimental flexible link, Transactions of the ASME 119 (2) (1997) 206–211.
[30] G. Zhu, T. Lee, S. Ge, Tip tracking control of a single-link flexible robot: A backstepping approach, Dynamics and Control 7 (1997) 341–360.
[31] A. Jnifene, A. Fahim, A computed torque/time delay approach to the end-point control of a one-link flexible manipulator, Dynamics and Control 7 (1997) 177–189.
[32] M. Ghanekar, D.W.L. Wang, R. Heppler, Scaling laws for linear controller of flexible link manipulators characterized by nondimensional groups, IEEE Transactions on Robotics and Automation 13 (1) (1997) 117–127.
[33] B. Liang, Y. Xu, M. Bergernan, Mapping a space manipulator to a dynamically equivalent manipulator, Journal of Dynamic Systems, Measurement, and Control 120 (3) (1998) 1–7.
[34] P. Tang, S. Lu, A video signal processing technique for vibration measurement of flexible beam, International Journal of Robotics Research 11 (6) (1992) 1610–1622.
[35] T. Fukuda, Control of flexible robot arm, Bulletin of the JSME 29 (250) (1986) 1269–1273.
[36] G.G. Hastings, W.J. Book, A linear dynamic model for flexible robotic manipulators, IEEE Control System Magazine 7 (1) (1987) 61–64.
[37] W.J. Wang, S.S. Lu, C.F. Hsu, Experiments on position control of a one-link flexible robot arm, IEEE International Journal of Robotics and Automation 5 (3) (1989) 373–377.
[38] N.G. Chalhoub, A.G. Ulsoy, Control of a flexible robot arm: Experiments and theoretical results, Journal of Dynamic System Measurement Control 109 (4) (1987) 299–309.
[39] N. Sundararajan, R.C. Montgomery, Experiments using lattice filters to identify the dynamics of a flexible beam, Journal of Dynamic System Measurement Control 107 (3) (1985) 187–191.
[40] A. Macchelli, C. Melchiorri, S. Stramigioli, Port-based modeling of a flexible link, IEEE Transactions on Robotics 23 (2) (2007) 650–660.
[41] Y. Xu, E. Ritz, Vision based flexible beam tip point control, IEEE Transactions on Control Systems Technology 17 (5) (2009) 1220–1227.
[42] L. Bascetta, P. Rocco, Two-time scale visual servoing of eye-in-hand flexible manipulators, IEEE Transaction on Robotics 22 (4) (2006) 818–830.
[43] J. Becedas, J.R. Trapero, V. Feliu, H. Sira-Ramírez, Adaptive controller for single-link flexible manipulators based on algebraic identification and generalized proportional integral control. IEEE Transactions on Systems, Man, and Cybernetics, Part B Cybernetics 39 (3) (2009) 735–751.
[44] M. Barczyk, A.F. Lynch, Flatness-based estimated state feedback control for a rotating flexible beam: Experimental results, IET Control Theory and Applications 2 (4) (2008) 288–302.

[45] M. Hosaka, T. Murakami, Vibration control of flexible arm by multiple observer structure, Electrical Engineering in Japan 154 (2) (2006) 68–75.
[46] A. Chatterjee, R. Chatterjee, F. Matsuno, T. Endo, Augmented stable fuzzy control for flexible robotic arm using LMI approach and neuro-fuzzy state space modeling, IEEE Transactions on Industrial Electronics 55 (3) (2008) 1256–1270.
[47] M. Dogan, Y. Istefanopulos, Optimal nonlinear controller design for flexible robot manipulators with adaptive internal model, IET Control Theory and Applications 1 (3) (2007) 770–778.
[48] C.A. Monje, F. Ramos, V. Feliu, B.M. Vinagre, Tip position control of a lightweight flexible manipulator using a fractional order controller, IET Control Theory and Applications 1 (5) (2007) 1451–1460.
[49] W.J. O'Connor, Wave-based analysis and control of lump-modeled flexible robots, IEEE Transactions on Robotics 23 (2) (2007) 342–352.
[50] X. Wang, D. Chen, Output tracking control of a one-link flexible manipulator via causal inversion, IEEE Transactions on Control Systems Technology 14 (1) (2006) 141–148.
[51] S.C.P. Gomes, V. Santos da Rosa, B. de Carvalho Albertini, Active control to flexible manipulators, IEEE/ASME Transactions on Mechatronics 11 (1) (2006) 75–83.
[52] F.Y. Wang, On the extremal fundamental frequencies of one-link flexible manipulators, International Journal of Robotics Research 13 (2) (1994) 162–170.
[53] F.Y. Wang, J.L. Russell, Minimum-weight robot arm for a specified fundamental frequency, Proceedings of the IEEE Conference on Robotics and Automation, Atlanta, GA 1 (1993) 490–495.
[54] F.Y. Wang, Optimum design of flexible manipulators: Integration of control and construction. Working Paper 40–91, SIE Department, University of Arizona, Tucson, AZ, 1991.

CHAPTER 3

Modeling of Flexible Manipulators

Chapter Outline

3.1 Introduction 16

3.2 Problem Description and Energy Calculations 17

3.2.1 Problem Statement 17

3.2.2 Kinetic Energy of the Beam 19

3.2.3 Kinetic Energy of the Tip Load 20

3.2.4 Total Potential Energy 21

3.2.5 Work Done by External Forces 21

3.3 Derivation of Equations of Motion 21

3.3.1 Euler—Bernoulli Beam Model Derivation 22

Variation with Respect to Variable θ 22

Variation with Respect to Variable w 24

3.3.2 Equations of Motion for Euler—Bernoulli Beam Model 26

3.3.3 Timoshenko Beam Model Derivation 27

Variation with Respect to Variable θ 27

Variation with Respect to Variable w 30

Variation with Respect to Variable φ 32

3.3.4 Equations of Motion for Timoshenko Beam Model 33

3.4 Linearization of the Beam Dynamic Models 34

3.4.1 Introduction 34

3.4.2 Euler—Bernoulli Model after Linearization 35

3.4.3 Timoshenko Model after Linearization 35

3.4.4 Dimensionless Functions, Variables, and Parameters 36

Euler—Bernoulli Model with Dimensionless Variables 36

Timoshenko Model with Dimensionless Variables 36

3.5 Finite-Dimensional Modeling of Flexible Manipulators 37

3.5.1 Natural Frequency and Modal Shapes 37

Modal Determinant 37

Modal Frequencies and Modal Shapes 39

3.5.2 Finite Modal Model of Euler—Bernoulli Beam 41

3.5.3 Finite Difference Model 47

3.5.4 Finite Element Model 51

References 57

Flexible Manipulators. DOI: 10.1016/B978-0-12-397036-7.00003-9

Copyright © 2012 Elsevier Inc. All rights reserved.

3.1 Introduction

The link flexibility of a robotic manipulator must be considered in modeling and control when the manipulator is of a large dimension or lightweight. Large manipulators play important roles in many applications, such as construction automation, environmental applications and space engineering. Lightweight arms have great potential in the design of high-performance industrial robotic manipulators since they allow high speed operation and low energy consumption. However, due to the complexity of the link deformation, which is a distributed parameter system, accurate modeling and high performance control of flexible manipulators pose a major challenge in practical design.

The concept of using flexible robotic manipulators was proposed as early as the 1970s by W.J. Book. Earlier models of arms are based on the simple assumed mode method. Some methods to improve the accuracy of the assumed mode method can be found in Gu and Tongue [1]. Over the last decade, a significant effort has been made in modeling and control of one-link flexible manipulators, which are essential for the understanding of general multiple-link flexible manipulators. The most commonly used deformation model in the current robotic literature uses the Euler–Bernoulli beam theory. Based on this theory, various dynamic equations have been formulated for one-link flexible manipulators [2–7]. The early works were conducted by Cannon and Schmitz [3] and Sakawa et al. [5]. Khorrami and Ozguner [4] modeled the link by a set of integral-partial differential equations and used the perturbation method to design control. Yang and Donath [8] considered the flexibility of the joints as well as the link flexibility. A comprehensive study on different dynamic equations under various boundary conditions for flexible manipulators was carried out by Bellezze et al. [2]. Wang and Wen [6] derived the dynamic equations for flexible manipulators subject to large rotation during the deformation and clarified some issues related to the specification of boundary conditions. Several investigations had also been made from the perspective of the mechanism where model complexity was not considered [9–11]. Issues related to control design have been studied by De Luca et al. [12,13], Tzes and Yurkovich [14], Wang and Vidyasagar [15,16], Kelemen and Bagchi [17], and Cetinkunt and Yu [18]. Various problems of optimal manipulator design based on the Euler–Bernoulli model have been investigated by Wang and Russell [19–23].

Most studies on the modeling and control of flexible manipulators have been made on the understanding of a single flexible link. Due to the complexity involved with link deformation however, establishing the exact dynamic model even for one link flexible manipulators is unrealistic, and certain simplifying approximations about the link deformation have to be made. In addition to small deformation, the most commonly used assumption in the robotic literature is that it can be satisfactorily modeled by the Euler–Bernoulli beam theory. Under such an assumption, the effects of both rotary inertia and shear deformation of a flexible link are neglected. However, it is well known in mechanics, particularly in beam and plate theory,

that both of them have significant effects on the dynamic behavior of flexible structures [24–29]. For example, it has been found that for shorter beams or thicker plates, the effects of rotary inertia or shear deformation could cause a magnitude of difference in the calculation of high order vibration frequencies. In Ref. [7] a similar conclusion has also been drawn by studying the influence of rotary inertia and shear deformation on vibration frequencies of flexible manipulators.

The purpose of this chapter is to conduct a detailed study of the modeling of one-link flexible manipulators. Section 3.2 presents basic equations for kinematic analysis and energy calculation. Based on Euler–Bernoulli and Timoshenko beam models, nonlinear dynamic equations and their linearized versions are given in Sections 3.3 and 3.4 respectively. Section 3.5 discusses some finite-dimensional modeling methods of flexible manipulators, including the assumed modal method, finite difference method and finite element method.

3.2 Problem Description and Energy Calculations

3.2.1 Problem Statement

Consider a flexible manipulator carrying a tip load. It consists of a flexible beam attached to a rigid hub in the horizontal plane. The coordinate systems are shown in Figure 3.1: (x_b,y_b) is a fixed base coordinate system, (x,y) is the local coordinate system attached to the hub. Figure 3.2 shows (a,b), the local coordinate system attached to the tip load. It is assumed that initially the neutral longitudinal axis (x-axis) of the beam and a-axis of the tip load coincide with the x_b-axis.

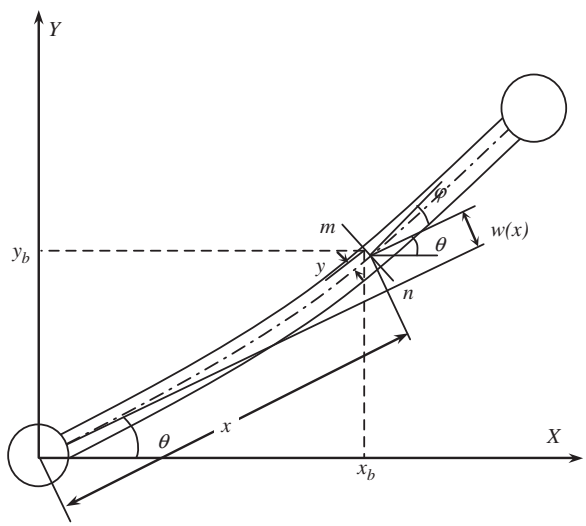

Figure 3.1: A Flexible Beam Fixed on a Rigid Hub in the Horizontal Plane.

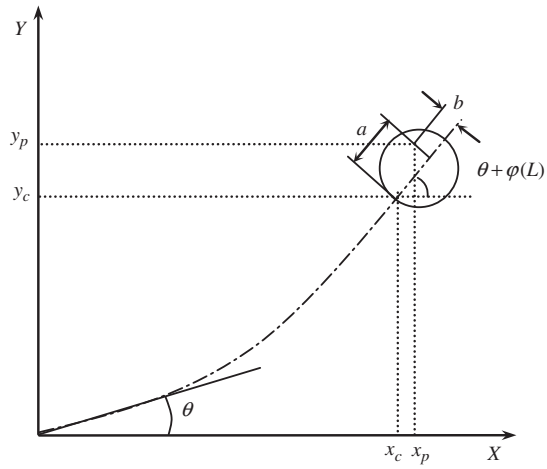

Figure 3.2: The Relation Between Local and Base Coordinate for Tip.

The motion of the manipulator system is described by the rotation angle $\theta(t)$ of the hub, lateral displacement $w(x,t)$ and rotation $\varphi(x,t)$ of the cross-section beam from the deformation position. We will use a prime to indicate the derivative with respect to x, and a dot for the derivative with respect to time. For example, $w' = \partial w/\partial x$, $\dot{w} = \partial w/\partial t$. Both Euler–Bernoulli and Timoshenko beam theories are investigated in this chapter. In the Euler–Bernoulli theory, the so-called normal plane assumption is used, i.e. it is assumed that any transverse section of the beam remains a plane and normal to the longitudinal axis of the beam after deformation [30]. In this case $\varphi = \partial w/\partial x = w'$ and the shear deformation of the beam is neglected. The Timoshenko theory takes the effect of shear deformation into account, replacing the normal plane assumption by the more accurate one plane assumption. The plane assumption states that any transverse section of the beam remains a plane but may not be perpendicular to the longitudinal axis of the beam after deformation [30]. As a result, beam rotation φ remains independent of w.

In the following, the equation of motion for flexible manipulators will be derived using Hamilton's principle [31]:

$$\int_{t_0}^{t_f} (\delta T + \delta W - \delta P)\mathrm{d}t = 0$$

where T, P, and W are the kinetic energy, potential energy of the system, and the work done by external forces respectively.

The total kinetic energy is calculated as follows:

$$T = \frac{1}{2} I_{\mathrm{H}} \dot{\theta}^2 + T_{\mathrm{b}} + T_{\mathrm{p}} \tag{3.1}$$

where I_H is the rotational inertia of the hub, whilst T_b and T_p are the kinetic energies of the beam and tip load respectively.

3.2.2 Kinetic Energy of the Beam

$$T_b = \int_0^L \iint_{s_b} 1/2\rho_v \left(\dot{x}_b^2 + \dot{y}_b^2\right) \mathrm{d}s_b \cdot \mathrm{d}x \tag{3.2}$$

Let

$$\begin{aligned} A &= \iint_{s_b} \mathrm{d}s_b && \text{area of beam section} \\ y_c &= \iint y \mathrm{d}s_b = 0 && \text{coordinate of center} \\ I &= \iint_{s_b} y^2 \mathrm{d}s_b && \text{moment of inertia} \\ \rho &= \rho_v A && \text{mass density per unit length} \end{aligned}$$

where s_b is the area of the cross-section, L is the length of the beam, and ρ_v is the mass density per unit volume.

Let a point on the beam have coordinates (x,y) before deformation. Its position in the base coordinate system is

$$x_b = x\cos\theta - w(x)\sin\theta - y\sin[\varphi(x) + \theta]$$

$$y_b = x\sin\theta + w(x)\cos\theta - y\cos[\varphi(x) + \theta]$$

$$T_b = \frac{1}{2}\int_0^L \rho\left[\left(x\dot{\theta} + \dot{w}\right)^2 + \left(w\dot{\theta}\right)^2 + S\left(\dot{\theta} + \dot{\varphi}\right)^2\right]\mathrm{d}x$$

Let

$$S = I/A \quad \text{and} \quad \Delta_x = x\dot{\theta} + \dot{w}(x,t), \quad \Delta_y = \dot{\theta}w(x,t) \tag{3.3}$$

Then

$$T_b = \frac{1}{2}\int_0^L \rho\left[\Delta_x^2 + \Delta_y^2 + S\left(\dot{\theta} + \dot{\varphi}^2\right)\right]\mathrm{d}x \tag{3.4}$$

Note that parameter S is the radius of gyration of the cross-section, reflecting the effect of rotary inertia. Ignoring the rotary inertia (setting $S = 0$) implies that one assumes that the velocity of every point on the same cross-section is identical and equal to the velocity of the point at the neutral axis on that cross-section.

3.2.3 Kinetic Energy of the Tip Load

The base coordinates of the point on the beam with $x = L$ after motion are

$$x_c = L\cos\theta - w(L)\sin\theta$$
$$y_c = L\sin\theta + w(L)\cos\theta$$

The kinetic energy of the tip mass (which represents the payload) is

$$T_p = \frac{1}{2}\iint_{sp} \rho_p\left(\dot{x}_p^2 + \dot{y}_p^2\right)\mathrm{d}s_p \tag{3.5}$$

where $\mathrm{d}s_\mathrm{p} = \mathrm{d}a\ \mathrm{d}b$ is the area occupied by the tip load. ρ_p is the mass density per unit area tip mass.

The base coordinate of a point (a,b) on the tip load is

$$x_p = L\cos\theta - w(L)\sin\theta + a\cos[\theta + \varphi(L)] - b\sin[\theta + \varphi(L)]$$
$$y_p = L\sin\theta + w(L)\cos\theta + a\sin[\theta + \varphi(L)] + b\cos[\theta + \varphi(L)]$$

where L is the length of the beam.

Let

$$M_p = \iint_{sp} \rho_p \mathrm{d}s_p \qquad \text{mass of tip}$$

$$J_p = \frac{1}{2}\iint_{sp} \rho_p\left(a^2 + b^2\right)\mathrm{d}s_p \qquad \text{moment of inertia of the tip mass w.r.t. the tip of the beam}$$

$$a_c = \iint_{sp} \rho_p a \mathrm{d}s_p / M_p \qquad \text{center of mass position in } (a, b) \text{ coordinates}$$

$$b_c = \iint_{sp} \rho_p b \mathrm{d}s_p / M_p \qquad \text{center of mass position in } (a, b) \text{ coordinates}$$

Therefore

$$\begin{aligned} T_p &= \frac{1}{2}\iint_{sp} \rho_p\left(\dot{x}_p^2 + \dot{y}_p^2\right)\mathrm{d}s_p \\ &= \frac{M_p}{2}[\Delta_x^2(L) + \Delta_y^2(L)] + \frac{J_p}{2}[\dot{\varphi}(L) + \dot{\theta}]^2 + M_p[\dot{\varphi}(L) + \dot{\theta}] \\ &\quad + \{[a_c\Delta_x(L) + b_c\Delta_y(L)]\cos\varphi(L) + [a_c\Delta_y(L) - b_c\Delta_x(L)]\sin\varphi(L)\} \end{aligned}$$

Let

$$G_x = a_c\Delta_x(L) + b_c\Delta_y(L)$$
$$G_y = a_c\Delta_y(L) - b_c\Delta_x(L)$$

We obtain the tip kinetic energy as

$$\begin{aligned} T_p &= \frac{1}{2}\iint_{sp} \rho_p \left(\dot{x}_p^2 + \dot{y}_p^2\right) \mathrm{d}s_p \\ &= \frac{M_p}{2}[\Delta_x^2(L) + \Delta_y^2(L)] + \frac{J_p}{2}[\dot{\varphi}(L) + \dot{\theta}]^2 \\ &\quad + M_p[\dot{\varphi}(L) + \dot{\theta}](G_x \cos\varphi + G_y \sin\varphi) \end{aligned} \tag{3.6}$$

If one assumes that the tip load is a point mass M_p, then $J_\mathrm{p} = 0$, $G_x = G_y = 0$.

3.2.4 Total Potential Energy

The relation between the bending moment and deformation is

$$M(x,t) = EI(x)\frac{\partial\varphi(x,t)}{\partial x}$$

and the relation between the shearing force and deformation is given by

$$Q(x,t) = kGA(x)(\varphi - w')$$

From beam theory [30], the total potential energy can be found as

$$P = \frac{1}{2}\int_0^L \left[D\varphi'^2 + C(\varphi - w')^2\right]\mathrm{d}s \tag{3.7}$$

where D and C are the bending rigidity and shear rigidity of the beam. For a beam of uniform cross-section, $D = EI$ and $C = kGA$, where E is Young's modulus, G the shear modulus, and k the shape factor [30,32].

3.2.5 Work Done by External Forces

The work done by external forces to the manipulator system is

$$\delta W = \tau\delta\theta \tag{3.8}$$

where τ is the torque applied at the hub.

3.3 Derivation of Equations of Motion

Substituting Eqs (3.1)–(3.6) into Hamilton's principle, we can get the equations of motion of flexible arms. This section presents the nonlinear equations that are obtained without ignoring any terms during the entire derivation process.

After a long and tedious process of variational calculation and simplification, the final results are summarized here.

3.3.1 Euler–Bernoulli Beam Model Derivation

For the Euler–Bernoulli model, there are three variables, θ, $w(x)$, and $\varphi(x)$. However, φ is related to w:

$$\varphi = \frac{\partial w}{\partial x}, \quad \dot{\varphi} = \frac{\mathrm{d}}{\mathrm{d}t}\left(\frac{\partial w}{\partial x}\right) = \dot{w}'.$$

Variation with Respect to Variable θ

The variation of the kinetic energy w.r.t. variable θ can be readily written as

$$\begin{aligned}\delta_\theta T = {} & I_H\dot{\theta}\,\frac{\mathrm{d}}{\mathrm{d}t}\delta\theta + \int_0^L \rho[(x\dot{\theta} + \dot{w}\ )x + w^2(x,t)\dot{\theta} + S(\dot{\theta} + \dot{w}')]\frac{\mathrm{d}}{\mathrm{d}t}\delta\theta\mathrm{d}x \\ & + M_p[(L\dot{\theta} + \dot{w}(L))L + w^2(L)\dot{\theta}]\frac{\mathrm{d}}{\mathrm{d}t}\delta\theta + J_p[\dot{\varphi}(L) + \dot{\theta}]\frac{\mathrm{d}}{\mathrm{d}t}\delta\theta \\ & + M_p\{(G_x\cos\varphi + G_y\sin\varphi) + [\dot{\varphi}(L) + \dot{\theta}][a_cL\cos\varphi(L) \\ & + b_c\cos\varphi(L)w(L) + a_c\sin\varphi(L)w(L) - b_cL\cos\varphi(L)]\}\frac{\mathrm{d}}{\mathrm{d}t}\delta\theta\end{aligned} \tag{3.9}$$

Let

$$\begin{aligned}F_x &= \Delta_x(L) + (a_c\cos\varphi - b_c\sin\varphi)(\dot{\varphi} + \dot{\theta}) \\ F_y &= \Delta_y(L) + (a_c\sin\varphi + b_c\cos\varphi)(\dot{\varphi} + \dot{\theta}) \\ F_{\varphi\theta} &= J_p[\dot{\varphi}(l) + \dot{\theta}] + M_p(G_x\cos\varphi + G_y\sin\varphi) \\ H_\theta &= \frac{\partial}{\partial t}\{F_{\varphi\theta} + M_p[LF_x + w(L)F_y]\}\end{aligned}$$

Substituting the foregoing equations into Eq. (3.9) and rearranging gives

$$\begin{aligned}\delta_\theta T = {} & I_H\dot{\theta}\frac{\mathrm{d}}{\mathrm{d}t}\delta\theta + \int_0^L \rho[(x\dot{\theta} + \dot{w}\ )x + w^2(x,t)\dot{\theta} + S(\dot{\theta} + \dot{w}')]\frac{\mathrm{d}}{\mathrm{d}t}\delta\theta\mathrm{d}x \\ & + \{F_{\varphi\theta} + M_p[F_xL + F_yw(L)]\}\frac{\mathrm{d}}{\mathrm{d}t}\delta\theta\end{aligned} \tag{3.10}$$

The potential energy is not a function of θ, so that the variation of potential energy is

$$\delta P_\theta = 0 \tag{3.11}$$

The virtual work due to nonconservative force is given by

$$\delta W_\theta = \tau\delta\theta \tag{3.12}$$

Substituting Eqs (3.10)–(3.12) into Hamilton's principle, we have

$$\begin{aligned}\delta_\theta &= \int_{t_0}^{t_f} (T + W - P)\mathrm{d}t \\ &= \int_{t_0}^{t_f} I_H \dot{\theta}\delta\dot{\theta}\mathrm{d}t + \int_{t_0}^{t_f}\int_0^L \rho[\dot{w}x + (x^2 + w^2(x,t))\dot{\theta} + S(\dot{\theta} + \dot{w}')]\mathrm{d}x\delta\dot{\theta}\mathrm{d}t \\ &\quad + \int_{t_0}^{t_f} \{F_{\varphi\theta} + M_p[F_x L + F_y w(L)]\}\delta\dot{\theta}\mathrm{d}t + \int_{t_0}^{t_f} \tau\delta\theta\mathrm{d}t\end{aligned} \tag{3.13}$$

We perform the following integration by parts with respect to time:

$$\int_{t_0}^{t_f} I_H \dot{\theta}\delta\dot{\theta}\mathrm{d}t = I_H \dot{\theta}\delta\theta\Big|_{t_0}^{t_f} - \int_{t_{0f}}^{t_f} I_H \ddot{\theta}\delta\theta\mathrm{d}t = -\int_{t_{0f}}^{t_f} I_H \ddot{\theta}\delta\theta\mathrm{d}t \tag{3.14}$$

where we take into account that $\delta\theta$ vanishes at $t = t_0$ and $t = t_f$. In a similar fashion, we obtain

$$\begin{aligned}&\int_{t_0}^{t_f}\int_0^L \rho[\dot{w}x + (x^2 + w^2(x,t))\dot{\theta} + S(\dot{\theta} + \dot{w}')]\mathrm{d}x\delta\dot{\theta}\mathrm{d}t \\ &\quad = \int_0^L \rho[\dot{w}x + (x^2 + w^2(x,t))\dot{\theta} + S(\dot{\theta} + \dot{w}')]\mathrm{d}x\delta\theta\Big|_{t_0}^{t_f} \\ &\qquad - \int_{t_0}^{t_f}\int_0^L \rho[\dot{w}x + (x^2 + w^2(x,t))\dot{\theta} + S(\dot{\theta} + \dot{w}')]\mathrm{d}x\delta\theta\mathrm{d}t\end{aligned} \tag{3.15}$$

and

$$\begin{aligned}&\int_{t_0}^{t_f} \{F_{\phi\theta} + M_p[F_x L + F_y w(L)]\}\delta\dot{\theta}\mathrm{d}t \\ &\quad = \{F_{\phi\theta} + M_p[F_x L + F_y w(L)]\}\delta\theta\Big|_{t_0}^{t_f} - \int_{t_0}^{t_f} \frac{\partial}{\partial t}\{F_{\phi\theta} + M_p[F_x L + F_y w(L)]\}\delta\theta\mathrm{d}t \\ &\quad = -\int_{t_0}^{t_f} \frac{\partial}{\partial t}\{F_{\phi\theta} + M_p[F_x L + F_y w(L)]\}\delta\theta\mathrm{d}t\end{aligned} \tag{3.16}$$

Substituting Eqs (3.14)–(3.16) into Eq. (3.13) and rearranging, we obtain

$$\begin{aligned}&\delta_\theta \int_{t_0}^{t_f} (T + W - P)\mathrm{d}t \\ &\quad = \left\{I_H \ddot{\theta} + \frac{\partial}{\partial t}\int_0^L \rho[x\dot{w} + (x^2 + w^2)\dot{\theta} + S(\dot{\theta} + \dot{w}')]\mathrm{d}x + H_\theta - \tau\right\}\delta\theta = 0\end{aligned}$$

Since the virtual displacements are arbitrary and independent, we must have

$$I_H\ddot{\theta} + \frac{\partial}{\partial t}\int_0^L \rho[x\dot{w} + (x^2 + w^2)\dot{\theta} + S(\dot{\theta} + \dot{w}')]\mathrm{d}x + H_\theta - \tau = 0$$

We get one motion equation

$$I_H\ddot{\theta} + \frac{\partial}{\partial t}\int_0^L \rho[x\dot{w} + (x^2 + w^2)\dot{\theta} + S(\dot{\theta} + \dot{w}')]\mathrm{d}x + H_\theta = \tau$$

Variation with Respect to Variable w

The variation of the kinetic energy w.r.t. variable w is

$$\begin{aligned}
\delta_w T = &\int_0^L \rho\left\{\left[(x\dot{\theta} + \dot{w})\frac{\mathrm{d}}{\mathrm{d}t}\delta w + w(x,t)\dot{\theta}^2\delta w + S(\dot{\theta} + \dot{w}')\right]\frac{\mathrm{d}}{\mathrm{d}t}\left(\frac{\partial}{\partial x}\delta w\right)\right\}\mathrm{d}x \\
&+ M_p\left[\Delta_x(L)\frac{\mathrm{d}}{\mathrm{d}t}\delta w + \Delta_y(L)\dot{\theta}\delta w\right] + J_p[\dot{\varphi}(L) + \dot{\theta}]\frac{\mathrm{d}}{\mathrm{d}t}\left(\frac{\partial}{\partial x}\delta w\right)\Big|_{x=L} \\
&+ M_p\left\{(G_x\cos\varphi + G_y\sin\varphi)\frac{\mathrm{d}}{\mathrm{d}t}\left(\frac{\partial}{\partial x}\delta w\right) + [\dot{\varphi}(L) + \dot{\theta}]\left[a_c\frac{\mathrm{d}}{\mathrm{d}t}\delta w + b_c\dot{\theta}\delta w\right]\cos\varphi\Big|_{x=L}\right. \\
&\qquad \left. -G_x\sin\varphi\frac{\partial}{\partial x}\delta w + \left[a_c\dot{\theta}\delta w - b_c\frac{\mathrm{d}}{\mathrm{d}t}\delta w\right]\sin\varphi\Big|_{x=L} + G_y\cos\varphi\frac{\partial}{\partial x}\delta w\right\} \\
= &\int_0^L \rho\{[(x\dot{\theta} + \dot{w})\dot{\delta w} + w(x,t)\dot{\theta}^2\delta w + S(\dot{\theta} + \dot{w}')]\delta\dot{w}'\}\mathrm{d}x \\
&+ M_p[\Delta_x(L)\delta\dot{w} + \Delta_y(L)\dot{\theta}\delta w] + J_p[\dot{\varphi}(L) + \dot{\theta}]\delta\dot{w}' \\
&+ M_p(G_x\cos\varphi + G_y\sin\varphi)\delta\dot{w}' + M_p(\dot{\varphi}(L) + \dot{\theta}))(a_c\sin\varphi + b_c\cos\varphi)\dot{\theta}\delta w \\
&+ (\dot{\varphi}(L) + \dot{\theta})(a_c\cos\varphi - b_c\sin\varphi)\delta\dot{w} + (\dot{\varphi}(L) + \dot{\theta})(G_y\cos\varphi - G_x\sin\varphi)\delta w'] \\
= &\int_0^L \rho\{[(x\dot{\theta} + \dot{w})\dot{\delta w} + w(x,t)\dot{\theta}^2\delta w + S(\dot{\theta} + \dot{w}')]\delta\dot{w}'\}dx + M_p[\Delta_x(L) \\
&+ (a_c\cos\varphi - b_c\sin\varphi)]\delta\dot{w} + \{J_p[\dot{\varphi}(L) + \dot{\theta}] + M_p(G_x\cos\varphi + G_y\sin\varphi)\}\delta\dot{w}' \\
&+ M_p[\Delta_y(L) + (\dot{\varphi}(L) + \dot{\theta})(a_c\sin\varphi + b_c\cos\varphi)]\dot{\theta}\delta w \\
&+ (\dot{\varphi}(L) + \dot{\theta})(G_y\cos\varphi - G_x\sin\varphi)\delta w'
\end{aligned}$$

Let $F_\varphi = (\dot{\varphi} + \dot{\theta})(G_y \cos\varphi - G_x \sin\varphi)$. The equation above can be rewritten as

$$\begin{aligned}\delta_w T = &\int_0^L \rho\{(x\dot{\theta} + \dot{w})\delta\dot{w} + \dot{\theta}^2 w\delta w + S(\dot{\varphi} + \dot{\theta})\delta\dot{w}'\}\mathrm{d}x + M_p F_x \delta\dot{w} \\ &+ M_p F_y \dot{\theta}\delta w + F_{\varphi\theta}\delta\dot{w}' + M_p F_\varphi \delta w'\end{aligned} \tag{3.17}$$

The variation of the potential energy is given by

$$\begin{aligned}\delta_w P &= \int_0^L D\varphi'\delta\varphi' dx = \int_0^L D\frac{\partial^2 w}{\partial x^2}\frac{\partial^2 \delta w}{\partial x^2}\mathrm{d}x \\ &= D\frac{\partial^2 w}{\partial x^2}\delta w'\Big|_0^L - \int_0^L Dw'''\delta w' dx \\ &= Dw''\delta w'\Big|_0^L - Dw'''\delta w\Big|_0^L + \int_0^L Dw''''\delta w\mathrm{d}x\end{aligned} \tag{3.18}$$

The work due to force

$$\delta_w W = 0 \tag{3.19}$$

Substituting Eqs (3.17)–(3.19) into Hamilton's principle gives

$$\begin{aligned}&\delta_w \int_{t_0}^{t_f} (T + W - P)\mathrm{d}t \\ &= \int_0^L\int_{t_0}^{t_f} \rho x\ddot{\theta}\delta w\mathrm{d}x\mathrm{d}t - \int_0^L\int_{t_0}^{t_f} \rho\ddot{w}\delta w\mathrm{d}x\mathrm{d}t + \int_0^L\int_{t_0}^{t_f} \rho\dot{\theta}^2 w\delta w\mathrm{d}x\mathrm{d}t - S\rho\int_{t_0}^{t_f}[\ddot{w}'\delta w\Big|_0^L \\ &\quad - \int_{t_0}^{t_f}\ddot{w}''\delta w\mathrm{d}x]\mathrm{d}t - S\rho\int_{t_0}^{t_f}\ddot{\theta}\delta w\Big|_0^L\mathrm{d}t + \int_{t_0}^{t_f}(M_p Fx\delta\dot{w} + M_p F_y\dot{\theta}\delta w + F_{\varphi\theta}\delta\dot{w}' + M_p F_\varphi\delta w')\mathrm{d}t \\ &\quad - \int_{t_0}^{t_f}(Dw''\delta w'\Big|_0^L - Dw'''\delta w\Big|_0^L + \int_0^L Dw''''\delta w\mathrm{d}x)\mathrm{d}t\end{aligned}$$

After performing the integration by parts with respect to time, we have

$$\delta_w \int_{t_0}^{t_f} (T + W - P)\mathrm{d}t$$

$$= \int_{t_0}^{t_f} \int_0^L [\rho(-x\ddot{\theta} - \ddot{w} + \dot{\theta}^2 w + S\ddot{w}'' - Dw'''')\delta w \mathrm{d}x\mathrm{d}t$$

$$+ \int_{t_0}^{t_f} (-\rho S\ddot{w}' - \dot{F}_x M_p + M_p F_y \dot{\theta} - \rho S\ddot{\theta} + Dw''')\Big|_0^L \delta w \mathrm{d}t$$

$$+ \int_{t_0}^{t_f} (-Dw'' - \dot{F}_{\varphi\theta} + M_p F\varphi)\Big|_0^L \delta w' \mathrm{d}t = 0$$

The displacement δw is arbitrary. Hence, we must have

$$[\rho(-x\ddot{\theta} - \ddot{w} + \dot{\theta}^2 w + S\ddot{w}'' - Dw'''] = 0$$

for the items:

$$(-\rho S\ddot{w}' - \dot{F}_x M_p + M_p F_y \dot{\theta} - \rho S\ddot{\theta} + Dw''')\Big|_0^L \delta w = 0$$
$$(-Dw'' - \dot{F}_{\varphi\theta} + M_p F\varphi)\Big|_0^L \delta w' = 0$$

According to our system, δw and $\delta w'$ vanish at the point $x = 0$, for $x = L$, δw and $\delta w' \neq 0$. We obtain boundary conditions:

$$x = 0, \quad w = 0, \quad w' = 0$$
$$x = L, \quad Dw'' + H_\varphi = 0, \quad (Dw'')' - \rho S(\ddot{w}' + \ddot{\theta}) - H_w = 0$$

and another equation of motion:

$$(Dw'')'' + \rho(x\ddot{\theta} + \ddot{w} - S\ddot{w}'' - \dot{\theta}^2 w) = 0$$

where

$$H_w = M_p(\dot{F}_x - \dot{\theta}F_y), \quad H_\varphi = \dot{F}_{\varphi\theta} - M_p F_\varphi$$

3.3.2 Equations of Motion for Euler–Bernoulli Beam Model

To summarize, the resulting motion equations are found to be

$$(Dw'')'' + \rho(x\ddot{\theta} + \ddot{w} - S\ddot{w}'' - \dot{\theta}^2 w) = 0 \tag{3.20}$$

$$I_H\ddot{\theta} + \frac{\partial}{\partial t}\int_0^L \rho[x\dot{w} + (x^2 + w^2)\dot{\theta} + S(\dot{\theta} + \dot{w}')]\mathrm{d}x + H_\theta = \tau \tag{3.21}$$

with the corresponding boundary conditions:

$$x = 0, \quad w = 0, \quad w' = 0 \tag{3.22}$$

$$x = L, \quad Dw'' + H_\varphi = 0, \quad (Dw'')' - \rho S(\ddot{w}' + \ddot{\theta}) - H_w = 0 \tag{3.23}$$

where

$$F_x = \Delta_x(L) + (a_c \cos\varphi - b_c \sin\varphi)(\dot{\varphi} + \dot{\theta})$$

$$F_y = \Delta_y(L) + (a_c \sin\varphi + b_c \cos\varphi)(\dot{\varphi} + \dot{\theta})$$

$$F_{\phi\theta} = J_p[\dot{\varphi}(l) + \dot{\theta}] + M_p(G_x \cos\varphi + G_y \sin\varphi)$$

$$H_\theta = \frac{\partial}{\partial t}\{F_{\varphi\theta} + M_p[LF_x + w(L)F_y]\}$$

$$H_w = M_p(\dot{F}_x - \dot{\theta}F_y), \quad H_\varphi = \dot{F}_{\varphi\theta} - M_pF_\varphi$$

3.3.3 Timoshenko Beam Model Derivation

For the Timoshenko model, there are three independent variables, θ, $w(x)$, and $\varphi(x)$.

Variation with Respect to Variable θ

The variation of the kinetic energy w.r.t. variable θ can be readily written as

$$\begin{aligned}\delta_\theta T = {} & I_H\dot{\theta}\frac{\mathrm{d}}{\mathrm{d}t}\delta\theta + \int_0^L \rho[(x\dot{\theta} + \dot{w})x + w^2(x,t)\dot{\theta} + S(\dot{\theta} + \dot{w}')]\frac{\mathrm{d}}{\mathrm{d}t}\delta\theta\mathrm{d}x \\ & + M_p[(L\dot{\theta} + \dot{w}(L))L + w^2(L)\dot{\theta}]\frac{\mathrm{d}}{\mathrm{d}t}\delta\theta + J_p[\dot{\varphi}(L) + \dot{\theta}]\frac{\mathrm{d}}{\mathrm{d}t}\delta\theta \\ & + M_p\{(G_x \cos\varphi + G_y \sin\varphi) + [\dot{\varphi}(L) + \dot{\theta}][a_cL\cos\varphi(L) \\ & + b_c \cos\varphi(L)w(L) + a_c \sin\varphi(L)w(L) - b_cL\cos\varphi(L)]\}\frac{\mathrm{d}}{\mathrm{d}t}\delta\theta\end{aligned} \tag{3.24}$$

Letting

$$
\begin{aligned}
F_x &= \Delta_x(L) + (a_c \cos\varphi - b_c \sin\kappa\varphi)(\dot{\varphi} + \dot{\theta}) \\
F_y &= \Delta_y(L) + (a_c \sin\varphi + b_c \cos\varphi)(\dot{\varphi} + \dot{\theta}) \\
F_{\varphi\theta} &= J_p[\dot{\varphi}(l) + \dot{\theta}] + M_p(G_x \cos\varphi + G_y \sin\varphi) \\
H_\theta &= \frac{\partial}{\partial t}\left\{F_{\varphi\theta} + M_p[LF_x + w(L)F_y]\right\}
\end{aligned}
$$

substituting the above equations into Eq. (3.24) and rearranging:

$$
\begin{aligned}
\delta_\theta T = I_H\dot{\theta}\frac{\mathrm{d}}{\mathrm{d}t}\delta\theta + \int_0^L \rho[(x\dot{\theta} + \dot{w}\ )x + w^2(x,t)\dot{\theta} + S(\dot{\theta} + \dot{w}')]\frac{\mathrm{d}}{\mathrm{d}t}\delta\theta\mathrm{d}x \\
+ \{F_{\phi\theta} + M_p[F_xL + F_yw(L)]\}\frac{\mathrm{d}}{\mathrm{d}t}\delta\theta
\end{aligned}
\tag{3.25}
$$

The potential energy is not a function of θ, so that the variation of the potential energy is simply

$$
\delta P_\theta = 0 \tag{3.26}
$$

The virtual work due to nonconservative force is given by

$$
\delta W_\theta = \tau\delta\theta \tag{3.27}
$$

Substituting Eqs (3.25)–(3.27) into Hamilton's principle, we have

$$
\begin{aligned}
&\delta_\theta \int_{t_0}^{t_f} (T + W - P)\mathrm{d}t \\
&= \int_{t_0}^{t_f} I_H\dot{\theta}\delta\dot{\theta}\mathrm{d}t + \int_{t_0}^{t_f}\int_0^L \rho[(\dot{w}x + (x^2 + w^2(x,t))\dot{\theta} + S(\dot{\theta} + \dot{w}')]\mathrm{d}x\delta\dot{\theta}\mathrm{d}t \\
&\quad + \int_{t_0}^{t_f} \{F_{\varphi\theta} + M_p[F_xL + F_yw(L)]\}\delta\dot{\theta}\mathrm{d}t + \int_{t_0}^{t_f} \tau\delta\theta\mathrm{d}t
\end{aligned}
\tag{3.28}
$$

We perform the following integration by parts with respect to time:

$$
\int_{t_0}^{t_f} I_H\dot{\theta}\delta\dot{\theta}\mathrm{d}t = I_H\dot{\theta}\delta\theta\Big|_{t_0}^{t_f} - \int_{t_{0f}}^{t_f} I_H\ddot{\theta}\delta\theta\mathrm{d}t = -\int_{t_{0f}}^{t_f} I_H\ddot{\theta}\delta\theta\mathrm{d}t \tag{3.29}
$$

where $\delta\theta$ vanishes at $t = t_0$ and $t = t_f$. In a similar fashion, we obtain

$$\begin{aligned}
&\int_{t_0}^{t_f}\int_0^L \rho[(\dot{w}x + (x^2 + w^2(x,t))\dot{\theta} + S(\dot{\theta} + \dot{w}')]\mathrm{d}x\delta\dot{\theta}\mathrm{d}t \\
&\quad = \int_0^L \rho[(\dot{w}x + (x^2 + w^2(x,t))\dot{\theta} + S(\dot{\theta} + \dot{w}')]\mathrm{d}x\delta\theta\Big|_{t_0}^{t_f} \\
&\qquad - \int_{t_0}^{t_f}\int_0^L \rho[(\dot{w}x + (x^2 + w^2(x,t))\dot{\theta} + S(\dot{\theta} + \dot{w}')]\mathrm{d}x\delta\theta\mathrm{d}t
\end{aligned} \tag{3.30}$$

and

$$\begin{aligned}
&\int_{t_0}^{t_f}\{F_{\varphi\theta} + M_p[F_xL + F_yw(L)]\}\delta\dot{\theta}\mathrm{d}t \\
&\quad = \{F_{\varphi\theta} + M_p[F_xL + F_yw(L)]\}\delta\theta\Big|_{t_0}^{t_f} - \int_{t_0}^{t_f}\frac{\partial}{\partial t}\{F_{\varphi\theta} + M_p[F_xL + F_yw(L)]\}\delta\theta\mathrm{d}t \\
&\quad = -\int_{t_0}^{t_f}\frac{\partial}{\partial t}\{F_{\varphi\theta} + M_p[F_xL + F_yw(L)]\}\delta\theta\mathrm{d}t
\end{aligned} \tag{3.31}$$

Substituting Eqs (3.29)–(3.31) into Eq. (3.28) and rearranging, we obtain

$$\begin{aligned}
&\delta_\theta\int_{t_0}^{t_f}(T + W - P)\mathrm{d}t \\
&\quad = \left\{I_H\ddot{\theta} + \frac{\partial}{\partial t}\int_0^L \rho[x\dot{w} + (x^2 + w^2)\dot{\theta} + S(\dot{\theta} + \dot{w}')]\mathrm{d}x + H_\theta - \tau\right\}\delta\theta = 0
\end{aligned}$$

The virtual displacement $\delta\theta$ is arbitrary and independent. We must have

$$I_H\ddot{\theta} + \frac{\partial}{\partial t}\int_0^L \rho[x\dot{w} + (x^2 + w^2)\dot{\theta} + S(\dot{\theta} + \dot{w}')]\mathrm{d}x + H_\theta - \tau = 0 \tag{3.32}$$

Therefore, the equation of motion is

$$I_H\ddot{\theta} + \frac{\partial}{\partial t}\int_0^L \rho[x\dot{w} + (x^2 + w^2)\dot{\theta} + S(\dot{\theta} + \dot{w}')]\mathrm{d}x + H_\theta = \tau$$

Variation with Respect to Variable w

The variation of the potential energy w.r.t. w is

$$\begin{aligned}
\delta_w T &= \int_0^L \rho[(x\dot{\theta} + \dot{w})\delta\dot{w} + \dot{\theta}^2 w\delta w]\mathrm{d}x + M_p(\Delta_x\delta\dot{w} + \Delta_y\delta w) \\
&\quad + M_p(\dot{\varphi}(L) + \dot{\theta})[(a_c\cos\varphi - b_c\sin\varphi)\delta\dot{w} + (a_c\sin\varphi + b_c\cos\varphi)\delta w\dot{\theta}] \\
&= \int_0^L \rho[(x\dot{\theta} + \dot{w})\delta\dot{w} + \dot{\theta}^2 w\delta w]\mathrm{d}x + M_p\delta\dot{w}(L)[\Delta_x + (\dot{\varphi}(L) + \dot{\theta}) \\
&\quad (a_c\cos\varphi - b_c\sin\varphi)] + M_p\dot{\theta}\delta w(L)\{[\dot{\varphi}(L) + \dot{\theta}](a_c\sin\varphi + b_c\cos\varphi) + \Delta_y\} \\
&= \int_0^L \rho[(x\dot{\theta} + \dot{w})\delta\dot{w} + \dot{\theta}^2 w\delta w]dx + M_p\delta\dot{w}(L)F_x + M_p\dot{\theta}\delta w(L)F_y
\end{aligned} \tag{3.33}$$

The variation of potential energy is given by

$$\delta_w P = \int_0^L c(\varphi - w')\left(-\frac{\partial}{\partial x}\delta w\right)\mathrm{d}x = -c(\varphi - w')\delta w\Big|_0^L + \int_0^L c(\varphi - w')'\delta w\mathrm{d}x \tag{3.34}$$

The work due to force is

$$\delta W_w = 0 \tag{3.35}$$

Substituting Eqs (3.33)–(3.35) into Hamilton's principle yields

$$\begin{aligned}
&\delta_w \int_{t_0}^{t_f} (T + W - P)\mathrm{d}t \\
&= \int_{t_0}^{t_f}\int_0^L \rho[(x\dot{\theta} + \dot{w})\delta\dot{w} + \dot{\theta}^2 w\delta w - c(\varphi - w')'\delta w]\mathrm{d}x\mathrm{d}t \\
&\quad + \int_{t_0}^{t_f}[M_p\delta\dot{w}(L)F_x + M_p\dot{\theta}\delta w(L)F_y]\mathrm{d}t + \int_{t_0}^{t_f} c(\varphi - w')\delta w\Big|_0^L\mathrm{d}t
\end{aligned} \tag{3.36}$$

We perform the following integration by parts with respect to time:

$$\begin{aligned}
&\int_{t_0}^{t_f}\int_0^L \rho[(x\dot{\theta}+\dot{w})\delta\dot{w}+\dot{\theta}^2 w\delta w - c(\varphi - w')'\delta w]\mathrm{d}x\mathrm{d}t \\
&= \int_0^L \mathrm{d}x\rho\left\{x\dot{\theta}\delta w\Big|_{t_0}^{t_f} - \int_{t_0}^{t_f} x\ddot{\theta}w\delta w\mathrm{d}t + \dot{w}\delta w\Big|_{t_0}^{t_f} - \int_{t_0}^{t_f}\ddot{w}\delta w\mathrm{d}t \right. \\
&\quad \left. + \int_{t_0}^{t_f}\dot{\theta}^2 w\delta w\mathrm{d}t - \int_{t_0}^{t_f} c(\varphi - w')'\delta w\mathrm{d}t\right\} \\
&= \int_0^L\int_{t_0}^{t_f}\rho\{(-x\ddot{\theta}-\ddot{w}+\dot{\theta}^2 w) - c(\varphi - w')'\}\delta w\mathrm{d}x\mathrm{d}t
\end{aligned} \tag{3.37}$$

where δw vanishes at $t = t_0$ and $t = t_f$. Similarly:

$$\begin{aligned}
&\int_{t_0}^{t_f}[M_p\delta\dot{w}(L)F_x + M_p\dot{\theta}\delta w(L)F_y]\mathrm{d}t \\
&= M_p\left[F_x\delta w\Big|_{t_0}^{t_f} - \int_{t_0}^{t_f}\dot{F}_x\delta w\mathrm{d}t\right] + \int_{t_0}^{t_f} M_p\dot{\theta}F_y\delta w\mathrm{d}t \\
&= -M_p\int_{t_0}^{t_f}\dot{F}_x\delta w\mathrm{d}t + \int_{t_0}^{t_f} M_p\dot{\theta}F_y\delta w\mathrm{d}t \\
&= \int_{t_0}^{t_f} -H_w\delta w\mathrm{d}t
\end{aligned} \tag{3.38}$$

Substituting Eqs (3.37) and (3.38) into Eq. (3.36), we obtain

$$\begin{aligned}
&\delta_w\int_{t_0}^{t_f}(T+W-P)\mathrm{d}t \\
&= \int_0^L\int_{t_0}^{t_f}\rho\{(-x\ddot{\theta}-\ddot{w}+\dot{\theta}^2 w) - c(\varphi - w')'\}\delta w\mathrm{d}x\mathrm{d}t + \int_{t_0}^{t_f}\{-H_w + c(\varphi - w')'\}\delta w(L)\mathrm{d}x\mathrm{d}t
\end{aligned}$$

The displacement δw is arbitrary. Hence, we must have

$$C(\varphi - w') + \rho(x\ddot{\theta} + \ddot{w} - \dot{\theta}^2 w) = 0 \tag{3.39}$$

$$C(\varphi - w') - H_w = 0 \quad \text{when } x = L \tag{3.40}$$

We get one equation of motion:

$$C(\varphi - w') + \rho(x\ddot{\theta} + \ddot{w} - \dot{\theta}^2 w) = 0 \tag{3.41}$$

with boundary conditions

$$\begin{aligned} x = 0, &\quad w = 0 \\ x = L, &\quad C(\varphi - w') - H_w = 0 \end{aligned} \tag{3.42}$$

Variation with Respect to Variable φ

Now we take the variation for the potential energy w.r.t. φ:

$$\begin{aligned} \delta_\varphi T &= \int_0^L \rho S(\dot{\varphi} + \dot{\theta})\delta\dot{\varphi}\mathrm{d}x + J_p[\dot{\varphi}(L) + \dot{\theta}]\delta\dot{\varphi} \\ &\quad + M_p(G_x \cos\varphi + G_y \sin\varphi)\delta\dot{\varphi} + M_p(\dot{\varphi}(L) + \dot{\theta})[(G_y \cos\varphi - G_x \sin\varphi)\delta\dot{\varphi} \\ &= \int_0^L \rho S(\dot{\varphi} + \dot{\theta})\delta\dot{\varphi}\mathrm{d}x + F_{\varphi\theta}\delta\dot{\varphi} + M_p F_\varphi \end{aligned} \tag{3.43}$$

The variation of potential energy is given by

$$\begin{aligned} \delta_w P &= \int_0^L [D\varphi'\delta\varphi' + c(\varphi - w')\delta\varphi]\mathrm{d}x \\ &= D\varphi'\delta\varphi\Big|_0^L - \int_0^L \{D\varphi''\delta\varphi\mathrm{d}x - c(\varphi - w')\}\delta\varphi\mathrm{d}x \end{aligned} \tag{3.44}$$

The work due to force is

$$\delta W_\varphi = 0 \tag{3.45}$$

Substituting Eqs (3.43)–(3.45) into Hamilton's principle:

$$\begin{aligned} &\delta_\varphi \int_{t_0}^{t_f} (T + W - P)\mathrm{d}t \\ &= \int_{t_0}^{t_f} \int_0^L \{\rho S(\dot{\varphi} + \dot{\theta})\delta\dot{\varphi} + [D\varphi''\delta\varphi - c(\varphi - w')]\delta\varphi\}\mathrm{d}x\mathrm{d}t \\ &\quad + \int_{t_0}^{t_f} [-D\varphi'\mathrm{d}t + M_p F_\varphi - \dot{F}_{\varphi\theta}]\delta\varphi(L)\mathrm{d}t \end{aligned}$$

We perform the following integration by parts with respect to time:

$$\begin{aligned}
&\int_{t_0}^{t_f}\int_0^L \{\rho S(\dot{\varphi}+\dot{\theta})\delta\dot{\varphi} + [D\varphi''\delta\varphi - c(\varphi - w')]\delta\varphi\}\mathrm{d}x\mathrm{d}t \\
&\quad = \int_0^L \mathrm{d}x\rho S\{(\dot{\varphi}+\dot{\theta})\delta\varphi\Big|_{t_0}^{t_f} - \int_{t_0}^{t_f}(\ddot{\varphi}+\ddot{\theta})\delta\varphi\mathrm{d}t\} + \int_{t_0}^{t_f}\int_0^L \{D\varphi'' - c(\varphi - w')\}\delta\varphi\mathrm{d}x\mathrm{d}t \\
&\quad = -\int_{t_0}^{t_f}(\ddot{\varphi}+\ddot{\theta})\delta\varphi\mathrm{d}t\} + \int_{t_0}^{t_f}\int_0^L \{D\varphi'' - c(\varphi - w')\}\delta\varphi\mathrm{d}x\mathrm{d}t
\end{aligned}$$

where we took into account $\delta\phi$ vanishing at $t = t_0$ and $t = t_f$:

$$\begin{aligned}
&\delta_\varphi \int_{t_0}^{t_f}(T + W - P)\mathrm{d}t \\
&\quad = \int_{t_0}^{t_f}[-D\varphi'\mathrm{d}t - H_\varphi]\delta\varphi(L)\mathrm{d}t + \int_{t_0}^{t_f}\int_0^L \{-\rho S(\ddot{\varphi}+\ddot{\theta}) + D\varphi'' - c(\varphi - w')\}\delta\varphi\mathrm{d}x\mathrm{d}t \\
&\quad = 0
\end{aligned}$$

The displacement $\delta\phi$ is arbitrary. Hence, we must have

$$\begin{gathered}
(D\varphi')' - c(\varphi - w') - \rho S(\ddot{\varphi}+\ddot{\theta}) = 0 \\
D\varphi' + H_\varphi = 0 \quad \text{when } x = L
\end{gathered}$$

We get another equation of motion:

$$(D\varphi')' - c(\varphi - w') - \rho S(\ddot{\varphi}+\ddot{\theta}) = 0$$

with boundary conditions

$$\begin{gathered}
x = 0, \quad \varphi = 0 \\
x = L, \quad D\varphi' + H_\varphi = 0
\end{gathered}$$

3.3.4 Equations of Motion for Timoshenko Beam Model

To summarize, the motion equations are found to be

$$(D\varphi')' - c(\varphi - w') - \rho S(\ddot{\varphi}+\ddot{\theta}) = 0 \tag{3.46}$$

$$C(\varphi - w') + \rho(x\ddot{\theta} + \ddot{w} - \dot{\theta}^2 w) = 0, \tag{3.47}$$

$$I_H\ddot{\theta} + \frac{\partial}{\partial t}\int_0^L \rho[x\dot{w} + (x^2 + w^2)\dot{\theta} + S(\dot{\theta} + \dot{w}')]\mathrm{d}x + H_\theta = \tau \tag{3.48}$$

with boundary conditions

$$x = 0, \quad w = 0, \quad \varphi = 0 \tag{3.49}$$

$$x = L, \quad D\varphi' + H_\varphi = 0, \quad C(\varphi - w') - H_w = 0 \tag{3.50}$$

where $H\theta$, $H\varphi$, and H_w are given by the same equations as in the Euler–Bernoulli model. Note that now we have three, instead of two, coupled motion equations.

3.4 Linearization of the Beam Dynamic Models

3.4.1 Introduction

In order to analyze fundamental vibration behavior and the time response of the manipulator system, we need to linearize the nonlinear dynamic equations. The dynamic models after linearization are easier to analyze and easier for control design.

To linearize the dynamic models described in the previous section, we neglect all deformation terms which are higher than the first order. This is justified due to the small deformation assumption. All the second or higher order displacement and strain terms are ignored [30] for both the Euler–Bernoulli and Timoshenko beam theories. In addition, we ignore all the second or higher order cross terms. Note that these simplifications have been adopted in almost all the published works on modeling of flexible manipulators. As we can see later from the simulation results, nonlinear terms have noticeable effects on dynamic responses of flexible arms only when motion speeds are extremely high.

After a tedious process of simplification, we arrive at the following relationships:

$$\begin{aligned} H_\theta &= H_\varphi + LH_w, \quad H_w = m_p\dot{F}_x, \quad H_\varphi = \dot{F}_{\varphi\theta} \\ F_x &= \Delta_x(x) + a_c(\dot{\varphi} + \dot{\theta}) \\ F_{\varphi\theta} &= J_p(\dot{\varphi} + \dot{\theta}) + a_c M_p \Delta_x(L) \end{aligned}$$

Therefore

$$\frac{\partial}{\partial t}\int_0^L \rho[s(\dot{w} + s\dot{\theta}) + S(\dot{\theta} + \dot{\varphi})]\mathrm{d}s + H_\theta = -D\varphi'(0) \tag{3.51}$$

which enables us to eliminate the integral terms in dynamic equations.

To make the form of dynamic equations simpler, we further define the total deflection ν and rotation α of the manipulator as

$$\nu(x,t) = w(x,t) + x\theta(t), \quad \alpha(x,t) = \varphi(x,t) + \theta(t) \tag{3.52}$$

In terms of the total deflection and rotation, the linearized dynamic equations of flexible manipulators can be summarized as follows.

3.4.2 Euler–Bernoulli Model after Linearization

Using Eq. (3.51), we have

$$(D\,v'')'' + \rho(\ddot{v} - S\ddot{v}'') = 0 \tag{3.53}$$

$$I_H\,\ddot{\theta} - Dv''(0) = \tau \tag{3.54}$$

with boundary conditions

$$x = 0, \quad v = 0, \quad v' = \theta \tag{3.55}$$

$$x = L, \quad Dv'' + J_p\ddot{v}' + a_cM_p\ddot{v} = 0, \quad (Dv'')' - \rho S\ddot{v}' = M_p(\ddot{v} + a_c\ddot{v}') \tag{3.56}$$

Note that in the dynamic models presented in Ref. [2], neither the rotary inertia nor the size of the tip load had been considered (i.e. $S = 0$ and $a_c = 0$ were assumed).

3.4.3 Timoshenko Model after Linearization

Similarly, we have

$$(D\alpha')' - C(\alpha - v') - \rho S\ddot{\alpha} = 0, \quad [C(\alpha - v')]' + \rho\ddot{v} = 0 \tag{3.57}$$

$$I_H\ddot{\theta} - D\alpha'(0) = \tau \tag{3.58}$$

with boundary conditions

$$x = 0, \quad v = 0, \quad \alpha = \theta \tag{3.59}$$

$$x = L, \quad D\alpha' + J_p\ddot{\alpha} + a_cM_p\ddot{v} = 0, \quad C(\alpha - v') = M_p(\ddot{v} + a_c\ddot{\alpha}). \tag{3.60}$$

Note that when no tip load is present, the equations in this case are the same as those given in Ref. [7].

From boundary conditions (3.55) or (3.56), we find that Eq. (3.56) can be used to calculate hub rotation θ and thus to eliminate θ from dynamic equations. To compensate for the lost boundary condition, Eq. (3.54) or (3.58) can be considered as the new condition. In fact,

Eq. (3.54) or (3.58) represents the dynamic torque balance equation of the hub according to the Euler–Bernoulli or Timoshenko beam model.

3.4.4 Dimensionless Functions, Variables, and Parameters

The linearized equation of motion may be further simplified by introducing the following dimensionless variables and parameters:

$$z(\xi) = \frac{v}{L}, \quad \xi = \frac{x}{L}, \quad \delta = \frac{S}{L^2}, \quad \sigma = \frac{CL^2}{D}, \quad c^2 = \frac{\rho L^2}{D} \tag{3.61}$$

$$\mu = \frac{M_p}{\rho L}, \quad \eta = \frac{I_H}{\rho L^3}, \quad \kappa = \frac{J_p}{\rho L^3}, \quad \zeta = \frac{a_c}{L} \tag{3.62}$$

The resulting equations are as follows.

Euler–Bernoulli Model with Dimensionless Variables

$$z'''' + c^2\ddot{z} - \delta c^2 \ddot{z}'' = 0 \tag{3.63}$$

with boundary conditions

$$z(0) = 0, \quad \eta c^2 \ddot{z}'(0) - z''(0) = \frac{\tau L}{D} \tag{3.64}$$

$$z''(1) + c^2[\kappa \ddot{z}'(1) + \zeta\mu\ddot{z}(1)] = 0, \quad z'''(1) - \delta c^2 \ddot{z}'(1) - \mu c^2[\ddot{z}(1) + \zeta\, \ddot{z}'(1)] = 0 \tag{3.65}$$

Timoshenko Model with Dimensionless Variables

$$\alpha'' - \sigma(\alpha - z') - \delta c^2 \alpha = 0, \quad \sigma(\alpha - z')' + c^2\ddot{z} = 0 \tag{3.66}$$

with boundary conditions

$$z(0) = 0, \quad \eta c^2 \ddot{\alpha}(0) - \alpha'(0) = \frac{\tau L}{D} \tag{3.67}$$

$$\alpha'(1) + c^2[\kappa\ddot{\alpha}(1) + \zeta\mu\ddot{z}(1)] = 0, \quad \sigma[\alpha(1) - z'(1)] - \mu c^2[\ddot{z}(1) + \zeta\ddot{\alpha}(1)] = 0 \tag{3.68}$$

A prime now indicates the differentiation with respect to the dimensionless coordinate ξ.

Note that if the shear deformation is very small, σ must be very large since the shear modulus G is large in this case. From Eq. (3.66), α must approach z' for all ξ in order to keep $\sigma(\alpha - z')$ of finite value. Actually, the first equation of Eq. (3.66) reveals that $\sigma(\alpha - z') \rightarrow \alpha'' - \delta c^2\ddot{\alpha} \rightarrow z''' - \delta c^2 \ddot{z}'$ as $\sigma \rightarrow \infty$. Substituting this result into the second equation and boundary conditions, we can easily show that the Timoshenko model reduces to the Euler–Bernoulli model when $\sigma \rightarrow \infty$.

Sometimes it is much easier to deal with a single higher-order decoupled partial differential equation than several coupled low-order equations. Using the technique developed in Ref. [33], the two coupled equations in Eq. (3.66) can be decoupled by the following transformation:

$$z = \phi', \quad \alpha = \phi'' - \frac{c^2}{\sigma}\ddot{\phi} \tag{3.69}$$

where ϕ is a new function that has to satisfy the equation:

$$\phi'''' - (\frac{1}{\sigma} + \delta)c^2\ddot{\phi}'' + c^2\ddot{\phi} + \frac{\delta}{\sigma}c^4\ddot{\phi} = 0 \tag{3.70}$$

Thus, we have replaced two coupled second-order equations involving two variables by an equivalent fourth-order equation with one variable.

3.5 Finite-Dimensional Modeling of Flexible Manipulators

The flexible manipulator system is an infinite-dimensional system. Previous sections have given the infinite-dimensional modeling approach of flexible manipulators.

3.5.1 Natural Frequency and Modal Shapes

Here we [34] focus on determining the natural frequencies and their associated modal shapes to achieve the state-space equation that will be used for control scheme design. Since modal shapes provide the basis for a state-space calculating system, these frequencies and their modal shapes will be extracted from a uniform beam.

Classical analytical techniques can be employed to derive the resonant frequencies and the modal shapes. The most useful technique is the separability of the modal shape, which is a function of a spatial variable only, from the time-varying amplitude of the modal shape, which is a function of time. The admissible modal functions will then satisfy the governing equations, (3.53) and (3.54). After taking the assumed form of the solution and substituting them for the beam boundary conditions (3.55) and (3.56) listed in Section 3.4.2, four simultaneous equations result and are applicable to the natural frequencies and their modal shapes.

Modal Determinant

For uniform flexible manipulators, the governing equation of Eq. (3.53) is

$$EI\, v'''' - \rho S\ddot{v}'' + \rho\ddot{v} = 0 \tag{3.71}$$

Assuming that the beam undergoes harmonic vibrations, i.e. $v(x,t) = \Psi(x)q(t)$, where $\Psi(x)$ is called the modal shape or eigenfunction and $q(t)$ is the time-varying amplitude of the mode shape, the admissible function is

$$q(t) = C_1 \sin(\omega t) + C_2 \cos(\omega t) \tag{3.72}$$

where ω is the resonant frequency of the system.
Applying Eq. (3.72) to Eq. (3.71), we have

$$EI\Psi'''' - \rho S\omega^2\Psi'' - \rho\omega^2\Psi = 0 \tag{3.73}$$

It is obvious that the eigenvalues of this equation are

$$\lambda_{1,2} = \pm\alpha, \quad \lambda_{3,4} = \pm i\beta \tag{3.74}$$

where

$$\alpha = \sqrt{\frac{\gamma - \rho S\omega^2}{2EI}}, \quad \beta = \sqrt{\frac{\gamma - \rho S\omega^2}{2EI}}, \quad \gamma = \sqrt{(\rho S\omega^2)^2 + 4EI\rho\omega^2}$$

The complementary solution of Eq. (3.73) is

$$\Psi(x) = A \cosh \alpha x + B \sinh \alpha\, x + C \cos \beta x + D \sin \beta x \tag{3.75}$$

which is the modal shape or eigenfunction. This assumed solution must meet the constraints of Eqs (3.55) and (3.56), which are, in terms of the above coefficients,

$$A + C = 0 \tag{3.76}$$

$$EI\alpha^2 A + I_h\omega^2\alpha B - EI\beta^2 C + I_h\omega^2\alpha_1 D = 0 \tag{3.77}$$

$$\alpha_1 A + \alpha_2 B + \alpha_3 C + \alpha_4 D = 0 \tag{3.78}$$

$$\beta_1 A + \beta_2 B + \beta_3 C + \beta_4 D = 0 \tag{3.79}$$

where

$$\begin{aligned}
\alpha_1 &= M_p\omega^2\cosh \alpha L + (\rho S\omega^2 + a_c M_p\omega^2)\,\alpha\sinh \alpha L + EI\alpha^3\sinh \alpha_1 \\
\alpha_2 &= M_p\omega^2\sinh \alpha L + (\rho S\omega^2 + a_c M_p\omega^2)\,\alpha\cosh \alpha L + EI\alpha^3\cosh \beta_1 \\
\alpha_3 &= M_p\omega^2\cosh \beta L + (\rho S\omega^2 + a_c M_p\omega^2)\,\beta\cos \beta L + EI\beta^3\sinh \beta_1 \\
\alpha_4 &= M_p\omega^2\sinh \beta L + (\rho S\omega^2 + a_c M_p\omega^2)\,\beta\cosh \beta L - EI\beta^3\cosh \beta_1 \\
\beta_1 &= EI\alpha^2\cosh \alpha L - J_p\omega^2\alpha\sinh \alpha L - M_p\alpha_c\omega^2\cosh \alpha L \\
\beta_2 &= EI\alpha^2\sinh \alpha L - J_p\omega^2\alpha\cosh \alpha L - M_p\alpha_c\omega^2\sinh \alpha L \\
\beta_3 &= -EI\beta^2\cosh \beta L - J_p\omega^2\beta\sinh \beta L - M_p\alpha_c\omega^2\cos \beta L \\
\beta_4 &= -EI\beta^2\sinh \beta L - J_p\omega^2\beta\cosh \beta L - M_p\alpha_c\omega^2\sin \beta L
\end{aligned}$$

The matrix form of Eqs (3.76)–(3.79) is

$$\begin{bmatrix} 1 & 0 & 1 & 0 \\ EI\alpha^2 & I_h\omega^2\alpha & -EI\beta^2 & I_h\omega^2\beta \\ \alpha_1 & \alpha_2 & \alpha_3 & \alpha_4 \\ \beta_1 & \beta_2 & \beta_3 & \beta_4 \end{bmatrix} \begin{bmatrix} A \\ B \\ C \\ D \end{bmatrix} = 0 \tag{3.80}$$

The natural frequencies are obtained by solving the determinant equal to zero.

Modal Frequencies and Modal Shapes

For a given material and parameters of a beam as in Table 3.1, if we set $A = 1$, then $C = -1$. Equation (3.80) is redundant, and for each frequency it becomes

$$\begin{bmatrix} \alpha_2 & \alpha_4 \\ \beta_2 & \beta_4 \end{bmatrix} \begin{bmatrix} B \\ D \end{bmatrix} = \begin{bmatrix} \alpha_3 - \alpha_1 \\ \beta_3 - \beta_1 \end{bmatrix} \tag{3.81}$$

By solving this, B and D are obtained. After normalizing the eigenfunction to meet

$$\int_0^L \Psi(x)^2 \mathrm{d}x = 1 \tag{3.82}$$

the coefficients are obtained with their frequencies, as shown in Table 3.2.

In fact, the number of modal shapes is infinite, because of the distributed parameter beam system. Only the first 10 modal shapes and their frequencies are listed in the calculation of the state-space equation in the next chapter. Generally, the more modal shapes involved in the system, the more complicated the system model will be. According to Hastings and Book [35,36] and Hughes [37], the first two modes have a greater influence on the model accuracy than the higher-order modes. For typical applications, the higher order must be truncated to meet the computation time. Also, many factors affect the modal shape, including hub position. Geniele et al. [38] showed that this affects the actual modal shape since Coulomb friction coefficients are related to hub position. The first 10 modal shapes are plotted as in Figures 3.3–3.12. Conventionally, the horizontal axis is the spatial coordinator, while the vertical is the amplitude meter. From these plots, it is clear that if the high-order modal shapes are not taken into account, the high-frequency terms in the system dynamics are eliminated. In later chapters, these terms are treated as model uncertainties in the controller design.

Table 3.1: Parameters of uniform beam

E	I	L	ρ	M	M_p	J_p	a_c	I_h
1.0	10.0	1.0	1.0	10.0	1.0	0.5	0.1	5.0

Table 3.2: Modal frequencies and coefficients of modal shapes

Mode	Frequency	*A*	*B*	*C*	*D*
1	2.1925	1	−0.7887	−1	0.1316
2	11.7525	1	−0.9543	−1	0.5303
3	52.3515	1	−0.2839	−1	−0.0018
4	114.7315	1	−1.5491	−1	0.2762
5	218.4795	1	−0.1982	−1	−0.0036
6	336.5055	1	−1.5622	−1	0.1500
7	497.3505	1	−0.1828	−1	−0.0025
8	671.0485	1	−1.5549	−1	0.1028
9	888.0655	1	−0.1774	−1	−0.0018
10	1117.5115	1	−1.5504	−1	0.0785

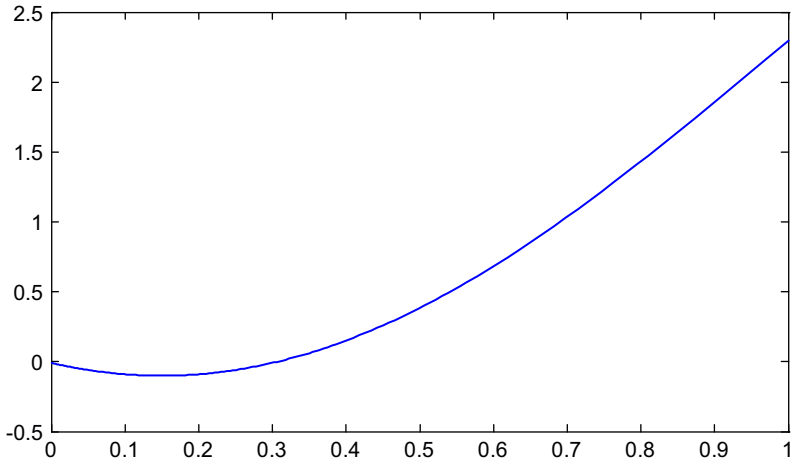

Figure 3.3: The First Modal Shape.

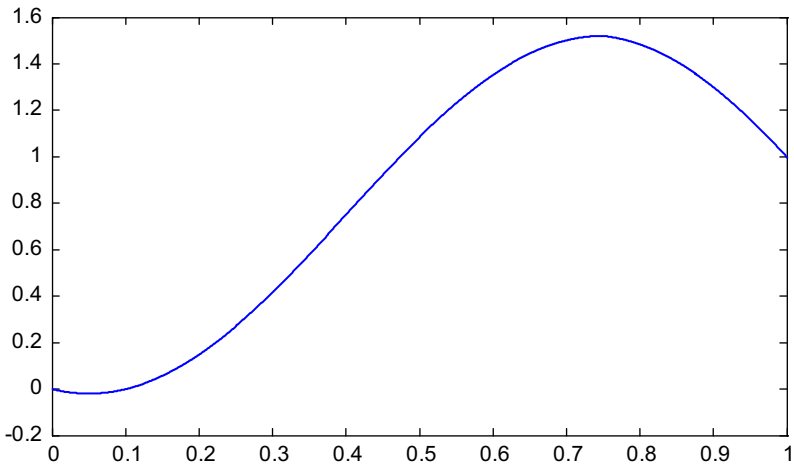

Figure 3.4: The Second Modal Shape.

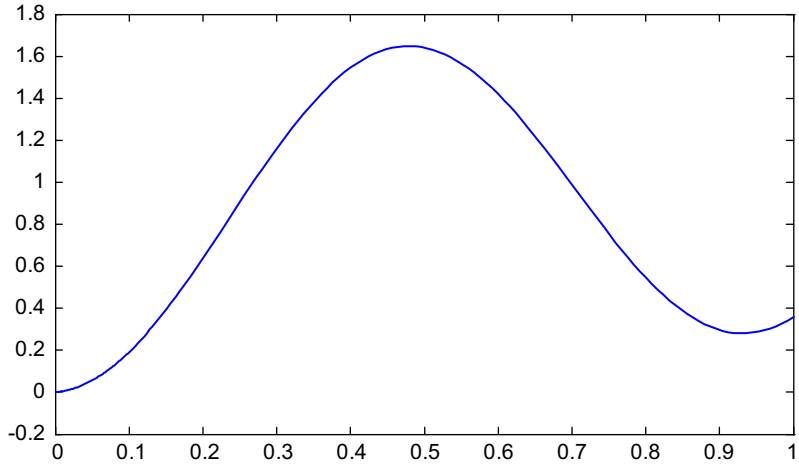

Figure 3.5: The Third Modal Shape.

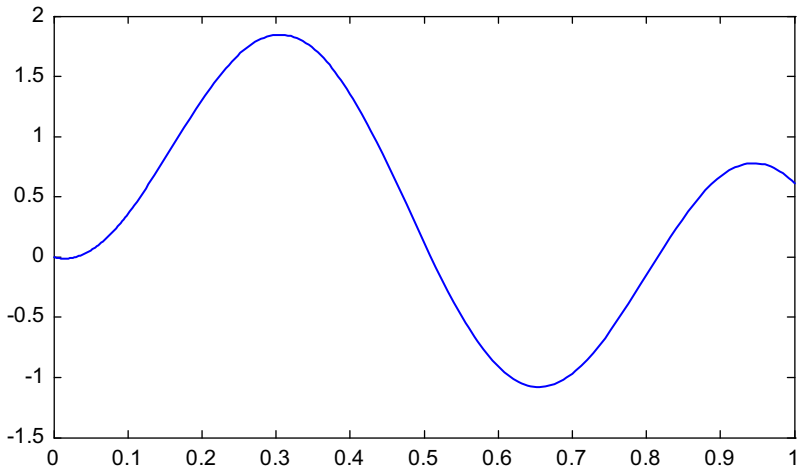

Figure 3.6: The Fourth Modal Shape.

In theory, the fundamental frequency of a rigid manipulator is infinitely large. Therefore, it can move quickly without vibration. Due to the beam flexibility, the resonant frequency is dramatically reduced (the first one is 2.1925 rad/s here). This means that it has to move slowly to experience small vibrations under normal operation. In later chapters we will design and control the flexible beam to achieve better results. But first let us derive a state-space model using these modal shapes.

3.5.2 Finite Modal Model of Euler–Bernoulli Beam

The dynamics of a flexible manipulator system are described by an infinite-dimensional mathematical model, since the model consists of partial differential equations. However, to

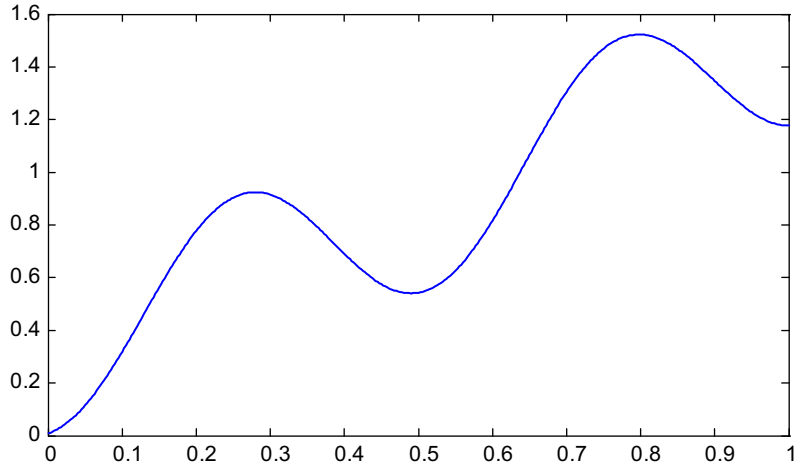

Figure 3.7: The Fifth Modal Shape.

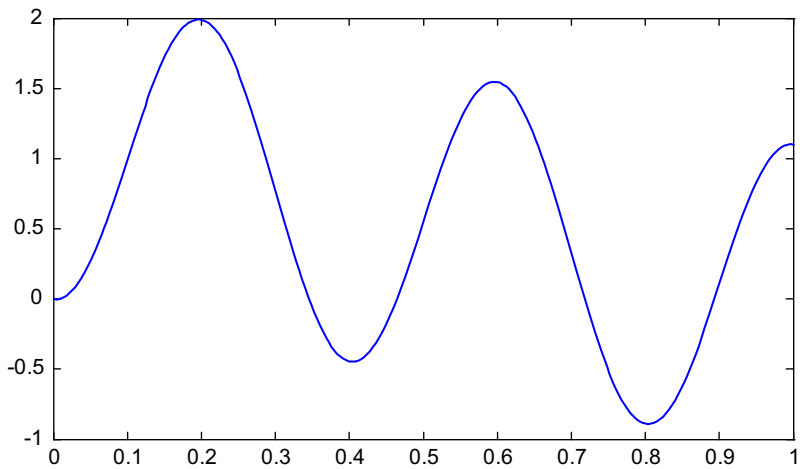

Figure 3.8: The Sixth Modal Shape.

design a finite-dimensional controller, a finite-dimensional system model is needed. To achieve this goal, a finite-dimensional approximation needs to be used to model the flexible manipulator, to retain a finite number of modes and to truncate the other, less significant modes based on the requirements of the controller. The N-mode expansion for the beam displacement $\omega(x,t)$ is given by

$$\omega(x,t) = \sum_{i=1}^{N} \varphi_i(x) q_i(t) \tag{3.83}$$

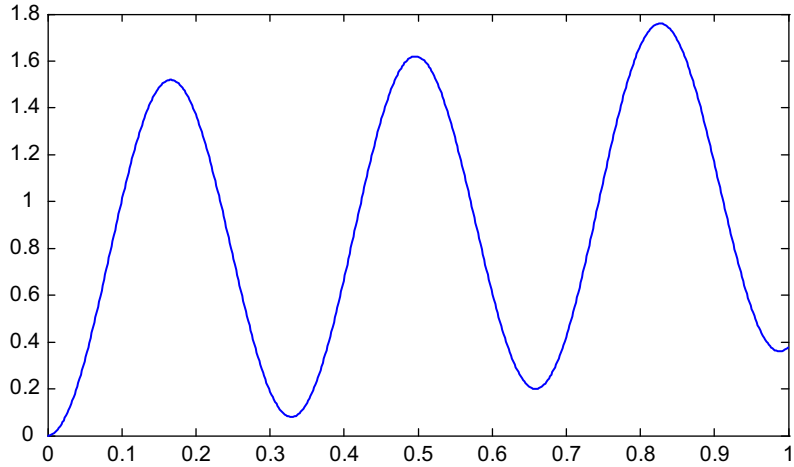

Figure 3.9: The Seventh Modal Shape.

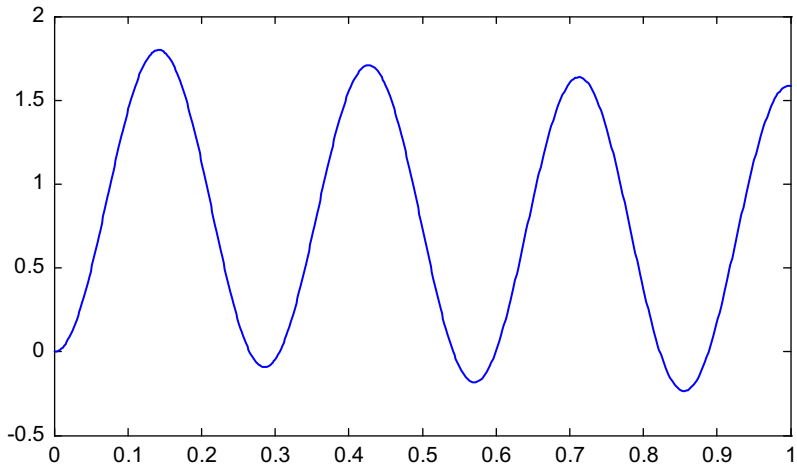

Figure 3.10: The Eighth Modal Shape.

The separability in this case refers to describing the displacement as a series of terms that are products of two separate functions, each of which is a function of a single variable, a spatial variable x and time t respectively. φ_i is the ith modal shape, or eigenfunction. q_i is the corresponding generalized modal coordinate describing the flexible deformation.

The scheme in developing a mathematical model is to use the Lagrangian method or Hamilton's principle for the total kinetic energy, total potential energy, and virtual work done by the torque actuated to the joint. This method will not introduce extra errors into the system and will be used to obtain the state-space model for a flexible manipulator suggested in this chapter [34].

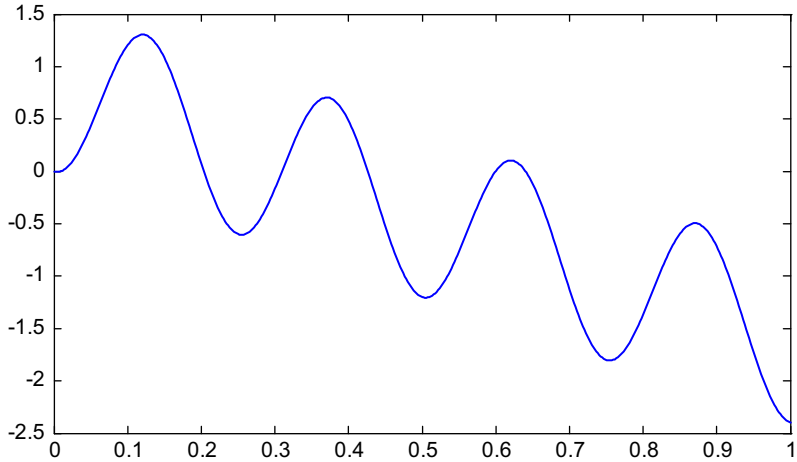

Figure 3.11: The Ninth Modal Shape.

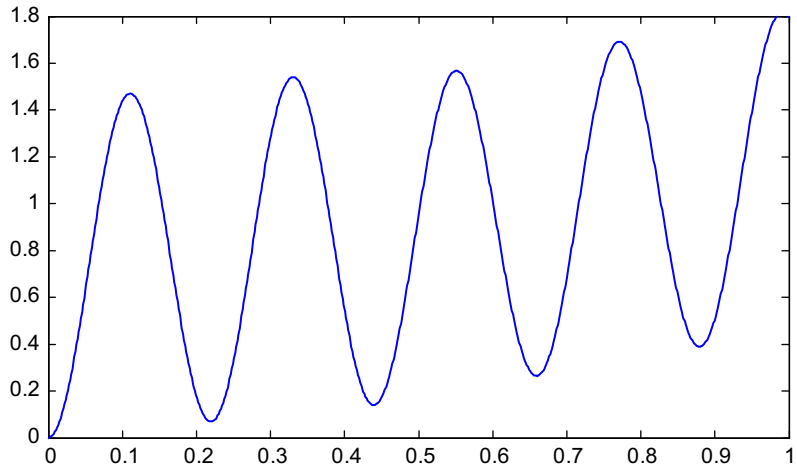

Figure 3.12: The Tenth Modal Shape.

The hub kinetics is written as

$$T_h = \frac{1}{2} I_h [\dot{\theta}^2 + \dot{\omega}^2(0,t)'] \tag{3.84}$$

where $\omega = \partial\omega/\partial x = \omega'$. After substituting Eq. (3.83) into Eq. (3.84), we have

$$T_h = \frac{1}{2} I_h \dot{\theta}^2 + \frac{1}{2} I_h \sum_{i=1}^{n} \sum_{j=1}^{n} \dot{q}_i \dot{q}_j \varphi_i'(0) \varphi_j'(0) \tag{3.85}$$

In the same way, the kinetics of the tip load is

$$T_p = \frac{1}{2}M_p(\dot{\theta}L + \dot{w}(L,t))^2 + \frac{1}{2}J_p(\dot{\theta} + \dot{w}(L,t'))^2 + a_c M(\dot{\theta} + \dot{w}(L,t'))(\dot{\theta}L + \dot{w}(L,t)) \quad (3.86)$$

which is the same as

$$T_p = \frac{1}{2}\Gamma_1\dot{\theta}^2 + \dot{\theta}\sum_{i=1}^{N}\dot{q}\Gamma_2(i) \; + \; \frac{1}{2}\sum_{i=1}^{N}\sum_{j=1}^{N}\dot{q}_i\dot{q}_j\Gamma_3(i,j) \quad (3.87)$$

where

$$\begin{aligned} \Gamma_1 &= (M_pL^2 + J_p + 2M_pLa_c) \\ \Gamma_2(i) &= (J_p + M_pLa_c)\Psi_i'(L) + (L + a_c)M_p\Psi_i(L) \\ \Gamma_3(i,j) &= J_p\Psi_i'(L)\Psi_j'(L) + M_p\Psi_i(L)\Psi_j(L) + 2a_cM_p\Psi_i'(L)\Psi_j(L) \end{aligned} \quad (3.88)$$

The kinetic energy of the link

$$T_L = \frac{1}{2}\int_0^L [(x\dot{\theta} + \dot{w})^2 + S(\dot{w}' + \dot{\theta})^2]\rho \mathrm{d}x \quad (3.89)$$

is equal to

$$T_L = \frac{1}{2}\Lambda_1\dot{\theta}^2 + \dot{\theta}\sum_{i=1}^{N}\dot{q}\Lambda_2(i) \; + \; \frac{1}{2}\sum_{i=1}^{N}\sum_{j=1}^{N}\dot{q}_i\dot{q}_j\Lambda_3(i,j) \quad (3.90)$$

where

$$\begin{aligned} \Lambda_1 &= \int_0^L (x^2 + S)\rho \mathrm{d}x \\ \Lambda_2(i) &= \int_0^L [x\Psi_i(x) + S\Psi_i'(x)]\rho \mathrm{d}x \\ \Lambda_3(i,j) &= \int_0^L [\Psi_i(x)\Psi_j(x) + S\Psi_i'(x)\Psi_j'(x)]\rho \mathrm{d}x \end{aligned} \quad (3.91)$$

S is a function of the cross-sectional area of the link. The total potential energy is

$$P = \frac{1}{2}\int_0^L EI(x)w^2(x)''\,\mathrm{d}x \;= \frac{1}{2}\sum_{i=1}^{N}\sum_{j=1}^{N} q_i q_j k(i,j) \tag{3.92}$$

where $k(i,j) = \int_0^L EI(x)\Psi_i''(x)\Psi_j''(x)\mathrm{d}x$.

The generalized virtual work is derived as

$$W = \tau v'(0,t) = \tau\theta + \tau w'(0,t) = \tau\theta + \tau\sum_{i=1}^{N}\Psi_i'(0)q_i(t) \tag{3.93}$$

In order to apply the Hamiltonian principle, let us substitute Eqs (3.85), (3.87), (3.89), (3.91), and (3.92) for the following formula and group it in terms of θ, δq_i, and their derivatives:

$$\begin{aligned}\Xi = T_L + T_h + T_p - P + W = \frac{1}{2}\Omega_1\dot{\theta}^2 + \dot{\theta}\sum_{i=1}^{N} q_i\Omega_2(i)\\ +\frac{1}{2}\sum_{i=1}^{N}\sum_{j=1}^{N} q_i q_j\Omega_3(i,j) + \tau\theta + \;+\tau\sum_{i=1}^{N}\dot{\Psi}_i(0)q - \frac{1}{2}\sum_{i=1}^{N}\sum_{j=1}^{N} q_i q_j k(i,j)\end{aligned} \tag{3.94}$$

where

$$\begin{aligned}\Omega_1 &= I_h + \Gamma_1 + \Lambda_1\\ \Omega_2 &= \Gamma_2(i) + \Lambda_2(i)\\ \Omega_3(i,j) &= I_h\Psi_i'(0)\Psi_j'(0) + \Gamma_3(i,j) + \Lambda_3(i,j)\end{aligned} \tag{3.95}$$

After applying the Hamiltonian method, we obtain

$$\begin{aligned}\delta\Xi = \Omega_1\dot{\theta}\delta\dot{\theta} + \sum_{i=1}^{N}\Omega(i)\dot{q}\delta\dot{\theta} + \dot{\theta}\sum_{i=1}^{N}\Omega_2(i)\delta\dot{q}_i\\ +\sum_{i=1}^{N}\sum_{j=1}^{N}\dot{q}_j\Omega_3(i,j)\delta\dot{q}_i + \tau\delta\theta + \tau\sum_{i=1}^{N}\Psi_i'(0)\delta q_i - \sum_{i=1}^{N}\sum_{j=1}^{N} q_j k(i,j)\delta q_i\end{aligned} \tag{3.96}$$

Since

$$\begin{aligned}\int_{t_0}^{t_f}\dot{\theta}\delta\dot{\theta}\mathrm{d}t = \dot{\theta}\delta\theta\Big|_{t_0}^{t_f} - \int_{t_0}^{t_f}\ddot{\theta}\delta\theta\mathrm{d}t = -\int_{t_0}^{t_f}\ddot{\theta}\delta\theta\mathrm{d}t, \quad \int_{t_0}^{t_f}\dot{q}_i\delta\dot{\theta}\mathrm{d}t = -\int_{t_0}^{t_f}\ddot{q}_i\delta\theta\mathrm{d}t\\ \int_{t_0}^{t_f}\dot{\theta}\delta\dot{q}_i\mathrm{d}t = -\int_{t_0}^{t_f}\ddot{\theta}\delta q_i\mathrm{d}t, \quad \int_{t_0}^{t_f}\dot{q}_i\delta\dot{q}_j\mathrm{d}t = -\int_{t_0}^{t_f}\ddot{q}_i\delta q_i\mathrm{d}t\end{aligned} \tag{3.97}$$

the extended Hamilton principle results in

$$\int_{t_0}^{t_f} \delta\Xi \mathrm{d}t = \int_{t_0}^{t_f} \left\{ \left[-\Omega_1 \ddot{\theta} - \sum_{i=1}^{N} \ddot{q}_i \Omega_2(i) + \tau \right] \delta\theta \right.$$
$$\left. - \left[\ddot{\theta} \sum_{i=1}^{N} \Omega_2(i) + \sum_{i=1}^{N} \sum_{j=1}^{N} \ddot{q}_j \Omega_3(i,j) + \sum_{i=1}^{N} \sum_{j=1}^{N} q_j k(i,j) - \tau \sum_{i=1}^{N} \Psi'_i(0) \right] \right] \delta q_i \Bigg\} \mathrm{d}t = 0 \tag{3.98}$$

These coefficients of $\delta\theta$, δq_i, $1 \le i \le N$ must be zero. That is,

$$\Omega_1 \ddot{\theta} + \sum_{i=1}^{N} \ddot{q}_i \Omega_2(i) - \tau = 0 \tag{3.99}$$

$$-\ddot{\theta}\, \Omega_2(i) - \sum_{j=1}^{N} \ddot{q}_j \Omega_3(i,j) - \sum_{j=1}^{N} q_j k(i,j) + \tau \Psi'_i(0) = 0, \quad 0 \le i \le N \tag{3.100}$$

or in matrix form:

$$M\ddot{x} + Kx = b\tau \tag{3.101}$$

where

$$x = [\theta, q_1, q_2, q_3, \ldots, q_N]^T_{(N+1,1)}, \quad b = [1, \Psi'_1(0), \Psi'_2(0), \ldots, \Psi'_N(0)]^T_{(N+1,1)}$$

$$M = \begin{bmatrix} \Omega_1 & \Omega_2(1) & \Omega_2(2) & \cdot & \Omega_2(N) \\ \Omega_2(1) & \Omega_3(1,1) & \Omega_3(1,2) & \cdot & \Omega_3(1,N) \\ \cdot & \cdot & \cdot & \cdot & \cdot \\ \Omega_2(N) & \Omega_3(N,1) & \Omega_3(N,2) & \cdot & \Omega_3(N,N) \end{bmatrix} \tag{3.102}$$

$$K = \begin{bmatrix} 0 & 0 & 0 & \cdot & 0 \\ 0 & k(1,1) & k(1,2) & \cdot & k(1,N) \\ \cdot & \cdot & \cdot & \cdot & \cdot \\ 0 & k(N,1) & k(N,2) & \cdot & k(N,N) \end{bmatrix}$$

As has been shown, $\Omega_3(i,j) = \Omega_3(j,i)$, $k(i,j) = k(j,i)$, thus the matrices M and K are symmetric and are called mass and rigidity matrices respectively.

3.5.3 Finite Difference Model

Consider transverse motions of a single-link flexible beam with tip load mass M_p. It is modeled as a beam of length L fixed on a rigid hub with rotary inertia I_H. When shear

deformations and rotary inertia of the beam are neglected, the Euler–Bernoulli dynamic equations and the corresponding boundary conditions can be expressed in terms of its total displacement, $y(x,t) = x\theta(t) + w(x,t)$, as

$$EI(x)\left(\frac{\partial^4 y}{\partial x^4}\right) + \rho A(x)\frac{\partial^2 y}{\partial t^2} = 0 \tag{3.103}$$

$$I_H\ddot{\theta} - EI(x)\left(\frac{\partial^2 y}{\partial x^2}\right)_{x=0} = \tau_{\text{in}} \tag{3.104}$$

$$y_{x=0} = 0, \quad y'_{x=0} = \theta \tag{3.105}$$

$$EI(x)\left(\frac{\partial^2 y}{\partial x^2}\right)_{x=L} + J_p\left(\frac{\partial \ddot{y}}{\partial x}\right)_{x=L} + a_c M_p \ddot{y} = 0 \tag{3.106}$$

$$EI(x)\left(\frac{\partial^3 y}{\partial x^3}\right)_{x=L} - M_p\left(\ddot{y} + a_c\frac{\partial \ddot{y}}{\partial x}\right)_{x=L} = 0 \tag{3.107}$$

where $(\ )' = \partial(\ )/\partial x$, w denotes the pure flexible beam deflection, θ the rigid hub rotation, and τ_{in} the torque applied on the hub. $EI(x)$ is the bending rigidity, which is a function of x for a non-uniform cross-section beam and a constant for a uniform cross-section beam. Primes indicate differentiation with respect to coordinate x.
The finite difference method (method of lines) is used to approximate partial differential equations. According to Refs [39,40], Eqs (3.103)–(3.107) can be transformed into vibration equations and then to first-order differential equations for convenience of solution.

According to the central difference method [41], the function $f(x)$ can be evaluated at values that lie to the left and right of x. Then centered formulas of order $O(h^2)$ are

$$\begin{aligned}
f'(x) &= \frac{1}{2\Delta x}[f(x+\Delta x) - f(x-\Delta x)] + O(h^2)\\
f''(x) &= \frac{1}{\Delta x^2}[f(x+\Delta x) - 2f(x) + f(x-\Delta x)] + O(h^2)\\
f'''(x) &= \frac{1}{2\Delta x^3}[f(x+2\Delta x) - 2f(x+\Delta x) + 2f(x-\Delta x) - 2f(x-2\Delta x)] + O(h^2)\\
f^4(x) &= \frac{1}{\Delta x^4}[f(x+2\Delta x) - 4f(x+\Delta x) + 6f(x) - 4f(x-\Delta x) + f(x-2\Delta x)] + O(h^2)
\end{aligned} \tag{3.108}$$

where Δx is step size and $O(h^2)$ is truncation error.

The flexible beam length L is divided into n segments, $\Delta x = L/n$, and thereby defines

$$x_i = i \cdot \Delta x, \quad y_i = y(i\Delta x, t), \quad \beta_i = \beta(i\Delta x) = EI(i \cdot \Delta x), \quad A_i = A(i\Delta x)$$
$$i = 0,\ 1,\ 2, \ldots, n$$

According to boundary equation (3.105), we obtain

$$y_{-1} = -\Delta x \cdot \theta, y_0' = \theta \tag{3.109}$$

Equation (3.104) can be rewritten as

$$I_h \ddot{\theta} - \beta_0 \frac{1}{(\Delta x)^2}(y_1 - \Delta x \cdot \theta) = \tau_{\text{in}} \tag{3.110}$$

Equation (3.103) can be approximated by the following:

for $i = 1$ we have

$$\frac{1}{2(\Delta x)^4}[(\beta_2 + 2\beta_1 - \beta_0)y_3 - 4(3\beta_1 - \beta_0)y_2 - 4(\beta_2 - 5\beta_1 - \beta_0)y_1 + 4(\beta_2 - 3\beta_1)y_0$$
$$-(\beta_2 - 2\beta_1 - \beta_0)y_{-1}] + \rho A_1 \ddot{y}_1 = 0 \tag{3.111}$$

for $i = 2$ we have

$$\frac{1}{2(\Delta x)^4}[(\beta_3 + 2\beta_2 - \beta_1)y_4 - 4(3\beta_2 - \beta_1)y_3 - 4(\beta_3 - 5\beta_2 - \beta_1)y_2 + 4(\beta_3 - 3\beta_2)y_1$$
$$-(\beta_3 - 2\beta_2 - \beta_1)y_0] + \rho A_2 \ddot{y}_2 = 0 \tag{3.112}$$

for $i = 3,\ldots,n-2$ we have

$$\frac{1}{2(\Delta x)^4}[(\beta_{i+1} + 2\beta_i - \beta_{i-1})y_{i+2} - 4(3\beta_i - \beta_{i-1})y_{i+1} - 4(\beta_{i+1} - 5\beta_i - \beta_{i-1})y_i + 4(\beta_{i+1} - 3\beta_i)y_{i-1}$$
$$-(\beta_{i+1} - 2\beta_i - \beta_{i-1})y_{i-2}] + \rho A_i \ddot{y}_i = 0 \tag{3.113}$$

and for $i = n - 1$

$$\frac{1}{(\Delta x)^2}(\beta_n y_n'' - 2\beta_{n-1} y_{n-1}'' + \beta_{n-2} y_{n-2}'') + \rho A_{n-1} \ddot{y}_{n-1} = 0 \tag{3.114}$$

Equations (3.106) and (3.107) can be approximately expressed as respectively

$$\beta_n y_n'' = \frac{J_p}{\Delta x}\ddot{y}_{n-1} - \left(\frac{J_p}{\Delta x} + a_c M_p\right)\ddot{y}_n \tag{3.115}$$

$$\beta_n y_n'' - \beta_{n-1} y_{n-1}'' = M_p[(\Delta x + a_c)\ddot{y}_n - a_c \ddot{y}_{n-1}] \tag{3.116}$$

Substituting Eq. (3.115) into Eqs (3.114) and (3.116), and replacing differential calculus with a difference quotient, we obtain

$$\begin{aligned}&\left(\frac{J_p}{(\Delta x)^3} + \rho A_{n-1}\right)\ddot{y}_{n-1} - \frac{1}{(\Delta x)^2}\left(\frac{J_p}{\Delta x} + a_c M_p\right)\ddot{y}_n \\ &\quad - \frac{1}{(\Delta x)^4}\left[2\beta_{n-1} y_n - \left(4\beta_{n-1} + \beta_{n-2}\right)y_{n-1} + \left(2\beta_{n-1} + 2\beta_{n-2}\right)y_{n-2} - \beta_{n-2} y_{n-3}\right] = 0\end{aligned} \tag{3.117}$$

$$\begin{aligned}&\left(\frac{J_p}{\Delta x} + a_c M_p\right)\ddot{y}_{n-1} - \left[\left(\frac{J_p}{\Delta x} + a_c M_p\right) + M_P(\Delta x + a_c)\right]\ddot{y}_n - \frac{\beta_{n-1}}{(\Delta x)^2}\left(y_n - 2y_{n-1} + y_{n-2}\right) \\ &\quad = 0\end{aligned} \tag{3.118}$$

Then, integrating Eq. (3.111) into Eq. (3.113), and using Eqs (3.117) and (3.118), we have a vibration equation in matrix form:

$$M\ddot{y} + K y = B\tau_{\text{in}} \tag{3.119}$$

where $y = [\theta, y_1, y_2, \ldots, y_{n-2}, y_{n-1}, y_n]_{n+1}^T$, B is the input matrix, $B = [1, 0, 0, \ldots, 0, 0, 0]_{n+1}^T$. M and K denote the mass and rigidity matrices of the system respectively, and are expressed as follows:

$$M = \begin{bmatrix} I_H & & & & & & \\ & \rho S_1 & & & & 0 & \\ & & \ddots & & & & \\ & & & \rho S_i & & & \\ & & & & \ddots & & \\ & 0 & & & & \frac{J_p}{\Delta x^3} + \rho S_{n-1} & -\frac{1}{\Delta x^2}\left(\frac{J_p}{\Delta x} + a_c M_p\right) \\ & & & & & \frac{1}{\Delta x^2}\left(\frac{J_p}{\Delta x} + a_c M_p\right) & -\frac{1}{\Delta x}\left(\frac{J_p}{\Delta x^2} + \frac{2a_c M_p}{\Delta x} + M_p\right) \end{bmatrix}_{n+1,n+1}$$

$$K = [K_1; K_2; K_3; \ldots K_i; \ldots K_n; K_{n+1}]$$

where

$$K_1 = [k_{11}, k_{12}, k_{13}, \ldots, k_{1n}, k_{1,n+1}]$$

$$K_2 = \frac{1}{2\Delta x^4}[k_{21}, k_{22}, k_{23}, \ldots, k_{2n}, k_{2,n+1}]$$

$$K_3 = \frac{1}{2\Delta x^4}[k_{31}, k_{32}, k_{33}, \ldots, k_{3n}, k_{3,n+1}]$$

$$K_i = \frac{1}{2\Delta x^4}[k_{i1}, k_{i2}, k_{i3}, \ldots, k_{in}, k_{i,n+1}]$$

$$K_n = \frac{1}{\Delta x^4}[k_{n1}, k_{n2}, k_{n3}, \ldots, k_{nn}, k_{n,n+1}],$$

$$K_{n+1} = \frac{1}{\Delta x^4}[k_{n+1,1}, k_{n+1,2}, k_{n+1,3}, \ldots, k_{n+1,n}, k_{n+1,n+1}]$$

and $k_{1,1} = \dfrac{\beta_0}{\Delta x}, \quad k_{1,2} = -\dfrac{\beta_0}{\Delta x^2}, \quad k_{1,3}, \ldots, k_{1,n+1} = 0$

$$k_{2,1} = -\Delta x(\beta_0 + 2\beta_1 - \beta_2), \quad k_{2,2} = -4(\beta_2 - 5\beta_1 + \beta_0), \quad k_{2,3} = -4(3\beta_1 - \beta_0)$$

$$k_{2,4} = (\beta_2 + 2\beta_1 - \beta_0), \quad k_{2,5}, k_{2,n+1} = 0$$

$$k_{3,1} = 0, \quad k_{3,2} = 4(\beta_3 - 3\beta_2), \quad k_{3,3} = -4(\beta_3 - 5\beta_2 + \beta_1), \quad k_{3,4} = -4(3\beta_2 - \beta_1)$$

$$k_{3,5} = (\beta_3 + 2\beta_2 - \beta_1), \quad k_{3,6}, k_{3,n+1} = 0$$

$$k_{i,1}, k_{i,i-3} = 0, \quad k_{i,i-2} = -(\beta_{i-2} + 2\beta_{i-1} - \beta_{i+1}), \quad k_{i,i-1} = -4(\beta_i - 3\beta_{i-1})$$

$$k_{i,i} = -4(\beta_i - 5\beta_{i-1} + \beta_{i-2}), \quad k_{i,i+1} = -4(3\beta_{i-1} - \beta_{i-2}), \quad k_{i,i+2} = (\beta_i + 2\beta_{i-1} - \beta_{i-1})$$

For the ith, $i \in (4, \ldots, n-1)$), row of matrix K, all the elements are zero, except the $(i-2)$th to $(i+2)$th ones and

$$k_{n,n-2} = \beta_{n-2}, \quad k_{n,n-1} = -2(\beta_{n-1} + \beta_{n-2}), \quad k_{n,n} = (4\beta_{n-1} + \beta_{n-2}), \quad k_{n,n+1} = -2\beta_{n-1}$$
$$k_{n+1,n-1} = -\beta_{n-1}, \quad k_{n+1,n} = 2\beta_{n-1}, \quad k_{n+1,n+1} = -\beta_{n-1}$$

On this basis, first-order differential equations and then the state-space equations can be easily obtained for dynamic analysis and the control scheme design.

3.5.4 Finite Element Model

It has been proved that the finite element method is an effective tool for many structural analysis problems, and it has been applied in the modeling and analysis of flexible manipulators [39,42,43]. Reference [42] presents a finite element/Lagrangian approach for

the mathematical modeling of lightweight flexible manipulators. Furthermore, owing to the characteristic of the method which uses a finite dimensional model to approximate an infinite dimensional subject, the finite element model is relatively intuitive and is easy to use in point-observation and point-control. And here it is also suitable for concurrent design and optimization of a flexible manipulator system including cross section optimization carried out in later sections. Early studies on flexible manipulators, both single-link and multi-link ones, adopting the finite element method, are all towards a uniform cross section flexible beam, while here we will firstly set up a uniform cross-sectional flexible beam model and then apply the model to the discussions of a non-uniform cross-sectional flexible beam.

When considering a single-link flexible manipulator mounted in the horizontal plane with a tip-mass payload, it consists of a beam of length L fixed on a rigid hub as shown in Figure 3.1, where X_0OY_0 and X_1OY_1 denote stationary and moving coordinates respectively. E, I, ρ, A, and M_p are Young's modulus, the moment of inertia of the cross-sectional area, beam density, cross-sectional area of the beam, and tip mass payload respectively.

The flexible manipulator is viewed as an Euler−Bernoulli beam and is divided into N segments. The following are some assumptions:

1. Rotary inertia and shear deformation are ignored.
2. Cross-sectional areas and mass density remain constant in each segment.
3. Perpendicular deformation is neglected since the beam is moving in the horizontal plane.

As for the Euler−Bernoulli beam, the motion can be described by the rigid rotation angle θ of the hub and flexible displacement w of the beam. Thus, the total displacement y of a point along the manipulator at a distance x from the hub is

$$y = x\theta(t) + w(x,\ t) \tag{3.120}$$

The length of each segment is $l = L/N$. As for the nth segment, flexible displacement $w(x,t)$ can be approximately expressed as

$$w_n(x,t) = N_n(x)\ \ Q_n(t) \tag{3.121}$$

where $N_n(x)$ and $Q_n(t)$ are the shape function and generalized coordinate respectively. While using the standard finite element method, the shape function can be defined as [40,43]

$$N_n(x) = [\Phi_1(x)\ \ \Phi_2(x)\ \ \Phi_3(x)\ \ \Phi_4(x)] \tag{3.122}$$

where

$$\Phi_1(x) = 1 - 3x^2/l^2 + 2x^3/l^3, \quad \Phi_2(x) = x - 2x^2/l + x^3/l^2, \quad \Phi_3(x) = 3x^2/l^2 - 2x^3/l^3$$
$$\Phi_4(x) = x^3/l^2 - x^2/l \quad 0 \le x \le l$$

The generalized coordinate of each node is

$$Q_n(t) = [w_n(t) \quad \theta_n(t) \quad w_{n+1}(t) \quad \theta_{n+1}(t)] \tag{3.123}$$

where $w_n(t)$, $w_{n+1}(t)$ denote flexible displacements respectively, while $\theta_n(t)$ and $\theta_{n+1}(t)$ denote rotation angles of the corresponding node. Substituting Eq. (3.121) into Eq. (3.120), we obtain the unified expression:

$$y(x,t) = x\theta + \sum_{n=1}^{N} N_n(x)\, Q_n(t) = N_n'(x)\, Q_n'(t) = [x\, N_n(s)][\theta(t)\, Q_n(t)]^T \tag{3.124}$$

where

$$s = x - \sum_{i=1}^{N-1} l_i$$

For the undamped free vibration system, the mass matrix reflects the kinetic energy of the system while the stiffness reflects the potential energy. According to the energy principle and basic finite element method, the mass matrix and stiffness matrix of each N segment of the beam can be obtained, and then the motion equations can be established. Here, the kinetic energy of the moving flexible manipulator, considering tip payload mass M_p, includes three parts:

1. The kinetic energy of the ith element t of the beam

$$E_{ki} = \frac{1}{2}[Q_n]_i^T [M_n]_i [Q_n]_i, \quad i = 1, 2, \ldots, N \tag{3.125}$$

2. The kinetic energy of tip payload mass

$$E_{kp} = \frac{1}{2}[Q_n]_N^T\, [M]_p\, [Q_n]_N \tag{3.126}$$

3. The rotational kinetic energy of the driving end

$$E_{km} = \frac{1}{2} I_H \theta^2 = \frac{1}{2}[Q_n]_1^T [M]_m [Q_n]_1 \tag{3.127}$$

where

$$[M_n]_i = \frac{\rho\, A_i l}{420} \begin{bmatrix} M_{11} & M_{12} & M_{13} & M_{14} & M_{15} \\ M_{22} & 156 & 22l & 54 & -13l \\ M_{23} & 22l & 4l^2 & 13l & -3l^2 \\ M_{24} & 54 & 13l & 156 & -22l \\ M_{25} & -13l & -3l^2 & -22l & 4l \end{bmatrix}$$

and in the matrix above

$$\begin{aligned} &M_{11} = 140\, l^2(3i^2 - 3i + 1), M_{12} = M_{21} = 21l(10i - 7) \\ &M_{13} = M_{31} = 7l^2(5i - 3), M_{14} = M_{41} = 21l(10i - 3) \\ &M_{15} = M_{51} = -7l^2(5i - 2) \end{aligned}$$

Generalized coordinates are

$$[Q_n]_i = [\theta \quad \theta_i \quad w_i \quad \theta_{i+1} \quad w_{i+1}] \tag{3.128}$$

The inertia matrix of tip payload mass M_p is

$$[M_n]_p = \begin{bmatrix} M_pL^2 & 0 & 0 & 0 & 0 \\ 0 & 0 & 0 & 0 & 0 \\ 0 & 0 & 0 & 0 & 0 \\ 0 & 0 & 0 & M_p & 0 \\ 0 & 0 & 0 & 0 & 0 \end{bmatrix}$$

Generalized coordinates are

$$[Q_n]_N = [\theta \quad \theta_N \quad w_N \quad \theta_{N+1} \quad w_{N+1}] \tag{3.129}$$

The kinetic energy inertia matrix of the driving end is expressed as

$$[M]_m = \begin{bmatrix} I_H & 0 & 0 & 0 & 0 \\ 0 & 0 & 0 & 0 & 0 \\ 0 & 0 & 0 & 0 & 0 \\ 0 & 0 & 0 & 0 & 0 \\ 0 & 0 & 0 & 0 & 0 \end{bmatrix}$$

where $I_H = I_h + \rho l^3/3$.

Generalized coordinates are

$$[Q_n]_1 = [\theta \quad \theta_1 \quad w_1 \quad \theta_2 \quad w_2] \tag{3.130}$$

The potential energy of the system is

$$E_p = \sum_{i=1}^{N} E_{pi} = \frac{1}{2}\sum_{i=1}^{N} [Q_n]_i^T [K_n]_i [Q_n]_i \tag{3.131}$$

The rigidity of the ith element $[K_n]_i$ is

$$[K_n]_i = \frac{EI_i}{l^3}\begin{bmatrix} 0 & 0 & 0 & 0 & 0 \\ 0 & 12 & 6l & -12 & 6l \\ 0 & 6l & 4l^2 & -6l & 2l^2 \\ 0 & -12 & -6l & 12 & -6l \\ 0 & 6l & 2l^2 & -6l & 4l^2 \end{bmatrix} \tag{3.132}$$

where A_i and I_i are the cross-sectional area and rotary inertia of the ith segment of the beam.

Integrating all the N segments and the payload mass, the total kinetic energy of the system can be obtained as

$$T = E_{km} + \sum_{i=1}^{N} [M_n]_i + E_{kp} = \frac{1}{2} Q_n^{*T} M_n^* Q_n^* \tag{3.133}$$

The total potential energy of the system is

$$K = \sum_{i=1}^{N} E_{pi} = \frac{1}{2}\sum_{i=1}^{N} [Q_n]_i^T [K_n]_i [Q_n]_i = \frac{1}{2} Q_n^{*T} K_n^* Q_n^* \tag{3.134}$$

where the local coordinate $Q_n^* = [[Q_n] \quad [Q_n]_2 \quad \dots \quad [Q_n]_N]^T$.

The general mass matrix is

$$M_n^* = \begin{bmatrix} [M_n]_1^* & \cdots & 0 \\ \vdots & \ddots & \vdots \\ 0 & \cdots & [M_n]_N^* \end{bmatrix} \tag{3.135}$$

The general stiffness matrix is

$$K_n^* = \begin{bmatrix} [K_n]_1^* & \cdots & 0 \\ \vdots & \ddots & \vdots \\ 0 & \cdots & [K_n]_N^* \end{bmatrix} \tag{3.136}$$

Considering node coordinates overlapping between neighborhood elements when assembled, the general coordinate is introduced as

$$Q_z = [\theta \quad \theta_1 \quad w_1 \quad \theta_2 \quad w_2 \quad \theta_3 \quad w_3 \quad \dots \quad \theta_{N-1} \quad w_{N-1} \quad \theta_N \quad w_N \quad \theta_{N+1} \quad w_{N+1}] \tag{3.137}$$

Then there exists the relationship between the local coordinate and the general coordinate $Q_n^* = \beta\, Q_z$, where the transformation matrix β is a $(5N) \times (2N+1)$ sparse matrix.

Then the mass matrix and stiffness matrix using general coordinates can be expressed as

$$\beta = \begin{bmatrix} 1 & & & & & & & & & & & & & & \\ & 1 & & & & & & & & & & & & & \\ & & 1 & & & & & & & & & & & & \\ & & & 1 & & & & & & & & & & & \\ & & & & 1 & & & & & & & & & & \\ 1 & & & & & & & & & & & & & & \\ & & & 1 & & & & & & & & & & & \\ & & & & 1 & & & & & & & & & & \\ & & & & & 1 & & & & & & & & & \\ & & & & & & 1 & & & & & & & & \\ & & & & & & & \ddots & & & & & & & \\ 1 & & & & & & & & & & & & & & \\ & & & & & & & & & 1 & & & & & \\ & & & & & & & & & & 1 & & & & \\ & & & & & & & & & & & 1 & & & \\ & & & & & & & & & & & & 1 & & \\ & & & & & & & & & & & & & 1 & \end{bmatrix}_{(5N)\times(2N+1)} \tag{3.138}$$

$$M_z = \beta^T \; M_n^* \;\; \beta^T \tag{3.139}$$

$$K_z = \beta^T \; K_n^* \;\; \beta^T \tag{3.140}$$

While taking boundary conditions into account, the beam is fixed at one end and it holds that $\theta_1 = w_1 \equiv 0$. Then θ_1 and w_1 can be removed from the general coordinates, while the corresponding row and column in the mass matrix and stiffness matrix can also be removed. Substituting them into the Lagrange equation, the motion equation based on general coordinates can be obtained:

$$M'\ddot{Q}' + D'\dot{Q}' + K'Q' = b'\tau \tag{3.141}$$

where M', K', and Q' are mass matrix, rigidity matrix, and general coordinates when substituting boundary conditions, respectively. $b' = [\,1 \quad 0 \quad \ldots \quad 0\,]$. τ is input torque. D' is the damping matrix and we choose the linear-type Rayleigh damping [44].

As for the flexible manipulator that contains rigid motion and elastic motion, the mass matrix can be expressed as

$$M' = \begin{bmatrix} M'_{\theta\theta} & M'_{\theta W} \\ M'_{\theta W} & M'_{WW} \end{bmatrix} \tag{3.142}$$

where M'_{WW} and $M'_{\theta\theta}$ denote the mass matrices relating to elastic motion and rigid motion respectively, and $M'_{\theta W}$ denotes the coupling parts of elastic and rigid motion.

Likewise, the stiffness matrix can be written as

$$K' = \begin{bmatrix} 0 & 0 \\ 0 & K'_{WW} \end{bmatrix} \tag{3.143}$$

where K'_{WW} denotes the stiffness matrix relating elastic motion, and it has no elastic and rigid motion coupling.

Then the total damping matrix can be written as

$$D' = \begin{bmatrix} 0 & 0 \\ 0 & D'_{WW} \end{bmatrix} \tag{3.144}$$

where linear Rayleigh damping [44]

$$D'_{WW} = \alpha M'_{WW} + \beta K'_{WW} \tag{3.145}$$

and

$$\alpha = \frac{2\omega_1\omega_2(\xi_1\omega_2 - \xi_2\omega_1)}{\omega_2^2 - \omega_1^2}, \quad \beta = \frac{2(\xi_2\omega_2 - \xi_1\omega_2)}{\omega_2^2 - \omega_1^2} \tag{3.146}$$

ω_1 and ω_2 denote the modal frequency. ξ_1 and ξ_2 are damping coefficients that can be determined according to engineering experience.

References

[1] K. Gu, B.H. Tongue, A method to improve the modal convergence for structures with external forcing, ASME Journal of Applied Mechanics 54 (4) (1987) 904–909.

[2] F. Bellezze, L. Lanari, G. Ulivi, Exact modeling of the flexible slewing link, IEEE 1990 International Conference on Robotics and Automation 2 (1990) 734–739.

[3] R.H. Cannon Jr., E. Schmitz, Precise control of flexible manipulators. Robotics Research: First International Symposium, MIT Press, Cambridge, MA, 1984, pp. 841–861.

[4] F. Khorrami, U. Ozguner, Perturbation method in control of flexible link manipulators, IEEE International Conference on Robotics and Automation 1 (1988) 310–315.

[5] T. Sakawa, F. Matsuno, S. Fukushima, Modeling and feedback control of a flexible arm, Journal of Robotic Systems 2 (1985) 453–472.

[6] F.Y. Wang, J.T. Wen, Nonlinear dynamical model and control for a flexible beam. CIRSSE Report No. 75, RPI, Tory, NY, 1990.

[7] F.Y. Wang, G.G. Guan, Influences of rotary inertia, shear deformation and tip load on vibrations of flexible manipulators, Journal of Sound and Vibrations 171 (4) (1994) 433–452.

[8] G.B. Yang, M. Donath, Dynamic model of a one link manipulator with both structural and joint flexibility, IEEE International Conference on Robotics and Automation 6 (3) (1988) 454–461.

[9] M. Boutaghou, A.G. Erdman, A unified approach for the dynamics of beams undergoing arbitrary spatial motion, Journal of Vibration and Acoustics—Transactions of the ASME 113 (4) (1991) 494–507.

[10] T.R. Kane, R.R. Ryan, A.K. Bamerjee, Dynamics of a cantilever beam attached to a moving bar, Journal of Guidance and Control 10 (1989) 139–151.

[11] J.C. Simo, L. Vu-Quoc, On the dynamics of flexible beams under large overall motions, Parts I and II, Journal of Applied Mechanics 53 (1986) 849–863.

[12] A. De Luca, P. Lucibello, G. Ulivi, Inversion techniques for trajectory control of flexible robot arms, Journal of Robotic Systems 6 (4) (1989) 325–344.

[13] A. De Luca, B. Siciliano, Trajectory control of non-linear one link flexible arm, International Journal of Control 50 (1989) 1699–1715.

[14] A.P. Tzes, S. Yurkovich, Application and comparison of one-line identification methods for flexible manipulator control, International Journal of Robotics Research 10 (5) (1991) 515–527.

[15] D. Wang, M. Vidyasagar, Control of a flexible beam for optimum step response, IEEE Conference on Robotics and Automation, Rayleigh, NC, 1987, pp. 1567–1572.

[16] D. Wang, M. Vidyasagar, Passive control of a stiff flexible link, International Journal of Robotics Research 11 (3) (1992) 572–578.

[17] M. Kelemen, A. Bagchi, Modeling and feedback control of a flexible arm of a robot for prescribed frequency-domain tolerances, IFAC Journal Automatica 29 (4) (1993) 899–909.

[18] S. Cetinkunt, W.L. Yu, Closed loop behavior of a feedback controlled flexible arm: A comparative study, International Journal of Robotics Research 10 (3) (1991) 263–275.

[19] F.Y. Wang, Optimum design of vibrating cantilevers: A classical problem revisited, Journal of Optimization Theory and Applications 84 (3) (1995) 635–652.

[20] F.Y. Wang, On the extremal fundamental frequencies of one-link flexible manipulators, International Journal of Robotics Research 13 (2) (1994) 162–170.

[21] F.Y. Wang, Finding the maximum bandwidth of a flexible arm, Proceedings of 32nd IEEE Conference on Decision and Control, San Antonio, TX, 1, (1993) 619–625.

[22] F.Y. Wang, J.L. Russell, Minimum-weight robot arm for a specified fundamental frequency, Proceedings of the IEEE Conference on Robotics and Automation, Atlanta, GA, 1, (1993) 490–495.

[23] F.Y. Wang, J.L. Russell, Optimum shape construction of flexible manipulators with total weight constraint, IEEE Transactions on Systems, Man, and Cybernetics 25 (3) (1995) 605–614.
[24] G.R. Cowper, On the accuracy of Timoshenko's beam theory, Journal of the Engineering Mechanics Division, Proceedings of the ASME 94 (1968) 1447–1453.
[25] R.M. Davies, A critical study of the Hopkins pressure bar. Philosophical Transactions of the Royal Society, Series A 240 (821) (1948) 454–461.
[26] S. Timoshenko, D.H. Young, W. Weaver Jr., Vibration Problems in Engineering, third ed, D. Van Nostrand, New York, 1957.
[27] T.C. Huang, The effect of rotary inertia and shear deformations on the frequency and nominal mode equations of uniform beams with simple end conditions, Journal of Applied Mechanics 28 (1961) 579–589.
[28] F.Y. Wang, F.B. He, Free vibration of transversely isotropic plates, Journal of Vibration and Shock 5 (1) (1986) 1–11.
[29] F.Y. Wang, Y. Zhou, On the vibration modes of three-dimensional micropolar elastic plates, Journal of Sound and Vibration 146 (1) (1991) 1–16.
[30] S. Timoshenko, G.H. MacCullough, Elements of Strength of Materials, third ed, D. Van Nostrand, New York, 1949.
[31] A. Pars, A Treatise on Analytical Dynamics, OX BOX Press, Woodbridge, CT, 1979.
[32] G.R. Cowper, The shear coefficients in Timoshenko's beam theory, Journal of Applied Mechanics 33 (1968) 335–339.
[33] F.Y. Wang, On the solutions of Eringen's micropolar plate equations and other approximate equations, International Journal of Engineering Science 28 (9) (1990) 919–935.
[34] P. Zhou, Mechatronic design of flexible manipulators. Ph.D. dissertation, Department of Systems and Industrial Engineering, University of Arizona, Tucson, 1999.
[35] G.G. Hastings, W.J. Book, A linear dynamic model for flexible robotic manipulators, IEEE Control System Magazine 7 (1) (1987) 61–64.
[36] G. Hastings, W.J. Book, Experiments in the optimal control of flexible manipulator, Proceedings of American Control Conference, Boston, MA, (1985) 728–729.
[37] P.C. Hughes, Space structure vibration mode: How many exit? Which ones are important? IEEE Control System Magazine 7 (1) (1984) 22–28.
[38] H. Geniele, R.V. Patel, K. Khorasani, End-point control of a flexible-link manipulator: Theory and experiments, IEEE Transactions on Control System Technology 5 (6) (1997) 556–570.
[39] Z. Xiao, Flexible manipulator system modeling and control optimization based on concurrent design. Ph.D. dissertation, Institute of Automation, Chinese Academy of Sciences, Beijing, 2004.
[40] P. Zhou, F.-Y. Wang, W. Chen, P. Lever, Optimal construction and control of flexible manipulators: A case study based on LQR output feedback, Mechatronics 11 (1) (2001) 59–77.
[41] J.H. Mathews, K.D. Fink, Numerical Methods using Matlab, third ed. Chinese translation. Pearson Education Asia Limited and Publishing House of Electronics Industry, 2002.
[42] P.B. Usoro, R. Nadira, S.S. Mahil, A finite element/Lagrange approach to modeling lightweight flexible manipulators, Journal of Dynamic Systems, Measurement and Control, Transactions of the ASME 108 (3) (1986) 198–205.
[43] E. Bayo, A finite-element approach to control the end-point motion of a single-link flexible robot, Journal of Robotic Systems 4 (1) (1987) 63–75.
[44] M.O. Tokhi, Z. Mohamed, H.H. Shaheed, Dynamic characterization of a flexible manipulator system, Robotica 19 (2001) 571–580.

CHAPTER 4

Analysis of Flexible Manipulators

Chapter Outline

4.1 Introduction 60

4.2 Dynamic Analysis of Vibrations of Flexible Manipulators Considering Effects of Rotary Inertia, Shear Deformation, and Tip Load 60

4.2.1 Introduction 60

4.2.2 Dynamic Models for One-Link Flexible Manipulators 61

Euler–Bernoulli Dynamic Model (Model A) 62

Euler–Bernoulli Dynamic Model with Rotary Inertia (Model B) 63

Timoshenko Dynamic Model (Model C) 63

Euler–Bernoulli Dynamic Model with Tip Load (Model D) 64

4.2.3 Characteristic Equations for Modal Frequencies and Vibration Modes 64

Euler–Bernoulli Dynamic Model (Model A) 65

Euler–Bernoulli Dynamic Model with Rotary Inertia (Model B) 66

Timoshenko Dynamic Model (Model C) 67

Euler–Bernoulli Dynamic Model with Tip Load (Model D) 69

4.2.4 Asymptotic Behavior of Modal Frequencies and Vibration Modes 70

Euler–Bernoulli Dynamic Model (Model A) 71

Euler–Bernoulli Dynamic Model with Rotary Inertia (Model B) 71

Timoshenko Dynamic Model (Model C) 71

Euler–Bernoulli Dynamic Model with Tip Load (Model D) 72

4.2.5 Experimental Verification and Numerical Analysis 72

Experimental Verification 72

Influence of Rotary Inertia 73

Influence of Shear Deformation 74

Influence of Tip Load 76

4.2.6 Natural Frequencies and Modal Shape Functions 80

Euler–Bernoulli Model 80

Timoshenko Model 83

4.2.7 Step Responses and General Solutions 88

4.3 Passivity, Control, and Stability Analysis 91

4.3.1 Nonlinear Dynamic Equations of Motion 91

4.3.2 Discretization of Nonlinear Model 92

4.3.3 Stability Analysis 94

References 97

Flexible Manipulators. DOI: 10.1016/B978-0-12-397036-7.00004-0
Copyright © 2012 Elsevier Inc. All rights reserved.

4.1 Introduction

In Euler–Bernoulli beam theory, both rotary inertia and shear deformation are completely neglected. It is well known from beam and plate theories, however, that both of these factors have significant effects on vibration behavior, especially for the high-order modal frequencies of beam or plate-like structures [1–5]. For example, it has been found, for high-order modal frequencies of shorter beams or thicker plates, that there is an order of magnitude difference between the frequencies calculated without considering rotary inertia or shear and those determined by taking them into account. From the control perspective, modal frequencies are poles of plate dynamics, and in order to design controllers with better performance, high vibration modes have to be included into plant dynamics for control synthesis. Based on these considerations, it is necessary to investigate the influences of rotary inertia and shear deformation on the vibration of flexible manipulators.

Another factor that obviously also affects the vibration of flexible manipulators is the load carried by end-effectors (the tip load). If the influence of the tip load on the vibration of flexible manipulators is shown to be significant, non-adaptive control approaches should be considered inappropriate or at least inefficient for the control of flexible manipulators. This is because the tip load is always changing with tasks and environments, but the design of non-adaptive controllers is usually based on a fixed nominal dynamic model. This implies, in this case, that the adaptive control method must be used for control of the flexible manipulator. To our knowledge, the effect of tip load has not been investigated in detail and no quantitative analysis has been performed.

4.2 Dynamic Analysis of Vibrations of Flexible Manipulators Considering Effects of Rotary Inertia, Shear Deformation, and Tip Load

4.2.1 Introduction

As indicated above, the main purpose here is to give a comprehensive study of the influence of rotary inertia, shear deformation, and tip load on the vibrations of one-link manipulators. First of all, this will help us to understand more about the dynamics of flexible manipulators as well as the effect of various factors. On the other hand, it will also provide us with valuable knowledge that is useful for the design of both non-adaptive and adaptive controllers for flexible manipulators.

It should be pointed out that in this study we have used the small deformation hypothesis and ignored longitudinal elongation. This is necessary in order to construct a linear model for flexible manipulators. Nonlinear models considering large deformation and coupling effects of a certain degree have been proposed for spinning beams in Refs [6–8]. While these models

are more accurate, they are too computationally intensive to serve as the dynamic model of flexible manipulators for real-time control purposes. In particular, our focus here is on the frequency of vibration, not the amplitude of vibration, for which nonlinear models are simply not appropriate. Linear theory is not valid for amplitude analysis since it predicts infinite vibration amplitude (for zero damping), which is physically impossible in reality. However, it is well known that linear theory is good enough to provide an accurate estimation of vibration frequencies for most engineering applications. This is the reason why the small deformation hypothesis is employed and longitudinal elongation is neglected in our study.

4.2.2 Dynamic Models for One-Link Flexible Manipulators

Chapter 3 presented detailed derivations of equations of motion for the Euler–Bernoulli beam and Timoshenko beam. Nonlinear dynamic equations and their linearized versions were given. For the convenience of study, this section considers the Euler–Bernoulli model, the Euler–Bernoulli model with rotary inertia, the Timoshenko model, and motion equations of the Euler–Bernoulli model with a tip load.

The flexible manipulator to be considered is a beam of uniform rectangular transverse section fixed on a hub with rotational inertia I_H in the horizontal plane, as shown in Figure 4.1, where (x^0,y^0) is the base coordinate frame system and (x,y) the coordinate system attached to the hub. The coordinate frame $AO'B$ of the tip load is fixed at the end of the flexible beam. It is assumed that the initial (neutral) longitudinal axis of the beam coincides with the x-axis. For the sake of convenience, the following differential notations have been used: $(\ )' = \partial(\ )/\partial x$ and $(\dot{\ }) = \partial(\ )/\partial t$.

The beam is of length L with a transverse section with moment of inertia I and area A. Young's modulus, shear modulus, and mass per unit length of the beam are denoted by E, G, and ρ respectively. The tip load is of mass M_p and inertia moment J_p, and its center of mass in $AO'B$ is denoted as (a_c,b_c). The motion of the manipulator is described by the

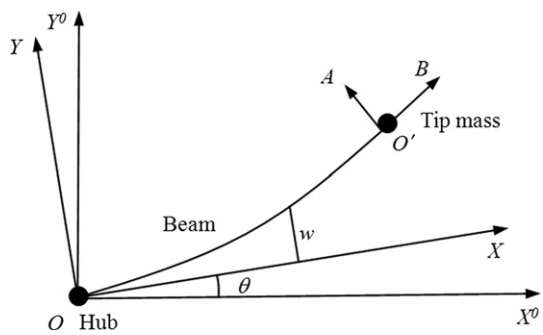

Figure 4.1: Coordinate Systems for One-Link Flexible Manipulators.

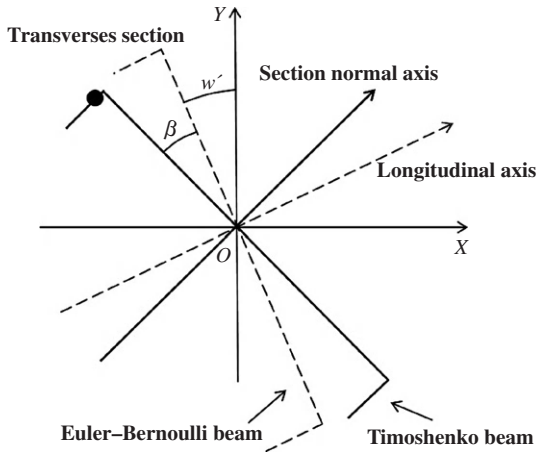

Figure 4.2: Motion of Transverse Section in Different Beam Theories.

angular rotation $\theta(t)$ due to the hub rotation, the flexible displacement $w(x,t)$, and the pure bending rotation $\psi(x,t)$ of the (neutral) longitudinal axis of the beam with respect to the (x,y) coordinate system, as shown in Figure 4.2. Small deformation and negligible elongation of the longitudinal axis have been assumed. Two functions, $\alpha = \psi + \theta$ and $v = w + x\theta$, are introduced to describe the dynamic motion equations of flexible manipulators. In what follows, we list four different sets of motion equations for one-link flexible manipulators. These equations have been derived by employing Hamilton's principle [9] and their detailed derivation can be found in Refs [10,11].

Euler—Bernoulli Dynamic Model (Model A)

The normal plane assumption is used in this model; that is, the entire transverse section of the beam, originally plane, remains plane and normal to the longitudinal axis of the beam after deformation [12]. Therefore, the pure bending rotation $\psi(x,t)$ is equal to zero in this case (Figure 4.2). This model also assumes the velocity of the point at the neutral axis on that transverse section. This means that the rotation of the transverse section is not considered, and therefore the rotary inertia is neglected. The governing dynamic equations of motion based on Euler—Bernoulli beam theory for one-link flexible manipulators can be found as

$$EI\, v'''' + \rho\, \ddot{v} = 0 \tag{4.1}$$

$$\tau - I_H\, \ddot{\theta} + EI\, v''|_{x=0} = 0 \tag{4.2}$$

with the boundary conditions

$$v(x,t) = 0,\ \ v'(x,t) = \theta(t), \quad x = 0, \qquad v''(x,t) = 0,\ \ v'''(x,t) = 0, \quad x = L \tag{4.3}$$

Euler–Bernoulli Dynamic Model with Rotary Inertia (Model B)

To take the rotary inertia of the beam into account, velocities at different points on a transverse section can no longer be considered the same, and will be calculated differently according to their own coordinates. However, the normal plane assumption is still used, and therefore the pure bending rotation $\psi(x,t)$ is still zero. The governing dynamic equations of motion for one-link flexible manipulators now become

$$EI\, v'''' - \rho S\ddot{v}'' + \rho\, \ddot{v} = 0 \tag{4.4}$$

$$\tau - I_H\, \ddot{\theta} + EI\, v''|_{x=0} = 0 \tag{4.5}$$

with the boundary conditions

$$v(x,t) = 0,\;\; v'(x,t) = \theta(t), \quad x = 0, \qquad v''(x,t) = 0,\;\; EIv'''(x,t) = \rho S\ddot{v}', \quad x = L \tag{4.6}$$

where $S = I/A$ is a parameter that characterizes the effect of rotary inertia. Clearly, when S is very small, this model reduces to the Euler–Bernoulli model.

Timoshenko Dynamic Model (Model C)

In Timoshenko beam theory, both rotary inertia and shear deformation are taken into account. The normal plane assumption is replaced by the more accurate plane assumption; that is, the entire transverse section of the beam, originally plane, remains plane but may not be normal to the longitudinal axis of the beam after deformation [13]. Therefore, ψ is no longer equal to zero in this case. Based on Timoshenko beam theory, the governing dynamic equations of motion for one-link flexible manipulators can be obtained as

$$EI\, \alpha'' + kGA(v' - \alpha) - \rho S\ddot{\alpha} = 0 \tag{4.7}$$

$$kGA(v'' - \alpha') - \rho\ddot{v} = 0 \tag{4.8}$$

$$\tau - I_H\, \ddot{\theta} + EI\, \alpha'|_{x=0} = 0 \tag{4.9}$$

with the boundary conditions

$$\alpha(x,t) = \theta(t),\;\; v'(x,t) = 0, \quad x = 0, \qquad \alpha'(x,t) = 0,\;\; v'(x,t) = \alpha(x,t), \qquad x = L \tag{4.10}$$

where k is a numerical shape factor (for a rectangular section, $k = 10(1+\nu)/(12+11\nu)$) and ν is the Poisson ratio.

Since Eqs (4.7) and (4.8) are coupled and hence are difficult to analyze, it is desirable to find an equivalent set of decoupled equations for them. It was shown by Wang and Wen [10] that by introducing a new function $\phi(x,t)$ and letting

$$\alpha = \phi'' - \rho\mu S\ddot{\phi}/EI, \quad v = \phi' \tag{4.11}$$

Eqs (4.7) and (4.8) are equivalent to the following single equation for ϕ:

$$EI\phi'''' - \rho S(1+\mu)\ddot{\phi}'' + \rho\ddot{\phi} + \mu\frac{\rho^2 S}{EA}\frac{\partial^4\phi}{\partial t^4} = 0 \tag{4.12}$$

where $\mu = E/(kG)$ is a parameter representing the effect of pure shear deformation.

Euler–Bernoulli Dynamic Model with Tip Load (Model D)

Only the Euler–Bernoulli dynamic model is included here for the case where a tip load is present. After a time-consuming derivation, it is found that the equations of motion can be described as

$$EI\, v''' + \rho\, \ddot{v} = 0 \tag{4.13}$$

$$\tau - I_H\, \ddot{\theta} + EI\, v''|_{x=0} = 0 \tag{4.14}$$

with the boundary conditions

$$v(x,\ t) = 0, \quad v'(x,\ t) = \theta(t) \tag{4.15}$$

$$EIv''(L,t) = -J_p\ddot{v}'(L,t) - M_p a_c\ddot{v}(L,t) \tag{4.16}$$

$$EIv'''(L,t) = -M_p a_c\ddot{v}'(L,t) + M_p\ddot{v}(L,t) \tag{4.17}$$

As expected, the tip load has an effect only on the boundary conditions at the end $x = L$. Note that only the x coordinate a_c of the center of mass (a_c,b_c) affects the boundary conditions. Similar equations have been derived in Ref. [14] in which the tip load has been considered as a shapeless point with mass M_p and moment of inertia J_p.

The above four dynamic models provide the basis for investigating the influence of rotary inertia, shear deformation, and tip load on the vibration of one-link flexible manipulators.

4.2.3 Characteristic Equations for Modal Frequencies and Vibration Modes

The Laplace transformation has been used to derive the characteristic equations for modal frequencies of one-link flexible manipulators. For this purpose, we have assumed the existence of the following Laplace transformations:

$$\Psi(x,s) = L[\psi(x,t)], \quad \Lambda(x,s) = L[\alpha(x,t)], \quad \Phi(x,s) = L[\phi(x,t)]$$
$$V(x,s) = L[v(x,t)], \quad W(x,s) = L[w(x,t)]$$
$$\Theta(s) = L[\theta(t)], \quad Z(s) = L[z(t)], \quad T(s) = L[\tau(t)], \quad F(s) = L[f(t)]$$

It is also assumed that Laplace transformations of derivatives of $v(x,t)$ and $\phi(x,t)$ with respect to x exist up to the fourth order. Therefore, we have the following equations:

$$V^{(n)}(x,s) = L[v^{(n)}(x,t)], \quad \Phi^{(n)}(x,s) = L[\phi^{(n)}(x,t)], \quad n \leq 4$$

One should notice that the existence of the Laplace transformations of functions in this section should not be of any concern. This is because the Laplace analysis to be conducted here is exactly the same as the classical modeling analysis used in mechanics. One can verify it simply by replacing s with $j\omega$, where $j = \sqrt{-1}$ and ω is the vibration frequency. The existence of vibration modal shape functions should be obvious. The reason for using Laplace analysis instead of standard modal analysis is that the treatment by Laplace transformations is more uniform and clear from the perspective of control theory.

For all the dynamic models given in the previous section, by applying the Laplace transformation to the governing equations of motion and the corresponding boundary conditions with homogeneous initial conditions, we obtain the following partial differential equations for Laplace transformations in the frequency domain.

Euler–Bernoulli Dynamic Model (Model A)

The governing dynamic equations of motion are transformed into

$$EI\, V'''' + \rho s^2\, V = 0 \tag{4.18}$$

$$T \; - \; s^2 I_H\, \Theta + EIV''|_{x=0} = 0 \tag{4.19}$$

with the boundary conditions

$$V(x,s) = 0, \;\; V'(x,s) = \Theta(s), \quad x = 0, \qquad V''(x,s) = 0, \;\; V'''(x,s) = 0, \quad x = L \tag{4.20}$$

Solving equations (4.18)–(4.20), we can obtain transfer functions as

$$\Theta(s) = H_{\theta\tau}(s)T(s), \quad H_{\theta\tau}(s) = 1/[s^2 I_H + EIK_1(m)] \tag{4.21}$$

and

$$\begin{aligned} V(x,s) &= H_{v\theta}(x,s)\Theta(s) = H_{v\tau}(x,s)T(s) \\ W(x,s) &= H_{w\theta}(x,s)\Theta(s) = H_{w\tau}(x,s)T(s) \end{aligned} \tag{4.22}$$

where

$$\begin{aligned} H_{v\theta}(x,s) = {} & [\sin(mx) + \sinh(mL)\cos m(L-x) + \sin(mL)\cosh m(L-x)] \\ & +[\sinh(mx) - \cos(mL)\sinh m(L-x) - \cosh(mL)\sin m(L-x)]/2m\Sigma_1(m) \end{aligned} \tag{4.23}$$

$$H_{w\theta}(x,s) = H_{v\theta}(x,s) - x, \quad H_{v\tau}(x,s) = H_{v\theta}(x,s)H_{\theta\tau}(s), \quad H_{w\tau}(x,s) = H_{w\theta}(x,s)H_{\theta\tau}(s) \tag{4.24}$$

and

$$K_1(m) = m[\sinh(mL)\cos(mL) - \cosh(mL)\sin(mL)]/\Sigma_1(m) \tag{4.25}$$

$$\Sigma_1(m) = 1 + \cos(mL)\cosh(mL), \quad m^4 = -\rho s^2/(EI) \tag{4.26}$$

The poles of the manipulator system are determined by the transcendental characteristic equation:

$$m^4(I_H/\rho) - K_1(m) = 0 \tag{4.27}$$

Denoting m as a root of the characteristic equation, the corresponding modal frequency of the manipulator can be obtained as

$$\omega = \sqrt{EI/\rho}m^2 \tag{4.28}$$

Euler—Bernoulli Dynamic Model with Rotary Inertia (Model B)

After Laplace transformation, we have in this case:

$$EIV'''' - \rho s^2 SV'' + \rho s^2 V = 0 \tag{4.29}$$

$$T - s^2 I_H \Theta + EIV''\big|_{x=0} = 0 \tag{4.30}$$

with the boundary conditions

$$V(0,s) = 0, \quad V'(0,s) = \Theta(s), \quad V''(L,s) = 0, \quad EIV^m(L,s) = \rho s^2 SV'(L,s) \tag{4.31}$$

Based on these equations, we can obtain transfer functions as

$$\Theta(s) = H_{\theta\tau}(s)T(s), \quad H_{\theta\tau}(s) = 1/[s^2 I_H + EIK_2(m)] \tag{4.32}$$

and

$$V(x,s) = H_{v\theta}(x,s)\Theta(s) = H_{v\tau}(x,s)T(s), \quad W(x,s) = H_{w\theta}(x,s)\Theta(s) = H_{w\tau}(x,s)T(s) \tag{4.33}$$

where

$$H_{v\theta}(x,s) = \sinh(m_1\, x)/m_1 - C_1[\cosh(m_1 x) - \cos(m_2 x)] - C_2[m_2 \sinh(m_1 x) - m_1 \sin(m_2 x)] \tag{4.34}$$

$$H_{w\theta}(x,s) = H_{v\theta}(x,s) - x, \quad H_{v\tau}(x,s) = H_{v\theta}(x,s)H_{\theta\tau}(s), \quad H_{w\tau}(x,s) = H_{w\theta}(x,s)H_{\theta\tau}(s) \tag{4.35}$$

and

$$\begin{aligned} 2m\Sigma_2(m)C_1 &= \beta_1^3\sinh(m_1L)\cos(m_2L) - \beta_2^3\cosh(m_1L)\sin(m_2L) \\ 2m^2\Sigma_2(m)C_2 &= 1 + \beta_1^2\sinh(m_1L)\sin(m_2L) + \beta_2^4\cosh(m_1L)\cos(m_2L) \end{aligned} \tag{4.36}$$

$$\begin{aligned} K_2(m) &= -C_1m^2\sqrt{4+S^2m^4}, \quad m_1 = m\beta_i \\ \beta_i &= \left[\left[\sqrt{4+S^2m^4} + (-1)^iSm^2\right]\Big/2\right]^{1/2}, \quad m^4 = -\rho s^2/(EI) \end{aligned} \tag{4.37}$$

$$\sum_2(m) = 1 + (1 + m^4S^2/2)\cosh(m_1L)\cos(m_2L) - (m^2S/2)\sinh(m_1L)\sin(m_2L) \tag{4.38}$$

The poles of the manipulator system are determined by

$$m^4(I_H/\rho) - K_2(m) = 0 \tag{4.39}$$

and the corresponding modal frequency is

$$\omega = \sqrt{EI/\rho}\ m^2 \tag{4.40}$$

Note that when $S = 0$, K_2 and Σ_2 become K_1 and Σ_1 respectively. Therefore, Eqs (4.27) and (4.39) give the same modal frequencies in this case.

Timoshenko Dynamic Model (Model C)

Instead of Eqs (4.7) and (4.8), Eqs (4.11) and (4.12) have been used here. We have

$$EI\Phi'''' - \rho s^2S(1+\mu)\Phi'' + \rho s^2\Phi + \mu(\rho^2S/EA)s^4\Phi = 0 \tag{4.41}$$

$$\Lambda = \Phi'' - \rho\mu s^2S\Phi/EI, \quad V = \Phi' \tag{4.42}$$

$$T - s^2I_H\Theta + EI\Lambda'\big|_{x=0} = 0 \tag{4.43}$$

with the boundary conditions

$$\Lambda(x,s) = \Theta(s),\ \ V(x,s) = 0, \quad x = 0, \qquad \Lambda'(x,s) = 0,\ \ V'(x,s) = \Lambda(x,s), \quad x = L \tag{4.44}$$

After many tedious manipulations, we arrive at the following equations:

$$\Theta(s) = H_{\theta\tau}(s)T(s), \quad H_{\theta\tau}(s) = 1/[s^2I_H + EIK_3(m)] \tag{4.45}$$

and

$$\begin{aligned} V(x,s) &= H_{v\theta}(x,s)\Theta(\sigma) = H_{\theta\tau}(x,s)T(s) \\ W(x,s) &= H_{w\theta}(x,s)\Theta(s) = H_{w\tau}(x,s)T(s) \end{aligned} \tag{4.46}$$

$$\psi(x,s) = H_{\psi\theta}(x,s)\Theta(s) = H_{\psi\tau}(x,s)T(s), \quad \Lambda(x,s) = H_{\alpha\tau}(x,s)\Theta(s) = H_{\alpha\tau}(x,s)T(s) \tag{4.47}$$

where

$$\begin{aligned} H_{\alpha\tau}(x,s) = \cosh(m_1x) + C_2(m_2^2 - \mu S m^4)[\cosh(m_1x) - \cos(m_2x)] \\ + C_3[m_2(m_1^2 + \mu S m^4)\sinh(m_1x) + m_1(m_2^2 - \mu S m^4)\sin(m_2x)] \end{aligned} \tag{4.48}$$

$$H_{v\theta}(x,s) = C_1m_1\sinh(m_1x) - C_2m_2\sin(m_2x) - m_1m_2C_3[\cosh(m_1x) - \cos(m_2x)] \tag{4.49}$$

$$H_{\omega\theta}(x,s) = H_{v\theta}(x,s) - x, \quad H_{v\tau}(x,s) = H_{v\theta}(x,s)H_{\theta\tau}(s), \quad H_{w\tau}(x,s) = H_{\omega\theta}(x,s)H_{\theta\tau}(s) \tag{4.50}$$

$$H_{\psi\theta}(x,s) = H_{\alpha\theta}(x,s) - 1, \quad H_{\alpha\tau}(x,s) = H_{\alpha\theta}(x,s)H_{\theta\tau}(s), \quad H_{\psi\tau}(x,s) = H_{\psi\theta}(x,s)H_{\theta\tau}(s) \tag{4.51}$$

and

$$\begin{aligned} 2m^6\textstyle\sum_3(m)C_1 &= m_2[(m_2^2 - \mu S m^4)(m_1 - m_2\sinh(m_1L)\sin(m_2L)) \\ &\quad + m_1(m_1^2 + \mu S m^4)\cosh(m_1L)\cos(m_2L)] \\ 2m^6\textstyle\sum_3(m)C_2 &= -m_1[(m_1^2 + \mu S m^4)(m_2 + m_1\sinh(m_1L)\sin(m_2L))] \\ &\quad - m_1m_2(m_2^2 - \mu S m^4)\cosh(m_1L)\cos(m_2L) \\ 2m^6\textstyle\sum_3(m)C_3 &= m_2(m_2^2 - \mu S m^4)\cosh(m_1L)\sin(m_2L) \\ &\quad - m_1(m_1^2 + \mu S m^4)\sinh(m_1L)\cos(m_2L) \\ K_3 &= m_1m_2(m_1^2 + m_2^2)C_3, \quad m_i = m\beta_i, \ \ i = 1,\ 2 \end{aligned} \tag{4.52}$$

$$\beta_i = \left[\left[\sqrt{4 + S^2(1-\mu)^2m^4} + (-1)^iS(1+\mu)m^2\right]\Big/2\right]^{1/2}, \quad m^4 = -\rho s^2/(EI) \tag{4.53}$$

$$\begin{aligned} \textstyle\sum_3(m) = \beta_1\beta_2 + \beta_1\beta_2\left[1 + (1-\mu)^2m^4S^2/2\right]\cosh(m_1L)\cos(m_2L) \\ -(1+\mu)(m^2S/2)\sinh(m_1L)\sin(m_2L) \end{aligned} \tag{4.54}$$

The poles are determined by

$$m^4(I_H/\rho) - K_3(m) = 0 \tag{4.55}$$

As before, one can obtain the corresponding resonant frequency of the manipulator once the roots of the characteristic equation have been found.

It is easy to check that when $\mu = 0$, K_3 and Σ_3 reduce to K_2 and Σ_2 respectively; furthermore, when both $\mu = 0$ and $S = 0$, K_3 and Σ_3 will reduce to K_1 and Σ_1 respectively. In a sense, this shows the correctness of the characteristic equation.

Euler–Bernoulli Dynamic Model with Tip Load (Model D)

Finally, when a tip load is present, we have

$$EIV'''' + \rho s^2 V = 0 \tag{4.56}$$

$$T - s^2 I_H \Theta + EIV''\big|_{x=0} = 0 \tag{4.57}$$

with boundary conditions

$$V(0,s) = 0, \quad V'(0,s) = \Theta(s) \tag{4.58}$$

$$EIV''(L,s) = -J_p s^2 V'(L,s) - M_p a_c s^2 V(L,s) \tag{4.59}$$

$$EIV'''(x,s) = M_p a_c s^2 V'(L,s) + M_p s^2 V(L,s) \tag{4.60}$$

Similarly, we have the following equations for transfer functions:

$$\Theta(s) = H_{\theta\tau}(s)T(s), \quad H_{\theta\tau}(s) = 1/[s^2 I_H + EIK_4(m)] \tag{4.61}$$

and

$$V(x,s) = H_{v\theta}(x,s)\Theta(s) = H_{v\tau}(x,s)T(s) \tag{4.62}$$

$$W(x,s) = H_{w\theta}(x,s)\Theta(s) = H_{w\tau}(x,s)T(s) \tag{4.63}$$

where

$$\begin{aligned} H_{v\theta}(x,s) = [&(1+\delta_1)\sin(mx) + (1-\delta_2)\sinh(mL)\cos m(L-x) \\ &+ (1-\delta_3)\sin(mL)\cosh m(L-x) + (1+\delta_1)\sinh(mx) \\ &- (1-\delta_2)\cos(mL)\sinh m(L-x) - (1-\delta_3)\cosh(mL)\sin m(L-x) \\ &- 2\xi_1\sinh(mL)\sin(L-x) - 2\xi_3\cosh(mL)\cos(L-x) \\ &+ 2\xi_1\sin(mL)\sinh(L-x) + 2\xi_3\cos(mL)\cosh(L-x)]/2m\Sigma_4(m). \end{aligned} \tag{4.64}$$

The dimensionless parameters are defined as

$$\delta_1 = -\xi_2^2 + \xi_1\xi_3, \quad \delta_2 = -\xi_2^2 + \xi_1\xi_3 + 2\xi_2, \quad \delta_3 = -\xi_2^2 + \xi_1\xi_3 - 2\xi_2 \tag{4.65}$$

$$\xi_1 = M_p m/\rho, \quad \xi_2 = M_p a_c m^2/\rho, \quad \xi_3 = J_p m^3/\rho \tag{4.66}$$

and

$$K_4(m) = m\{(\xi_2^2 - \xi_1\xi_3 + 1)[\sinh(mL)\cos(mL) - \cosh(mL)\sin(mL)] - 2\xi_1\sin(mL)\sin(mL) - 2\xi_2[\sinh(mL)\cos(mL) + \cosh(mL)\sin(mL)] - 2\xi_3\cosh(mL)\cos(mL)\}/\Sigma_4(m) \tag{4.67}$$

$$\Sigma_4(m) = [1 + \cos(mL)\cosh(mL)] - \xi_1[\cosh(mL)\sin(mL) - \cos(mL)\sinh(mL)] - 2\xi_2[\sin(mL)\sinh(mL)] - \xi_3[\sinh(mL)\cos(mL) + \sin(mL)\cosh(mL)] + (\xi_2^2 - \xi_1\xi_3)[\cosh(mL)\cos(mL) - 1] \tag{4.68}$$

The characteristic equation now becomes

$$m^4(I_H/\rho) - K_4(m) = 0 \tag{4.69}$$

When no tip load is present, all ξs and therefore δs vanish and, as expected, K_4 and Σ_4 reduce to K_1 and Σ_1 respectively.

As a by-product of the above derivations, we can find vibration modes (or mode shape functions) from transfer functions $H_{\upsilon\theta}$ for different models. Specifically, let mn be the nth root of a characteristic equation. The corresponding vibration mode can then be found as

$$\psi_n^d = H_{\upsilon\theta}^d 2m_n^2/K_d \tag{4.70}$$

where $d = 1, 2, 3, 4$ corresponds to the four dynamic models.

Finally, in all four dynamic models, one can identify $\Sigma_d = 0$, $d = 1, 2, 3, 4$, as the corresponding characteristic equation for modal frequencies when a flexible manipulator is considered as a beam fixed on a hub with an infinitely large moment of inertia.

4.2.4 Asymptotic Behavior of Modal Frequencies and Vibration Modes

Since characteristic equations are transcendental equations, they specify an infinite (but countable) number of natural modal frequencies and vibration modes for a one-link flexible manipulator. Therefore, it is very useful analytically to know the properties of high-order (or large) modal frequencies and the corresponding vibration modes. This is even more important for the purpose of numerical analysis, because as the order of the vibration modes increases, the computation of the exponential functions involved in the characteristic equations and expressions of vibration modes becomes extremely difficult (almost impossible) to accomplish with reasonable accuracy. In this section, we present results of the asymptotic behavior for high-order vibrations of one-link flexible manipulators.

Euler–Bernoulli Dynamic Model (Model A)

The asymptotic expression for high-order frequencies can be obtained by considering the characteristic equation (4.27). As m approaches infinity, $K_1(m)$ approaches $m[\cos(mL) - \sin(mL)]/\cos(mL)$. Therefore, in order to satisfy the characteristic equation, for large m, it must be that $\cos(mL) \to 0$, which leads to the asymptotic expression for large modal frequencies:

$$\omega_n^1 = [(2n-1)\pi/(2L)]^2\sqrt{EI/\rho}, \quad n >> 1 \tag{4.71}$$

For the corresponding vibration modes, after a similar process, one can find the simple asymptotic expression:

$$\psi_n^1(x) = -\sin(k_n x) + \cos(k_n x), \quad 0 < x < L; \;\; k_n^4 = \rho\omega_n^2/(EI) \tag{4.72}$$

Note that the asymptotic expressions for high-order vibration modes are not valid at the two ends of the manipulators, where the boundary conditions should be used.

Euler–Bernoulli Dynamic Model with Rotary Inertia (Model B)

Applying the same technique to the characteristic equation in this case, we can see that as m becomes larger, it must be true that $\cos(m^2\sqrt{S}L) \to 0$. Therefore, the asymptotic expression for high-order frequencies becomes

$$\omega_n^2 = ((2n-1)\pi/(2L\sqrt{S}))\sqrt{EI/\rho}, \quad n >> 1 \tag{4.73}$$

Similarly, for high-order vibration modes:

$$\begin{gathered} \psi_n^2(x) = -(k_2^3/k_1^3)\sin(k_2 x) - \cos(k_2 x), \quad 0 < x < L \\ k_1 = \sqrt{-\sigma/2 + \sqrt{\sigma^2/4 + \sigma/S}}, \quad k_2 = \sqrt{k_1^2 + \sigma}, \;\; \sigma = \rho S\omega_n^2/(EI) \end{gathered} \tag{4.74}$$

Timoshenko Dynamic Model (Model C)

For the Timoshenko dynamic model, the asymptotic expressions for high-order modal frequencies and vibration modes can be obtained as

$$\begin{gathered} \omega_n^3 = ((2n-1)\pi/(2L\sqrt{S\mu}))\sqrt{EI/\rho}, \quad n >> 1 \\ \psi_n^3(x) = ((k_1^3 + \sigma_1 k_1)/(k_2^3 - \sigma_1 k_2))\sin(k_2 x) - \cos(k_2 x), \quad 0 < x < L \end{gathered} \tag{4.75}$$

$$\begin{gathered} k_1 = \sqrt{-\sigma/2 + \sqrt{\sigma^2/4 + \sigma_1/(\mu S) - \sigma_1^2/\mu}}, \quad k_2 = \sqrt{\sigma + k_1^2} \\ \sigma = \rho S(1+\mu)\omega_n^2/(EI), \quad \sigma_1 = \rho\mu S\omega_n^2/(EI) \end{gathered} \tag{4.76}$$

ω_n^3 and ω_n^2 have the same magnitude, and have a constant ratio $1/\sqrt{\mu}$.

Euler–Bernoulli Dynamic Model with Tip Load (Model D)

In this case, the asymptotic expression for high-order frequencies becomes more involved. After some manipulations, we can show that

$$\omega_n^4 = \left[\frac{\arctan((1+\xi_1-\xi_3+\xi_2^2-\xi_1\xi_3)/(\xi_1+2\xi_2+\xi_3))}{L} + (n-1)\pi/L\right]^2 \sqrt{EI/\rho}, \quad n >> 1 \tag{4.77}$$

The corresponding vibration modes are

$$\psi_n^4(x) = -\sin(k_n x) + \cos(k_n x), \quad 0 < x < L \tag{4.78}$$

which is the same as the high-order vibration modes of Eq. (4.72). Therefore, the tip load has no effect on the high-order vibration modes, but it does affect the corresponding frequencies.

All of these asymptotic expressions have been verified numerically. In most cases, they give very accurate results for $n > 8$.

4.2.5 Experimental Verification and Numerical Analysis

The results of experimental verification and numerical analysis for various cases are presented in this section. A detailed comparison between different dynamic models is made on the basis of those results.

Experimental Verification

A one-link very flexible manipulator has been built at the NASA Center for Intelligent Robotic Systems for Space Exploration (CIRSSE) at the Rensselaer Polytechnic Institute. The parameters of the CIRSSE flexible manipulator are given in Table 4.1, where three tip load parameters are defined as

$$\lambda_1 = M_p/(\rho L), \quad \lambda_2 = a_c/L, \quad \lambda_3 = J_p/I$$

The experimentally obtained modal frequencies for the first nine vibration modes [5], and the corresponding frequencies calculated from the characteristic equations of the first three dynamic models, are listed in Table 4.2. In all the cases, the analytical predictions agree with the experimental data to within $\pm 5\%$. Note that for this particular manipulator, all three models give almost the same results, since both parameter S and the width-to-height ratio of the beam are very small and, therefore, the effect of rotary inertia and shear deformation is negligible. Clearly, the experimental results have verified the accuracy of the three dynamic models.

Table 4.1: Parameters of the CIRSSE one-link flexible manipulator

Variable	Definition	Value
L	Beam length	1.098 m
B	Beam width	1.5875e-3 m
H	Beam height	0.103 m
E	Young's modulus for material	60676.0e6 N/m^2
γ	Material density of beam	2.713e3 kg/m^3
I_H	Hub inertia	0.0175 kg m^2
ν	Poisson's ratio for beam	0.3
A	Beam transverse area	1.6351e-4 m^2
I	Beam transverse inertia	3.4340e-11 kg m^2
ρ	Beam mass per unit length	0.4436 kg/m
k	Shape factor	0.8497
S	$= I/A$	2.1001e-7 m^2
μ	$= 2(1+\nu)/k$	3.0600
λ_1^*	Tip weight factor	0.150%
λ_2^*	Tip length factor	0.150%
λ_3^*	Tip inertia factor	0.150%

*No tip load was present in the experiments: these parameters are just for the calculation in model D.

Table 4.2: Comparison of experimental and analytical results for modal frequencies

	Resonant Frequency			
Mode Order	*Model A (Hz)*	*Model B (Hz)*	*Model C (Hz)*	*Experiment (Hz)*
0	0	0	0	0
1	2.9692	2.9692	2.9692	2.850
2	7.2608	7.2608	7.2608	7.200
3	17.977	17.977	17.977	18.42
4	34.752	34.751	34.751	35.65
5	57.277	57.276	57.273	58.70
6	85.482	85.480	85.472	88.00
7	119.35	119.34	119.33	126.3
8	158.87	158.86	158.84	166.6
9	204.04	204.03	203.98	214.4
10	254.86	254.84	254.77	N/A
11	311.33	311.30	311.20	N/A
12	373.45	373.41	373.27	N/A
13	441.22	441.16	440.97	N/A
14	514.63	514.55	514.29	N/A
15	593.69	593.58	593.24	N/A

Influence of Rotary Inertia

The influence of rotary inertia on the vibration frequencies is through the parameter S, which is equal to $B^2/12$ (B is the width of the beam). Actually, S reflects the ratio of the beam width to the beam height (H), i.e. B/H. Figure 4.3 shows the influence of rotary inertia on the

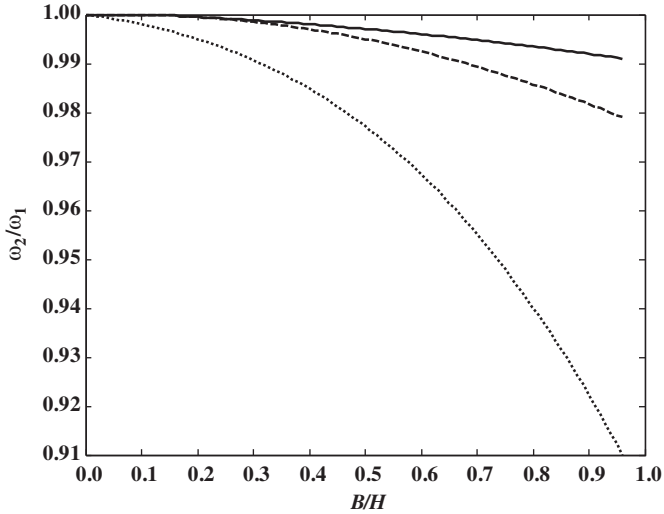

Figure 4.3: Influence of Rotary Inertia.
$\nu = 0.3$; ω_1 = frequency of model A; ω_2 = frequency of model B. (—) mode 1; (----) mode 2; (· · · ·) mode 3.

first-, second-, and sixth-order modal frequencies with Poisson's ratio $\nu = 0.3$, as B/H increases from 0 to 1. The results show that the frequencies calculated become smaller when the effect of rotary inertia is considered. Since the differences are within $\pm 10\%$, the results also indicate that, for lower vibration modes, the effect of rotary inertia is not very significant and generally can be ignored. For high-order vibration modes, however, as will be indicated later in the following subsection, the effect is indeed significant.

Influence of Shear Deformation

Both the beam shape and Poisson's ratio ν play a role in the effect of shear deformation on the vibration of flexible manipulators. Figure 4.4 shows the influence of shear deformation on the first-, second-, and sixth-order modal frequencies with Poisson's ratio $\nu = 0.3$ as B/H increases from 0 to 1. Similar to the case of rotary inertia, the results show that the frequencies calculated become smaller when shear deformation is included. For the sixth-order frequency, the difference is already more than $\pm 26\%$, and therefore the effect of shear deformation generally cannot be ignored. The results also demonstrate that the effect of shear deformation is much more significant than that of rotary inertia, a conclusion that should be expected since rotary inertia has already been considered in shear deformation.

In Figure 4.5, different modal frequencies calculated from Euler–Bernoulli, Euler–Bernoulli with rotary inertia, and Timoshenko models respectively are illustrated,

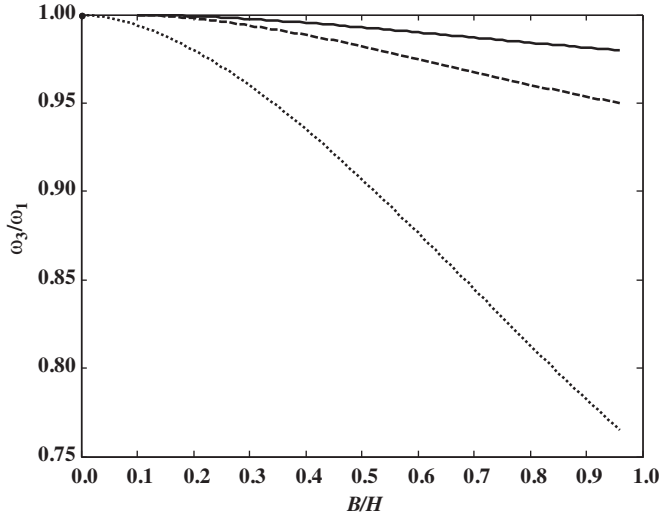

Figure 4.4: Influence of Shear Deformation.
$\nu = 0.3$; $\omega_1 =$ frequency of model A; $\omega_2 =$ frequency of model C. (—) mode 1; (----) mode 2; (· · · ·) mode 3.

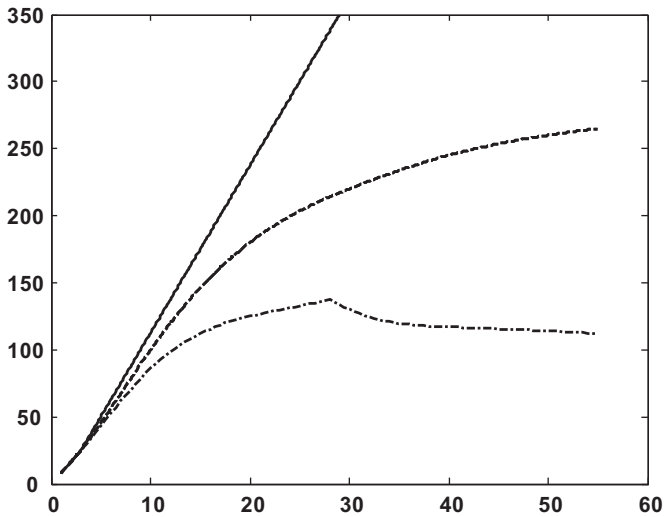

Figure 4.5: Influence of Rotary Inertia and Shear Deformation.
(—) Euler—Bernoulli; (---) Euler—Bernoulli with rotary inertia; (-· · ·-) Timoshenko.

in terms of $(4\omega L/(n+1)\pi)\sqrt{\rho/EI}$ vs. $(n+1)/(2L)$. This indicates clearly that the effect of rotary inertia and shear deformation is profound for high-order vibration modes. This figure is very similar to the classical results obtained in the theory of elasticity on the influence of rotary inertia and shear deformation on vibrations of beams and plates [1—5].

Influence of Tip Load

The influence of the tip load through the three parameters λ_1, λ_2, and λ_3, for the first-, second-, and sixth-order vibration modes, is shown in Figures 4.6–4.14. In these figures, all parameters except the varying one take the values specified in Table 4.1. The results indicate that the mass of the tip load is the most significant factor regarding the effect of tip load on

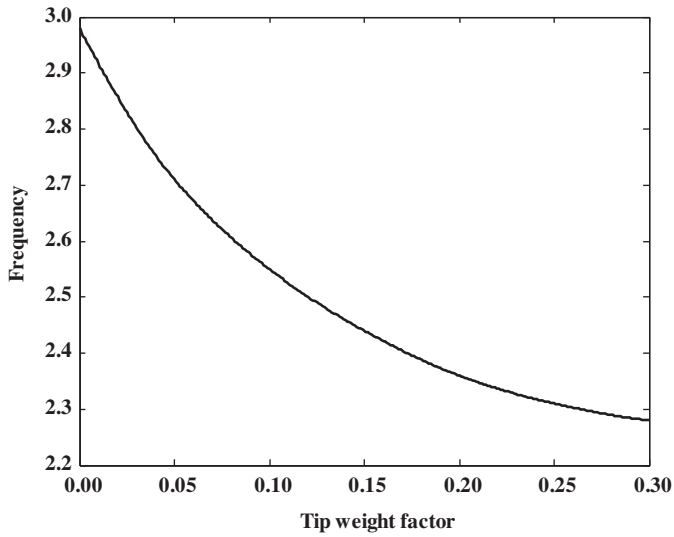

Figure 4.6: Influence of Tip Mass: First Order.

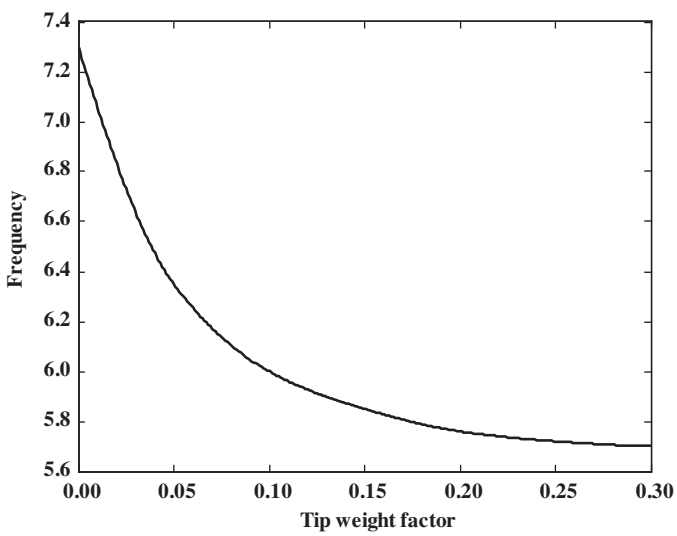

Figure 4.7: Influence of Tip Mass: Second Order.

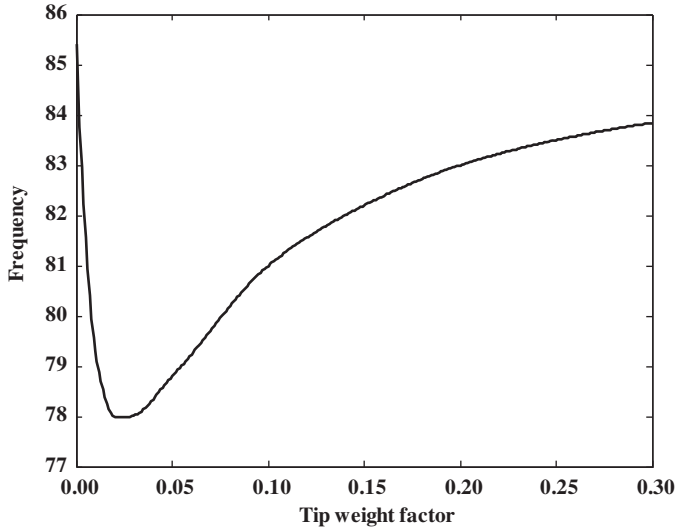

Figure 4.8: Influence of Tip Mass: Sixth Order.

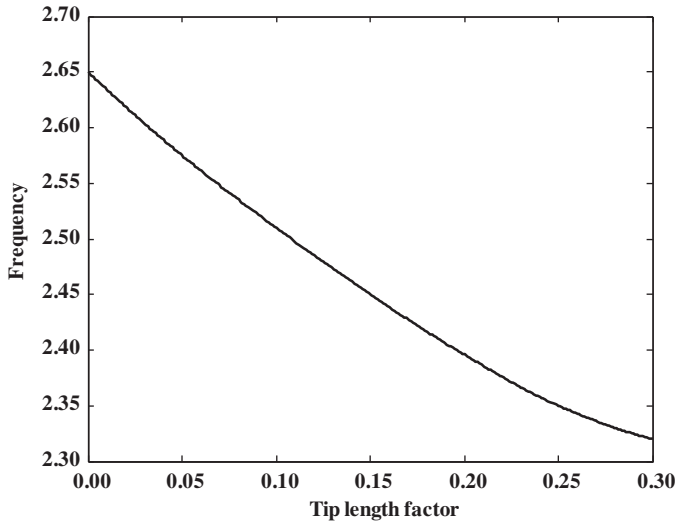

Figure 4.9: Influence of Tip Length: First Order.

vibration. For example, it drives the first-order frequency down by 10% when the mass of the tip load is 5% of the beam mass, and down by 25% when the mass is 30% of beam mass. Therefore, when a load with a large mass is grasped by a flexible manipulator, the dynamics of the manipulator will be changed dramatically. If the controller of the manipulator cannot predicate this change in dynamics, its performance will degenerate. This observation is important since, in civil construction and space applications, a flexible manipulator is usually

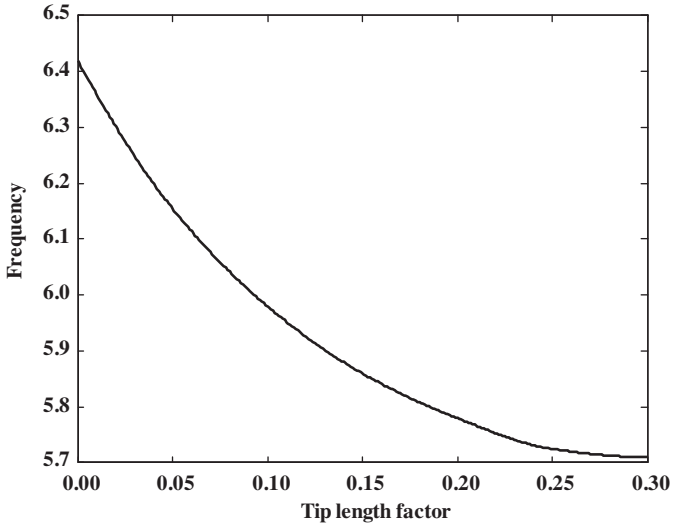

Figure 4.10: Influence of Tip Length: Second Order.

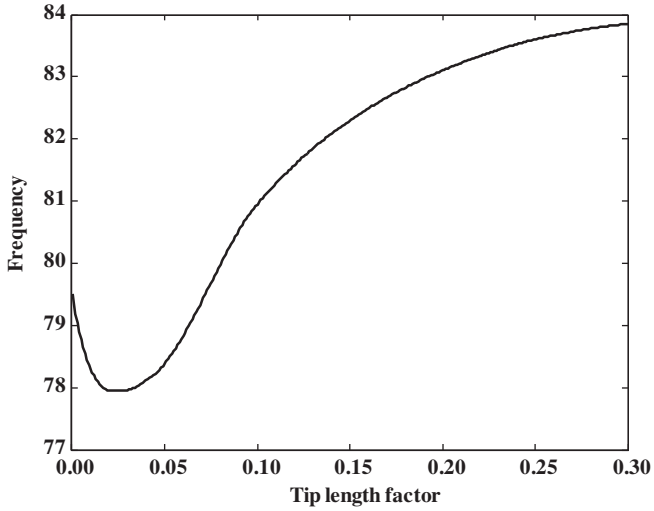

Figure 4.11: Influence of Tip Length: Sixth Order.

expected to deal with loads of relatively large mass compared to its own. The length of the tip load affects the modal frequencies in a similar fashion, but the variation of frequencies is generally less than that induced by the change in the tip mass. To our surprise, the moment of inertia of the tip load is the least significant factor of the three, and has almost no influence on the lower order vibration modes (see Figure 4.12).

The most surprising result is the influence of the tip mass and length on the higher order vibration modes (see Figures 4.8, 4.10, 4.13, and 4.14). First of all, for vibration modes with

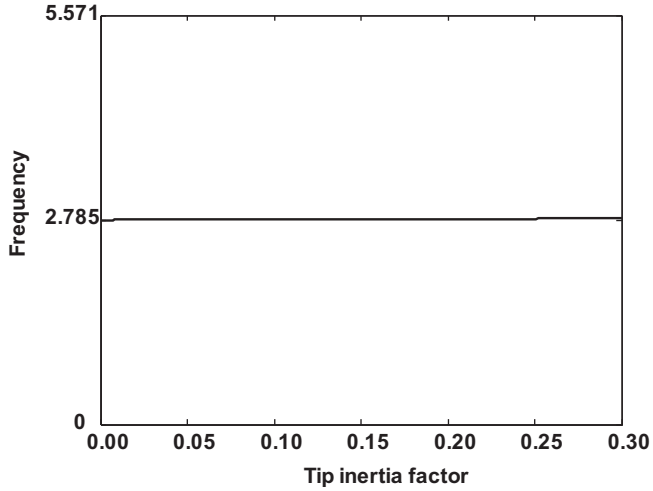

Figure 4.12: Influence of Tip Inertia: First Order.

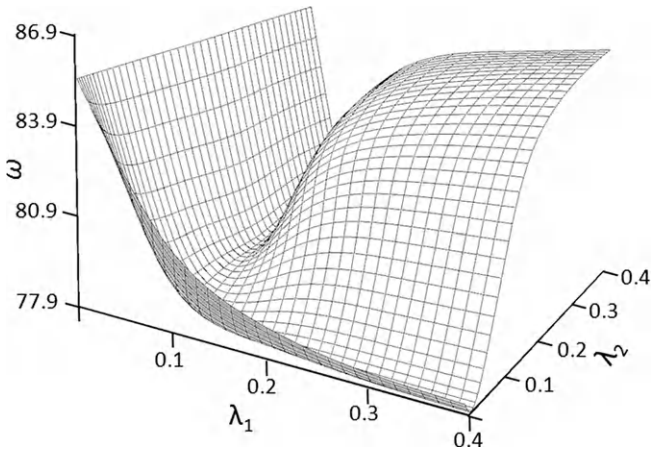

Figure 4.13: Sixth-Order Frequency vs. λ_1 and λ_2.

an order higher than six, the frequencies vary dramatically with change in tip mass and length. The unexpected result, however, is that when the tip mass or length exceeds certain values (e.g. for the sixth-order vibration mode, $\lambda_1 > 0.02$ or $\lambda_2 > 0.02$), modal frequencies increase with the tip mass or length, instead of decreasing as we would expect intuitively. A careful inspection of the numerical results indicates that this phenomenon is caused by the increased distance between the modal frequencies of two vibration modes. In other words, the distribution of modal frequencies is changed when the tip mass or length becomes large. More specifically, within a given frequency range, one can find more vibration modes for a very small tip mass or length, but fewer for a large tip mass or length.

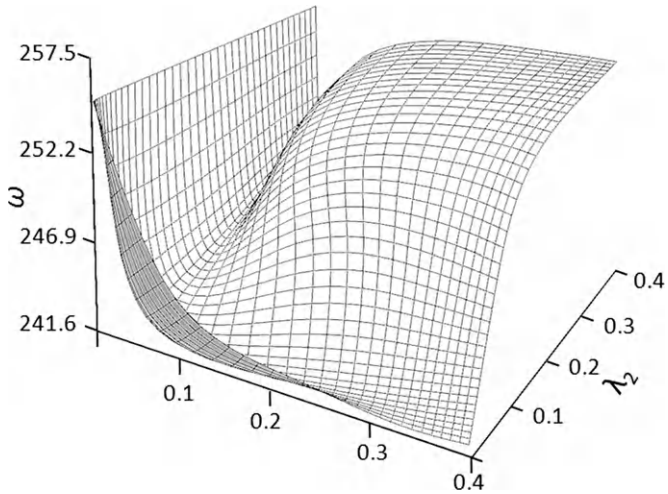

Figure 4.14: Tenth-Order Frequency vs. λ_1 and λ_2.

4.2.6 Natural Frequencies and Model Shape Functions

Based on the results in Chapter 3, it is straightforward to obtain the harmonic vibration equations of one-link flexible manipulators as follows.

Euler—Bernoulli Model

Mathematically, synchronous motions imply that the solution of Eqs (3.63)—(3.65) is separable in the spatial variable and time, and hence it has the form:

$$z(\xi, t) = z(\xi)\mathrm{e}^{iwt} \tag{4.79}$$

where $z(\xi)$ depends on the spatial position alone and e^{iwt} depends on time alone.

Substituting Eq. (4.79) into Eqs (3.63)—(3.65), we can write

$$z'''' + \delta m^2 z'' - m^2 z = 0 \tag{4.80}$$

with boundary conditions

$$z(0) = 0, \quad z''(0) + \eta m^2 z'(0) = 0 \tag{4.81}$$

$$z''(1) - m^2[\kappa z'(1) + \zeta\mu z(1)] = 0, \quad z'''(1) + m^2[(\delta + \mu\zeta)z'(1) + \mu z(1)] = 0 \tag{4.82}$$

where $m = c\omega$ is the dimensionless frequency and ω is the circular vibration frequency.

The solution of Eq. (4.80) has exponential form:

$$z(\xi) = A\mathrm{e}^{\lambda\xi} \tag{4.83}$$

Introducing Eq. (4.83) into Eq. (4.80) and dividing through by $Ae^{\lambda\xi}$, we obtain the characteristic equation:

$$\lambda^4 + \delta m^2 \lambda^2 - m^2 = 0 \tag{4.84}$$

and

$$\lambda_{1,3} = \pm m\left(\frac{-\delta + \sqrt{\delta^2 + 4m^{-2}}}{2}\right)^{\frac{1}{2}}, \quad \lambda_{2,4} = \pm m\left(\frac{\delta + \sqrt{\delta^2 + 4m^{-2}}}{2}\right)^{\frac{1}{2}} i \tag{4.85}$$

Let

$$\beta_1 = \left[\frac{\sqrt{\delta^2 + 4m^{-2}} + \delta}{2}\right]^{\frac{1}{2}}, \quad \beta_2 = \left[\frac{\sqrt{\delta^2 + 4m^{-2}} - \delta}{2}\right]^{\frac{1}{2}} \tag{4.86}$$

$$\begin{gathered} \lambda_j = \begin{cases} \pm m\beta_1 i \\ \pm m\beta_2 \end{cases}, \quad j = 1,\ 2,\ 3,\ 4 \\ k = \frac{m\lambda_1\lambda_2}{\lambda_1^2 + \lambda_2^2} = \frac{1}{\sqrt{\delta^2 + 4m^{-2}}} \end{gathered} \tag{4.87a}$$

It follows that the solution of Eq. (4.80) has the harmonic form:

$$z(\xi) = C_1 \sin \lambda_1\xi + C_2 \cos \lambda_1\xi + C_3 \sinh \lambda_2\xi + C_4 \cosh \lambda_2\xi \tag{4.87b}$$

C_1, C_2, C_3, and C_4 can be determined by using the boundary conditions:

$$\begin{aligned} C_2 &= -C_4 \\ C_4 &= -\frac{\eta m^2}{\lambda_1^2 + \lambda_2^2}(C_1\lambda_1 + C_3\lambda_2); \end{aligned}$$

The general solution (4.87b) can be rewritten as

$$\begin{aligned} z(\xi) &= C_1 \sin \lambda_1\xi + C_3 \sinh \lambda_2\xi - \frac{\eta m^2}{\lambda_1^2 + \lambda_2^2}(C_1\lambda_1 + C_3\lambda_2)(\cos \lambda_1 - \xi \cosh \lambda_2\xi) \\ &= C_1 \sin \lambda_1\xi + \lambda_1 \frac{\eta m^2}{\lambda_1^2 + \lambda_2^2}(\cos \lambda_1\xi - \cosh \lambda_2\xi) \\ &\quad + C_3 \sinh \lambda_1\xi + \lambda_2 \frac{\eta m^2}{\lambda_1^2 + \lambda_2^2}(\cos \lambda_1\xi - \cosh \lambda_2\xi) \\ &= A_1[\beta_2 \sin \lambda_1\xi + \eta k(\cos \lambda_1\xi - \cosh \lambda_2\xi)] \\ &\quad + A_2[\beta_1 \sin \lambda_2\xi + \eta k(\cos \lambda_1\xi - \cosh \lambda_2\xi)] \end{aligned}$$

where

$$A_1 = C_1/\beta_2, \quad A_1 = C_3/\beta_1, \quad k = \frac{m\lambda_1\lambda_2}{\lambda_1^2 + \lambda_2^2} = \frac{1}{\sqrt{\delta^2 + 4m^{-2}}}$$

The characteristic equation for determining the natural frequency can be found as

$$\sum \delta(m) = \begin{bmatrix} z_{11}(m) & z_{12}(m) \\ z_{21}(m) & z_{22}(m) \end{bmatrix} = 0$$

where

$$\begin{bmatrix} z_{11} & z_{12} \\ z_{21} & z_{22} \end{bmatrix} = \begin{bmatrix} Z''(1) - m^2(\kappa Z'(1) + \zeta\mu Z(1)) \\ Z'''(1) + m^2((\delta + \mu\zeta)Z'(1) + \mu Z(1) \end{bmatrix}$$

in which the function $Z = (z_s, z_h)$ is defined as

$$z_s(\xi) = \beta_2 \sin \lambda_1\xi + \eta k(\cos \lambda_1\xi - \cosh \lambda_2\xi)$$

$$z_h(\xi) = \beta_1 \sin \lambda_2\xi + \eta k(\cos \lambda_1\xi - \cosh \lambda_2\xi)$$

Figure 4.15 presents ratios of the first-, second-, and third-order natural frequencies calculated from the Euler–Bernoulli model without ($\delta = 0$) and with ($\delta \neq 0$) the rotary inertia taken into account respectively. No tip load is assumed in these figures. Clearly, the effect of rotary inertia on vibration frequency is significant, especially for higher order vibration modes.

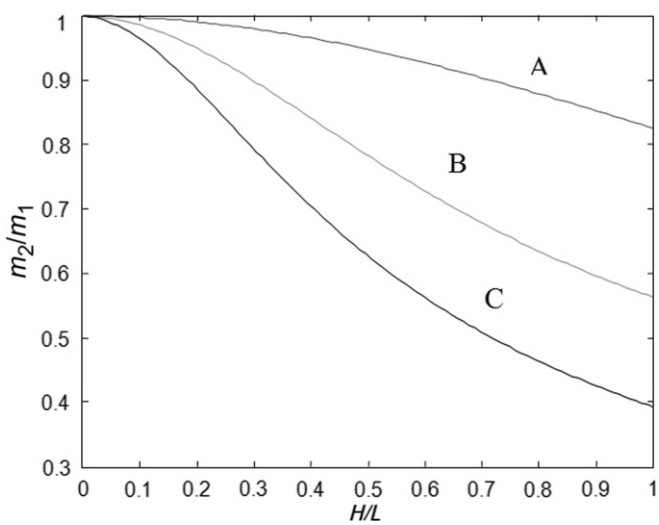

Figure 4.15: Influence of Rotary Inertia.

In Figure 4.15, H is the beam height and L is the beam length. m_2 and m_1 are the frequencies of the models with and without rotary inertia respectively. Curve A is the first mode, B is the second, and C is the third.

The normalized modal shape functions of the natural vibration can be found as

$$\begin{aligned} z(\xi;m) &= z_s(\xi) - \frac{z_{11}(m)}{z_{12}(m)} z_h(\xi) \\ z_i(\xi) &= \frac{z(\xi;m)}{\langle z(\xi;m_i)|z(\xi;m_i)\rangle_\delta}, \quad i = 0,\ 1,\ 2,\ \ldots \end{aligned} \tag{4.88}$$

where $\langle *|*\rangle_\delta$ is the generalized inner product for the Euler–Bernoulli model:

$$\begin{aligned} \langle f|z\rangle_\delta \equiv \int_0^1 (fz + \delta f' z')d\xi + \eta f'(0)z'(0) + \mu f(1)z(1) \\ + \mu\zeta[f'(1)z(1) + f(1)z'(1)] + \kappa f'(1)z'(1) \end{aligned}$$

One can show the following orthogonal relationship between modal shape functions:

$$\langle z_i|z_j\rangle_\delta = \delta_{ij}, \quad \int_0^1 z_i'' z_j'' d\xi = m^2\delta_{ij}, \quad \delta_{ij} = \begin{cases} 0 & i \neq j \\ 1 & i = j \end{cases} \tag{4.89}$$

For high vibration modes, the computation of exponential functions involved in cosh and sinh functions becomes very difficult. Therefore, it is very important to know the asymptotic behavior of high-order vibrations. For $\delta = 0$, one can show that

$$\lambda_1 \to \sqrt{m}, \quad \lambda_2 \to \sqrt{m}, \quad \text{as } m \to \infty.$$

However, for $\delta \neq 0$:

$$\lambda_1 \to \sqrt{\delta m}, \quad \lambda_2 \to 1/\sqrt{\delta}, \quad \text{as } m \to \infty$$

Therefore, some cosh and sinh functions of z_s and z_h will approach a constant value for high vibration modes, a very useful fact in numerical calculation.

Timoshenko Model

Mathematically, synchronous motions imply that the solution of Eqs (3.66)–(3.68) is separable in the spatial variable and time, and hence it has the form:

$$\varphi(\xi, t) = \varphi(\xi)\mathrm{e}^{iwt} \tag{4.90}$$

where $\phi(\xi)$ depends on the spatial position alone and e^{iwt} depends on time alone.

Introducing Eq. (4.90) into Eqs (3.66)–(3.68), we can write

$$\phi'''' - \left(\frac{1}{\sigma} + \delta\right) m^2 \phi'' + m^2 \phi + \frac{\delta}{\sigma} c^2 m^2 \phi = 0 \tag{4.91a}$$

with boundary conditions

$$\begin{gathered} \phi'(0) = 0, \quad \phi'''(0) + \frac{m^2}{\sigma}\phi'(0) + \eta m^2 \left[\phi''(0) + \frac{m^2}{\sigma}\phi(0)\right] = 0 \\ \phi'''(1) - m^2 \kappa \phi(1) + m^2 \left(\frac{1}{\sigma} - \zeta\mu\right)\phi'(1) - \kappa m^4 \phi(1) = 0 \end{gathered} \tag{4.91b}$$

$$\zeta\mu\phi''(1) + \mu\phi'(1) + \left(1 + \zeta\frac{\mu}{\sigma}\right)\phi(1) = 0 \tag{4.92}$$

The solution of Eq. (4.91a) has exponential form:

$$\phi(\xi) = A e^{\lambda\xi} \tag{4.93}$$

Introducing Eq. (4.93) into Eq. (4.91a) and dividing through by $Ae^{\lambda\xi}$, we obtain the characteristic equation:

$$\lambda^4 + \left(\delta + \frac{1}{\sigma}\right) m^2 \lambda^2 - \left(1 + \frac{\delta c^2}{\sigma}\right) m^2 = 0 \tag{4.94}$$

which has the roots

$$\lambda_{1,3} = \pm m \left(\frac{-\delta_s + \sqrt{\delta_s^2 + 4\delta_d m^{-2}}}{2}\right)^{\frac{1}{2}}, \quad \lambda_{2,4} = \pm m \left(\frac{\delta_s + \sqrt{\delta_s^2 + 4\delta_d m^{-2}}}{2}\right)^{\frac{1}{2}} i \tag{4.95}$$

where

$$\delta_s = \left(\frac{1}{\sigma} + \delta\right), \quad \delta_d = \left(\frac{\delta}{\sigma} c^2 + 1\right)$$

Let

$$\beta_1 = \left[\frac{\sqrt{\delta_d^2 + 4\delta_d m^{-2}} + \delta_s}{2}\right]^{\frac{1}{2}}, \quad \beta_2 = \left[\frac{\sqrt{\delta_d^2 + 4\delta_d m^{-2}} - \delta_s}{2}\right]^{\frac{1}{2}} \tag{4.96}$$

$$\lambda_j = \begin{cases} \pm m\beta_1 i \\ \pm m\beta_2 \end{cases}, \quad j = 1,\ 2,\ 3,\ 4$$
$$k_i = \frac{m^3[m^2 + (-1)^i \sigma\lambda_i^2]}{\sigma\lambda_1\lambda_2(\lambda_1^2 + \lambda_2^2)} = \frac{m[1 + (-1)^i \sigma\beta_i^2]}{\sigma\beta_1\beta_2(\beta_1^2 + \beta_2^2)} \tag{4.97a}$$

It follows that the solution of Eq. (4.91a) has the harmonic form:

$$\phi(\xi) = C_1 \sin\lambda_1\xi + C_2\cos\lambda_1\xi + C_3\sinh\lambda_2\xi + C_4\cosh\lambda_2\xi \tag{4.97b}$$

C_1, C_2, C_3, and C_4 can be determined by using the boundary conditions.

From $\phi'(0) = 0$ we obtain

$$C_1 = -C_3\frac{\lambda_2}{\lambda_1}$$

From

$$\phi'''(0) + \frac{m^2}{\sigma}\phi'(0) + \eta m^2\left[\phi''(0) + \frac{m^2}{\sigma}\varphi(0)\right] = 0$$

we obtain

$$C_3 = -\frac{\eta m^2}{\lambda_2(\lambda_1^2 + \lambda_2^2)}\left[C_2\left(\frac{m^2}{\sigma} - \lambda_1^2\right) + C_4\left(\frac{m^2}{\sigma} + \lambda_2^2\right)\right]$$

Therefore, the general solution (4.97b) can be rewritten as

$$\begin{aligned}
\phi(\xi) &= C_2\cos\lambda_1\xi + C_4\cosh\lambda_2\xi - \frac{\eta m^2}{\lambda_2(\lambda_1^2 + \lambda_2^2)} \\
&\quad \left[C_2\left(\frac{m^2}{\sigma} - \lambda_1^2\right) + C_4\left(\frac{m^2}{\sigma} + \lambda_2^2\right)\right]\left(\sinh\lambda_2\xi - \frac{\lambda_2}{\lambda_1}\xi\sin\lambda_1\xi\right) \\
&= C_2\left\{\cos\lambda_1\xi - \frac{\eta m^2}{\lambda_2(\lambda_1^2 + \lambda_2^2)}\left(\frac{m^2}{\sigma} - \lambda_1^2\right)\left(\sinh\lambda_2\xi - \frac{\lambda_2}{\lambda_1}\sin\lambda_1\xi\right)\right\} \\
&\quad + C_4\left\{\cosh\lambda_2\xi - \frac{\eta m^2}{\lambda_2(\lambda_1^2 + \lambda_2^2)}\left(\frac{m^2}{\sigma} + \lambda_2^2\right)\left(\sinh\lambda_2\xi - \frac{\lambda_2}{\lambda_1}\sin\lambda_1\xi\right)\right\} \\
&= C_2\{\cos\lambda_1\xi + \eta k_1(\beta_2\sinh\lambda_1\xi - \beta_1\sin\lambda_2\xi)\} \\
&\quad + C_4\{\cosh\lambda_2\xi + \eta k_2(\beta_2\sinh\lambda\xi - \beta_1\sin\lambda_2\xi)\}
\end{aligned}$$

where

$$k_i = \frac{m^3[m^2 + (-1)^i \sigma \lambda_i^2]}{\sigma \lambda_1 \lambda_2 (\lambda_1^2 + \lambda_2^2)} = \frac{m[1 + (-1)^i \sigma \beta_i^2]}{\sigma \beta_1 \beta_2 (\beta_1^2 + \beta_2^2)}$$

The characteristic equation for determining the natural frequencies is

$$\sum \sigma(m) = \det \begin{bmatrix} \phi_{11}(m) & \phi_{12}(m) \\ \phi_{21}(m) & \phi_{22}(m) \end{bmatrix} = 0$$

where

$$\begin{bmatrix} \phi_{11} & \phi_{12} \\ \phi_{21} & \phi_{22} \end{bmatrix} = \begin{bmatrix} \Phi'''(1) - m^2 \kappa \Phi''(1) + m^2(1/\sigma - \zeta\mu)\Phi'(1) - \kappa m^4 \Phi(1)/\sigma \\ \zeta\mu\Phi''(1) + \mu\Phi'(1) + (1 + \zeta\mu/\sigma)\Phi(1) \end{bmatrix}$$

in which $\Phi = (\phi_s, \phi_h)$ is defined as

$$\phi_s(\xi) = \cos \lambda_1 \xi + \eta k_1 (\beta_2 \sin \lambda_1 \xi - \beta_1 \sinh h\lambda_2 \xi)$$

$$\phi_h(\xi) = \cosh \lambda_2 \xi + \eta k_2 (\beta_2 \sin \lambda_1 \xi - \beta_1 \sinh h\lambda_2 \xi)$$

Figure 4.16 presents ratios of the first-, second-, and sixth-order frequencies calculated from the Euler–Bernoulli model ($\delta = 0$) and Timoshenko ($\delta = 0$, $\sigma \neq 0$) model respectively. The tip load is set to zero. Like the rotary inertia, the effect of shear deformation on vibration frequency is also significant, especially for higher order vibration modes. Figures 4.6 and 4.7 agree with the results given in Ref. [15].

In Figure 4.16, H is the beam height and L is the beam length; m_3 and m_1 are the frequencies of the models with shear deformation and without rotary inertia respectively. Curve A is the first mode, curve B is the second mode, and curve C is the sixth mode.

In Figure 4.17, different modal frequencies calculated from Euler–Bernoulli with and without rotary inertia and Timoshenko models respectively are illustrated in terms of $(4\omega L/(n+1)\pi)\sqrt{\rho/EI}$ vs. $(n+1)/(2L)$. This indicates clearly that the effect of rotary inertia and shear deformation is profound for high-order vibration modes. In Figure 4.17, ω is the natural frequency, $c = L\sqrt{\rho/EI}$, and n is the order of the vibration mode.

Curve A is the Euler–Bernoulli model without rotary inertia, curve B is the Euler–Bernoulli model with rotary inertia, and curve C is the Timoshenko model.

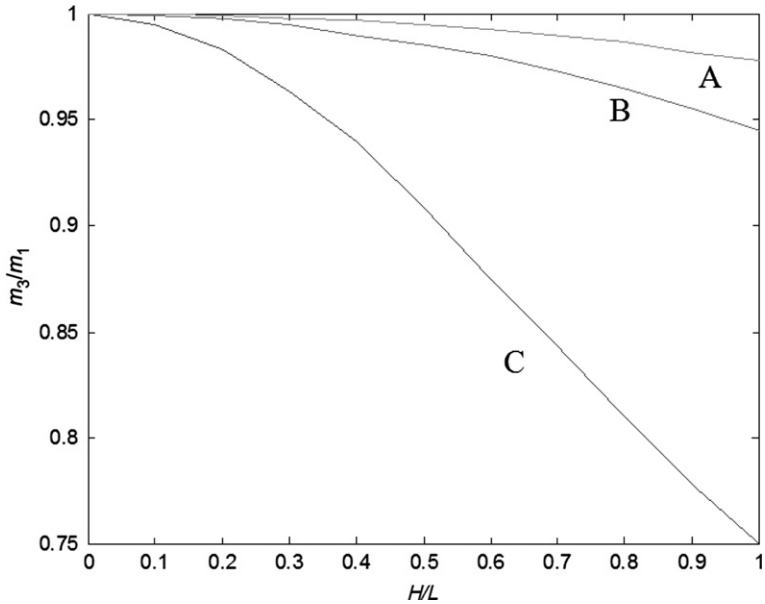

Figure 4.16: Influence of Shear Deformation.

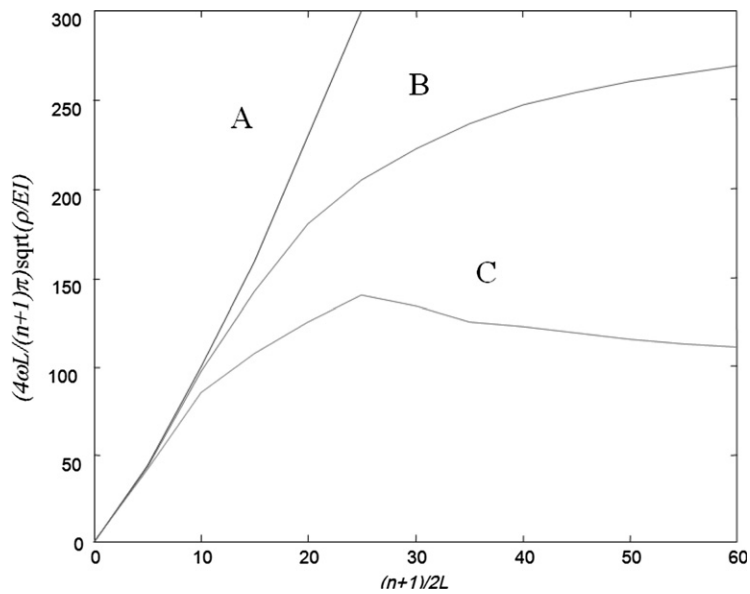

Figure 4.17: Influence of Rotary Inertia and Shear Deformation.

The normalized modal shape functions of natural vibration can be found as

$$\phi(\xi;m) = \phi_s(\xi) - \frac{\phi_{11}(m)}{\phi_{12}(m)}\phi_h(\xi), \quad z(\xi;m) = \phi'(\xi;m)$$

$$\alpha(\xi;m) = \phi''(\xi;m) + \frac{m^2}{\sigma}\phi(\xi;m)$$

$$z_{\sigma i}(\xi) = \frac{z(\xi;m)}{\langle z(\xi;m_i), \alpha(\xi;m_i)|z(\xi;m_i), \alpha(\xi;m_i)\rangle_\sigma}$$

$$\alpha_i(\xi) = \frac{\alpha(\xi;m)}{\langle z(\xi;m_i), \alpha(\xi;m_i)|z(\xi;m_i), \alpha(\xi;m_i)\rangle_\sigma}$$

$$i = 0,\ 1,\ 2,\ \ldots$$

where $\langle *|*\rangle_\delta$ is the generalized inner product for the Timoshenko model:

$$\langle f|z\rangle_\sigma \equiv \int_0^1 (fz + \delta g\alpha)\mathrm{d}\xi + \eta g(0)\alpha(0) + \mu f(1)z(1) + \mu\zeta[g(1)z(1) + f(1)\alpha(1)] + \kappa g(1)\alpha(1) = 0$$

Similar to the Euler–Bernoulli model, the following orthogonal relationship is true:

$$\langle z_{\sigma i}, \alpha_i | z_{\sigma j}, \alpha_j\rangle_\sigma = \delta_{ij}, \quad \int_0^1 \alpha_i'\alpha_j' + \sigma(\alpha - z_i')(\alpha - z_j')\mathrm{d}\xi = m^2\delta_{ij} \tag{4.98}$$

Note that $\langle f|z\rangle_\sigma = \langle f, f'|z, z'\rangle_\sigma$. When $m^2 > \sigma/\delta$, β_2 becomes an imaginary number. In this case:

$$\beta_i = \left[\frac{\delta_s - (-1)^i\sqrt{\delta_d^2 + 4m^{-2}}}{2}\right]^{\frac{1}{2}}, \quad k_i = \frac{m[1 - \sigma\beta_i^2]}{\sigma\beta_1\beta_2(\beta_1^2 + \beta_2^2)}, \quad i = 1,\ 2$$

and cosh and sinh functions in ϕ_s and ϕ_h are replaced by cos and sin functions respectively. Therefore, for large natural vibration frequencies, the computational problem associated with the exponential functions is not an issue here.

4.2.7 Step Responses and General Solutions

In this section, we present analytic expressions of step and general responses for flexible manipulators. The results in Section 4.2.5 are used extensively here. The detailed derivation of these responses is quite tedious and only the final results are given in this section.

For step input $\tau =$ constant, one can find step responses of the systems (3.63)−(3.65) and (3.66)−(3.68) as

$$z(\xi,t) = z_{\delta p}(\xi,t) + \tau \sum_{i=0}^{\infty} \left[c_{i1}^{\delta} \cos\, \omega_i(t-t_0) + c_{i2}^{\delta} \sin\, \omega_i(t-t_0)\right] z_i(\xi) \tag{4.99}$$

$$z_{\sigma}(\xi,t) = z_{\sigma p}(\xi,t) + \tau \sum_{i=0}^{\infty} \left[c_{i1}^{\sigma} \cos\, \omega_i(t-t_0) + c_{i2}^{\sigma} \sin\, \omega_i(t-t_0)\right] z_{\sigma i}(\xi) \tag{4.100}$$

$$\alpha(\xi,t) = \alpha_{\sigma p}(\xi,t) + \tau \sum_{i=0}^{\infty} \left[c_{i1}^{\sigma} \cos\, \omega_i(t-t_0) + c_{i2}^{\sigma} \sin\, \omega_i(t-t_0)\right] \alpha_i(\xi) \tag{4.101}$$

where z and (z_{σ},α) are for the Euler−Bernoulli (Timoshenko) and $z_{\delta p}$, $z_{\sigma p}$, and $\alpha_{\sigma p}$ are the corresponding particular solutions of these models:

$$(z_{\delta p}, z_{\sigma p}) = a\tau \left[\frac{\xi(t-t_0)^2}{2} - c^2(A_{\delta}, A_{\sigma})\right]; \quad \alpha_{\alpha p} = a\tau \left[\frac{(t-t_0)^2}{2} - c^2 A_{\alpha}\right]$$

where

$$A_{\delta}(\xi) = \frac{\xi^5}{5!} - c_3\frac{\xi^3}{3!} + c_2\frac{\xi^2}{2!}$$

$$A_{\sigma}(\xi) = \frac{\xi^5}{5!} - \left(c_3 + \frac{1}{\sigma}\right)\frac{\xi^3}{3!} + c_2\frac{\xi^2}{2!} + \frac{c_1}{\sigma}\xi$$

$$A_{\alpha}(\xi) = \frac{\xi^4}{4!} - c_3\frac{\xi^2}{2!} + c_2\xi$$

and

$$c_1 = \frac{1}{2} + (1+\zeta)\mu, \quad c_2 = \frac{1}{3} + \delta + \kappa + 2\zeta\mu + \mu, \quad c_3 = c_1 + \delta, \quad a = \frac{1}{\rho L^3(\eta + c_2)}$$

To determine the coefficients in Eqs (4.92)−(4.94), we consider the initial conditions:

$$z(\xi,t_0) = H_{\delta 0}(\xi), \quad \dot{z}(\xi,t_0) = \dot{H}_{\delta 0}(\xi)$$

$$z_{\sigma}(\xi,t_0) = H_{\sigma 0}(\xi), \quad \dot{z}_{\sigma}(\xi,t_0) = \dot{H}_{\sigma 0}(\xi)$$

$$\alpha(\xi,t_0) = A_{\sigma 0}(\xi), \quad \dot{\alpha}(\xi,t_0) = \dot{A}_{\sigma 0}(\xi)$$

Using the orthogonal relationships Eqs (4.84) and (4.87b) we find:

$$c_{i1}^{\delta} = ac^2\beta^{\delta} + \langle H_{\delta 0}|z_i\rangle_{\delta}, \quad c_{i2}^{\delta} = \frac{c}{m_i}\langle \dot{H}_{\delta 0}|z_i\rangle_{\delta}$$

$$c_{i1}^{\sigma} = ac^2\beta_i^{\sigma} + \langle H_{\sigma 0}, A_{\sigma 0}|z_{\sigma i}, \alpha_i\rangle_{\sigma}, \quad c_{i2}^{\sigma} = \frac{c}{m_i}\langle \dot{H}_{\sigma 0}, \dot{A}_{\sigma 0}|z_{\sigma i}, \alpha_i\rangle_{\sigma}$$

where

$$\beta_i^{\delta} = \langle A_{\delta}|z_i\rangle_{\delta}, \quad \beta_i^{\sigma} = \langle A_{\sigma}, A_{\alpha}|z_{\sigma i}, \alpha_i\rangle_{\sigma}$$

For zero initial conditions, the step responses become

$$z(\xi, t) = z_{\delta p}(\xi, t) + \tau \sum_{i=0}^{\infty} \beta_i^{\delta} \cos\, \omega_i(t - t_0) z_i(\xi)$$

$$z_{\sigma}(\xi, t) = z_{\sigma p}(\xi, t) + \tau \sum_{i=0}^{\infty} \beta_i^{\sigma} \cos\, \omega_i(t - t_0) z_{\sigma i}(\xi)$$

$$\alpha(\xi, t) = \alpha_{\sigma p}(\xi, t) + \tau \sum_{i=0}^{\infty} \beta_i^{\sigma} \cos\, \omega_i(t - t_0) \alpha_i(\xi)$$

Therefore, after taking derivatives with respect to time, we find the impulse responses of flexible manipulators as

$$z_h(\xi, t) = a\xi(t - t_0) - \sum_{i=0}^{\infty} \beta_i^{\delta} \omega_i \sin\, \omega_i(t - t_0) z_i(\xi) \tag{4.102}$$

$$z_{h\sigma}(\xi, t) = a\xi(t - t_0) - \sum_{i=0}^{\infty} \beta_i^{\sigma} \omega_i \sin\, \omega_i(t - t_0) z_{\sigma i}(\xi) \tag{4.103}$$

$$\alpha_h(\xi, t) = a(t - t_0) - \sum_{i=0}^{\infty} \beta_i^{\sigma} \omega_i \sin\, \omega_i(t - t_0) \alpha_i(\xi) \tag{4.104}$$

Using Duham's Theorem [9], we can find the response of a flexible manipulator in a general input $\tau = \tau(t)$. For the Euler−Bernoulli model, the response is

$$z(\xi, t) = \int z_h(\xi, t)\tau(t - s)\mathrm{d}s \tag{4.105}$$

and for the Timoshenko model:

$$z_{\sigma}(\xi, t) = \int_{t_0}^{t} z_{\sigma h}(\xi, t)\tau(t - s)\mathrm{d}s, \quad \alpha(\xi, t) = \int_{t_0}^{t} \alpha_h(\xi, t)\tau(t - s)\mathrm{d}s \tag{4.106}$$

The corresponding transfer functions can be determined easily as

$$H_{z\tau}^{\delta}(\xi,s)=\frac{\Gamma(z(\xi,t))}{\Gamma(\tau(t))}=\frac{a\xi}{s^2}-\sum_{i=1}^{\infty}\frac{\beta_i^{\delta}\omega_i}{s^2+\omega_i^2}z_i(\xi) \tag{4.107}$$

$$H_{z\tau}^{\sigma}(\xi,s)=\frac{\Gamma(z_{\sigma}(\xi,t))}{\Gamma(\tau(t))}=\frac{a\xi}{s^2}-\sum_{i=1}^{\infty}\frac{\beta_i^{\sigma}\omega_i}{s^2+\omega_i^2}z_{\sigma i}(\xi) \tag{4.108}$$

$$H_{\alpha\tau}(\xi,s)=\frac{\Gamma(\alpha(\xi,t))}{\Gamma(\tau(t))}=\frac{a\xi}{s^2}-\sum_{i=1}^{\infty}\frac{\beta_i^{\sigma}\omega_i}{s^2+\omega_i^2}\alpha_i(\xi) \tag{4.109}$$

These results are very useful in control design for flexible manipulators.

4.3 Passivity, Control, and Stability Analysis

Based on the discretization of a nonlinear dynamic model of one-link flexible manipulators, a Lyapunov energy function method is proposed for the stability analysis in this section [10].

4.3.1 Nonlinear Dynamic Equations of Motion

The flexible manipulator to be considered is a beam of length L fixed on a hub with rotational inertia I_H in the horizontal plane as shown in Figure 4.1. Let (x^0,y^0) be the inertial coordinate system and (x,y) be the coordinate system that rotates with the hub. The motion of the manipulator is described by the angular rotation ϕ due to the hub rotation, and the horizontal displacement u and the vertical displacement w of the beam with respect to (x,y) coordinates. Let θ be the angle between the tangent of the deflected axis and x-axis.

Using a variational approach, the nonlinear dynamic model [10] for one-link flexible manipulators undergoing large deformation has been developed by applying Hamilton's principle. The governing integro-partial difference equations are given by

$$EI\frac{\partial^2\theta}{\partial x^2}=\int_x^L\rho\{[\dot{\phi}\Delta_y(\xi)-\dot{\Delta}_x(\xi)]\sin\theta(x)+[\dot{\phi}\Delta_x(\xi)+\dot{\Delta}_y(\xi)]\cos\theta(x)\}\mathrm{d}\xi \tag{4.110}$$

$$\tau=I_H\ddot{\phi}+\frac{\mathrm{d}}{\mathrm{d}t}\int_0^L\rho[(u+\xi)\Delta_y(\xi)-w\Delta_x(\xi)]\mathrm{d}\xi \tag{4.111}$$

with the boundary conditions

$$\theta(0,t)=0;\quad \theta'(L,t)=0\qquad x=L \tag{4.112}$$

4.3.2 Discretization of Nonlinear Model

Equations (4.110)–(4.112) are integro-differential equations that are difficult to work with directly. We adopt the approach of linearizing the equation of motion and obtain the natural modes first, and then use the natural modes as a basis of expansion for the general solution of the nonlinear equation. The eigenfunction expansion (4.113) can be used to discretize the nonlinear dynamic equation given in Eqs (4.110)–(4.112):

$$v(x,t) = \sum_{n=0}^{\infty} q_n(t)\psi_n(x) \tag{4.113}$$

where $q_n(t)$ is called the modal amplitude function and $\psi_n(x)$ is called the mode shape q_1. To keep the equations tractable, we assume small bending, i.e. w is small. Specifically, w and w' are assumed to be of the same order, say $O(\varepsilon)$, where ε is small. All velocities are assumed to be of order 1. Terms with up to quadratic power of ε are kept in the expansion, so the equation of motion is valid up to the linear term in ε. This approach is the same as that in Ref. [16], except we do not assume a small velocity. This results in nonzero centrifugal and Coriolis forces, which were missing in the equation in Ref. [16]. The importance of these terms is in the preservation of the conservative property of the open-loop system after the approximation. We shall see that this has important consequences in stability analysis. With the stated approximation, the kinetic energy becomes

$$T = \frac{1}{2}\rho \int_0^L \dot{v}^2 \, \mathrm{d}x + \frac{1}{2} I_H \dot{\phi}^2 + \frac{1}{2}\rho \int_0^L \left[\dot{u}^2 + w^2\dot{\phi}^2 - 2w\,\dot{u}\dot{\phi} + 2u\dot{\phi}\dot{v}\right] \tag{4.114}$$

where u and $\dot{u}$ are approximated by

$$u(x,t) = -\frac{1}{2}\int_0^x w'(\xi,t)^2 \mathrm{d}\xi \tag{4.115}$$

$$\dot{u}(x,t) = -\int_0^x w'(\xi,t)\dot{w}'(\xi,t)\mathrm{d}\xi \tag{4.116}$$

The kinetic energy can be expanded along the natural modes of the linearized system. Then:

$$T = \frac{1}{2}\dot{q}^T M(q) q$$

where the mass matrix is

$$
\begin{aligned}
M(q) = aI &+ \int_0^L A(x)qq^T A(x)dx + q^T A_1 q \Psi'(0)\Psi'^T(0) \\
&+ 2q^T \left[\int_0^L (\Psi(x) - x\Psi'(0))A(x)\mathrm{d}x \right] q\Psi'^T(0) - \Psi'(0)\, q^T \int_0^L A(x)q\Psi^T(x)\mathrm{d}x
\end{aligned}
\tag{4.117}
$$

q, $\Psi(x)$, and $\Psi'(0)$ are infinite dimensional vectors for modal amplitudes, eigenfunctions evaluated at x, and the spatial derivative of the eigenfunction evaluated at 0 respectively, and

$$
A(x) = \int_0^x (\Psi'(\xi) - \Psi'(0))(\Psi'(\xi) - \Psi'(0))^T \mathrm{d}\xi
$$

$$
A_1 = \int_0^L (\Psi(x) - x\Psi'(0))(\Psi(x) - x\Psi'(0))^T \mathrm{d}x
$$

The modal coordinate q is a generalized coordinate and the discretized kinetic energy can be used to find the Coriolis and centrifugal accelerations from

$$
C(q,\dot{q})\dot{q} = \frac{\mathrm{d}}{\mathrm{d}t}\left(\frac{\partial T}{\partial \dot{q}}\right) - \frac{\partial T}{\partial q}
$$

After some algebra, the following expression is obtained:

$$
\begin{aligned}
C(q,\dot{q})\dot{q} = \Bigg\{ \Bigg[&\int_0^L \left(\frac{L^2}{2} - \frac{x^2}{2}\right)(\Psi'(x) - \Psi'(0))(\Psi'(x) - \Psi'(0))^T \mathrm{d}x \\
&- \int_0^L (\Psi(x) - x\Psi'(0))(\Psi(x) - x\Psi'(0))^T \mathrm{d}x \Bigg] q\dot{q}^T \Psi'(0)\Psi'^T(0) \\
&+ 2\Psi'(0)q^T \int_0^L (\Psi(x) - x\Psi'(0))(\Psi(x) - x\Psi'(0))^T \mathrm{d}x \Psi'^T(0)\dot{q} \\
&- 2\dot{q}^T \Psi'(0) \int_0^L \left(\frac{L^2}{2} - \frac{x^2}{2}\right)(\Psi'(x) - \Psi'(0))(\Psi'(x) - \Psi'(0))^T \mathrm{d}x \; q\Psi'^T(0) \\
&+ 2(\dot{q}^T \otimes I)\Bigg[\int_0^L \left(\left(\int_x^L \Psi(\xi)\mathrm{d}\xi \right) \otimes (\Psi'(x) - \Psi'(0))(\Psi'(x) - \Psi'(0)) \right)^T \mathrm{d}x \Bigg] q\Psi'^T(0) \\
&- 2(\dot{q}^T \otimes I) \int_0^L ((\Psi'(x) - \Psi'(0)) \otimes \left(\int_x^L \Psi(\xi)\mathrm{d}\xi) \right)(\Psi'(x) - \Psi'(0))^T \mathrm{d}x \; q\Psi'(0)^T \Bigg\} \dot{q}
\end{aligned}
\tag{4.118}
$$

The discretized nonlinear dynamic equation accurate up to quadratic terms in w and w' can now be stated:

$$M(q)\ddot{q} + C(q,\dot{q})\dot{q} + a\,\Omega^2 q = \rho^{-1}\Psi'(0)\tau = B\tau \tag{4.119}$$

This can be shown to correspond to the discretization of the following partial differential equation:

$$\begin{aligned}&\ddot{w} + x\ddot{\phi} + \frac{EI}{\rho}\frac{\partial^4 w}{\partial x^4} + w\dot{\phi}^2 + \dot{\phi}^2\frac{\mathrm{d}}{\mathrm{d}x}\left[\left(\frac{L^2}{2} - \frac{x^2}{2}\right)w'\right]\\ &+ 2\,\dot{\phi}\left\{\frac{d}{dx}\left[w'\int_x^L \dot{w}d\xi\right] - \int_0^x \dot{w}'\dot{w}'\mathrm{d}\xi\right\} + \left\{\frac{\mathrm{d}}{\mathrm{d}x}\left[w'\int_x^L\int_0^\xi \dot{w}'2\mathrm{d}\eta\,\mathrm{d}\xi\right] - \int_0^x \dot{w}'2\mathrm{d}\xi\,w'\right\}\end{aligned} \tag{4.120}$$

The boundary conditions and the dynamic equation for ϕ are the same as before:

$$\tau - I_H\ddot{\phi} + EI\,w''(0,t) = 0 \tag{4.121}$$

$$w(0,t) = 0, \quad w'(0,t) = 0, \quad w''(L,t) = 0, \quad w'''(L,t) = 0 \tag{4.122}$$

This model generalizes the one in Ref. [17] in which only the nonlinear term

$$\dot{\phi}^2\frac{\mathrm{d}}{\mathrm{d}x}\left[\left(\frac{L^2}{2} - \frac{x^2}{2}\right)w'\right]$$

was included. This model also generalizes the one in Ref. [18], in which some, but not all, of the nonlinear terms are included, which implies that the conservative nature of the open-loop system is not preserved in the approximation.

4.3.3 Stability Analysis

The centrifugal and Coriolis term $C(q,\dot{q})\dot{q}$ is related to the nonlinear mass matrix in an important way. Defining M_D from the following relationship:

$$\dot{M}(q,\dot{q})z = M_D(q,z)\dot{q}$$

then it is easy to show (as in Ref. [19]) that one choice of C (it is not unique) is

$$C(q,\dot{q}) = M_D(q,\dot{q}) - \frac{1}{2}M_D^T(q,\dot{q}) \tag{4.123}$$

This relationship has been exploited extensively in the rigid robotics literature for stability analysis and control design; for an example see Refs [13,19]. In fact, we can now show that

joint angle proportional-derivative (PD) control is a stabilizing control law. Consider the following Lyapunov function candidate:

$$V(q,\dot{q}) = \frac{1}{2}\dot{q}^T M(q)\dot{q} + a\frac{1}{2}q^T\Omega^2 q + \frac{1}{2}q^T B K_p B^T q \tag{4.124}$$

The derivative of V along the solution is

$$\begin{aligned}\dot{V}(q,\dot{q}) &= \dot{q}^T\left(-a\,\Omega^2 q + B\tau - C(q,\dot{q})\dot{q} + \frac{1}{2}\dot{M}(q,\dot{q}) + a\Omega^2 q\right)\\ &= \dot{q}^T B\tau\end{aligned}$$

where Ω is a diagonal matrix with nth diagonal entry ω_n, and B is a column with nth element $\psi_n'(0)/\rho$. Note that the contribution due to $C(q,\dot{q})$ drops out due to the structure given in (4.123). The above Lyapunov energy analysis confirms the fact that the map from τ to $B^T\dot{q}$ (i.e. the joint angular velocity) is passive, which is also the well-known sensor/actuator collocation condition. Note that if nonlinear terms are only retained in M but not in C, as in Ref. [16] (i.e. setting it to zero, by assuming small $\dot{q}$), there would be an $\dot{M}$ term in $\dot{V}$. Thus, the passivity property would be destroyed. If τ is chosen as a simple joint angle PD control law:

$$\tau = -K_p B^T(q - q_{des}) - K_v B^T\dot{q} \tag{4.125}$$

where q_{des} is chosen to satisfy

$$\begin{aligned}B^T q_{des} &= \phi_{des}\\ \Omega q_{des} &= 0\end{aligned}$$

simultaneously. It is possible to choose such q_{des} since $\begin{bmatrix} B^T \\ \Omega \end{bmatrix}$ is ??? (note that the first component of B is $\rho^{-1}(L^3/3 + I_H/\rho)$, which is nonzero).

With the joint angle PD control, the closed-loop system is stable due to the fact that $\dot{V} = -K_v(B^T\dot{q})^2 \leq 0$. Since $\dot{V} \leq 0$ implies all trajectories are uniformly bound in t, by Ref. [20], the joint angular velocity $B^T\dot{q}(t)$ tends to zero as $t \to \infty$. From the governing equation (4.119), all higher derivatives q are uniformly bounded. Using Proposition 1 in Ref. [21], it follows that $B^T[\mathrm{d}^k q(t)/\mathrm{d}t^k]$ converges to zero in norm for k ≥ 0.

At this point, we revert to a local analysis for the linearized system, i.e. consider a neighborhood of the zero equilibrium where $\dot{q}$ is sufficiently small, in which asymptotic convergence for first-order vertical form of the linearized partial differential equations:

$$\begin{bmatrix}\dot{q}\\ \ddot{q}\end{bmatrix} = \begin{bmatrix}0 & I\\ -\Omega^2 & 0\end{bmatrix}\begin{bmatrix}q\\ \dot{q}\end{bmatrix} + \begin{bmatrix}0\\ a^{-1}B\end{bmatrix}\tau \tag{4.126}$$

implies asymptotic convergence for the nonlinear system described by (4.119). If only a finite number of modes is undamped, and the damping operator D is bounded relative to Ω^2, the closed-loop infinitesimal generator

$$A' = \begin{bmatrix} 0 & I \\ -(\Omega^2 + BK_pB^T) & -(D + BK_vB^T) \end{bmatrix} \tag{4.127}$$

has compact resolvent [22], which implies that all bounded trajectories are precompact [23]. Hence the invariance principle can be applied to the closed-loop infinite-dimensional system, i.e.

$$Q \triangleq \{(q,\ \dot{q}) :\ B^T\dot{q} = 0\} \tag{4.128}$$

If $B^T\dot{q}$ is detectable, then the largest invariant set in Q is just the origin and the zero equilibrium is asymptotically stable. When does the detectability condition hold? Without loss of generality, assume the first N modes are undamped. Therefore, to check detectability, we only need to check the observability of the first N modes. By forming the observability matrix, it follows that if the $N \times N$ matrix is

$$O \triangleq \begin{bmatrix} B^T \\ B^TK^2 \\ \vdots \\ B^TK^{2(N-1)} \end{bmatrix}$$

where $K \triangleq \Omega^2 + BK_pB^T$ is invertible, then the observability condition holds and the flexible beam, with N unstable modes, is in a stabilizable condition from joint torque.

The above discussion can also be viewed from a general passivity perspective (this line of reasoning was originally proposed for flexible joint control [24]). This discussion is best understood through a number of steps:

First, consider just the joint angular position feedback $\tau = \tau_1 - K_pB^T\Delta q$. Then the map from τ_1 to $B^T\dot{q}$ is passive by following the above Lyapunov argument.

Let C be any strict passive map that takes $B^T\dot{q}$ to τ_1:

$$\tau_1 = \tau_2 - C(B^T\dot{q})$$

The constant gain K_v feedback is a special case.

By the passivity theorem [25], the map that takes τ_2 to $B^T\dot{q}$ is L_2- input/output stable.

If the closed-loop system is detectable with respect to $B^T\dot{q}$ and stabilizable with respect to τ_2, then the system is internally asymptotically stable.

If the feedback C is restricted to be linear, then it must be strictly positive real [15,26]. An open and very interesting problem is choosing a strictly positive real C so that some performance measure (e.g. H_∞ norm of some input/output pair for the linearized system) is optimized. Another implication of the above discussion is that any feedback controller from $B^T\dot{q}$ to τ_1, which is self-stable, can be "robustified" by adding in a suitable amount of constant-gain feedback. A sample data system can be included in this discussion by including the sampler and zero-order hold in the consideration of passivity for the feedback system.

References

[1] R.M. Davies, A critical study of the Hopkins pressure bar. Philosophical Transactions of Royal Society, Series A 240 (1948) 454–461.

[2] S. Timoshenko, D.H. Young, W. Weaver Jr., Vibration Problems in Engineering, third ed., D. Van Nostrand, New York, 1957.

[3] F.Y. Wang, F.B. He, Free vibration of transversely isotropic plates, Journal of Vibration and Shock 5 (1) (1986) 1–11.

[4] F.Y. Wang, Y. Zhou, On the vibration modes of three-dimensional micropolar elastic plates, Journal of Sound and Vibration 146 (1) (1991) 1–16.

[5] D. Hughes, J.T. Wen, J. Beseler, J. Chow, Modeling, identification and control of flexible structures. Computer Integrated Manufacturing, Proceedings of Rensselaer's Second International Conference (1990) 412–417.

[6] M. Boutaghou, A.G. Erdman, A unified approach for the dynamics of beams undergoing arbitrary spatial motion, Journal of Vibration and Acoustics—Transactions of the ASME 113 (4) (1991) 494–507.

[7] T.R. Kane, R.R. Ryan, A.K. Bamerjee, Dynamics of a cantilever beam attached to a moving bar, Journal of Guidance and Control 10 (1989) 139–151.

[8] J.C. Simo, L. Vu-Quoc, On the dynamics of flexible beams under large overall motions, Parts I and II, Journal of Applied Mechanics 53 (1986) 849–863.

[9] A. Pars, A Treatise on Analytical Dynamics, OX BOX Press, Woodbridge, CT, 1979.

[10] F.Y. Wang, J.T. Wen, Nonlinear dynamical model and control for a flexible beam, CIRSSE Report No. 75. RPI, Tory, NY, 1990.

[11] F.Y. Wang, Exact dynamic solutions of one-link flexible manipulators with different dynamic models. SIE Working Paper, Department of Systems and Industrial Engineering, University of Arizona, Tucson, 1991.

[12] S. Timoshenko, G.H. MacCullough, Elements of Strength of Materials, third ed., D. Van Nostrand, New York, 1949.

[13] M. Takegaki, S. Arimoto, A new feedback method for dynamic control of manipulators, ASME Journal of Dynamic System, Measurement and Control 102 (June) (1981) 119–125.

[14] F. Bellezze, L. Lanari, G. Ulivi, Exact modeling of the flexible slewing link, IEEE 1990 International Conference on Robotics and Automation 2 (1990) 734–739.

[15] P. Ioannou, G. Tao, Frequency domain conditions for strictly positive real functions, IEEE Transactions on Automatic Control 32 (10) (1987) 53–54.

[16] C.E. Padilla, A.H. von Flotow, Nonlinear strain–displacement relations in the dynamics of a two-link flexible manipulator. SSL Report 6–89, Massachusetts Institute of Technology, 1989. May.

[17] L. Meirovith, Analytic Methods in Vibration, MacMillan, 1967.

[18] T.J. Tarn, X. Ding, A.K. Bejczy, Feedback linearization of a one-link flexible robot arm modeled by partial differential-integral equations, in: J. Descusse, M. Fliess, A. Isidori, D. Leborgne (Eds.), New Trends in Nonlinear Control Theory, Springer-Verlag, Berlin, 1989, pp. 474–481.

[19] J.T. Wen, D.S. Bayard, A new class of control laws for robotic manipulators, Part I: Non-adaptive case, International Journal of Control 47 (5) (1988) 1361–1385.

[20] J. Hale, Ordinary Differential Equations, Robert E. Krieger, 1980.
[21] J.S.C. Yuan, W.M. Wohnam, Probing signals for model reference identification, IEEE Transactions on Automatic Control 22 (4) (1977) 530–538.
[22] J.S. Gibson, D.L. Mingori, Modeling and control of flexible structures, JPL Pubilication, 1988. 88–40, Jet Propulsion Laboratory, December.
[23] J. Walker, Dynamic Systems and Evolution Equations: Theory and Applications, Plenum Press, New York, 1980.
[24] J.T. Wen, L. Lanari, A family of asymptotic stable control laws for flexibly robots based on a passivity approach. CIRSSE Report 76, Rensselaer Polytechnic Institute, 1990. December.
[25] C.A. Desoer, M. Vidyasagar, Feedback Systems: Input–Output Properties, Academic Press, New York, 1975.
[26] J.T. Wen, Stability of a class of interconnected evolution systems, IEEE Transactions on Automatic Control 37 (3) (1992) 342–347.

CHAPTER 5

Optimization of Flexible Manipulators

Chapter Outline

5.1 Optimum Design of Flexible Beams with a New Iteration Approach 100

5.1.1 Introduction 101

5.1.2 Basic Equations 102

5.1.3 Analysis of Singularity at the Free End 104

Case where $q \neq 0$ *105*

Case where $q = 0$ *105*

5.1.4 Solution by Successive Iterations: New Formulation 106

Case where $p = 1$ *106*

Case where $p > 1$ *and* $q = 0$ *108*

Case where $p > 1$ *and* $q \neq 0$ *109*

5.1.5 Numerical Examples 111

Case where $p = 1$ *111*

Cases where $p = 2$ *and* $p = 3$ *112*

5.2 Geometrically Constrained and Composite Material Designs 116

5.2.1 Minimum and Maximum Radius Constraints 116

5.2.2 Uniform and Variable Tunnel Cross-Section Designs 116

5.2.3 Composite Material Designs 119

5.3 Optimum Shape Design of Flexible Manipulators with Tip Loads 120

5.3.1 Problem Setup 120

5.3.2 Euler—Bernoulli Equations 122

Design Model 122

Vibration Equations 124

5.3.3 Analytical Solutions 125

Optimality Equations 125

Iterative Solution 128

Numerical Results and Discussion 131

5.3.4 Segmentized Optimization Approach 133

Segmentized Formulation 133

Segmentized Optimization Solutions 137

Numerical Results and Discussion 140

5.3.5 Multiple Tip Load and Multiple Link Optimum Designs 142

Minimax Optimum Design 142

Two-link Optimum Design 143

5.3.6 Sensitivity Analysis 146

5.4 Optimum Shape Construction with Total Weight Constraint 148

5.4.1 Basic Equations and the Variation Formulation 148

Flexible Manipulators. DOI: 10.1016/B978-0-12-397036-7.00005-2

Copyright © 2012 Elsevier Inc. All rights reserved.

5.4.2 Analytical Approach of Unconstrained Shape Design 151
Scheme: Case where p = *1 153*
Iteration Scheme: Case where p > *1 155*
5.4.3 Optimization Approach of Constrained Shape Design 156
Nonlinear Programming Method: Single Tip Load 157
Minimax Design Method: Multiple Tip Loads 158
5.4.4 Numerical Examples and Discussion 159
Unconstrained Design 159
Constrained Design 162
Minimax Design 164
5.4.5 Sensitivity Analysis of the Optimal Frequency 164
5.5 Minimum-Weight Design of Flexible Manipulators for a Specified Fundamental Frequency 166
5.5.1 Basic Equations 166
5.5.2 Problem Formulation 168
5.5.3 Solution by Iterations 169
Case where p = *1 170*
Case where p > *1 171*
5.5.4 Numerical Examples 172
5.6 Optimum Design of Flexible Manipulators: The Segmentized Solution 172
5.6.1 Basic Equations 174
5.6.2 Segmentized Solutions 175
5.6.3 Optimization Formulations for Linear Mass and Bending Rigidity Distributions 178
Maximum Speed Design Problem 179
Minimum Mass Design Problem 179
Design Formulations for Multiple Loads 180
5.6.4 Practical Issues in Link Construction 181
Strain/Stress and Deflection Constraints 181
Link Construction Constraints 182
References 182

5.1 Optimum Design of Flexible Beams with a New Iteration Approach

Optimum design of vibrating cantilevers is a classical problem widely discussed in the literature and textbooks in structural optimization. The problem, originally formulated and solved by Karihaloo and Niordson [1], is to find the optimal beam shape that will maximize the fundamental vibration frequency of a cantilever. Upon reexamination of the problem, it has been found that the original analysis and solution procedure can be simplified and substantially improved. Specifically, the time-consuming inner loop devised for solving the Lagrange multiplier in the original work has been proven to be totally unnecessary and thus should not be considered in the solution to the problem. This conclusion has led to a new set of simplified equations for the construction of iteration schemes. In this section new asymptotic expressions for the optimum design solution have been obtained and verified by numerical results.

5.1.1 Introduction

Since the pioneering works of Beesack [2], Schwarz [3,4], and especially Niordson [5], considerable progress has been made in the optimum design of vibrating elastic structures. Niordson [5] first showed that, for simply supported beams with geometrically similar cross-sections, an increase of 6.6% in the lowest frequency of vibration can be achieved through optimum shape design. Later, Karihaloo and Niordson [6] studied the optimum design of vibrating cantilever beams and found considerably larger increases in the lowest frequency. For example, the lowest frequency of the optimum cantilever with geometrically similar cross-sections is 57.8% larger than that of the corresponding one with a uniform cross-section. Similar work and extensions have also been conducted by many other researchers [7–10]. Since then, the problem has become a classical one and has been discussed widely in the literature and textbooks on structural optimization.

Wang [11] investigated the problem of the optimum shape design of flexible manipulators. The objective is to increase the fundamental vibration frequency of a flexible manipulator so that a larger bandwidth can be obtained for the manipulator control system. The problem formulation is almost the same as that in Ref. [6]. However, different boundary conditions have made the optimization problem for flexible manipulators much more difficult than the corresponding problem for cantilever beams.

Initially, we attempted to follow the iteration schemes in Ref. [6] in order to solve the corresponding optimization problem for flexible manipulators. However, for all cases tried, the iterative schemes of Ref. [6] did not converge. It was also found that the implicit equation (so-called inner loop) for solving the Lagrange multiplier in those schemes took a significant amount of computation time. After careful reexamination of the original problem, we found that the time-consuming inner loop in the original iteration schemes was redundant and could be removed completely in the solution process. Eliminating this redundant equation from the iteration process leads to a new formulation for the iterations, and consequently to substantial simplification of the iteration equations and significant improvement in convergence rates. For example, three simplified iteration schemes are needed to solve the optimum design problem completely using this method, whereas five different sophisticated schemes were required in Ref. [6]. These results have provided useful information for solving the optimization problem for manipulators [11,12].

As in Ref. [6], we assume throughout this paper the following relationship between the moment of inertia I and the area A of a cross-section of the beam:

$$I = cA^p(x), \quad p \geq 1 \tag{5.1}$$

where c is a constant. Three cases ($p = 1, 2, 3$) are especially interesting to us, since they correspond to beams with rectangular cross-sections of given uniform height, geometrically

similar cross-sections, and rectangular cross-sections of given uniform width respectively. The treatment in this section, however, is valid for all cases with $p \geq 1$.

5.1.2 Basic Equations

Consider the small harmonic transverse vibrations of a tapered cantilever beam carrying a mass Q at its tip. If both the rotary inertia and shear deformations are neglected, the differential equation of motion and the boundary conditions can be written in the following dimensionless form:

$$(\alpha^p y'')'' - \lambda \alpha y = 0 \tag{5.2}$$

$$y(1) = y(1) = 0, \quad \alpha^p y''(0) = 0, \quad (\alpha^p y'')'(0) = \lambda\, q y(0) \tag{5.3}$$

Here, y is the amplitude of the lateral displacement in the plane of bending and the prime indicates differentiation with respect to the dimensionless coordinate $\xi = x/l$. The dimensionless area function is denoted as $\alpha = Al/V$, in which l is the length of the beam and V is the total volume of the beam. The dimensionless eigenvalue λ and mass parameter q in the boundary conditions are defined as

$$\lambda = \omega^2 \gamma\, l^{p+3}/cEV^{p-1}, \quad q = Q/\gamma V \tag{5.4}$$

where ω is the natural vibration frequency and γ the mass density of the beam. From the definition, α must be non-negative and satisfy the following constraint:

$$\int_0^1 \alpha(\xi) \mathrm{d}\xi = 1 \tag{5.5}$$

The problem of the optimum design of vibrating cantilevers is to find the optimal area function that will maximize the fundamental vibration frequency. Using the Rayleigh quotient and variational calculus, we find the equation for determining the optimum area function as

$$p\alpha^{p-1}(y'')^2 - \lambda y^2 = \lambda a^2 \tag{5.6}$$

where a^2 is the Lagrange multiplier introduced for the constraint (5.5).

Equations (5.2), (5.3), and (5.6) are fundamental for solving the optimum design problem. Note that in order to be consistent with the original work by Karihaloo and Niordson, all notation used in Ref. [6] has been kept here. Detailed derivation of these equations is given in Ref. [6].

The Rayleigh quotient can be obtained by multiplying both sides of Eq. (5.2) by y and integrating over the interval [0,1]. Integrating by parts and taking the boundary conditions (5.3) into account, we have

$$\lambda = \left[\int_0^1 \alpha^p y''^2 \mathrm{d}\xi\right] \Big/ \left[\int_0^1 \alpha y^2 \mathrm{d}\xi + q y^2(0)\right] \tag{5.7}$$

Furthermore, by substituting Eq. (5.6) into (5.7), we obtain the following implicit equation for the Lagrange multiplier:

$$a^2 = (p-1)\int_0^1 \left[\lambda(y^2 + a^2)/p(y'')^2\right]^{1/(p-1)} y^2 \mathrm{d}\xi + pqy^2(0) \tag{5.8}$$

Expressions (5.7) and (5.8) can be considered as the consequences of Eqs (5.2)–(5.3) and (5.5)–(5.6). That is, as long as y and α satisfy (5.2)–(5.3) and (5.5)–(5.6), both (5.7) and (5.8) will be satisfied automatically. Therefore, in order to solve the optimization problem, one only needs to work with Eqs (5.2)–(5.3) and (5.5)–(5.6). This observation will serve as the basis for the development of our new formulations of iteration schemes. Note that, except for the case $p = 2$, the Lagrange multiplier a^2 cannot be expressed explicitly in terms of y. For $p \neq 2$ the so-called inner loop has been used in Ref. [6] to find a^2 for a given y in their iteration schemes. The numerical simulation indicates that most of the computation time is spent on this inner-loop operation. Hence, by removing Eq. (5.8) completely from the solution process, the rate of convergence of the iteration schemes can be significantly improved.

To this end, we notice that for a given area function and eigenvalue, y and a^2 cannot be determined uniquely from Eqs (5.2)–(5.3) and (5.5)–(5.6). To see this, let (y,a^2,α,λ) be a solution of (5.2)–(5.3) and (5.5)–(5.6). Then, $(ny,n^2a^2,\alpha,\lambda)$ is obviously another solution for any nonzero constant n. This non-uniqueness offers us a way to remove the Lagrange multiplier completely from (5.6) by selecting $n = 1/a$. In other words, for the optimization problem, we only need to find the unknown function $u = y/a$, instead of y and a^2 separately. Another method for solving the non-uniqueness problem is to impose some normalization scheme on y. This method has been used widely in structural optimization [13,14]; however, it still requires the Lagrange multiplier to be found.

In terms of the new function u, Eqs (5.2), (5.3), and (5.6) can be rewritten as

$$(\alpha^p u'')'' - \lambda\alpha\, u = 0 \tag{5.9}$$

$$p\alpha^{p-1}(u'')^2 - \lambda u^2 = \lambda \tag{5.10}$$

$$u(1) = u'(1) = 0, \quad \alpha^p u''(0) = 0, \quad (\alpha^p u'')'(0) = \lambda q u(0) \tag{5.11}$$

It follows from these equations that

$$\int_0^1 \alpha(\xi)\mathrm{d}\xi = (p-1)\int_0^1 \left[\lambda(u^2+1)/p(u'')^2\right]^{1/(p+1)} u^2 \mathrm{d}\xi + pqu^2(0) \tag{5.12}$$

Note that this identity does not require the constraint (5.5) to hold.

From (5.10), for $p > 1$, we can find α in terms of u and λ:

$$\alpha(\xi) = \phi_u(\xi)/\beta, \quad \beta = (p/\lambda)^{1/(p-1)} \tag{5.13a}$$

$$\lambda = p/\beta^{p-1}, \quad \phi_u(\xi) = \left[\left(u^2(\xi) + 1\right)/u''^2(\xi)\right]^{1/(p-1)} \tag{5.13b}$$

When the constraint (5.5) is satisfied, we have

$$\beta = \int_0^1 \phi_u(\xi)\mathrm{d}\xi \tag{5.14}$$

The following integral formulas are useful in our discussion (see Section 5.2.4):

$$\int_0^\xi \int_0^x G(s)\mathrm{d}s\mathrm{d}x = \xi^2 \int_0^1 (1-x)G(x\xi)\mathrm{d}x \tag{5.15}$$

$$\int_\xi^1 \int_x^1 G(s)\mathrm{d}s\mathrm{d}x = (1-\xi)^2 \int_0^1 xG[\xi + x(1-\xi)]\mathrm{d}x \tag{5.16}$$

By formal integration of (5.9), after satisfying the boundary conditions at $\xi = 0$, substituting α from (5.13) into (5.9) and using (5.15), we find that

$$u''(\xi) = \frac{[u^2(\xi) + 1]^{p/(p+1)}}{\left\{p\xi\left[\beta q u(0) + \xi \int_0^1 (1-x)\phi_u(x\xi)u(x\xi)\mathrm{d}x\right]\right\}^{(p-1)/(p+1)}} \tag{5.17}$$

which will be used as the basic formula for the construction of new iteration schemes.

5.1.3 Analysis of Singularity at the Free End

When $p \neq 1$, the solutions of Eqs (5.9)–(5.11) are singular at the free end $\xi = 0$; therefore, the numerical method cannot be applied to finding the solution directly. To make numerical solution possible, we first have to determine the behavior of the solution near the free end. This can be done by assuming that the solutions can be expanded in a power series of ξ with a characteristic term ξ^k near the free end. A standard procedure was used by Karihaloo and Niordson [6] to derive the characteristic equations for determining the singularity k. Here, however, a direct and much simpler method is employed to find the singularity.

Case where $q \neq 0$

In this case, since u is finite at $\xi = 0$, we can see from Eqs (5.9)–(5.11) that at $\xi = 0$:

$$\alpha^p u'' = 0, \quad (\alpha^p u'')' = \text{finite}, \quad (\alpha^p u'')'' = \text{finite}, \quad \alpha^{p-1}(u'')^2 = \text{finite}$$

Therefore, in the neighborhood of $\xi = 0$:

$$\alpha^p u'' = a_1\xi + a_2\xi^2 + \ldots, \quad \alpha^{p-1}u''^2 = b_1 + \ldots$$

where a_1, a_2, and b_1 are constants. Solving the above equations for α and u'', we get

$$\alpha(\xi) = c_1\xi^{2/(p+1)} + \ldots \tag{5.18}$$

$$u''(\xi) = d_1\xi^{-(p-1)/(p+1)} + \ldots \tag{5.19}$$

where c_1 and d_1 are two new constants. Then the behavior of u near the free end can be found as

$$u(\xi) = d_1\xi^{(p+3)/(p+1)} + \ldots \tag{5.20}$$

Therefore, the singularity of u at $\xi = 0$ is

$$k = (p+3)/(p+1)$$

Case where $q = 0$

Expanding both u and α in a power series of ξ at $\xi = 0$:

$$u(\xi) = u_0\xi^k + \ldots \tag{5.21a}$$

$$\alpha(\xi) = a_0\xi^m + \ldots \tag{5.21b}$$

Substituting these expressions into Eq. (5.10) we get

$$2k = m(p-1) + 2(k-2), \quad \lambda = pa_0^{p-1}k^2(k-1)^2$$

Similarly, from Eq. (5.9) we get

$$\lambda a_0 = a_0^p k(k-1)(m+k+2)(m+k+1)$$

By eliminating λ and a_0 from these equations we find that

$$m = 4/(p-1) \tag{5.22}$$

$$[k(p-1) + 2(p+1)][k(p-1) + p + 3] - p(p-1)^2k(k-1) = 0 \tag{5.23}$$

For $p = 2$, we find $k = -2$, and for $p = 3$ we find $k = -1$. In both cases, the results are the same as those obtained in Ref. [6] using the standard procedure.

5.1.4 Solution by Successive Iterations: New Formulation

In this section, we present a new simplified formulation for solving Eqs (5.9)–(5.11) using successive iterations. We first discuss in detail the degenerate case in which $p = 1$ and then investigate the cases where $p > 1$, $q = 0$ and $p > 1$, $q \neq 0$ respectively.

Case where $p = 1$

For $p = 1$, function α drops out of Eq. (5.10) and we have a degenerate case. Equations (5.9)–(5.11) now have the form:

$$(\alpha u'')'' - \lambda \alpha u = 0 \tag{5.24}$$

$$(u'')^2 = \lambda(u^2 + 1) \tag{5.25}$$

$$u(1) = u'(1) = 0, \quad au''(0) = 0, \quad (au'')'(0) = \lambda q u(0) \tag{5.26}$$

and the identity (5.12) becomes

$$qu^2(0) = \int_0^1 \alpha(\xi)\mathrm{d}\xi$$

The above equation indicates that for $q = 0$, the solution to the optimum design problem of a vibrating cantilever beam does not exist, since the constraint (5.5) cannot be satisfied by any solution of (5.24)–(5.26). Actually, as pointed out in Ref. [6], the vibration frequency of a cantilever can be increased indefinitely in this case by selecting α appropriately. For $q \neq 0$, if we choose

$$q = 1/u^2(0) \tag{5.27}$$

then α obtained by solving Eq. (5.24) with boundary conditions (5.26) will satisfy the constraint (5.5) automatically. This observation leads to an inverse approach to solve the problem in this case. In other words, starting with a given λ, we determine u by solving (5.25) with the first two boundary conditions in (5.26) and then calculate the corresponding q using (5.27). This will establish a relationship between the mass parameter q and the optimum eigenvalue λ, which will enable us to find λ for a given q, and hence solve the optimization problem. Note that this process does not involve the computation of α. Once u and q have been found for a given λ, α can be obtained by solving (5.24) with the last two boundary conditions in (5.26). It is guaranteed that the resulting α will meet the constraint (5.5).

For very large q, an asymptotic relationship between q and λ can be obtained. Since λ is very small in this case, we can use $\varepsilon = \sqrt{\lambda}$ as a small parameter and solve (5.25) by the perturbation method [15], i.e. expand u in a power series of ε:

$$u(\xi) = u_0(\xi) + \varepsilon u_1(\xi) + \ldots$$

Substituting the above expression into (5.25), we get

$$u_0 = 0, \quad u_1 = (1/2)(1-\xi)^2, \ \ldots \tag{5.28}$$

Hence, from Eqs (5.24), (5.26), and (5.27), we have

$$\lambda q \cong 4, \quad \alpha(\xi) \cong 2\xi \tag{5.29}$$

when q is very large.

For a cantilever beam of uniform cross-section and the same length and volume as the optimum beam, $\alpha(\xi) = 1$ and the characteristic equation for the eigenvalue λ_c is (see Ref. [16])

$$1 + \cos\theta\cosh\theta + q\theta(\cos\theta\sinh\theta - \sin\theta\cosh\theta) = 0, \quad \theta = \lambda_c^{1/4} \tag{5.30}$$

From this, we find that for very large q:

$$\lambda_c q \cong 3 \tag{5.31}$$

Therefore, for a large tip mass, a relative increase of

$$\omega/\omega_c - 1 = \sqrt{\lambda/\lambda_c} - 1 = \sqrt{4/3} - 1 = 15.47\%$$

in the lowest natural frequency can be achieved with the optimum tapering of cantilever beams.

To develop a successive iteration scheme for general $q \neq 0$, we formally integrate (5.24) and (5.25) with boundary conditions (5.26). Application of formulas (5.15) and (5.16) leads to

$$u(\xi) = \sqrt{\lambda}(1-\xi)^2 \int_0^1 x\sqrt{u^2[\xi + x(1-\xi)] + 1}\ \mathrm{d}x \tag{5.32}$$

$$\alpha(\xi) = \sqrt{\lambda}\xi \frac{1/u(0) + \xi\int_0^1 (1-x)\alpha(x\xi)u(x\xi)\ \mathrm{d}x}{\sqrt{u^2(\xi)+1}} \tag{5.33}$$

Based on Eqs (5.32) and (5.33), the iteration scheme can now be outlined as follows.

- Step 1. For a given λ, select an initial $u_0(\xi)$. Update u_i until a specified accuracy is obtained:

$$u_{i+1}(\xi) = \sqrt{\lambda}(1-\xi)^2 \int_0^1 x\sqrt{u_i^2[\xi + x(1-\xi)] + 1}\ \mathrm{d}x$$

- Step 2. For u obtained in Step 1, calculate q according to Eq. (5.27).

- Step 3. Select an initial $\alpha_0(\xi)$ and update α_i until a specified accuracy is obtained:

$$\alpha_{i+1}(\xi) = \sqrt{\lambda}\xi \frac{1/u(0) + \xi \int_0^1 (1-x)\alpha_i(x\xi)u(x\xi)\mathrm{d}x}{\sqrt{u^2(\xi)+1}}$$

Clearly, compared with the corresponding scheme presented in Ref. [6], the new formulation in this case is simpler.

Case where $\mathrm{p} > 1$ *and* $\mathrm{q} = 0$

In order to avoid the singularity of u at $\xi = 0$, we introduce two new functions:

$$f(\xi) = \xi^k u(\xi), \quad z(\xi) = \xi^{k+2} u''(\xi) \tag{5.34}$$

where k is the singularity of u at $\xi = 0$ determined from Eq. (5.23). Both f and z are regular over the entire interval $0 \le \xi \le 1$. It is easy to show that

$$f(1) = f'(1) = 0, \quad f(0) = z(0)/k(k+1) \tag{5.35}$$

In terms of f and z, the function ϕ_u and parameter β can be rewritten as

$$\phi_u(\xi) = \xi^{4/(p-1)}\phi(\xi), \quad \beta = \int_0^1 \xi^{4/(p-1)}\phi(\xi)\mathrm{d}\xi \tag{5.36a}$$

$$\phi(\xi) = [(f^2(\xi) + \xi^{2k})/z^2(\xi)]^{1/(p-1)} \tag{5.36b}$$

From Eq. (5.34) and Eqs (5.15)–(5.17), we get

$$f(\xi) = \xi^k (1-\xi)^2 \int_0^1 \frac{xz[\xi + x(1-\xi)]}{[\xi + x(1-\xi)]^{k+2}}\mathrm{d}x, \quad 0 < \xi \le 1 \tag{5.37}$$

$$z(\xi) = \frac{\left[f^2(\xi) + \xi^{2k}\right]^{p/(p+1)}}{\left[p\int_0^1 (1-x)x^{4/(p-1)-k}\phi(x\xi)f(x\xi)\mathrm{d}x\right]^{(p-1)/(p+1)}} \tag{5.38}$$

Now, the scheme for successive iterations can be specified as follows:

- Step 1. Select an initial $z_0(\xi)$.
- Step 2. Update $f_i(\xi)$ according to

$$f_{i+1}(\xi) = \xi^k(1-\xi)^2 \int_0^1 \frac{xz_i[\xi + x(1-\xi)]}{[\xi + x(1-\xi)]^{k+2}} \mathrm{d}x, \quad 0 < \xi \le 1$$

$$f_{i+1}(0) = z_i(0)/k(k+1)$$

- Step 3. Update $\phi_i(\xi)$:

$$\phi_{i+1}(\xi) = \left[\left(f_{i+1}^2(\xi) + \xi^{2k}\right)/z_i^2(\xi)\right]^{1/(p-1)}$$

- Step 4. Update $z_i(\xi)$:

$$z_{i+1}(\xi) = \frac{\left[f_{i+1}^2(\xi) + \xi^{2k}\right]^{p/(p+1)}}{\left[p\int_0^1 (1-x)x^{4/(p-1)-k}\phi_{i+1}(x\xi)f_{i+1}(x\xi)\mathrm{d}x\right]^{(p-1)/(p+1)}}$$

- Step 5. If a given accuracy is not obtained, go back to Step 2.

Once f and z have been obtained within the specified accuracy, one can find the parameter β. Then the optimum eigenvalue λ, the function ϕ_u, and the optimum α can be determined according to Eqs (5.36), (5.14), and (5.13) respectively. Clearly, the proposed new procedure is much simpler than the one developed in Ref. [6].

Case where $\mathsf{p} > 1$ *and* $\mathsf{q} \neq 0$

In this case, we need only to consider the singularity of u'' at $\xi = 0$. To this end, we introduce the new function:

$$z(\xi) = \xi^{2-k}u''(\xi) \tag{5.39}$$

where $k = (p+3)/(p+1)$, according to the expression (5.20). The function z is regular over the entire interval $0 \le \xi \le 1$.

In terms of z, we can find that

$$u(\xi) = (1-\xi)^2 \int_0^1 \frac{xz[\xi + x(1-\xi)]}{[\xi + x(1-\xi)]^{2-k}} \mathrm{d}x, \quad 0 \le \xi \le 1 \tag{5.40}$$

For the purpose of numerical calculation, we need to specify $u(0)$ explicitly:

$$u(0) = \int_0^1 x^{2/(p+1)}z(x)\mathrm{d}x \tag{5.41}$$

Similarly, for ϕ_u and β, we have

$$\phi_u(\xi) = \xi^{2/(p+1)}\phi(\xi), \quad \beta = \int_0^1 \xi^{2/(p+1)}\phi(\xi)\,\mathrm{d}(\xi) \tag{5.42a}$$

$$\phi(\xi) = [(u^2(\xi)+1)/z^2(\xi)]^{1/(p-1)} \tag{5.42b}$$

From Eq. (5.17) we get

$$z(\xi) = \frac{\left[u^2(\xi)+1\right]^{p/(p+1)}}{\left\{p\left[\beta q u(0) + \xi^{(p+3)/(p+1)}\int_0^1 (1-x)x^{2/(p+1)}\phi(x\xi)u(x\xi)\mathrm{d}x\right]\right\}^{(p-1)/(p+1)}} \tag{5.43}$$

The iteration scheme here is similar to that of the previous case and is given below:

- Step 1. Select an initial $z_0(\xi)$.
- Step 2. Update $u_i(\xi)$ according to

$$u_{i+1}(\xi) = (1-\xi)^2 \int_0^1 \frac{x z_i[\xi + x(1-\xi)]}{[\xi + x(1-\xi)]^{2-k}}\mathrm{d}x, \quad 0 \le \xi \le 1$$

$$u_{i+1}(0) = \int_0^1 x^{2/(p+1)} z_i(x)\mathrm{d}x$$

- Step 3. Update $\phi_i(\xi)$:

$$\phi_{i+1}(\xi) = \left[\left(u_{i+1}^2(\xi)+1\right)/z_i^2(\xi)\right]^{1/(p-1)}$$

- Step 4. Update $z_i(\xi)$:

$$z_{i+1}(\xi) = \frac{\left[u_{i+1}^2(\xi)+1\right]^{p/(p+1)}}{\left\{p\left[\beta q u_{i+1}(0) + \xi^{(p+3)/(p+1)}\int_0^1 (1-x)x^{2/(p+1)}\phi_{i+1}(x\xi)u_{i+1}(x\xi)\mathrm{d}x\right]\right\}^{(p-1)/(p+1)}}$$

- Step 5. If a given accuracy is not obtained, go back to Step 2.

Again, the new iteration scheme in this case is simpler than the one used in Ref. [6].

5.1.5 Numerical Examples

To verify the correctness and efficiency of our new formulation, several numerical examples have been considered. Some results are described in this section.

Case where $p = 1$

The iteration processes in this case are subject to the following accuracy criteria:

$$\|u_{i+1} - u_i\|/\|u_{i+1}\| < \varepsilon, \qquad \|\alpha_{i+1} - \alpha_i\|/\|\alpha_{i+1}\| < \varepsilon$$

To simplify the numerical computation, we have approximated both u and α using spline functions through interpolation over their values at $N + 1$ uniformly distributed discrete points in $0 \le \xi \le 1$. Throughout this section, $N = 10$ and $\varepsilon = 10^{-4}$ have been used in all examples. The numerical integrations in the iterations are carried out using the recursive Simpson formula.

The iteration for u starts with u_0, found by solving Eq. (5.25) using the fifth-order Runge–Kutta formulas. The iteration for α starts with $\alpha_0(\xi) = 1$. For various values of the nondimensional mass parameter q, Table 5.1 summarizes the percentage increase in the lowest frequency in comparison with that of the cantilever beam having uniform rectangular cross-sections and having the same length, volume, and material as the optimum beam. The corresponding results obtained in Ref. [6] have also been included in the table. As one can see, a large discrepancy exists between the two results. We believe that our results are more accurate, since they agree with the prediction from the asymptotic expressions (5.29) and (5.31); i.e. for large q:

$$\sqrt{\lambda/\lambda_c} = \sqrt{4/3} = 1.1547$$

It is also obvious that, for $q = 1.1027$, the result $\sqrt{\lambda/\lambda_c} = 0.28$ in Ref. [6] is simply not logical, since λ should always be greater than or equal to λ_c.

Figure 5.1 illustrates the corresponding variation in width of the rectangular cross-section as a function of nondimensional coordinate ξ. Figure 5.2 presents the relationship between the eigenvalue λ and the mass parameter q for the optimum beam. The dashed curve in the figure is the corresponding result obtained from Eq. (5.30) for a cantilever beam of uniform cross-section. From these curves, one can find the eigenvalue λ, and hence the lowest frequency of beams for a given mass parameter q. The percentage increase in the lowest frequency

Table 5.1: Values of $\sqrt{\lambda/\lambda_c}$ for various values of q ($p = 1$)

	$q = 0.0375$	$q = 0.2233$	$q = 1.1027$	$q = 4 \times 10^4$
$p = 1$	2.3235	1.5025	1.2388	1.1547
$p = 1$	28.42*	2.56*	0.28*	—

*Results obtained by Karihaloo and Niordson [6].

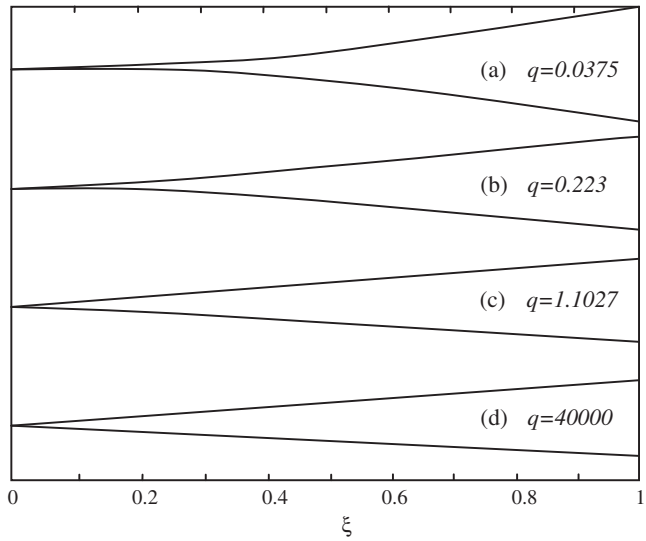

Figure 5.1: Optimum Tapering of Rectangular Cross-Section of Given Height ($p = 1$).

achieved through the optimum design is given in Figure 5.3. Clearly, the results here have verified the asymptotic expressions (5.29) and (5.31).

Cases where $\mathsf{p} = 2$ *and* $\mathsf{p} = 3$

The iteration processes are continued until

$$\|f_{i+1} - f_i\| / \|f_{i+1}\| \quad \text{or} \quad \|u_{i+1} - u_i\| / \|u_{i+1}\| < \varepsilon$$
$$\|z_{i+1} - z_i\| / \|z_{i+1}\| < \varepsilon$$

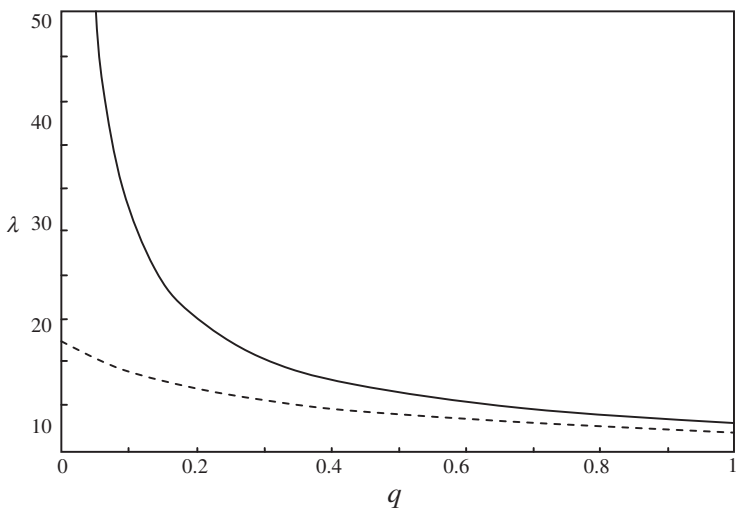

Figure 5.2: Fundamental Frequencies vs. Mass Parameter q ($p = 1$).

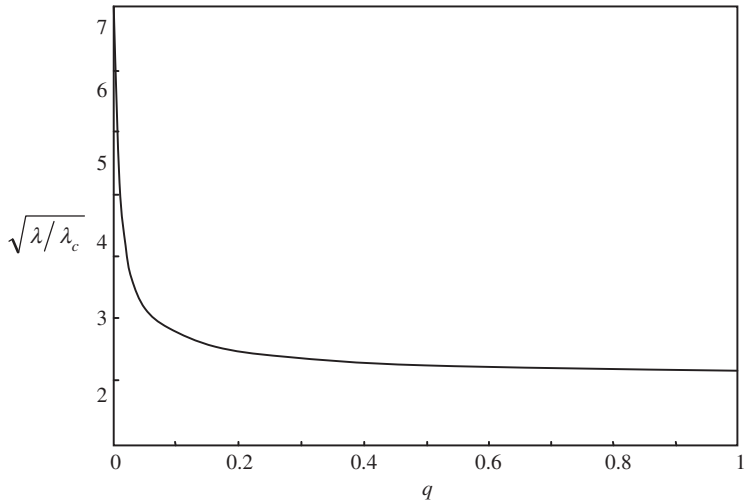

Figure 5.3: Ratio of $\sqrt{\lambda/\lambda_c}$ vs. Mass Parameter q ($p = 1$).

As in the previous case, f (or u for $q \neq 0$) and α are approximated using spline functions through interpolation over their values at $N + 1$ uniformly distributed discrete points on $0 \leq \xi \leq 1$.

The iterations always start with $z_0(\xi) = 1$ for all the cases. For various values of the nondimensional mass parameter q, Table 5.2 summarizes the increase in the lowest frequency in comparison with that of the corresponding cantilever beam of uniform cross-section. The results of Ref. [6] have also been included.

For large q, using the perturbation method, we can find that

$$\lambda_q \approx [(p+3)/(p+1)]^{p+1}, \quad \alpha(\xi) \approx [(p+3)/(p+1)]\xi^{2/(p+1)} \tag{5.44}$$

Equation (5.29) is a special case of Eq. (5.44). From Eqs (5.31) and (5.44), for large tip mass one can find by simple calculation that increases of 24.23% and 29.90% in the lowest natural frequency can be achieved by optimum tapering of the cantilever beams for $p = 2$ and $p = 3$ respectively. From Table 5.2, the results for $q = 100$ using the new iteration scheme are quite close to these two values, whereas a relatively large discrepancy is found for the results given in Ref. [6].

Table 5.2: Values of $\sqrt{\lambda/\lambda_c}$ for various values of q ($p = 2, 3$)

	$q = 0$	$q = 0.0003$	$q = 0.03$	$Q = 100$
$p = 2$	7.0025	4.5984	2.3450	1.2432
$p = 2$	6.78*	5.48*	3.36*	1.27*
$p = 3$	4.2937	3.3201	2.2868	1.2998
$p = 3$	4.25*	3.71*	2.30*	1.33*

*Results obtained by Karihaloo and Niordson [6].

Figures 5.4 and 5.5 present the corresponding variation of the linear dimension of the cross-section as a function of the nondimensional coordinate ξ. Figure 5.6 describes the changes of the eigenvalue λ versus the mass parameter q for the optimum beam ($p = 2$ only). The dashed curve in the figure is the corresponding result obtained from (5.30) for a cantilever

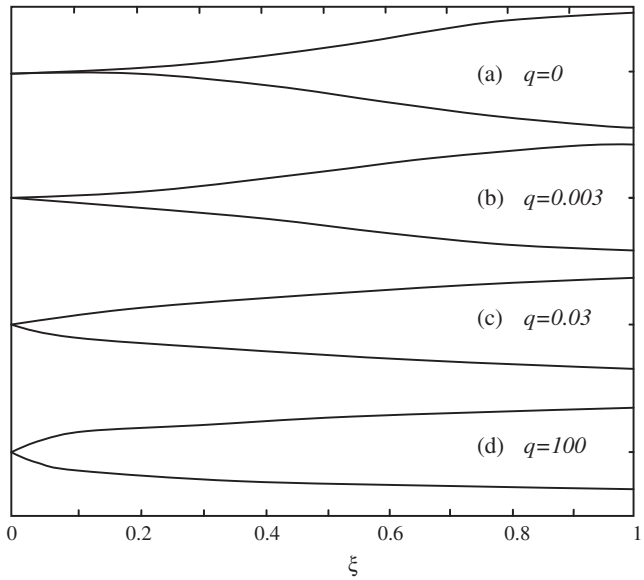

Figure 5.4: Optimum Tapering of Geometrically Similar Cross-Section ($p = 2$).

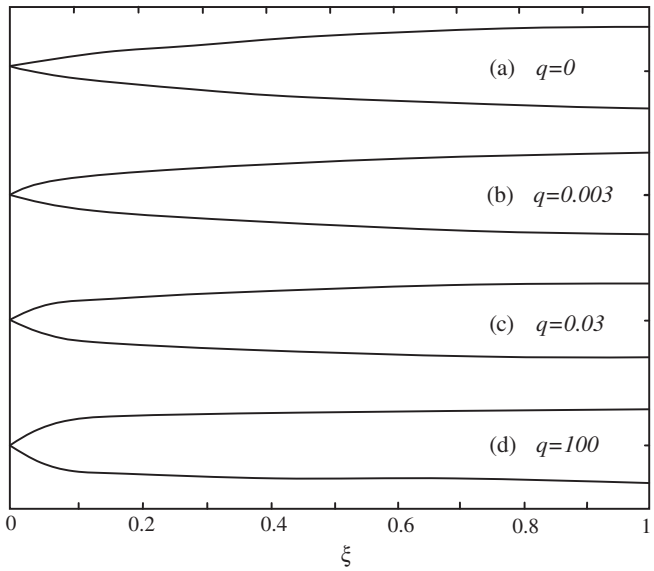

Figure 5.5: Optimum Tapering of Rectangular Cross-Section of Given Width ($p = 3$).

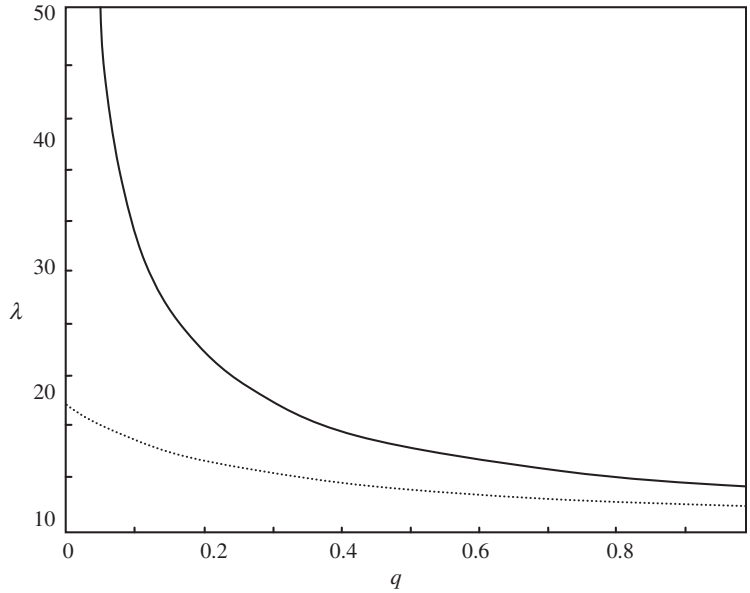

Figure 5.6: Fundamental Frequencies vs. Mass Parameter q ($p = 2$).

beam of uniform cross-section. The percentage increase in the lowest frequency achieved through optimum design is illustrated in Figure 5.7 ($p = 2$ only).

Numerical computations show that the new successive iteration formulations converge much faster than those used in Ref. [6]. For example, for the case where $p = 2$ and $q = 0$, it takes

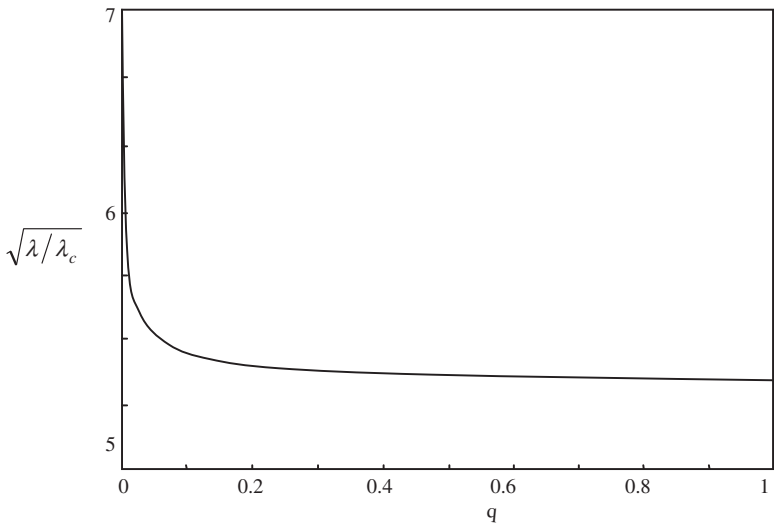

Figure 5.7: Ratio of $\sqrt{\lambda/\lambda_c}$ vs. Mass Parameter q ($p = 2$).

134 iterations to achieve the specified accuracy by using the iteration scheme in Ref. [6], whereas only 33 iterations are needed with the new scheme.

5.2 Geometrically Constrained and Composite Material Designs

Many applications of flexible manipulators will impose constraints on the geometry of the link and its material characteristics. First, the simple constraints of minimum and maximum radius are considered. Since technological advances in link manufacturing capabilities now permit hollow tunnel cross-sections, these designs will be examined and compared to the corresponding optimum solid link designs. New composite materials have been introduced in flexible link design, due to their extremely high bending rigidity to mass ratios. Simple composite designs have been considered and analyzed [17].

5.2.1 Minimum and Maximum Radius Constraints

Generally, a manipulator arm will have to adhere to at least minimum and maximum radius constraints. For geometrically similar cross-sections, this is equivalent to minimum and maximum constraints on the cross-sectional area function. Now, since the IHR algorithm requires these two constraints as part of the optimal design, it will be used to demonstrate how convenient it is to generate a constrained link design.

Figure 5.8 shows three shapes for different area constraints, which can be compared with the unconstrained shape at the top left. We see that the fundamental frequency of vibration is always lower for the constrained shapes, as expected. The lowest fundamental frequency of vibration results from the simultaneous constraints of both minimum and maximum area.

5.2.2 Uniform and Variable Tunnel Cross-Section Designs

It has long been known in the field of structural optimization that beams with hollow tunnel cross-sections are more rigid than the corresponding solid beams. This is because the bending rigidity is equal to the product of the moment of cross-sectional inertia and Young's modulus of elasticity. As the mass is moved away from the beam's neutral axis, the moment of inertia increases dramatically. Thus, hollow links should be much less flexible than the corresponding solid links. The basic DP solution, which was converted into a program called *UniTunnel*, will be utilized to examine the gain over the optimized solid link. In Figure 5.9, the top left plot shows the optimum frequency versus the radius of the uniform tunnel. It is clear that a larger tunnel gives a much better fundamental frequency of vibration. But most applications cannot tolerate huge allocations of space for a flexible manipulator, and this is especially true in space applications where every cubic centimeter must be fully utilized. So, constraints must be placed at least on the outside radius of the link. Specialized

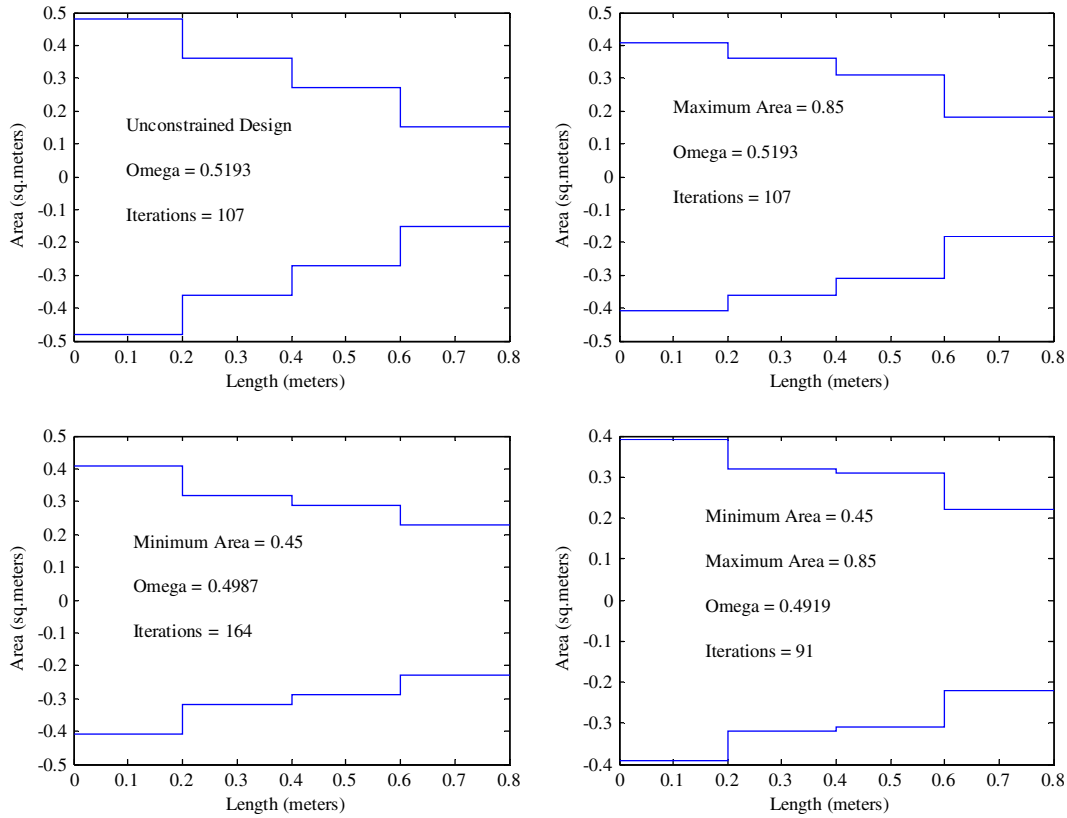

Figure 5.8: Constrained Optimum Designs.

applications may require other constraints, such as minimum/maximum inner radius and minimum wall thickness, to avoid buckling.

A very important design is that of the variable tunnel cross-section. This design can be used to model any flexible link with a hollow interior and will have many practical applications due to the large gain in frequency over the corresponding optimum solid link. Thus, for the same frequency, the total mass can be greatly reduced. Obviously, this design is most relevant for space applications. To implement this design, the IHR algorithm presented in the previous chapter had to be renovated due to the fact that there are two simultaneous design variables of area A and inside radius R_{in}. The following constraints on the design variables were required:

1. $\Sigma_{I=1}^{N} A_{i\Delta i} =$ Constant total volume.
2. $R_{\text{in}}\text{Min } N \leq R_{\text{in}}(\text{N}) \leq R_{\text{in}}\text{Max } N$ for segment N.
3. $R_{\text{in}}\text{Min} \leq R_{\text{in}}(j) \leq R_{\text{in}}\text{Max}$ for segment $j < N$.
4. $R_{\text{in}}(j+1) \leq R_{\text{in}}(j) \leq R_{\text{out}}(j+1) - 0.1WIDTH(j+1)$ for $j < N$.

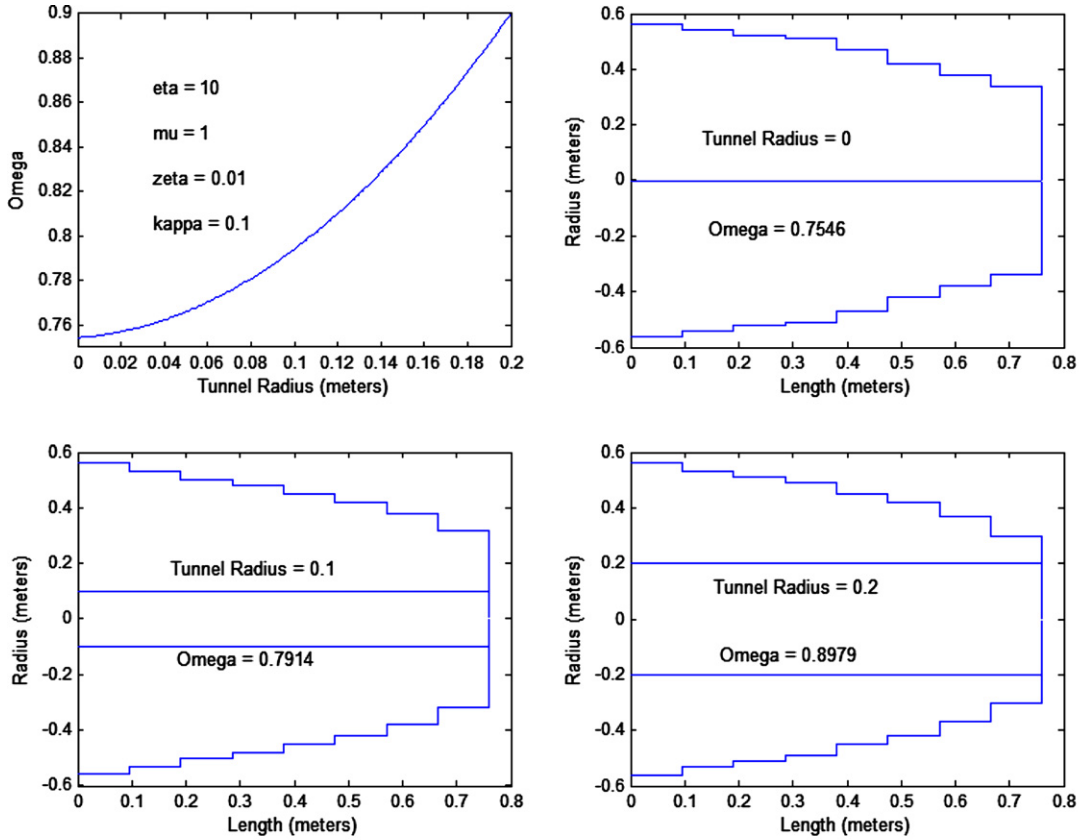

Figure 5.9: Optimum Shapes for Uniform Tunnel Design.

Here, $WIDTH(j+1) = R_{out}(j+1) - R_{in}(j+1)$, R_{in}Min N is the minimum inside radius of segment N, R_{in}Max N is the maximum inside radius of segment N, R_{in}Min is the overall minimum inside radius, and R_{out} is the outside radius.

Constraint 2 is imposed so that end effectors can be attached to the link. Constraint 3 limits the overall outside diameter of the link, when combined with the area constraints A_{min} and A_{max}. Constraint 4 requires a minimum 10% overlap of segment areas to maintain mechanical strength at segment interfaces. This constraint also requires the shape to be monotonically decreasing, which greatly reduces the computation time. The constraints can, of course, be reformulated to adhere to any particular set of design requirements.

Figure 5.10 gives four shapes computed by the program *VarTunnel*. The top left shape was computed using the same design vector as for the uniform tunnel design of Figure 5.9. The constraints here were $A_{min} = 0$, $A_{max} = 2$ m^2, R_{in}Min $= R_{in}$Min $N = 0.002$ m, and R_{in}Max $=$ R_{in}Max $N = 0.2$ m. Notice that the shape and frequency are very close to the uniform tunnel

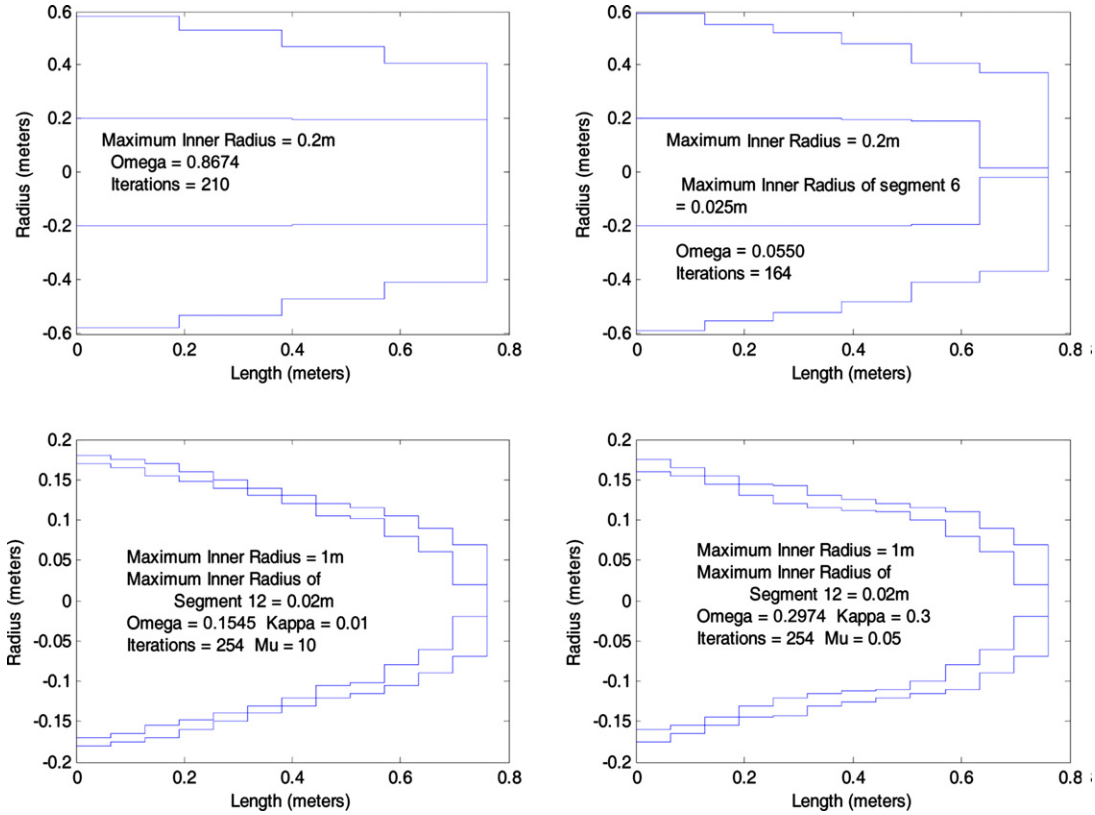

Figure 5.10: Optimum Shapes for Variable Tunnel Design.

design. This example is very important in that it points out that the optimum frequency will always be attained by moving the mass of the link to the constraint limits of R_{in}Max, in the absence of additional constraints. The shape at the top right is the same design with the exception of R_{in}Max $N = 2.5$ cm, which was set to accommodate the shaft of an end effector. The two lower plots in Figure 5.10 show how changes in μ and K affect the shape and frequency.

5.2.3 Composite Material Designs

We have seen that the segmentized formulation lends itself easily to geometrical constraints. The other possible types of constraints are material characteristics such as density and Young's modulus. Since the density and Young's modulus of each segment can be specified individually, the IHR program will be adapted for these optimizations. We are interested in seeing how the optimum frequency and shape are affected when the left half of the link has a different density or Young's modulus from the right half of the link. The two top shapes in Figure 5.11 show the effect of a change in p between the left and right halves of the link. We see that the denser right side of the link gives a slightly higher fundamental frequency

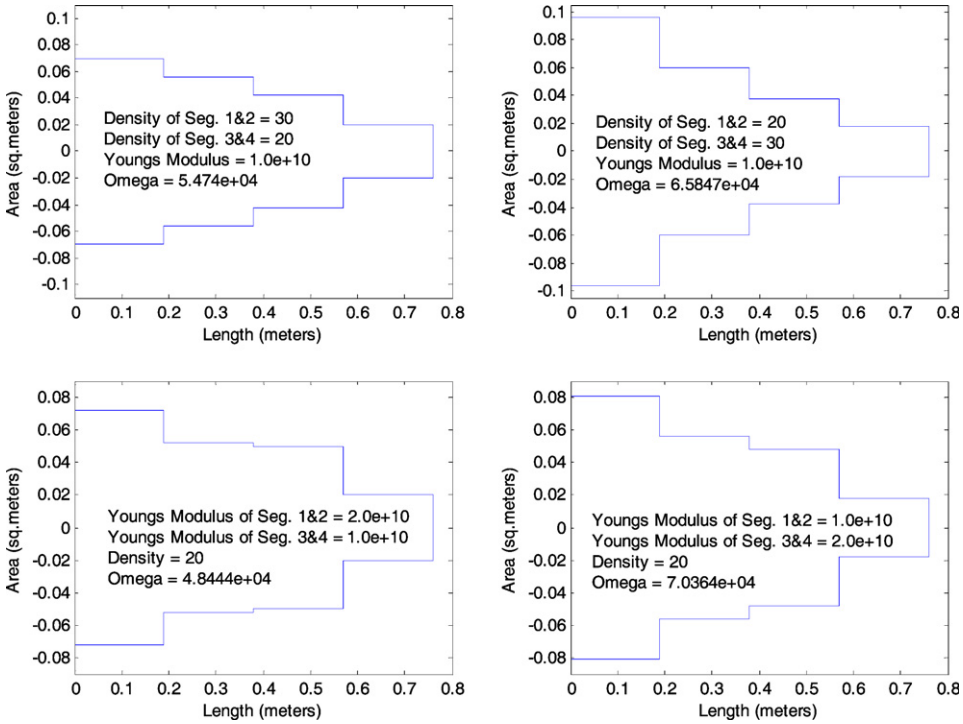

Figure 5.11: Optimum Shapes for Composite Material Design.

of vibration. The two lower shapes show the effect of a change in Young's modulus between the left and right halves of the link. A larger Young's modulus in the left half gives a somewhat higher frequency. Also notice the similarity in shapes between the top and bottom figures. The right-hand shapes have a smaller segment 4 due to the larger density and Young's modulus there, in comparison with the left-hand shapes.

Thus, if an optimum design cannot produce the required frequency within a given maximum area or radius constraint, a material of higher density or Young's modulus may be substituted to generate a higher fundamental frequency of vibration in a shape with a smaller radius.

5.3 Optimum Shape Design of Flexible Manipulators with Tip Loads

5.3.1 Problem Setup

Research on flexible manipulators is most relevant in the design of new-generation industrial robotic manipulators and in the field of robotic space applications. Many techniques have been applied to overcome tip oscillations caused by manipulator flexibility. Here, the control problem is addressed from a design perspective. The goal is to build a high-performance

flexible manipulator such that the effect of its oscillation is reduced during normal operation. This design should also improve the performance of control algorithms. An important direction in flexible link research is the search for structural designs that optimize manipulator mass and speed. The design problems are as follows:

1. Given a fixed mass for the link, find a shape that maximizes its speed.
2. Given a fixed speed for the link, find a shape that minimizes its mass.

How can these objectives be achieved? We need a design variable that relates directly to the maximum speed of the manipulator and is a function of shape, as well as material properties. The only design variable that fits these requirements is the fundamental frequency of vibration. Thus, problem 1 is equivalent to finding a shape that maximizes the fundamental frequency of vibration of the link. A large fundamental frequency is desired since it generates a large bandwidth for the flexible manipulator, and this allows for fast motion and stable endpoint control. Problem 2 is known as the minimum weight problem and is dual to problem 1. This problem is very important in that a significant reduction in energy costs can be achieved by using the optimally designed link. Also for space applications, where flexible manipulators have been generally recognized as an ideal tool for material handling and space-structure construction, minimum-weight manipulators are of special interest due to the strict weight constraints imposed by the loading capacity of space vehicles [18].

What is the difference between a flexible and a rigid manipulator? A rigid manipulator, in theory, has an infinitely large fundamental frequency of vibration and thus can move at any desired speed without significant tip deflection. The drawbacks to this design are a large link mass and correspondingly low energy efficiency. A flexible manipulator, on the other hand, has a much lower mass but experiences significant tip deflection under normal operating conditions, and the oscillations become severe when the manipulator speed approaches its fundamental frequency. The amount of deflection depends upon the following factors:

- Rotational velocity of the link
- Total length of the link
- Material properties of the link
- Shape of the link
- Mass, placement, and moment of tip load.

In general, only one of these factors is not a specified design requirement and that is the link's shape function. So, the objective is to develop a flexible manipulator that is capable of high-speed motion with less energy consumption by increasing the fundamental frequency of vibration through optimum shape design.

It has been shown that the fundamental frequency of a flexible manipulator can be increased substantially through the optimum tapering of its cross-section. For example, numerical analysis indicates that, depending on the values of hub inertia and tip load parameters, an

increase of up to 625% in the fundamental frequency can be achieved for manipulators with links of geometrically similar cross-sections [11].

The first attempts to optimize a flexible beam using the fundamental frequency of vibration were made by engineers working in the field of structural optimization. Niordson first showed that the optimum design of a simply supported beam will have a fundamental frequency of vibration that is 6.6% larger than that of the corresponding uniform beam [5]. This work was extended by others to include specific design requirements [7–9]. In the early 1970s, Karihaloo and Niordson showed that an increase of up to 678% in the fundamental frequency of vibration was possible for vibrating cantilevers with a tip mass [6]. This research was concerned with beams that were rigidly attached to an inertial frame, meaning simply supported beams at both ends and the cantilever supported at only one end. But flexible robotic links must rotate about an axis at the link's base. Also, the base of the flexible link usually must be rigidly attached to a rotating hub for mechanical support. Thus, the results from structural optimization cannot be carried over into the field of robotics. This is an important point and one that is often overlooked.

Early work on flexible manipulators was carried out by Cannon and Schmitz [19], Book [20], Nguyen et al. [21], Sakawa et al. [22], and many others. Khorrami and Ozguner [23] presented a set of *integro-partial* equations and used a perturbation method for control purposes. Yang and Donath [24] considered the flexibility of the joint as well as link flexibility. A complete study of different dynamic equations under various boundary conditions for flexible manipulators was conducted by Bellezze et al. [25]. Wang and Wen [26] derived the dynamic equations for flexible manipulators subject to large angular deformations and clarified some issues relating to the specification of boundary conditions. A comprehensive study on the influence of rotary inertia, shear deformation, and tip load on the vibration behavior of one-link flexible manipulators has been conducted by Wang and Guan [16]. Asada et al. [27] addressed the optimal design problem using a finite element computational model. As part of their effort towards a control-configured flexible arm, they tried to increase the fundamental frequency of vibration of a flexible manipulator through optimum tapering of a beam of varying rectangular cross-section. A theoretical increase of 43% in the fundamental frequency of the manipulator was obtained.

5.3.2 Euler–Bernoulli Equations

Design Model

The system model of the flexible manipulator is composed of a hub rigidly attached to a flexible link of length L with a tip load (see Figure 5.12). The hub has a rotational inertia given by I_H. The tip load is modeled by its mass, M_P, and moment of inertia, I_P. A constant torque, τ, is applied to the hub, which is located to the left of $x_1 = 0$. The angular displacement

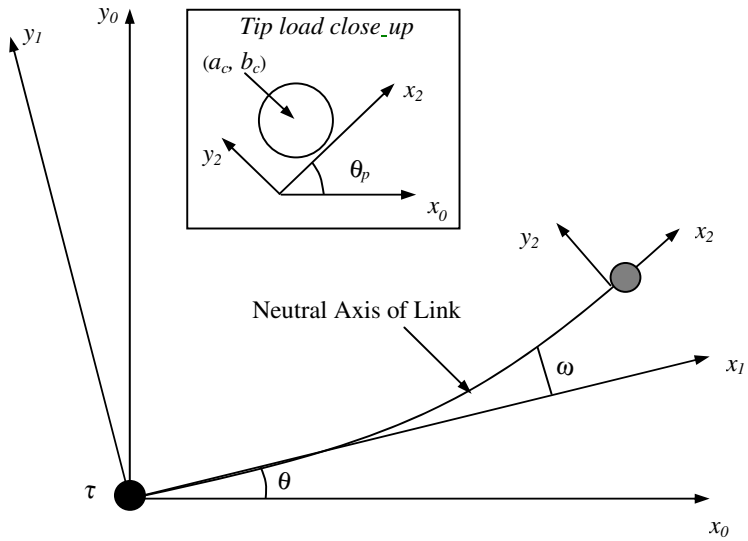

Figure 5.12: Design Model of Flexible Manipulator.

of the link axis, x_1, is given by θ. The transverse displacement of the link's neutral axis from the x_1-axis is given by ω. The tip load center of mass, which also includes the end-effector mass, is located at (a_c,b_c) in the (x_2,y_2) frame. Three coordinate systems are employed in the subsequent analytical derivation: inertial (x_0,y_0), link (x_1,y_1), and tip load (x_2,y_2).

The dynamics of the flexible link will be modeled using the Euler–Bernoulli beam theory. Rotary inertia, as well as shear deformation, will be ignored since these factors have been shown to have only a negligible effect on the fundamental frequency of vibration [16]. No rotary inertia implies that the velocity of every point on a given cross-section has the same velocity as the point of intersection with the neutral axis. The normal plane assumption is also used, which means that each transverse section remains plane and normal to the neutral axis after deformation.

According to the derivations in Sections 3.2–3.4, the linearized Euler–Bernoulli model is summarized as

$$I_H\ddot{\theta} - D(0)v''(0) = \tau \tag{5.45}$$

$$I_H\ddot{\theta} - D(0)v''(0) = \tau \tag{5.46}$$

with boundary conditions

$$v(0) = 0, \quad v'(0) = \theta \tag{5.47}$$

$$D(L)v''(L) + I_p\ddot{v}'(L) + M_p a_c\ddot{v}(L) = 0 \tag{5.48}$$

$$[D(L)v''(L)]' - M_p[\ddot{v}(L) + a_c\ddot{v}'(L)] = 0 \tag{5.49}$$

where $v(x_1, t) = w(x_1, t) + x_1\theta(t)$ is the total displacement of the link.

Equation (5.45) is the well-known dynamics equation, which all flexible links must satisfy. Equation (5.46) is the torque relationship. Equation (5.47) is the boundary condition at the hub, while Eqs (5.48) and (5.49) are the boundary conditions at the tip load. These are the linearized equations of motion for the system, upon which all subsequent derivations will be based. Note that the endpoint boundary conditions are independent of b_c, the transverse placement of the tip load center of mass. This makes sense mechanically, since small deformations were assumed in the linearization process.

Vibration Equations

Suppose the link undergoes harmonic vibrations in its plane of motion. Then, the total displacement can be expressed as

$$v(x_1, t) = v(x_1)\sin(\omega t), \quad \theta = \theta_0 \sin(\omega t) \tag{5.50}$$

where ω is the frequency of vibration. The governing equations of harmonic vibration can then be written as

$$[D(x_1)v''(x_1, t)]'' - \rho\omega^2 A(x_1)v(x_1) = 0 \tag{5.51}$$

$$I_H v'(0)\omega^2 + D(0)v(0)'' = 0 \tag{5.52}$$

with boundary conditions

$$v(0) = 0 \tag{5.53}$$

$$D(L)v''(L) - I_p\omega^2 v'(L) - M_p a_c \omega^2 v(L) = 0 \tag{5.54}$$

$$[D(L)v''(L)]' + M_p\omega^2 v(L) + M_p a_c \omega^2 v'(L) = 0 \tag{5.55}$$

Here, the second boundary condition from Eq. (5.47) has been substituted into the torque equation. The substitution, $\lambda(x_1) = \rho A(x_1)$, has been used, where ρ is the volumetric mass density and $A(x_1)$ is the cross-sectional area function. Now, we change to a variable, $\xi = x_1/L$, which indicates the position along the link axis in dimensionless coordinates. Then:

$$\frac{\partial}{\partial x_1} = \frac{1}{L}\frac{\partial}{\partial \xi}, \quad \frac{\partial^2}{\partial x_1^2} = \frac{1}{L^2}\frac{\partial^2}{\partial \xi^2}, \quad 0 \le \xi \le 1$$

The equations of vibration become

$$[D(\xi)v''(\xi)]'' - \rho L^4 \omega^2 A(\xi)v(\xi) = 0 \tag{5.56}$$

$$I_H L\omega^2 v'(0) + D(0)v(0)'' = 0 \tag{5.57}$$

with boundary conditions

$$v(0) = 0 \tag{5.58}$$

$$D(1)v''(1) - I_p L\omega^2 v'(1) - M_p a_c L^2 \omega^2 v(1) = 0 \tag{5.59}$$

$$[D(1)v''(1)]' + M_p L^3 \omega^2 v(1) + M_p a_c L^2 \omega^2 v'(1) = 0 \tag{5.60}$$

Multiplying Eq. (5.56) by $v(\xi)$, integrating by parts, and applying one boundary condition at each integration, the following equation can be derived:

$$-2M_p a_c L^2 \omega^2 v'(1)v(1) - M_p L^3 \omega^2 v(1)^2 - I_p L\omega^2 v'(1)^2$$
$$-I_H L\omega^2 v'(0)^2 + \int_0^1 D(\xi)v''(\xi)^2 \mathrm{d}\xi - \rho L^4 \omega^2 \int_0^1 A(\xi)v(\xi)^2 \mathrm{d}\xi = 0$$

Solving this for ω^2 gives

$$\omega^2 = \frac{\int_0^1 D(\xi)[v''(\xi)]^2 \mathrm{d}\xi}{\rho L^4 \int_0^1 A(\xi)v^2(\xi)\mathrm{d}\xi + LI_H v'(0)^2 + G_p} \tag{5.61}$$

where

$$G_p = M_p L^3 v(1)^2 + 2a_c M_p L^2 v(1)v'(1) + I_p L v'(1)^2$$

Equation (5.61) is the basic equation of vibration that our system model must satisfy. Note that G_p is due only to the tip load and, if a tip load is absent, then $G_p = 0$.

5.3.3 Analytical Solutions

Optimality Equations

Now the optimality equations will be derived using variational calculus, similar to that of Haftka et al. [14]. In order to simplify computations, the following moment−area relationship will be used:

$$I(\xi) = \gamma_p A^p(\xi) \;\; p = 1,\ 2,\ 3 \tag{5.62}$$

where $p = 1 \Rightarrow$ rectangular cross-sections of uniform height, $p = 2 \Rightarrow$ geometrically similar cross-sections, and $p = 3 \Rightarrow$ rectangular cross-sections of uniform width.

This relation was first used by Brach [7] in the optimization of vibrating cantilevers, and is very useful in comparing different designs. Here, A is the cross-sectional area of the link and γ_p is a constant. It should be noted that for $p = 2$, γ_p will depend on the shape of the cross-section. For example, the geometrically similar cross-section can be circular, square, or rectangular, each having its own unique moment.

Now, the nondimensional shape function is defined as

$$\alpha(\xi) = \frac{\rho L}{M} A(\xi)$$

where M is the total link mass. The frequency equation, Eq. (5.61), then becomes

$$\omega^2 = \frac{\gamma_p E M^{p-1}}{\rho^p L^{p+3}} \left\{ \frac{\int_0^1 \alpha^p(\xi)[v''(\xi)]^2 \mathrm{d}\xi}{\int_0^1 \alpha(\xi) v^2(\xi) \mathrm{d}\xi + M^{-1} L^{-3} [L I_H v'(0)^2 + G_p]} \right\} \tag{5.63}$$

Converting parameters into their dimensionless form:

$$\lambda = \left[\frac{\rho^p L^{p+3}}{\gamma_p E M^{p-1}} \right] \omega^2 \quad \text{dimensionless eigenvalue}$$

$$\eta = \frac{I_H}{ML^2} \quad \text{relative hub moment}$$

$$\mu = \frac{M_p}{M} \quad \text{relative tip load mass}$$

$$\zeta = \frac{a_c}{L} \quad \text{relative tip load placement}$$

$$\kappa = \frac{I_p}{ML^2} \quad \text{relative tip load moment}$$

Eq. (5.63) now becomes

$$\lambda = \frac{\int_0^1 \alpha^p(\xi)[v''(\xi)]^2 \mathrm{d}\xi}{\int_0^1 \alpha(\xi) v^2(\xi) \mathrm{d}\xi + \eta v'(0)^2 + H(1)} \tag{5.64}$$

where

$$H(1) = 2\zeta\mu\ \upsilon(1)\upsilon'(1) + \kappa\upsilon'(1)^2 + \mu\,\upsilon(1)^2$$

The fundamental frequency eigenvalue, λ_f, is obtained by minimizing Eq. (5.64) over all admissible displacements:

$$\lambda_f = \min_{\upsilon(\xi)} \lambda \tag{5.65}$$

The maximum fundamental frequency eigenvalue, $\lambda_{f(\max)}$, is obtained by maximizing Eq. (5.65) over all admissible shape functions:

$$\lambda_{f(\max)} = \max_{\alpha(\xi)} \lambda_f \tag{5.66}$$

where the shape function must satisfy

$$\int_0^1 \alpha(\xi)\mathrm{d}\xi = 1 \quad \text{constant-volume constraint} \tag{5.67}$$

Without this constraint, optimization would be meaningless since the volume, and likewise the mass, could be increased indefinitely making $\lambda_{f(\max)}$ as large as desired. The optimum shape design problem now becomes:

Find a shape function α_{opt} that satisfies the above constraint and maximizes the fundamental frequency eigenvalue, $\lambda_{f(\max)}$.

In order to derive the optimization equations, we convert to an unconstrained problem by defining

$$L_\upsilon = \lambda_{f(\max)} - \sigma\left\{\int_0^1 \alpha(\xi)\mathrm{d}\xi - 1\right\} \tag{5.68}$$

which is a function of α and υ. Here, σ is a Lagrange multiplier. Setting the total variation of L_υ to zero generates the following equations:

$$[\alpha^p \upsilon'']'' - \lambda\alpha\upsilon = 0 \quad \text{Dynamics equation} \tag{5.69}$$

$$p\alpha^{p-1}\upsilon''^2 - \lambda\upsilon^2 = \lambda\sigma \quad \text{Optimality equation} \tag{5.70}$$

with boundary conditions

$$\upsilon(0) = 0, \quad \alpha^p(0)\upsilon''(0) + \lambda\eta\upsilon'(0) = 0 \tag{5.71}$$

$$\alpha^p(1)v''(1) - \kappa\lambda v'(1) - \zeta\mu\lambda v(1) = 0 \tag{5.72}$$

$$[\alpha^p(1)v''(1)(1)]' + \zeta\mu\lambda v'(1) + \mu\lambda v(1) = 0 \tag{5.73}$$

It is easy to see that this solution is not unique. If $(v,\sigma,\alpha,\lambda)$ is a valid solution, then $(cv,c^2\sigma,\alpha,\lambda)$ is also a valid solution for any nonzero constant c. We can utilize this non-uniqueness in a constructive way by choosing $c = 1/\sqrt{\sigma}$. Then, the solution can be expressed as $(v/\sqrt{\sigma}, 1, \alpha, \lambda)$. Thus, we only need to find $v/\sqrt{\sigma}$ instead of v and σ separately. And since the displacement function v is not unique, we can set $\sigma = 1$, thereby simplifying the problem considerably.

Now, the optimality condition, Eq. (5.70), becomes

$$p\alpha^{p-1}v''^2 - \lambda v^2 = \lambda \tag{5.74}$$

Equation (5.74), along with Eqs (5.69) and (5.71)–(5.73), constitute the optimality equations upon which the following iterative solution will be based. Note that for $p = 1$, the shape function α disappears, and special techniques must be employed to find the solution [17].

The most important case is $p = 2$, as it gives the greatest increase in frequency in comparison to the other possible cross-sectional shapes [11]. Thus, only geometrically similar cross-sections will be considered in the following solutions for the above reason and the fact that the $p = 1$ and $p = 3$ shapes and frequencies are mostly a rescaling of the $p = 2$ case.

Iterative Solution

The optimality equations derived above constitute a nonlinear eigenvalue problem, which in general has no closed form solution. Thus, an iterative scheme is developed to find the numerical solution for a specified design vector, $D = [\eta,\mu,\zeta,\kappa]$. Formal integration of the dynamics equation, Eq. (5.69), yields, upon applying one boundary condition at each integration:

$$v''(\xi) = \frac{s[v^2(\xi) + 1]^{\frac{p}{p+1}}}{\left|p\beta g(\xi) + p(1-\xi)^2 \int_0^1 Q(x,\xi)\mathrm{d}x\right|^{\frac{p-1}{p+1}}} \tag{5.75}$$

where s is the sign of the denominator and

$$Q(x,\xi) = x\phi_v[\xi + x(1-\xi)]v[\xi + x(1-\xi)] \tag{5.76}$$

$$g(\xi) = \kappa v'(1) + \zeta\mu v(1) + \mu(1-\xi)(\zeta v'(1) + v(1)) \tag{5.77}$$

$$\alpha(\xi) = \frac{\phi_v}{\beta}, \quad \phi_v(\xi) = \left[\frac{v^2(\xi) + 1}{v''^2(\xi)}\right]^{\frac{1}{p-1}}, \quad \beta = \left(\frac{p}{\lambda}\right)^{\frac{1}{p-1}} = \int_0^1 \phi_v(\xi)\mathrm{d}\xi \tag{5.78}$$

with boundary conditions, Eq. (5.71), expressed as

$$v(0) = 0, \quad v'(0) = -\frac{v''(0)}{p\eta\beta|v''(0)|^{\frac{2p}{p-1}}} \tag{5.79}$$

Standard integration gives v as

$$v(\xi) = v'(0)\xi + \xi^2 \int_0^1 (1-x)v''(x\xi)\mathrm{d}x \tag{5.80}$$

Here, the integral relations given below have been utilized, since single integration is much less computationally intensive than double integration:

$$\int_0^\xi \int_0^x G(s)\mathrm{d}s\mathrm{d}x = \xi^2 \int_0^1 (1-x)G(x\xi)\mathrm{d}x \tag{5.81}$$

$$\int_\xi^1 \int_x^1 G(s)\mathrm{d}s\mathrm{d}x = (1-\xi)^2 \int_0^1 xG[\xi + x(1-\xi)]\mathrm{d}x \tag{5.82}$$

The successive iteration scheme shown below is a variation of the one developed by Karihaloo and Niordson [6] for cantilever optimization:

1. Specify a design vector $D = [\eta,\mu,\zeta,\kappa]$.
2. Select an initial β_0 and $v_0''(\xi)$.
3. Update $v_i(\xi)$by using $v_i''(\xi)$and β_i.
4. Update $v_i''(\xi)$ by using $v_{i+1}(\xi)$ and $v_i''(\xi)$.
5. Update β_i by using $v_{i+1}(\xi)$ and $v_{i+1}''(\xi)$.
6. If a specified tolerance is not met, go to Step 3. Here:

$$\text{Tolerance} = \frac{|\beta_{i+1} - \beta_i|}{|\beta_{i+1}|} + \frac{\|v_{i+1} - v_i\|}{\|v_{i+1}\|} + \frac{\|v_{i+1}'' - v_i''\|}{\|v_{i+1}''\|}$$

7. Using Eq. (5.78), $\lambda_{f(\max)} = p/\beta^{p-1}$ and $\alpha_{\text{opt}} = \phi_v/\beta$.

When the specified accuracy is met (typically 0.001), the shape function α_{opt} and the fundamental frequency eigenvalue $\lambda_{f(\max)}$ are computed. The actual optimum cross-sectional area of the link can then be computed using Eq. (5.63). The optimum fundamental frequency of vibration ω_{opt} is found from the eigenvalue relation below Eq. (5.64). Cubic splines were

used to approximate all functions and a recursive Simpson formula was used for numerical integration.

In the introduction, the basic dual problems were given as:

1. Given a link mass M_0, find α_{opt} that gives $\omega_{\max}$.
2. Given a frequency ω_0, find α_{opt} that gives $M_{\min}$.

Problem 1 is based on finding a shape α_{opt} that gives $\lambda_{f(\max)}$ under the constraint of constant volume, V_0. Suppose there is a smaller mass M_1 and a smaller volume V_1 that generates the frequency λ_1. Now, the density, ρ, is given by M_1/V_1. Thus, $M_1 = \rho V_1$. Substitution of $V_1 = \int_0^L A(x_1)\, dx_1$ gives $M_1 = \rho \int_0^L A(x_1)\mathrm{d}x_1$. Thus, if M_0 decreases to M_1, then $A(x_1)$ must also decrease. Now, the bending rigidity, EI, is a function of A by Eq. (5.62). So a decrease in A will cause a decrease in the bending rigidity, which will have the unavoidable effect of decreasing λ_f. Thus, it should be obvious that a smaller mass means a smaller fundamental frequency of vibration for links of the same length and density. All of this leads to the fact that M_0 must necessarily be the minimum mass, $M_{\min}$. This implies that each optimum shape α_{opt} and frequency $\lambda_{\text{opt}} = \lambda_{f(\max)}$ correspond to one unique mass M_{opt} that is minimum for that particular frequency. And since $\lambda_{f(\max)}$ is directly proportional to $\omega^2_{\max}$, via the relation below in Eq. (5.64):

$$\omega_{\max} = \omega_0 \quad \Leftrightarrow \quad M_0 = M_{\min}$$

Note that this is true even if the optimum shape α_{opt} is not unique for that particular λ_{opt}. To date, the mathematical proof of the uniqueness of α_{opt} for each λ_{opt} has not been *successfully* demonstrated, although all of the numerical results point to this conclusion.

Utilizing this knowledge, the above relationship can be combined with the above iterative solution to problem 1 in a simple algorithm that solves problem 2. Here, λ_{opt} is computed using the above iterative solution. The algorithm is:

1. Set ω, ρ, L, E, and $\Xi = [I_H, M_p, a_c, I_p]$.
2. Initialize link mass, M_k.
3. Compute design vector $D = [\eta, \mu, \zeta, \kappa]$, where η, μ, and κ are functions of M_k.
4. Get λ_k, where $\lambda_k = C_M/M_k$ and $C_M = \rho^2 L^5 \omega^2/\gamma_2 E$ using the relation below Eq. (5.64).
5. Using D, find λ_{opt}.
6. Set error $= |\lambda_{opt} - \lambda_k|$.
7. If tolerance is not met, change mass and go to Step 3.

The minimum mass design is found at the intersection of the λ_{opt} and λ_k plots versus mass. For a separate solution to problem 2 based upon the optimality equations, see Wang and Russell [28].

Numerical Results and Discussion

Again, we have only considered the $p = 2$ case and, in particular, links with circular cross-sections. The advantage of circular cross-sections is that the frequency of vibration will be the same, regardless of the direction of movement in a three-dimensional space frame. For example, a rectangular link will have different dynamical characteristics if the motion of the link is diagonal to a side as opposed to being perpendicular. Circular cross-sections also give a larger increment in the fundamental frequency of vibration compared with other possible shapes.

First, a general overview of the dynamic relations between $\lambda_{f(\max)}$ and the four design parameters, η, μ, ζ, and κ, will be given. It is easy to see that an increase in tip load mass μ will generate a larger bending moment in the link that manifests as a larger tip deflection during motion. Similarly, when the tip load moment κ is increased, a larger bending moment will be induced in the link, particularly towards the end of the link near the tip load. This should also increase the tip deflection during motion. Now, an increase in tip deflection implies a corresponding decrease in the fundamental frequency of vibration. So, increasing μ or κ should cause $\lambda_{f(\max)}$ to decrease. From mechanics, it should be obvious that the further away the tip load center of mass from the endpoint of the link, the larger the induced bending moment will be, especially near the end of the link. As with the other parameters, we should expect a larger ζ to generate a smaller $\lambda_{f(\max)}$, although if ζ is small (of the order of 0.05), the effect should only be slight.

Now, consider the effect of a change in hub inertia, η, on $\lambda_{f(\max)}$. Large hub inertia will give the link a very stable platform. On first examination, this stability might seem to reduce vibrations and tip deflection, but in fact it has just the opposite effect. The reason for this is that large hub inertia means that the base of the link is very stable. This stability exacerbates tip deflection since the vibrations cannot be damped out by hub rotational vibrations. Conversely, when the hub is small and easy to rotate, it effectively damps out much of the link's vibrational modes. Thus, we should expect a smaller hub inertia to give a larger fundamental frequency of vibration. The numerical results given in Figure 5.13 reflect the validity of these intuitive observations.

The following analysis is the result of extensive numerical simulations of different design vectors, D, using the above successive iteration scheme. The convergence of this method is very quick for large hub inertias ($\eta > 4$). Usually, only 5−8 iterations at 10 seconds per iteration on Matlab are required. For small hub inertias ($\eta < 1$), the required number of iterations increases dramatically, and if a large tip load is also present it may not converge at all. These facts, along with the dynamics analysis given above, serve to point out that the hub inertia is very important for the optimum shape design. This is substantiated in the numerical results, as evidenced in Figure 5.13. We also see that λ_{opt} is relatively insensitive to variations in normal tip load placements ($\zeta < 0.1$). A thorough sensitivity analysis of each design parameter will be presented in Section 5.4.6.

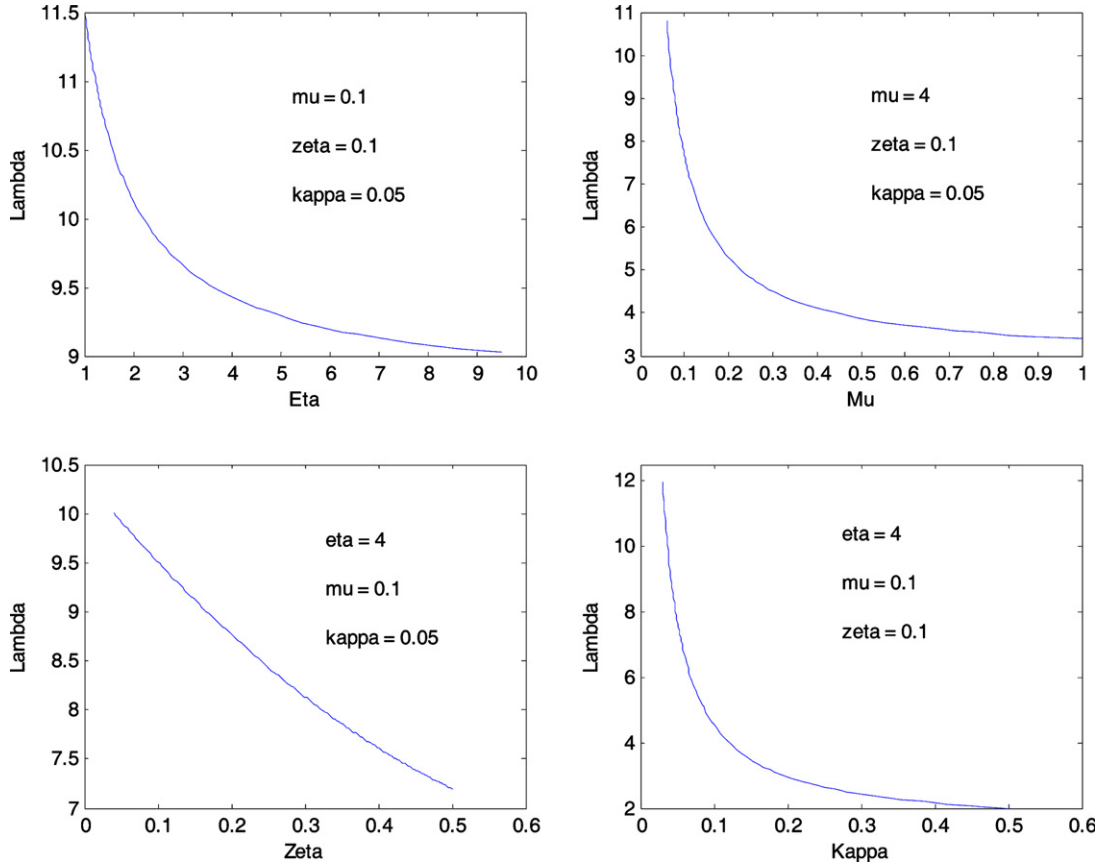

Figure 5.13: λ_{opt} vs. $D = [\eta,\mu,\zeta,\kappa]$.

In general, as the fundamental frequency of vibration decreases due to an increase in one or more of the parameters, the optimum frequency approaches that of a uniform link. This does not necessarily mean that the optimum shape becomes uniform. An example of this is μ, which generates a large amount of tapering near the tip load of the optimum shape for large parameter values (see Figure 5.14). Also, note the almost uniform shape generated by $\kappa = 1.0$. The reason for this can be explained from dynamics principles. When the manipulator slows down or speeds up, the large tip load moment will generate a large bending force near the end of the link. This would increase flexibility and thus lower the frequency. To compensate, the optimization scheme puts more mass here.

In Table 5.3, the gain in λ_f of the optimized link versus the uniform link is given. Note that although λ_{opt} decreases with η, the gain in λ_f actually increases. Thus, a smaller hub will give a smaller advantage in frequency to the optimized link. When $\kappa = 0.5$, there is very little gain in frequency since the shape becomes practically uniform. This serves to point out an important

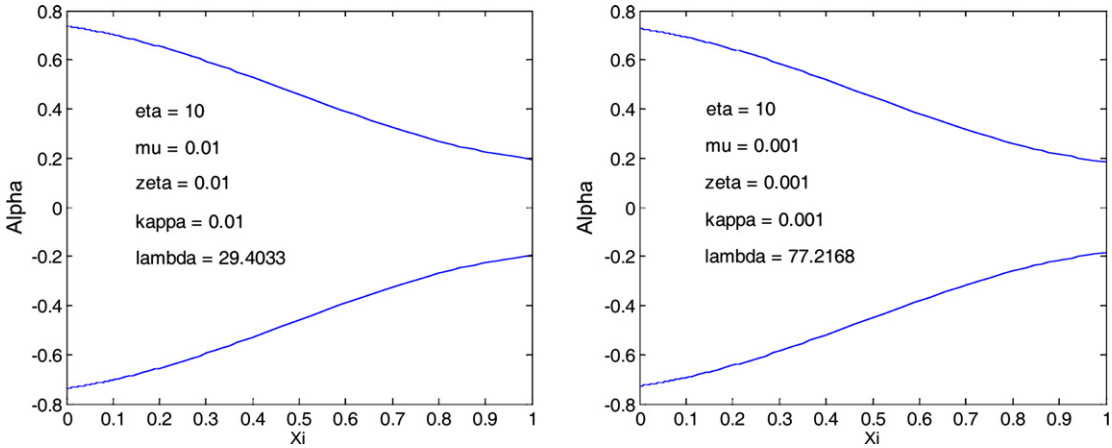

Figure 5.14: Optimum Shapes for Small Tip Load.

Table 5.3: Ratio of λ_{opt}/λ_u

	$(\mu,\zeta,\kappa) =$ (0.10,0.1,0.05)	$(\mu,\zeta,\kappa) =$ (0.05,0.1,0.05)	$(\mu,\zeta,\kappa) =$ (0.10,0.1,0.50)	$(\mu,\zeta,\kappa) =$ (0.50,0.1,0.10)
$\eta = 1.2$	3.6704	3.8694	1.0843	1.8172
$\eta = 2$	4.0219	4.5408	1.1602	1.9821
$\eta = 4$	4.4335	5.0578	1.1959	2.0775
$\eta = 8$	4.6478	5.335	1.2066	2.0961

fact of optimum shape design, and that is if the manipulator will be handling tip loads with relatively large moments, then it will most likely be more economical to use a less expensive uniform link. The largest gain, both here and in general, will be realized when the tip load parameters are small ($\mu = \kappa \leq 0.05$). As this is the case with many robotic applications, there will be many possibilities for optimum shape design in commercial and industrial situations. For example, when $\mu = \zeta = \kappa = 0.001$, the gain in ω over that of the corresponding uniform link is 625% (see Figure 5.15).

5.3.4 Segmentized Optimization Approach

Segmentized Formulation

Much of the work being done on the design of optimum controllers for flexible manipulators is also based upon the fundamental frequency of vibration. Currently, this frequency has to be approximated using modal shape functions developed for uniform links. But since the links are non-uniform, there is an inherent inaccuracy in the design.

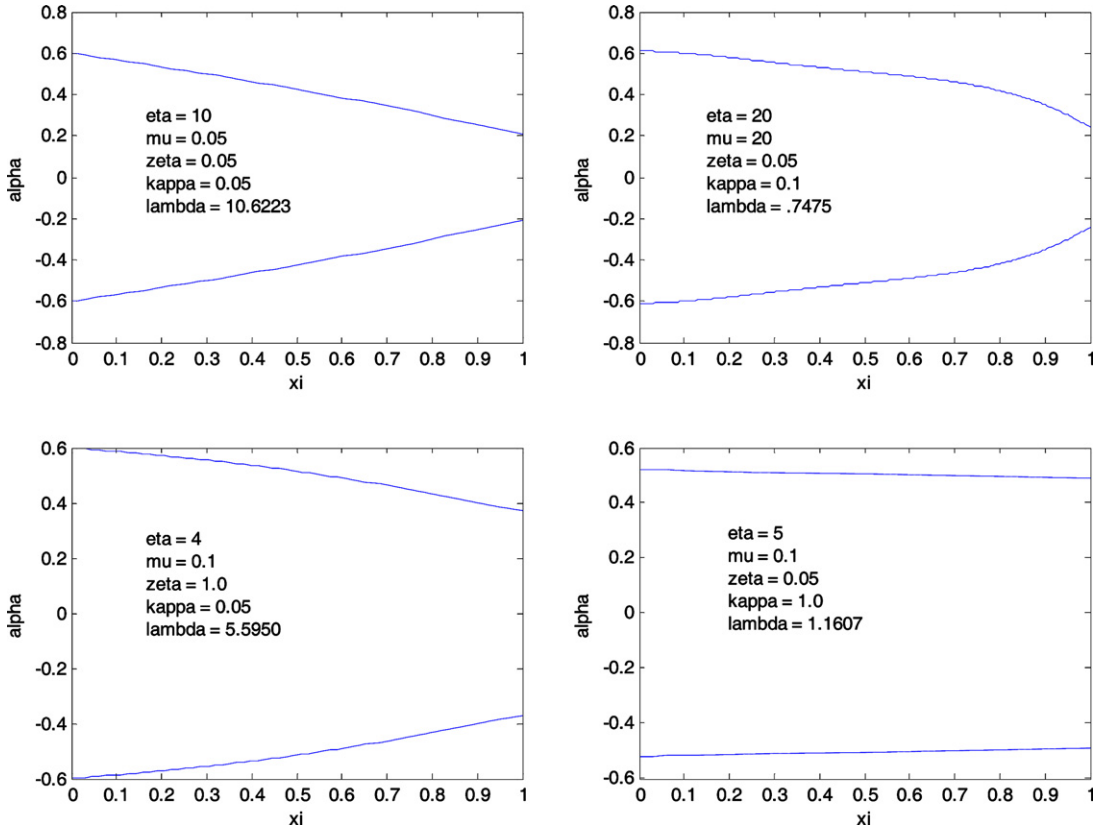

Figure 5.15: Optimum Shapes for large η, μ, ζ, and κ.

An efficient method to find the fundamental frequency of vibration to any required degree of accuracy would result in a considerable improvement in optimum controllers. The analytical solution of Section 5.3.3 is for an unconstrained design. But we would like a model to which any practical constraint could be applied. Also, we would like to have a more formal optimization method that allows the utilization of mathematical programming techniques. For these reasons, an innovative design method has been developed based on a segmentized solution of the vibration equations.

The flexible link is approximated by N discrete segments, each having a constant cross-sectional area. A model of this design is shown in Figure 5.16. The link, of length L, is rigidly attached to a hub of inertia I_H. Here, x is the link axis and w is the transverse displacement of the link's neutral axis from the x-axis.

We define local coordinates by

$$\xi_i = \frac{x - x_{i-1}}{\Delta_i}, \quad \Delta_i = x_i - x_{i-1}, \quad x_{i-1} \le x \le x_i \tag{5.83}$$

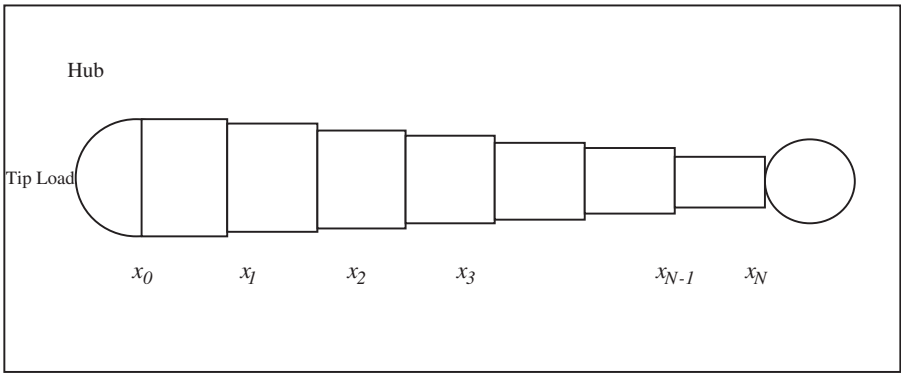

Figure 5.16: Design Model of Segmentized Link.

where

$$\frac{\partial}{\partial x} = \frac{1}{\Delta_i}\frac{\partial}{\partial \xi_i}, \quad \frac{\partial}{\partial x^2} = \frac{1}{\Delta_i^2}\frac{\partial^2}{\partial \xi_i^2}, \quad \sum_{i=1}^{N} \Delta_i = L \tag{5.84}$$

The bending rigidity and linear mass density of segment i are defined, respectively, as $\beta_i = (EI)_i$ and $\gamma_i = (\rho A)_i$. Now each segment must satisfy the following four boundary conditions [29]:

1. Displacement must be continuous at $\xi_{i-1} = 1$ and $\xi_i = 0$:

$$v_{i-1}(\xi_{i-1}) = v_i(\xi_i) \tag{5.85}$$

2. The first derivative must be continuous at $\xi_{i-1} = 1$ and $\xi_i = 0$:

$$\frac{1}{\Delta_{i-1}}\frac{\partial v_{i-1}(\xi_{i-1})}{\partial \xi_{i-1}} = \frac{1}{\Delta_i}\frac{\partial v_i(\xi_i)}{\partial \xi_i} \tag{5.86}$$

3. Bending moments must be equal at $\xi_{i-1} = 1$ and $\xi_i = 0$:

$$\frac{\beta_{i-1}}{\Delta_{i-1}^2}\frac{\partial^2 v_{i-1}(\xi_{i-1})}{\partial \xi_{i-1}^2} = \frac{\beta_i}{\Delta_i^2}\frac{\partial^2 v_i(\xi_i)}{\partial \xi_i^2} \tag{5.87}$$

4. Shearing forces must be equal at $\xi_{i-1} = 1$ and $\xi_i = 0$:

$$\frac{\beta_{i-1}}{\Delta_{i-1}^3}\frac{\partial^3 v_{i-1}(\xi_{i-1})}{\partial \xi_{i-1}^3} = \frac{\beta_i}{\Delta_i^3}\frac{\partial^3 v_i(\xi_i)}{\partial \xi_i^3} \tag{5.88}$$

Using the dynamics equation of vibration, Eq. (5.56):

$$\frac{\partial^4 v_i(\xi_i)}{\partial \xi_i^4} - k_i^4 v_i(\xi_i) = 0, \quad \text{where} \quad k_i^4 = \frac{\gamma_i \Delta_i^4}{\beta_i}\omega^2 \tag{5.89}$$

The solution is given by

$$v_i^{(j)}(\xi_i) = \phi_{ij} C_i \tag{5.90}$$

where

$$C_i = [\, C_{0i} \quad C_{1i} \quad C_{2i} \quad C_{3i} \,]^T \quad (C_{mn} = \text{constant})$$

$$\phi_{i0} = [\sin(k_i\xi_i) \quad \sinh(k_i\xi_i) \quad \cos(k_i\xi_i) \quad \cosh(k_i\xi_i)]$$

$$\phi_{i1} = \phi'_{i0} \quad \phi_{i2} = \phi'_{i1} \quad \phi_{i3} = \phi'_{i2} \quad \phi_{i4} = k_i^4 \phi'_{i0}$$

The torque equation and boundary conditions, Eqs (5.57)–(5.60), become

$$[I_H \omega^2 \Delta_1 \phi_{11}(0) + \beta_1 k_1 \phi_{12}(0)] C_1 = 0, \qquad \phi_{10}(0) C_1 = 0 \tag{5.91}$$

$$[\beta_N k_N^2 \phi_{N2}(k_N) - I_p \omega^2 \Delta_N k_N \phi_{N1}(k_N) - a_c M_p \omega^2 \Delta_N^2 \phi_{N0}(k_N)] C_N = 0 \tag{5.92}$$

$$[\beta_N k_N^3 \phi_{N3}(k_N) + a_c M_p \omega^2 k_N \Delta_N^2 \phi_{N1}(k_N) + M_p \omega^2 \Delta_N^3 \phi_{N0}(k_N)] C_N = 0 \tag{5.93}$$

Reformulating the interfacial relations, Eqs (5.85)–(5.88), into transfer matrices:

$$C_i = \psi^{-1} M_{i-1} C_{i-1} \tag{5.94}$$

where

$$\psi = \begin{bmatrix} 0 & 0 & 1 & 1 \\ 1 & 1 & 0 & 0 \\ 0 & 0 & -1 & 1 \\ -1 & 1 & 0 & 0 \end{bmatrix}, \quad M_j = \begin{bmatrix} sn_j & sh_j & cs_j & ch_j \\ \tau_j cs_j & \tau_j ch_j & -\tau_j sn_j & \tau_j sh_j \\ -\gamma_j sn_j & \gamma_j sh_j & -\gamma_j cs_j & \gamma_j ch_j \\ -\theta_j cs_j & \theta_j ch_j & \theta_j sn_j & \theta_j sh_j \end{bmatrix} \tag{5.95}$$

$$sn_j = \sin(k_j\xi_j), \quad sh_j = \sinh(k_j\xi_j), \quad cs_j = \cos(k_j\xi_j), \quad ch_j = \cosh(k_j\xi_j)$$

$$\tau_j = \frac{k_j}{k_{j+1}}, \quad \delta_j = \frac{\Delta_{j-1}}{\Delta_j}, \quad T_j = \frac{\beta_j}{\beta_{j-1}}, \quad \gamma_j = \frac{\tau_j^2}{\tau_{j+1}\delta_{j+1}^2}, \quad \theta_j = \frac{\tau_j^3}{\tau_{j+1}\delta_{j+1}^3}$$

Relating the interior coefficient vectors, Eq. (5.94):

$$C_i = \phi_{i-1} C_{i-1}, \quad \phi_i = \psi^{-1} M_i \tag{5.96}$$

and the endpoint coefficient vector relation can now be expressed as

$$C_N = \phi C_1, \quad \text{where } \phi = \prod_{N-1}^{1} \phi_i \tag{5.97}$$

Substitution of C_N into the boundary equations, Eqs (5.92) and (5.93), gives

$$QC_1 = 0 \tag{5.98}$$

where

$$Q = \begin{bmatrix} 0 & 0 & 1 & 1 \\ I_H \Delta_1 \omega^2 & I_H \Delta_1 \omega^2 & -\beta_1 k_1 & \beta_1 k_1 \\ & R_1 \phi & & \\ & R_2 \phi & & \end{bmatrix} \tag{5.99}$$

Here, R_1 and R_2 are the matrix coefficients of C_N in Eqs (5.92) and (5.93) respectively. Requiring the determinant of Q to be zero gives the frequency of the link. The maximum speed design problem becomes

$$\begin{aligned} &\max \omega(X_\beta, X_\gamma; \Xi) \quad \text{subject to} \\ &\Delta X_\gamma^T = M_T, \quad X_\gamma^L \le X_\gamma \le X_\gamma^U, \quad X_\beta^L \le X_\beta \le X_\beta^U \end{aligned} \tag{5.100}$$

where $X_\beta = [\beta_1, \beta_2, \ldots, \beta_N]$, $X_\gamma = [\gamma_1, \gamma_2, \ldots, \gamma_N]$, $\Xi = [I_H, M_p, a_c, I_p]$, $\Delta = [\Delta_1, \Delta_2, \ldots, \Delta_N]$, and M_T is the total link mass.

Segmentized Optimization Solutions

The solution to the segmentized formulation can be achieved through the use of a number of mathematical programming methods. Here, two particular methods are presented: a dynamic programming (DP) algorithm and an adaptive random search algorithm (IHR).

Dynamic Programming Solution

The DP algorithm has been developed explicitly for this problem, considering the previous optimum results in Section 5.4.3. Knowledge of the optimum shapes generated by the iterative solution can simplify the algorithm considerably. Perhaps the most useful observation is that the optimum shape is monotonically decreasing towards the tip load. Of course, the constant-volume constraint must always be satisfied.

These heuristics have been successfully integrated into a DP algorithm where the stages are represented by the number of segments in the current design, and the states at each stage are

all admissible combinations of segment areas [30]. The general algorithm is presented below:

1. Set the tolerance of ω_{opt}.
2. Set the link parameters to the desired values.
3. Set the number of links, N, to 1.
4. Find $\omega_{opt}(1)$.
5. Set $N = 2N$.
6. Find $\omega_{opt}(N)$.
7. If tolerance is met, stop. Else, go to Step 5.

Here, Step 4 finds the uniform link frequency corresponding to the prescribed parameter values using equal segment lengths. Step 6 is obviously the crucial element in the algorithm. First, consider a two-segment link. Since we know that in the optimum design, the area of segment 1 must be greater than or equal to that of segment 2, we begin by incrementing the area of segment 1 and decrementing the area of segment 2 by the same amount. This way the total volume will stay constant as required. So the areas are changed slowly until a peak in ω is reached. For a two-segment design, this will be optimal. If the tolerance of ω_{opt} has not been reached, the link will be divided into four segments. Then segments 3 and 4 are optimized, after which segments 1 and 2 are optimized. One of the drawbacks to the above algorithm is that the number of links must double on each iteration of Steps 5–7, since an even number of equal segments cannot be split into an odd number of equal segments.

Here, a constant ρ and E are assumed. Also, the moment–area relation, Eq. (5.62), for circular cross-sections has been used. In Step 4, area $A = M_T/(\rho L)$. In successive steps, A is kept constant by the balanced increments described above. This will ensure a constant volume. The above algorithm works very well because the fundamental frequency of vibration ω is a smooth function of area increments, as can be seen in Figure 5.17. The figure on the left results from splitting a two-segment link, while the figure on the right is due to the splitting of segments 7 and 8 in an eight-segment design.

Adaptive Random Search Solution

The IHR algorithm will now be considered. This algorithm is a slight modification of the Improving Hit and Run algorithm recently developed by Zabinsky et al. [31]. The modification of the algorithm was necessary to ensure a constant volume during the optimization process. The modified IHR algorithm is:

1. Set design vector $\Xi = [I_H, M_p, a_c, I_p]$ and number of segments, N. Set step multiplier MUL to 1 and FACTOR to 8.
2. Calculate ω_0 (frequency for uniform link).
3. Set minimum and maximum area constraints, A_{min} and A_{max}. Set $j = 1$.

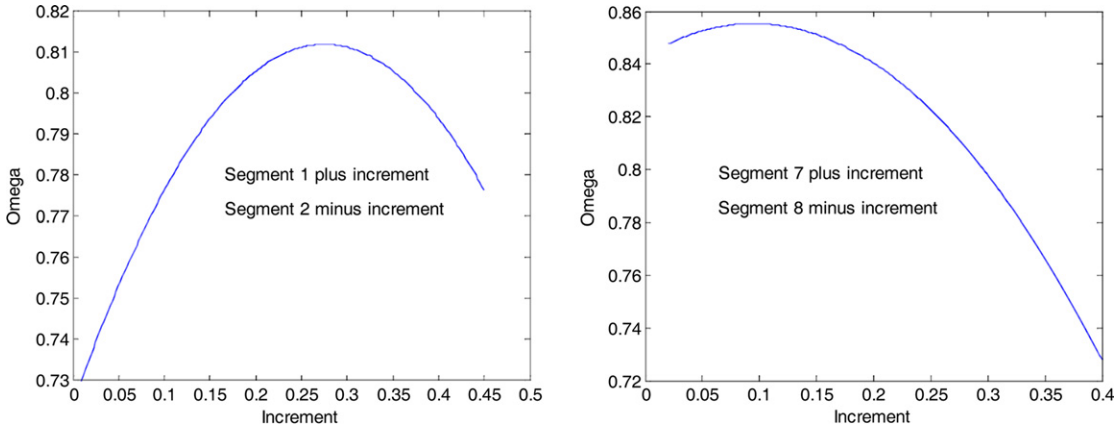

Figure 5.17: ω vs. Segment Increments.

4. Randomly select $N/2$ of the N segments and mark them with a 1 in vector D_j of length N. Mark the remaining $N/2$ segments with a -1. If N is odd, one randomly selected area will remain constant and will be marked by a 0.
5. Get $N/2$ samples from an $N(0,1)$ normal distribution and place them in each position of D_j where there is a 1. Place the negatives of this same sample in each position of D_j where there is a -1. This arrangement will ensure a constant volume during optimization. Here, D_j is called the direction vector.
6. Generate a step size, S_j, uniformly from L_j, the set of feasible step sizes in the direction D_j, where

$$L_j = \{S_j \in \Re : A_{\min} < A_j + S_j D_j < A_{\max}\}$$

$$\text{If } L_j = 0, \quad \text{go to Step 4.}$$

7. Set $S_j = S_j * \text{MUL}$ while $|\text{MUL}| < 1$.
8. Update the area vector, A; if the frequency is improving:

$$A_{j+1} = \left\{ \frac{A_j + S_j D_j \quad \text{if } \omega(A_j + S_j D_j) > \omega_j}{A_j \qquad \text{otherwise}} \right\}$$

$$\text{Set } \omega_{j+1} = \omega(A_{j+1}).$$

9. If ω_{j+1}/ω_j, set $\text{TRIM} = \dfrac{|\omega_{j+1} - \omega_j|}{\omega_j} * \text{FACTOR}$ and $\text{MUL} = \text{MUL} - \text{MUL} * \text{TRIM}$.
10. If the stopping criteria are met, stop. Otherwise, increment j and go to Step 4.

Notice that the area function A_j is not updated unless the frequency is improving. Also, the step size S_j is adapted to the proportional increase in frequency when ω is improving through

the use of MUL, which is set in Step 9. Thus, as the segmentized shape approaches its optimum, the segment areas will change less and less. This is highly desirable since it eliminates the high fluctuations in the random direction vector D_j as the design approaches optimality.

Numerical Results and Discussion

In Figure 5.19, the optimum shapes and frequencies are given for one-, two-, four-, and eight-segment designs. The segmentized shapes were produced by the above DP algorithm with design vector $\Xi = [10,10,0.05,0.1]$. The corresponding optimum shape from Section 5.4.3 has been overlaid for comparison purposes. This particular example was chosen because of its highly nonlinear shape. Here, with only eight segments, the segmentized frequency is within 1% of optimum! Generally, most designs can be approximated very closely with only a few segments ($N < 10$).

One obvious goal is to have the analytic design of Section 5.4.3 and the optimization design presented above agree with each other, i.e. the same shape should produce a similar frequency. To accomplish this comparison, the optimum shape α_{opt} and frequency λ_{opt} were computed using the iterative solution of Section 5.3.3 for two different designs as specified in Figure 5.7. Then, α_{opt} was converted to an area function using Eq. (5.63), which was then used to approximate the area of each segment at its midpoint. The segmentized frequency was then computed for $N = 1$ to 25. The results can be seen in Figure 5.18. Here, the first frequency, $N = 1$, is for the uniform link corresponding to the chosen design parameters. It is also apparent here that the segmentized frequency rapidly approaches that of the analytic optimum.

The IHR results are also very impressive. Obviously, the number of required iterations will be somewhat higher than that of the DP algorithm, depending on the number of segments in the design. One advantage of the IHR algorithm is that it is a truly impartial optimization process.

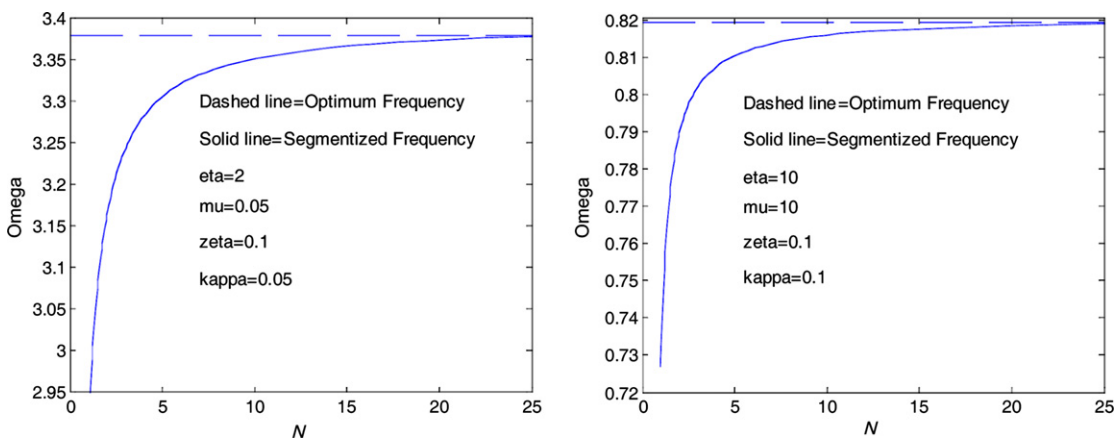

Figure 5.18: ω_{opt} vs. N.

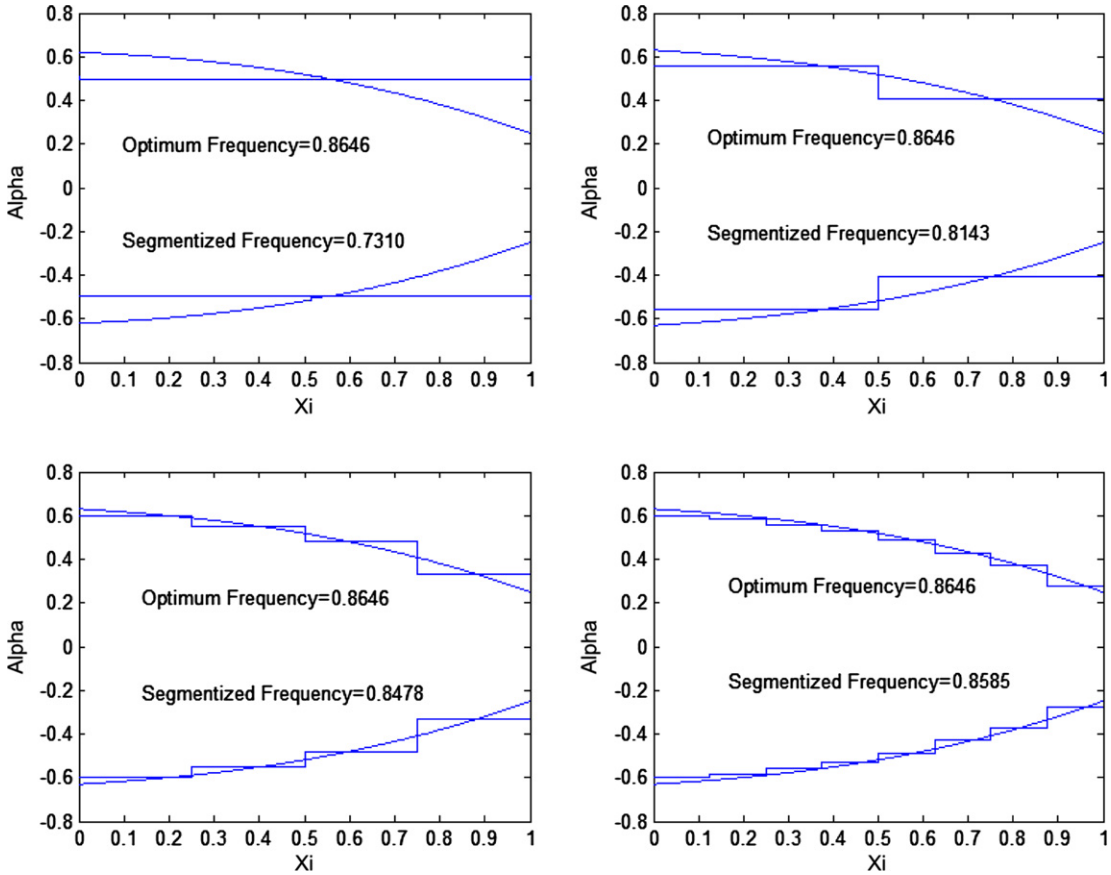

Figure 5.19: DP Optimum Shapes for $N = 1, 2, 4$, and 8.

That is, the segment area increments are chosen randomly in each iteration. Thus, this gives us yet one more valuable tool in comparing the merit of the other optimization processes.

The IHR algorithm has been tested on two-, four-, and eight-segment designs, and the results are very good. The average number of iterations needed to achieve 1% accuracy compared with the DP solution of Figure 5.19 is only 6 for a two-segment design. For a four-segment design the required number of iterations is 27 and for an eight-segment design the required number of iterations is 138. Figure 5.20 gives the results of the IHR solution using the same design vector as the DP solution shown in Figure 5.19.

Both the DP and IHR algorithms lend themselves readily to the incorporation of constraints into the design. Two common constraints are maximum and minimum area. Indeed, these are required in the IHR algorithm to compute the step size. One important constrained design is that of the circular tunnel cross-section. This shape gives a very high rigidity factor with a smaller total mass. An added bonus is that the arm is hollow so that control cables and even

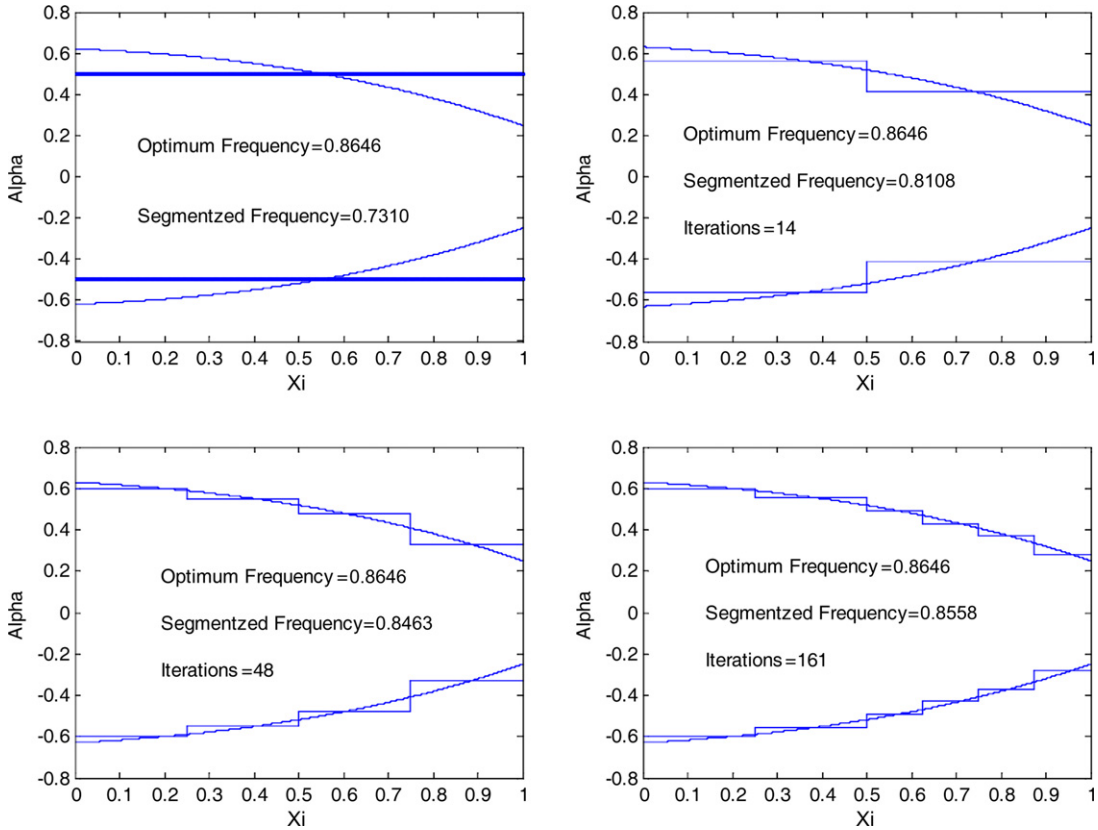

Figure 5.20: IHR Optimum Shapes for $N = 1, 2, 4$, and 8.

mechanical drives can be located here inside the link. This is also the most commonly used design in the new composite links, which promise to be exceptionally useful. For optimization results of the circular tunnel cross-section and composite design implementations, see Russell [17].

5.3.5 Multiple Tip Load and Multiple Link Optimum Designs

Most manipulators must be multifunctional, which usually translates to handling multiple-sized tip loads. An optimum design model for this case is presented along with numerical results and discussions. A two-link optimum model is then given and implemented using the single-link analytic model.

Minimax Optimum Design

In most cases, a flexible manipulator has to perform tasks in different situations, particularly with different tip loads. This is reflected by different values of vector Ξ. Results from

Section 5.4.3 indicate that the fundamental frequency of vibration varies dramatically with a change in tip load parameters. This naturally leads to the question of what is an "optimum" design for a manipulator dealing with multiple task situations? Consider the case of a finite number of task situations, i.e. $\Xi \in \{\Xi_1, \ldots, \Xi_n\}$. Ξ is defined in Eq. (5.100).

Using the segmentized formulation of Section 5.4.4, the maximum speed design problem for multiple tip loads can be formulated as

$$\max_{z} \sum_{k=1}^{n} \omega_k f(X_\gamma, X_\beta, \Xi_k) \tag{5.101}$$

$$\text{subject to} \quad \Delta X_\gamma^T = \gamma_s, \qquad Z^L \le X_\beta \le X_\beta^U$$

$$X_\gamma^L \le X_\gamma \le X_\gamma^U, \qquad X_\beta^L \le X_\beta \le X_\beta^U \tag{5.102}$$

where $\Sigma_{k=1}^{n} \omega_k = 1$, and $\omega_i = 1$ represents the weight assigned to situation i. For circular cross-sections, X_γ and X_β can be expressed as functions of an independent design vector Z.

In particular, if we choose $\omega_i = 1$ when $f(X_\alpha, X_\beta; \Xi_k) = \min_{1 \le k \le n} f(X_\alpha, X_\beta; \Xi_k)$ $\omega_i = 0$ when $k \ne i$, then Eqs (5.101) and (5.102) constitute the minimax design formulation [32], i.e. the objective is to *maximize the worst-case fundamental frequency.*

To illustrate the minimax design procedure, an example will be solved where $\Xi = [\Xi_1, \Xi_2, \Xi_3]$, $\Xi_1 = [10, 0.1, 0.1, 0.1]$, $\Xi_2 = [10, 0.01, 0.1, 0.15]$, $\Xi_3 = [10, 0.27, 0.2, 0.05]$. The optimal shapes for the two-segment design corresponding to Ξ_1, Ξ_2, Ξ_3 are Shape 1, Shape 2, and Shape 3. These are shown in Figure 5.21. $Shape_M$ is the minimax design shape. This example is particularly illustrative because the three shape frequencies can be plotted versus the segment increment (see Figure 5.22). The minimax design is specified by the intersection of the ω_2 and ω_3 plots.

Note that the frequency of the minimax design will always be less than or equal to the maximum of the shape with the minimum frequency. Equality only holds when the frequencies of the other shapes lie above this lowest frequency. When using the minimax design in practice, the average tip load will be specified along with upper and lower bounds in the usable range. These values will be used to select the weights ω_i, with the weight corresponding to the average expected tip load being the largest. Once the minimax design vectors and weights have been specified, either the DP or IHR algorithm can be used to find the solution to Eqs (5.101) and (5.102) by searching all combinations of shapes and design vectors.

Two-link Optimum Design

Since a single-link manipulator has few practical applications, a two-link flexible manipulator will now be considered. The optimization model will be based on the single-link solutions presented in Section 5.4.3. Figure 5.23 gives a view of the design model, which is composed

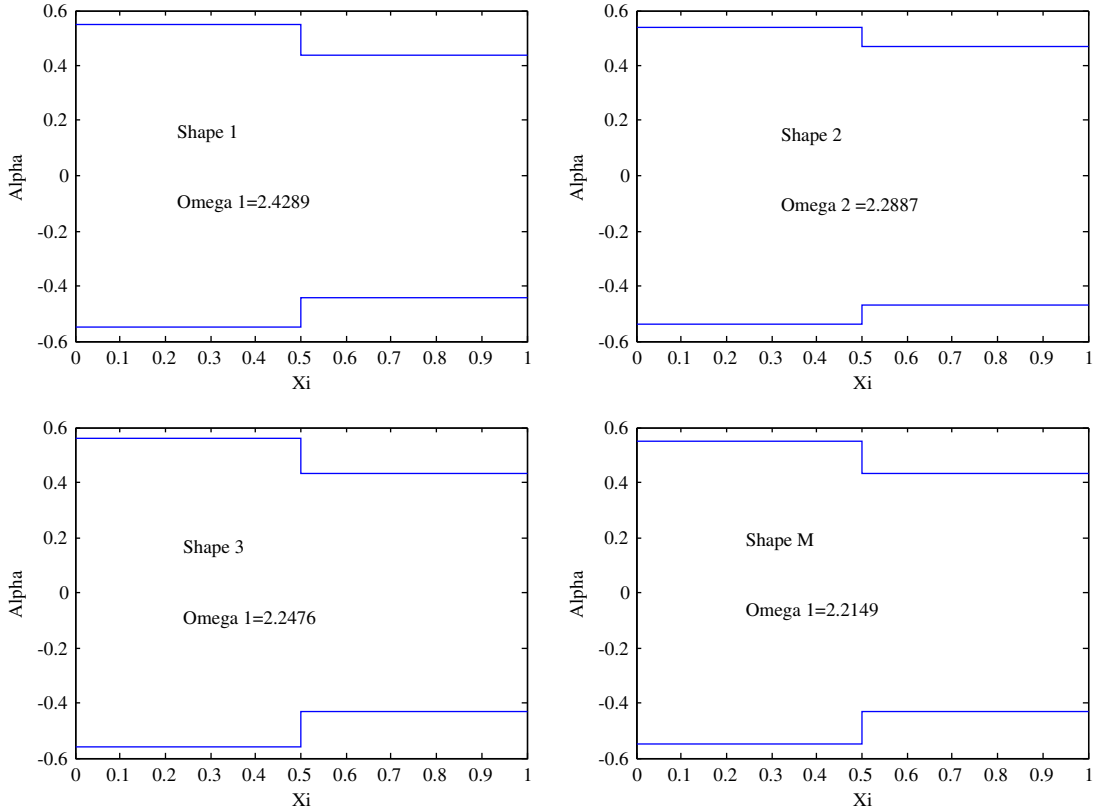

Figure 5.21: Optimum Shapes for Minimax Design.

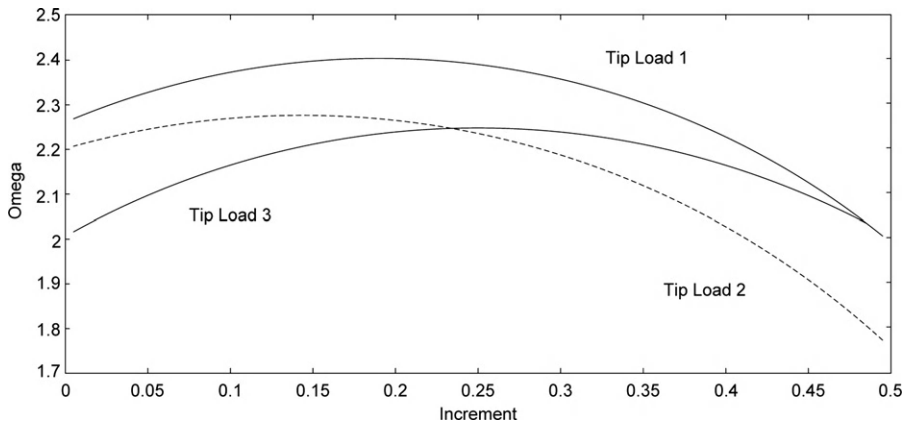

Figure 5.22: Omega vs. Increment.

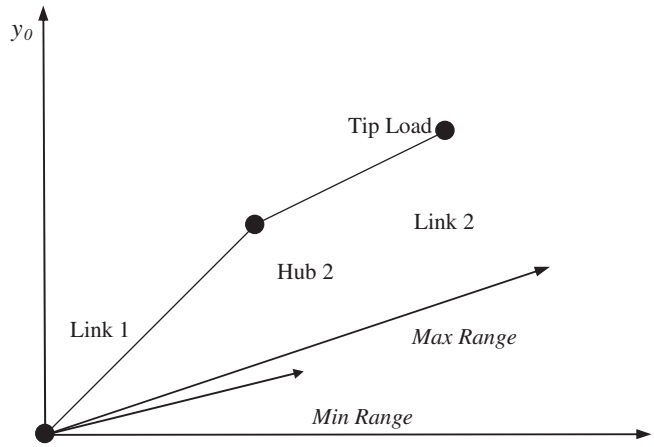

Figure 5.23: Two-Link Design Model of Flexible Manipulator.

of two flexible links, Link 1 and Link 2, having respective masses M_1 and M_2. Link 1 has length L_1, while Link 2 has length L_2. Link 1 is rigidly attached to a hub H_1 at its base. Link 2 is also rigidly attached to a hub H_2 at its base, and this same hub is attached to an axis at the endpoint of Link 1. The working tip load is positioned at the endpoint of Link 2 with the normal tip load parameters given previously.

The general specifications for a two-link manipulator are its total mass M_T and its working range, which must satisfy the following requirements:

$$L_1 + L_2 = MaxRange$$
$$|L_1 - L_2| \leq MinRange$$
$$M_1 + M_2 = M_T$$

Note that although the total mass and working range are given as specifications, there is a choice of mass and length distribution between the two links. Thus, both the mass and length distribution become design variables in the optimization process. It is straightforward to place constraints on these variables in this optimization process.

The tip load and hub parameters for Link 1 are specified by

$$\eta_1 = \frac{I_{H1}}{M_1 L_1^2}, \quad \mu_1 = \frac{M_2 + M_P + M_{H2}}{M_1}, \quad \zeta_1 = \frac{L_2}{2L_1} \tag{5.103}$$

$$k_1 = \frac{1}{12} M_2 L_2^2 + \left(\frac{L_2}{2}\right)^2 M_P + \left(\frac{L_2}{2}\right)^2 M_{H2} \tag{5.104}$$

where M_{H2} is the mass of Hub 2. The moment k_1 is approximated by the moment of inertia of Link 2, including Hub 2 and the tip load about its center of mass, which was assumed to be at

$L^2/2$. The center of mass could be more accurately calculated numerically by using M_2 and the current shape function α for Link 2. But this would drastically increase the computation time, which is already large. The tip load and hub parameters for Link 2 are specified by

$$\eta_2 = \frac{I_{H2}}{M_1 L_2^2}, \quad \mu_2 = \frac{M_P}{M_2}, \quad \zeta_2 = \frac{a_c}{L_2}, \quad k_2 = \frac{I_P}{M_2 L_2^2} \tag{5.105}$$

The optimization scheme is:

1. Initialize $L_1 = L_2$ and $M_1 = M_2$.
2. Optimize Link 2 using its tip load and Hub 2.
3. Optimize Link 1 using Hub 1 and Link 2 as its tip load.
4. Error $= |Freq1 - Freq2|$.
5. Change mass distribution and go to Step 2 if tolerance is not met.
6. Change length distribution and reset $M_1 = M_2$. Go to Step 2 if tolerance is not met.

Since the speed of the manipulator will be limited by the lowest fundamental frequency of vibration of either Link 1 or 2, the best possible system frequency occurs when $\omega_1 = \omega_2$. As can be expected from the previous analysis in Section 5.4.3, the large values of μ_1, ζ_1, and k_1 will require more mass to be placed in Link 1 when $L_1 = L_2$. We could also expect Link 1 to be shorter in length than Link 2. Both a shorter length and a higher mass would increase the fundamental frequency of vibration of Link 1.

In the following results, it should be remembered that the analytical optimum of Section 5.4.3 is based on small deformations. Thus, this optimization scheme yields only an approximation of the actual governing system fundamental frequency of vibration. The amount of variation will depend upon material characteristics, as well as the average relative angular position of Link 2 relative to Link 1. Figure 5.24 gives the optimum design for a specified total mass and working range. The following values were used in the optimization process:

$$MaxRange = 1\text{ m}, \quad MinRange = 0.3\text{ m}, \quad M_T = 10\text{ kg}, \quad I_{H1} = 20\text{ kgm}^2, \quad I_{H2} = 4\text{ kgm}^2,$$
$$E = 6.06\text{e}10\text{ N/m}^2, \quad \text{density} = 70\text{ kg/m}^3, \quad \text{and} \quad \Xi = [20, 0.5, 0.02, 0.5]$$

5.3.6 Sensitivity Analysis

A variation in the hub inertia, or more likely in the tip load, will induce a corresponding change in the frequency of the link. For the purpose of link design, it is extremely important to know how sensitive the optimal frequency is with respect to changes in the design vector, D. For the optimal fundamental frequency λ_{opt}, from Eq. (5.66), a variation of λ_{opt} due to small changes in η, μ, ζ, and k can expressed as

$$\frac{\delta\lambda_{\text{opt}}}{\lambda_{\text{opt}}} = -S_\eta \frac{\delta\eta}{\eta} - S_\mu \frac{\delta\mu}{\mu} - S_{\mu\zeta} \frac{\delta(\mu\zeta)}{\mu\zeta} - S_k \frac{\delta k}{k} \tag{5.106}$$

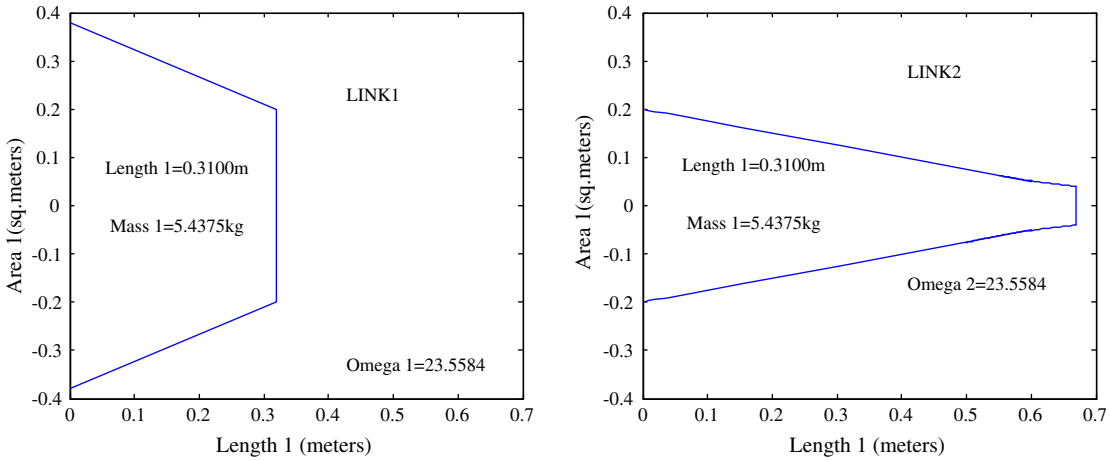

Figure 5.24: Optimum Shapes for Two-Link Design.

where sensitivity indices can be calculated according to

$$(S_\eta, S_\mu, S_{\mu\zeta}, S_k) = \frac{(\eta v'(0)^2, \mu v(1)^2, 2\zeta\mu v(1)v'(1), kv'(1)^2)}{\int_0^1 \alpha v^2 d\xi + \eta v'(0)^2 + \mu v(1)^2 + 2\zeta\mu v(1)v'(1) + kv'(1)^2} \tag{5.107}$$

Note that although $\delta\eta$, $\delta\mu$, $\delta\zeta$, and δ_k generate corresponding variations δv and $\delta\alpha$, these variations will not affect the value of λ_f when small terms of order 2 or higher are ignored, since λ_f arrives at one of its stationary values at v_{opt} and α_{opt}. This is why we do not need to consider the variations of v and α. It should be pointed out that sensitivity indices can also be formally defined as follows:

$$S_x = -\frac{\%\text{change in } \lambda}{\%\text{change in } x} = -\frac{\delta\lambda/\lambda}{\delta x/x} = -\frac{x}{\lambda}\frac{\delta\lambda}{\delta x}, \quad x = \eta,\ \mu,\ \mu\zeta,\ k \tag{5.108}$$

Clearly, from Eq. (5.107), $0 \le S_x \le 1$; therefore, *the vibration frequency always decreases as system parameters increase in value*, a conclusion that has been verified by numerical analysis (see Figure 5.13). Using Eqs (5.106) and (5.107), one can find the actual numerical values of sensitivity indices for any particular optimum shape design. In this section, numerical analysis is used to investigate the sensitivity of an optimum design to variations in $D = [\eta,\mu,\zeta,k]$.

In Figure 5.25, the frequency response to variations in particular design parameters is given. The optimum design vector is $D = [4,0.1,0.1,0.05]$, which generates an optimum frequency, $\lambda_{\text{out}} = 9.4331$. Note that the frequency is particularly sensitive to η and k. It is somewhat less sensitive to μ and almost completely insensitive to ζ.

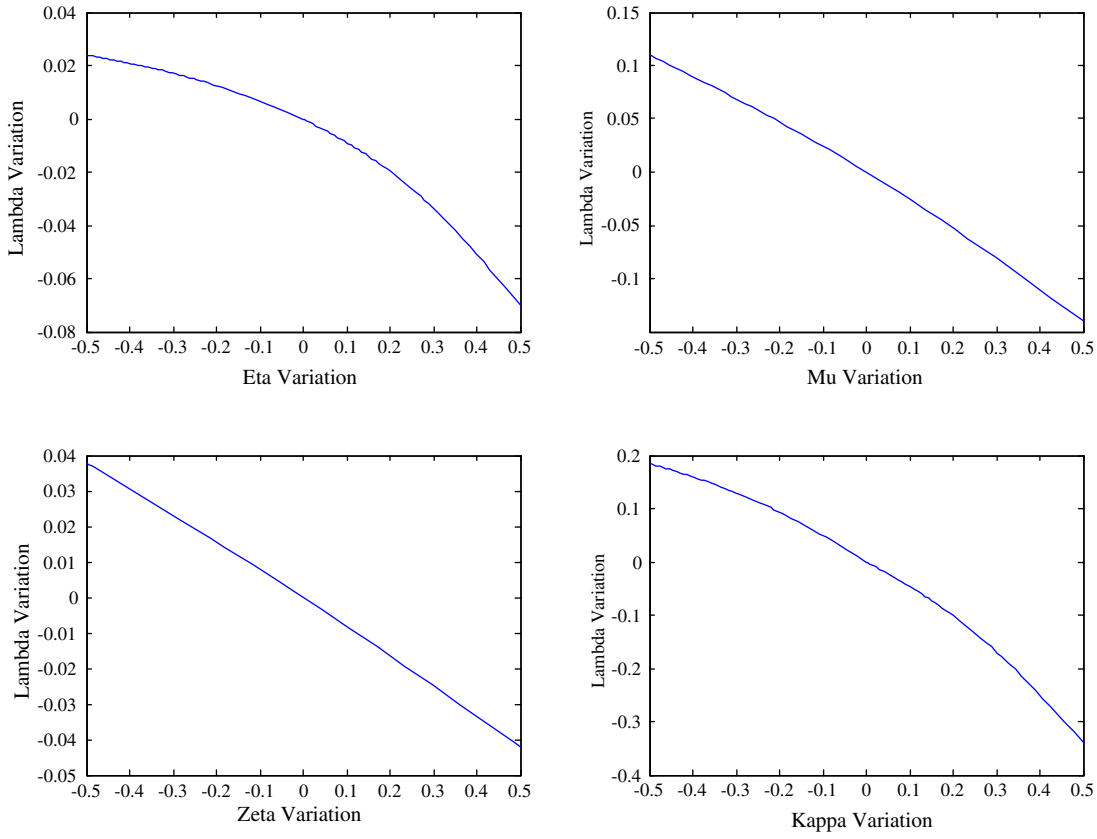

Figure 5.25: $\delta\lambda/\lambda_{out}$ **vs.** $\delta X/X_{out}$.

5.4 Optimum Shape Construction with Total Weight Constraint

In this section we consider the optimum shape design problem of flexible manipulators carrying tip loads [33]. A tip load is characterized by its mass, moment of inertia, and position of the center of mass. Furthermore, to avoid the design of optimum shapes that are not acceptable for some real applications, we also investigate the constrained optimum shape design problem by imposing both upper and lower bounds on the shape of flexible manipulators. Nonlinear programming methods are used to solve the constrained design problem. The preliminary results with these considerations have been reported in Wang and Russell [28].

5.4.1 Basic Equations and the Variation Formulation

The flexible manipulator is modeled as a flexible beam fixed on a rigid hub with rotational inertia I_H in the horizontal plane. Based on different beam bending theories, different dynamic

models can be established for the flexible manipulator. A comprehensive study of the influence of rotary inertia, shear deformation, and tip load on vibration behavior of flexible manipulators has been conducted by Wang and Guan [16] using the results derived from three different dynamic models, i.e. the Euler−Bernoulli model, the Euler−Bernoulli model with rotary inertia, and the Timoshenko model. The first model neglects the effect of both rotary inertia and shear deformation, the second considers only rotary inertia, while the third takes both into account. Asymptotic analysis and numerical computations indicate that the effect of shear deformation cannot be ignored for high-order vibration frequencies. However, for the fundamental vibration frequency, the study has shown that both rotary inertia and shear deformation have very little influence and thus can be neglected. Since we only need the fundamental frequency in optimum shape design, here we will use the Euler−Bernoulli model to describe the vibration of the flexible manipulator. Accordingly, the governing equation of harmonic vibration and the boundary conditions can be written as follows [16,25]:

$$(EIv'')'' - \rho A\omega^2 v = 0 \tag{5.109}$$

$$v(0) = 0, \quad \mathrm{I_H}\omega^2 v'(0) + EIv''(0) = 0 \tag{5.110}$$

$$EIv''(L) - J_p\omega^2 v'(L) - a_c M_p \omega^2 v(L) = 0 \tag{5.111}$$

$$(EIv'')'(L) + a_c M_p \omega^2 v'(L) + M_p \omega^2 v(L) = 0 \tag{5.112}$$

where v is the total displacement of the beam ($v = w(x) + x\theta$), w is beam deflection, θ is hub rotation, ω is the natural vibration frequency, EI is the bending rigidity, A is the area of cross-section, ρ is the mass density per unit volume, L is the length, and M_p, J_p, a_c are the mass, moment of inertia and x-coordinate (with respect to the beam tip) of the center of mass of the tip load respectively. A prime indicates differentiation with respect to the coordinate x along the longitudinal axis of the beam. Note that a_c represents the position effect of the tip load. When a_c is set to zero, Eqs (5.109)−(5.112) are the same as the corresponding equations developed in Ref. [25].

To find the optimal shape, which for a given total weight will maximize the fundamental frequency of the flexible manipulator, we need to have an explicit expression for w from Eqs (5.109)−(5.112). To this end, we multiply both sides of (5.109) by v and integrate it over $0 \le x \le L$. After several steps of integrating by parts and taking the boundary conditions (5.111) and (5.112) into account, we find

$$\omega^2 = \frac{\int_0^L Elv''^2 \mathrm{d}x}{\int_0^L \rho A v^2 \mathrm{d}x + I_H v'(0)^2 + G(L)}$$

where

$$G(L) = M_p v(L)^2 + 2a_c M_p v(L) v'(L) + J_p v'(L)^2 \tag{5.113}$$

Since the fundamental frequency is the smallest frequency among all the natural vibration frequencies, the following must be true for the fundamental frequency:

$$\omega = \min_v \frac{\int_0^L EIv''^2 \mathrm{d}x}{\int_0^L \rho A v \mathrm{d}x + Iv'(0) + G(L)} \tag{5.114}$$

where v is any admissible displacement function.

On the other hand, by variational calculus it is straightforward to show that if v satisfies only the geometric boundary condition $v(0) = 0$ and is the solution of the variational problem (5.114), then it must satisfy all equations in (5.109)–(5.112). Therefore, the variational problem (5.114) and Eqs (5.109)–(5.112) are equivalent. The variational form (5.114) will serve as the basis for the problem of optimum shape design of the flexible manipulator.

To facilitate our discussion, we will assume the following relationship between the moment I and the area A of the cross-section of the beam:

$$I(x) = \gamma A^p(x), \quad p \geq 1 \tag{5.115}$$

where γ is a shape constant. Three cases, namely $p = 1$, 2, and 3, are of special interest since they correspond to beams with rectangular cross-sections of given uniform height, geometrically similar cross-sections, and rectangular cross-sections of given uniform width respectively. Many similar sections can be classified as geometrically similar sections, for example hollow circular or rectangular sections when all their inner and outer radii or widths and heights vary proportionally to a single variable. Note that this includes the case of solid circular or rectangular sections, which should emphasize the relationship (5.115). This is not essential in our treatment. As we will see in Section 5.5.3, the optimization method proposed there can handle any relationship between I and A.

Using (5.115), the problem of optimum shape design can now be formulated as a variational problem in the following dimensionless form:

$$\lambda = \max_\alpha \min_v \frac{\int_0^1 \alpha^p v''^2 \mathrm{d}\xi}{\int_0^1 \alpha v^2 \mathrm{d}\xi + \eta v(0)^2 + H(1)} \tag{5.116}$$

$$H(1) = \mu v(1)^2 + 2\zeta\mu v(1)v'(1) + \kappa v'(1)^2 \tag{5.117}$$

where a prime indicates differentiation with respect to the dimensionless coordinate $\xi = x/L$. The dimensionless eigenvalue λ, shape function α, hub inertia parameter η, and tip load parameters μ, ζ, κ are defined respectively by

$$\lambda = \frac{\rho^p L^{3+p}}{\gamma E W^{p-1}}\omega^2, \quad \alpha = \frac{\rho L A}{W}, \quad \eta = \frac{I_H}{WL^2} \tag{5.118}$$

$$\mu = \frac{M_p}{W}, \quad \varsigma = \frac{a_c}{L}, \quad \kappa = \frac{J_p}{WL^2} \tag{5.119}$$

in which W is the given total weight (mass) of the beam of the flexible manipulator. From the definition, α must be non-negative and satisfy the following constraint:

$$\int_0^1 \alpha(\xi)\mathrm{d}\xi = 1 \tag{5.120}$$

Equations (5.116)–(5.120) complete the mathematical specification for the optimum shape design problem of flexible manipulators, i.e.

Find the shape function α that satisfies constraint (5.120) along with other possible additional constraints and maximizes eigenvalue λ defined by (5.116).

In the following we will divide our discussion into two parts: the unconstrained and constrained optimum shape design problems.

5.4.2 Analytical Approach of Unconstrained Shape Design

Here we will try to solve the optimum shape design problem analytically without considering additional constraints on shape function α other than the total weight constraint of (5.120). In order to obtain the set of differential equations and boundary conditions for solving the optimum shape design problem, we have to reformulate the optimization problem (5.116) into a completely unconstrained form. This can be achieved by utilizing the Lagrange multiplier technique, i.e. by incorporating constraint (5.116) into variational (5.114) via the following generalized variational equation:

$$\lambda^* = \max_{\alpha} \min_{v} \frac{\int_0^1 \alpha^p v''^2 \mathrm{d}\xi}{\int_0^1 \alpha v^2 \mathrm{d}\xi + \eta v'(0)^2 + H(1) + \sigma\left(\int_0^1 \alpha \mathrm{d}\xi - 1\right)} \tag{5.121}$$

where $v(0) = 0$ and σ is the Lagrange multiplier, which can easily be shown to be a positive number.

The variational problem for optimum design is now unconstrained with respect to variational expression (5.121). After tedious variational calculus, we find that the generalized variational formulation leads to the following Euler equations, along with the corresponding natural boundary conditions:

$$(\alpha^p v'')'' - \lambda\alpha v = 0 \tag{5.122}$$

$$p\alpha^{p-1}(v'')^2 - \lambda v^2 = \lambda\sigma \tag{5.123}$$

$$v(0) = 0, \qquad \alpha^p v''(0) + \lambda\eta v'(0) = 0 \tag{5.124}$$

$$\alpha^p v''(1) - \kappa\lambda v'(1) - \varsigma\mu\lambda v(1) = 0 \tag{5.125}$$

$$(\alpha^p v'')'(1) + \varsigma\mu\lambda v'(1) + \mu\lambda v(1) = 0 \tag{5.126}$$

These equations, together with constraint (5.120), form the complete set of basic equations for solving the optimum shape design problem for a one-link flexible manipulator.

Clearly, the solution of Eq. (5.121) and Eqs (5.122)–(5.126) is not unique, since if $(v,\sigma,\alpha,\lambda)$ is a solution, then $(cv,c^2\sigma,\alpha,\lambda)$ is also a solution for any nonzero constant c. At first glance, the non-uniqueness of a solution may seem to create problems in numerical computation, but it actually offers us a way to completely remove the Lagrange multiplier from (5.123) by selecting $c = 1/\sqrt{\sigma}$. In other words, we only need to find the unknown function $v/\sqrt{\sigma}$ instead of v and σ individually. Therefore, we can assume $\sigma = 1$ in (5.123). As has been found for the optimum design of vibrating cantilever beams [23], this observation eliminates the necessity of finding σ and therefore simplifies the problem substantially.

An important identity can be obtained by multiplying both sides of Eq. (5.122) by v and integrating over $0 \le \xi \le 1$. Integrating by parts and taking the boundary conditions (5.124)–(5.126) into account, we have after applying (5.123):

$$\int_0^1 \alpha(\xi)\mathrm{d}\xi = (p-1)\int_0^1 \alpha(\xi)v(\xi)^2\mathrm{d}\xi + p[\eta v'(0)^2 + H(1)] \tag{5.127}$$

Note that this identity does not require constraint (5.120) to be satisfied. This identify is used for construction of iteration equations in the next section.

Equations (5.120) and (5.122)–(5.126) constitute a nonlinear eigenvalue problem for the frequency parameter λ. Obtaining the optimum shape α of a flexible manipulator is equivalent to finding an α that maximizes the smallest eigenvalue of the problem. Since, in general, the solution of this eigenvalue problem cannot be obtained in closed form, successive iteration schemes are developed to find the solution numerically.

The iteration schemes are based upon formal integration, with the introduction of one of the boundary conditions at each integration. The following two integral formulas are very useful in the construction of the iteration schemes:

$$\int_0^{\xi}\int_0^{x} G(s)\mathrm{d}s\mathrm{d}x = \xi^2\int_0^1 (1-x)G(x\xi)\mathrm{d}x \tag{5.128}$$

$$\int_{\xi}^{1}\int_{x}^{1} G(s)\mathrm{d}s\mathrm{d}x = (1-\xi)^2\int_0^1 xG[\xi + x(1-\xi)]\mathrm{d}x \tag{5.129}$$

Note that compared with double integration, single integration saves computation time and hence is preferred numerically.

Scheme: Case where $p = 1$

For $p = 1$, the function α drops out of (5.123) and we have a degenerate case. Equation (5.127) now becomes

$$\eta v'(0)^2 = \int_0^1 \alpha(\xi)\mathrm{d}\xi - \mu v(1)^2 - 2\varsigma\mu v(1)v'(1) - \kappa v'(1)^2$$

Therefore, if we choose

$$\eta = \frac{1 - \mu v(1)^2 - 2\varsigma\mu v(1)v'(1) - \kappa v'(1)^2}{v'(0)^2} \tag{5.130}$$

then α obtained by solving (5.122) with boundary conditions in Eqs (5.124)–(5.126) must satisfy constraint (5.120) automatically. This observation leads to an inverse approach to solving the optimization problem for $p = 1$. In other words, for a given λ, we determine v and α by solving Eqs (5.122)–(5.126) with η calculated by (5.130). This will establish a relationship between the hub inertia parameter η and the optimum eigenvalue λ, which in turn will enable us to find λ for a given η and tip load parameters, and hence solve the real optimization problem.

To develop a successive iteration scheme, we formally integrate Eqs (5.122) and (5.123) with boundary conditions (5.124)–(5.126). Application of formulas (5.128) and (5.129) leads to

$$v(\xi) = \xi v'(0) + \sqrt{\lambda}\xi^2\int_0^1 (1-x)\sqrt{v^2(x\xi) + 1}\,\mathrm{d}x \tag{5.131}$$

$$\alpha(\xi) = \sqrt{\frac{\lambda}{v^2(\xi)+1}}\left[g(\xi) + (1-\xi)^2 \int_0^1 x\alpha v(\xi + x(1-\xi))\mathrm{d}x\right] \tag{5.132}$$

where $g(\xi) = \kappa v'(1) + \zeta\mu v(1) + \mu(1-\xi)(\zeta v'(1) + v(1))$.

After application of (5.130), the second equation of boundary conditions (5.124) can be replaced by

$$v'(0) = \frac{\mu v(1)^2 + 2\zeta\mu v(1)v'(1) + \kappa v'(1)^2 - 1}{H(1) + \int_0^1 x\alpha(x)v(x)\mathrm{d}x} \tag{5.133}$$

Based on Eqs (5.131)–(5.133), the iteration scheme can be outlined as follows:

1. For a given λ, select initial $v_0'(0)$, $v_0(\xi)$, and $\alpha_0(\xi)$.
2. Update v_i according to

$$v_{i+1}(\xi) = \xi v_i'(0) + \sqrt{\lambda}\xi^2 \int_0^1 (1-x)\sqrt{v_i^2(x\xi)+1}\,\mathrm{d}x$$

3. Update α_i according to

$$\alpha_{i+1}(\xi) = \sqrt{\frac{\lambda}{v_{i+1}^2(\xi)+1}}\left[g(\xi) + (1-\xi)^2 \int_0^2 Z_{i+1}(x,\xi)\mathrm{d}x\right]$$
$$Z_{i+1}(x,\xi) = x\alpha_i v_{i+1}(\xi + x(1-\xi)) \tag{5.134}$$

   where g_i is obtained by replacing v in g by v_i.
4. Update $v_i'(0)$ according to

$$v_{i+1}'(0) = \frac{\mu v_i(1)^2 + 2\zeta\mu v_i(1)v_i'(1) + \kappa v_i'(1)^2}{Y_i + \kappa v_i'(1)^2 + \int_0^1 x\alpha_{i+1}(x)v_{i+1}(x)\mathrm{d}x}$$
$$Y_i = \mu v_i(1)^2 + 2\zeta\mu v_i(1)v_i'(1) \tag{5.135}$$

5. If a given accuracy is not satisfied, go back to Step 2.

Iteration Scheme: Case where p > *1*

In this case, formal integration of (5.122) yields, after satisfying the boundary conditions at $\xi = 1$ and using (5.123):

$$v''(\xi) = \frac{s[v^2(\xi) + 1]^{(p/p+1)}}{\left\{p\beta g(\xi) + p(1-\xi)^2 \int_0^1 Q(x,\xi)\mathrm{d}x\right\}^{(p-1/p+1)}} \tag{5.136}$$

where s is the sign of the denominator and

$$Q(x,\xi) = x\phi_v[\xi + x(1-\xi)]v[\xi + x(1-\xi)] \tag{5.137}$$

$$\alpha(\xi) = \frac{\phi_v}{\beta}, \quad \phi_v(\xi) = \left[\frac{v^2(\xi)+1}{v''^2(\xi)}\right]^{(1/p-1)} \tag{5.138}$$

$$\beta = \left(\frac{p}{\lambda}\right)^{(1/p-1)} = \int_0^1 \phi_v(\xi)\mathrm{d}\xi \tag{5.139}$$

Furthermore, boundary conditions (5.124) can be rewritten as

$$v(0) = 0, \quad v'(0) = -\frac{v''(0)}{p\eta\beta\left|v''(0)\right|^{(2p/p-1)}} \tag{5.140}$$

The expression for $v(\xi)$ is obtained by using standard integration and then applying Eq. (5.128):

$$v(\xi) = v'(0)\xi + \xi^2 \int_0^1 (1-x)v''(x\xi)\mathrm{d}x \tag{5.141}$$

Based on Eqs (5.136)–(5.141) and experience from a previous study [11], an iteration scheme for this case can be suggested as follows:

1. Select an initial β_0 and an initial $v_0''(\xi)$.
2. Update $v_i(\xi)$ according to Eqs (5.140)–(5.141) by using $v_i''(\xi)$ and β_i.
3. Update $v_i''(\xi)$ according to (5.136) by using $v_{i+1}(\xi)$ and $v_i''(\xi)$.
4. Update β_i according to (5.139) by using $v_{i+1}(\xi)$ and $v_{i+1}''(\xi)$.
5. If a specified accuracy is not satisfied, go to Step 2.

After β, v, and v'' have been determined within the specified accuracy, one can find the optimum eigenvalue λ, the function ϕ_v and then the optimum α respectively, according to Eqs (5.138) and (5.139). The linear dimension of the cross-section of the beam is $\alpha^{(1/p)}(\xi)$.

5.4.3 Optimization Approach of Constrained Shape Design

Unconstrained shape design may create some optimal shape functions that are not acceptable for some real applications. For example, the cross-section of the optimal shape may become too small or too large in certain parts of the beam. In practice, this may cause some problems. Small cross-sections may make the beam too weak to support the required load, while large ones may not be allowed by task environments. Therefore, additional constraints such as upper and lower bounds on the shape function may have to be imposed in order to generate a realistic shape design. Introduction of any meaningful constraints, however, would make it impossible to follow the analytical approach described in the previous section. Hence, in this section we will use nonlinear programming methods to solve the constrained shape design problem directly based on the variational form (5.116).

For this purpose, we will approximate v by

$$v(\xi) = \sum_{k=1}^{N_v} v_k \phi_k(\xi) = \phi(\xi) U \tag{5.142}$$

where v_k are real numbers and $\{\phi_k(\xi)\}$ is a set of base functions, $k = 1, \ldots, N_v$. Row base function vector ϕ and column coefficient vector U are defined as

$$\phi(\xi) = (\phi_1(\xi), \ldots, \phi_{N_v}(\xi)), \quad U = (v_1, \ldots, v_{N_v})^T \in R^{N_v}$$

respectively. Each of the base functions can be taken as some modal shape function of vibration, e.g. modal shape functions of flexible manipulators with beams of uniform cross-sections [34]. Obviously, the finite element method can also be used here.

It is clear from (5.116) that λ does not change if we multiply v by an arbitrary nonzero scalar. Therefore, in order to guarantee a unique solution in numerical computation, we will impose the normalization condition. We will impose the normalization condition $\|U\| = 1$ on U. Note that other conditions may also be used and may actually produce a better result.

We will approximate the shape function as a piecewise uniform cross-sectional shape, i.e.

$$\alpha(\xi) = \sum_{k=1}^{N_\alpha} \alpha_k \varepsilon_k(\xi) = \varepsilon(\xi) \Lambda \tag{5.143}$$

where $\alpha_k, \ k = 1, \ldots, N_\alpha$ are positive real numbers and the function ε_k is defined as

$$\varepsilon_k(\xi) = \begin{cases} 1 & \text{for } \xi_{k-1} \le \xi \le \xi_k \\ 0 & \text{otherwise} \end{cases}$$

where $0 = \xi_0 < \xi_1 < \ldots < \xi_{N_\alpha} = 1$ is a division of [0,1]. Row shape function vector ε and column coefficient vector Λ are defined as

$$\varepsilon(\xi) = (\varepsilon_1(\xi), \ldots, \varepsilon_{N_v}(\xi)), \quad \Lambda = (\alpha_1, \ldots, \alpha_{N_v})^T \in R^{N_\alpha}$$

respectively. Of course, other functions such as spline functions can also be used for α.

Let $\Delta = (\xi_1 - \xi_0, \ldots, \xi_{N_\alpha} - \xi_{N_\alpha - 1})^T$, then constraint (5.120) can be written as $\Lambda^T \Delta = 1$. The lower and upper bounds can be imposed on the shape function as

$$\Lambda_L \leq \Lambda \leq \Lambda_U \tag{5.144}$$

where Λ_L and Λ_U are two positive vectors in R^{N_α}.

Nonlinear Programming Method: Single Tip Load

We now consider the case where the manipulator is subject to a single tip load. Substituting approximations (5.142) and (5.143) into Eq. (5.116), we find that the problem of optimum shape design can be reformulated as a constrained nonlinear programming problem:

$$\lambda = \min_{\Lambda} \min_{U} \frac{U^T \Phi(\Lambda) U}{U^T \Omega(\Lambda; d) U} \tag{5.145}$$

subject to

$$\|U\| = 1, \quad \Lambda^T \Delta = 1, \quad \Lambda_L \leq \Lambda \leq \Lambda_U \tag{5.146}$$

where $d = (\mu, \zeta, \kappa)^T$ is the vector of tip load parameters. Λ and Ω are two matrices that can be found from (5.116) as

$$\Phi(\Lambda) = \int_0^1 1(\varepsilon\Lambda)^p \phi''(\xi) \mathrm{d}\xi \tag{5.147}$$

$$\begin{aligned} \Omega(\Lambda; d) = &\int_0^1 \phi(\xi)^T \phi(\xi) \varepsilon(\xi) \Lambda \mathrm{d}\xi + \eta \phi'(0)^T \phi'(0) \\ &+ \mu \phi(1)^T \phi(1) + 2\varsigma\mu \phi(1)^T \phi'(1) + \kappa \phi'(1)^T \phi'(1) \end{aligned} \tag{5.148}$$

Note that both Φ and Ω are positive definitive matrices.

Obviously, Eqs (5.145) and (5.146) do not constitute a standard programming problem (see Ref. [35]), since they involve first a minimization problem with respect to U for given Λ and then a maximization problem with respect to Λ. It is also clear that the standard minimax algorithm in mathematical programming cannot be applied directly (see, e.g., Ref. [36]). But the problem is certainly solvable since we can simply divide it into two optimization problems, though this division may not be an efficient way to solve the problem.

To solve the minimization problem with respect to U, it is not difficult to see that for given Λ and d the result of minimization is equal to the minimum eigenvalue of the following generalized eigenvalue problem:

$$\det[\Phi(\Lambda) - \lambda\Omega(\Lambda;\ d)] = 0 \tag{5.149}$$

Since Ω is a nonsingular matrix, it can easily be reduced to an ordinary eigenvalue problem.

Minimax Design Method: Multiple Tip Loads

In most cases, a flexible manipulator has to perform tasks in different situations, particularly with different values of tip loads. This is reflected by different values of tip load parameter vector d. As we will see later from the numerical results presented in Section 5.5.4, the optimum frequency of a manipulator changes dramatically with the variation in tip load parameters. This naturally leads to the question of what is an "optimal" shape for a manipulator handling multiple tip loads. A reasonable criterion of optimum shape design in this case is to *maximize the worst-case fundamental frequency of the flexible manipulator.* We will consider only the case of a finite number of task situations. Specifically, let $D = \{d_1,\ldots,d_n\}$ be a set of possible values of parameter vector d. Then the problem of optimum shape design in this case can be formulated as a standard minimax problem:

$$\max_{\Lambda}\ \min_{1\le i\le n}\{\lambda_i(\Lambda)\}, \quad \lambda_i(\Lambda) = \min_{U}\ \lambda(\Lambda, U; d_i), \ \ i = 1,\ldots,n \tag{5.150}$$

subject to

$$\|U\| = 1, \quad \Lambda^T\Delta = 1, \quad \Lambda_L \le \Lambda \le \Lambda_U \tag{5.151}$$

where λ_i is actually the minimum eigenvalue of Eq. (5.149) for a given shape Λ and tip load d_i.

Several minimax algorithms may be used to solve this problem. In this paper the Pshenichnyi—Pironneau—Polak algorithm with exact line search (PPP-ELS) [37] has been utilized. This algorithm requires the gradient information of λ_i with respect to Λ, i.e.

$$\frac{\partial\lambda_i}{\partial\Lambda} = (\lambda_{i,1},\ldots,\lambda_{i,N_\alpha}), \quad \lambda_{i,k} = \frac{\partial\lambda_i}{\partial\alpha_k}, \ \ i = 1,\ldots,N_\alpha$$

From Eq. (5.149) it is not difficult to see that the gradient $\lambda_{i,k}$ is the minimum eigenvalue of the generalized eigenvalue problem:

$$\det[\Phi_{\bullet k}(\Lambda) - \lambda_i\Omega_{\bullet k}(\Lambda; d_i) - \Lambda_{i,k}\Omega(\Lambda; d_i)] = 0 \tag{5.152}$$

where

$$\Phi_{,k} = \frac{\partial\Phi}{\partial\alpha_k}, \quad \Omega_{,k} = \frac{\partial\Omega}{\partial\alpha_k}, \quad i = 1,\ldots,N_\alpha$$

Again, since Ω is nonsingular, it can be reduced to an ordinary eigenvalue problem.

Although the optimization approach is an approximate method for solving the optimum shape design problem, it offers several advantages, especially the following:

1. Sophisticated constraints, such as maximum stress restraint, can be included in the optimization formulation.
2. The general relationship between EI and ρA can be considered in straightforward fashion. Equation (5.115) may be important for the analytical approach, but is certainly not so for the optimization approach.
3. The coefficient vector U found during optimization may be useful for modeling the dynamics of the optimum flexible manipulator for control purposes, since this vector represents the modal shape of vibration corresponding to the fundamental frequency.

The result of the analytical approach, in which no approximation is made with respect to the basic equations, can be used to verify the result of the optimization approach since, we can also apply the latter approach to the case of unconstrained shape design.

5.4.4 Numerical Examples and Discussion

Many numerical examples have been conducted based on the previous iteration schemes. In this section we only present the results for $p = 2$, i.e. manipulators having beams of geometrically similar cross-sections. Specifically, we have chosen a circular cross-section with varying radius in all our numerical investigations.

Unconstrained Design

The successive iteration processes of the analytical approach are controlled by the following accuracy criterion:

$$\frac{|\beta_{i+1} - \beta_i|}{|\beta_{i+1}|} + \frac{\|v_{i+1} - v_i\|}{\|v_{i+1}\|} + \frac{\|v''_{i+1} - v''_i\|}{\|v''_{i=1}\|} < \varepsilon$$

To simplify numerical computations, we have approximated all functions using spline functions through interpolation over their values at $N + 1$ uniformly distributed discrete points in $0 \leq \xi \leq 1$. Throughout this section, $N = 10$ and $\varepsilon = 10^{-2}$ have been used in all computations. In all cases for which convergence is achieved we can find a solution for any $\varepsilon > 0$, but for values of ε below 10^{-2} the number of required iterations increases dramatically while the optimal frequencies and shapes obtained show very little change (less than 5%). For the purpose of comparison, ε is quite sufficient. All numerical integrations are carried out using the recursive Simpson formula.

The iteration process begins with $\beta_0(0) = 1$ and $v''_0(\xi) = -1$. For large hub inertias ($\eta \geq 4$) and small tip loads ($\mu = \zeta = \kappa \leq 0.1$), convergence is usually achieved in five to six iterations.

For a small hub inertia ($\eta \leq 1$) the speed of convergence is very slow and, if a large tip load is also present, the process does not converge at all. From a physical standpoint the reason for this is obvious. Remember that we are dealing with a system composed of three parts: the hub, the beam, and the tip load. The flexibility of this system is increased by decreasing the hub inertia or by increasing the tip load (κ, ζ, or μ). Thus, we should expect rapid convergence for a rigid or stable system and slow or even nonconvergence for a highly flexible or unstable system. This is exactly what the numerical computation processes show.

For various values of hub inertia parameter η and tip load parameters μ, ζ, and κ, Table 5.4 summarizes the increment for the unconstrained shape design in the fundamental frequency in comparison with that of a flexible manipulator with a beam of uniform cross-section and the same length, volume, and material as the optimum flexible manipulator. The dimensionless fundamental frequency of the uniform flexible manipulator is denoted by λ_c. Results from Table 5.4 show that the gain in the optimum shape design is substantial (increases range from 149.76% to 642.31%).

From this table, it is also very clear that the optimal frequency varies dramatically with the change in tip load parameters. For example, given $\zeta = 0.1$ and $\kappa = 0.05$, when mass parameter μ is reduced from 0.10 to 0.05, the corresponding increase in frequency is reduced from 296.22% to 149.76%. Note that even for flexible manipulators with beams of uniform rectangular cross-sections, their vibration frequencies change dramatically with variations in tip load [11].

Another interesting point can be found by observing the values in the last two columns of Table 5.4. These show that by exchanging the values of μ and κ, the results of optimum design can be quite different. This shows that the effect of tip load mass and tip load moment is not symmetrical. Finally, as one can clearly see in Table 5.4, the frequency increase is larger as the hub inertia increases. This conclusion has also been confirmed by our previous results [11].

For small μ and κ, the optimum shape is approximately a linearly tapered beam (Figure 5.27). For large values of μ, the beam tapers dramatically near the tip (Figure 5.28). If κ is large, the beam becomes almost uniform (Figure 5.29). This is most likely due to the large bending

Table 5.4: Ratio of $\sqrt{\lambda/\lambda_c}$ for unconstrained shape design ($p = 2$)

	$(\mu,\zeta,\kappa) =$ (0.10,0.10,0.05)	$(\mu,\zeta,\kappa) =$ (0.10,0.10,0.05)	$(\mu,\zeta,\kappa) =$ (0.10,0.10,0.05)	$(\mu,\zeta,\kappa) =$ (0.10,0.10,0.05)
$\eta = 1$	3.9622	2.4976	4.7175	3.6207
$\eta = 2$	4.3725	3.1135	5.3285	4.3241
$\eta = 3$	5.8935	3.7837	6.0134	6.9039
$\eta = 4$	7.0013	4.3752	7.4231	5.8128

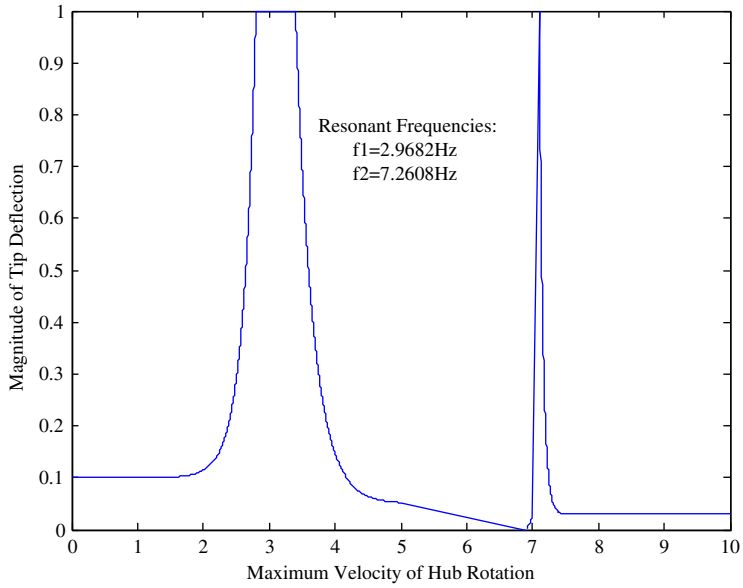

Figure 5.26: Motion Speed and Tip Deflection.

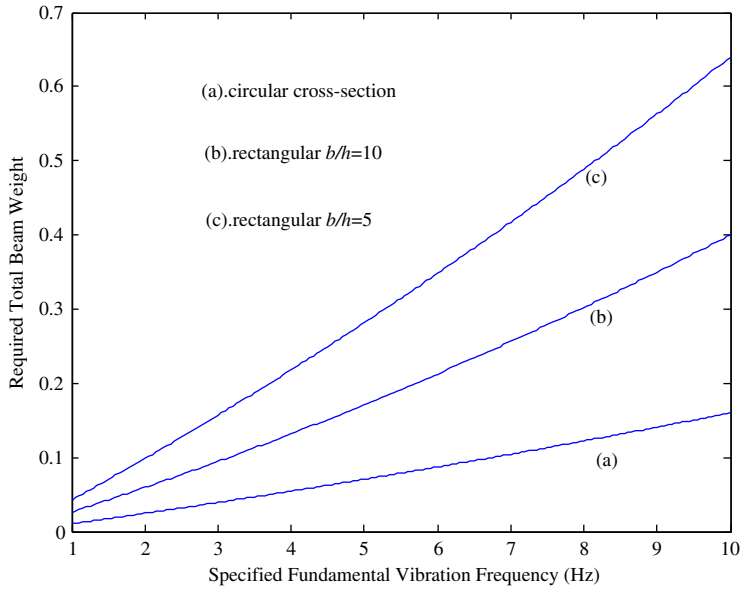

Figure 5.27: Beam Weight and Specified Fundamental Frequency.

moment that is induced towards the end of the beam by the large moment of inertia of the tip load. In order to counteract this, the beam assumes a uniform shape with no tapering. Also, the frequency and optimum shape seem to be relatively insensitive to the placement of the tip load relative to the end of the beam.

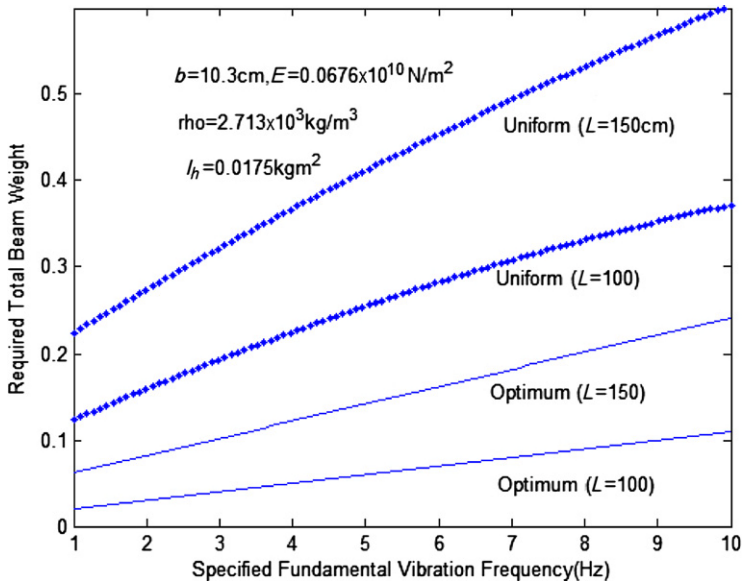

Figure 5.28: Uniform Beam vs. Optimum Design: $p = 2$.

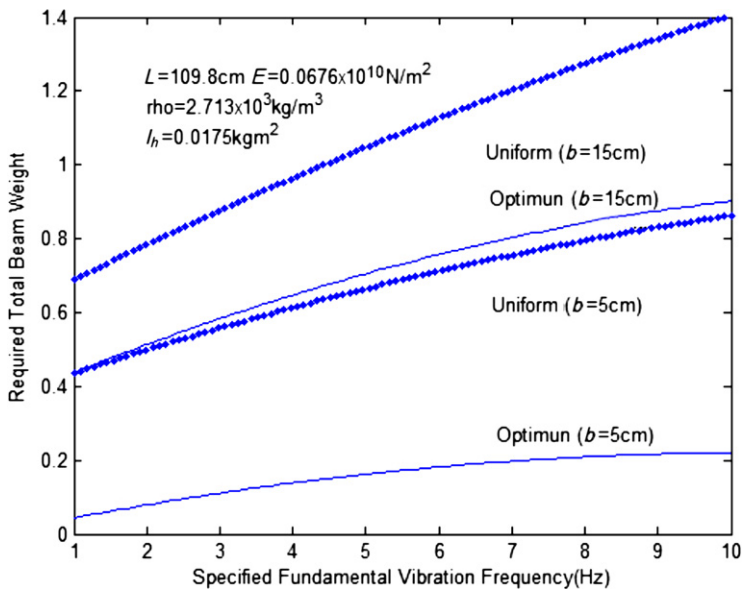

Figure 5.29: Uniform Beam vs. Optimum Design: $p = 3$.

Constrained Design

To evaluate the effect of lower and upper constraints imposed on the shape function, numerical analysis has been conducted by introducing a lower bound and an upper bound. The lower bound is 5% larger than the actual smallest value of α obtained in the

corresponding unconstrained shape design, whereas the upper bound is 5% smaller than the largest value of α obtained in the unconstrained design. The optimization approach discussed in Section 5.3.4 has been used in the numerical computations. The nonlinear programming algorithm used is the Broyden–Fletcher–Goldfarb–Shanno (BFGS) method with constraints.

Corresponding to Table 5.4, Table 5.5 presents the results of the constrained shape design of single tip loads for the same combinations of hub inertia and tip load parameters. It is very clear that the increases in the fundamental frequency have been reduced due to the further constraints on the shape functions. However, the numerical results indicate that the profiles of the optimal beam shapes are very similar in the cases of unconstrained and constrained designs (see Figure 5.30).

Table 5.5: Ratio of $\sqrt{\lambda/\lambda_c}$ for constrained shape design ($p = 2$)

	$(\mu,\zeta,\kappa) =$ (0.10,0.10,0.05)	$(\mu,\zeta,\kappa) =$ (0.10,0.10,0.05)	$(\mu,\zeta,\kappa) =$ (0.10,0.10,0.05)	$(\mu,\zeta,\kappa) =$ (0.10,0.10,0.05)
$\eta = 1$	3.2938	2.1162	3.9149	3.2414
$\eta = 2$	3.6777	2.7735	4.3105	3.5734
$\eta = 3$	4.7557	3.1579	4.9537	5.9869
$\eta = 4$	5.7087	3.7556	6.4859	4.8637

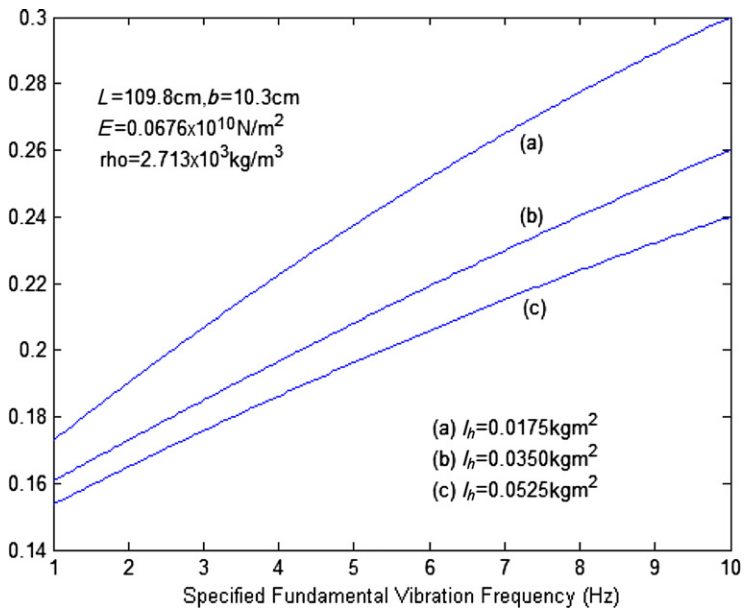

Figure 5.30: Weight Ratio of Optimum and Uniform Arms: $p = 2$.

Minimax Design

To illustrate the minimax design procedure in the case of multiple tip loads, three tip load situations (labeled as A, B, and C respectively) have been studied. The tip load parameters for three cases are $(\mu_A,\mu_B,\mu_C) = (0.10,0.05,0.10)$, $(\zeta_A,\zeta_B,\zeta_C) = (0.10,0.10,0.10)$, and $(\kappa_A,\kappa_B,\kappa_C) = (0.05,0.05,0.50)$. The hub inertia parameter is fixed at $\eta = 4$. No lower or upper bound is imposed on the shape function in this case. The corresponding optimal shapes designed for each of the individual cases are called $Shape_A$, $Shape_B$, and $Shape_C$ respectively. The optimal shape obtained by the minimax method is called $Shape_M$.

Table 5.6 summarizes the result of the minimax design. As one can see from the table, the performance of the optimal shape degrades when the tip load is not the one given in its design specification. However, we have found that the optimal shapes always obtain higher frequencies than the uniform shapes. It is clear from the table that the optimal shape constructed by the minimax design gives a fundamental frequency that is always higher than the lowest frequency produced by the other three optimal shapes in all three tip load cases, as would be expected. Figure 5.31 shows the profiles of four shapes:

$$(S_\eta,\ S_\mu,\ S_{\mu\zeta},\ S_\kappa) = \frac{(\eta v'(0)^2,\ \mu v(1)^2,\ 2\zeta\mu v(1)v'(1),\ \kappa v'(1)^2)}{\int_0^1 \alpha v^2 \mathrm{d}\xi + \eta v'(0)^2 + \mu v(1)^2 + 2\zeta\mu v(1)v'(1) + \kappa v'(1)^2} \tag{5.153}$$

5.4.5 Sensitivity Analysis of the Optimal Frequency

A variation in hub inertia, or more likely in tip load, will induce a corresponding change in the frequency of flexible arms. For the purpose of arm design, it is extremely important to know how sensitive the optimal frequency is with respect to changes in system parameters. The sensitivity information can be used to specify the accuracy of the machining operation during the real construction of the optimal shapes. This section investigates the problem of sensitivity analysis for the unconstrained optimum shape design only.

Table 5.6: Ratio of $\sqrt{\lambda/\lambda_c}$ for minimax shape design ($p = 2$, $\eta = 4$)

	$(\mu,\zeta,\kappa)_A = (0.10,0.10,0.05)$	$(\mu,\zeta,\kappa)_B = (0.10,0.10,0.05)$	$(\mu,\zeta,\kappa)_C = (0.10,0.10,0.05)$
$Shape_A$	4.3725	2.3412	4.2134
$Shape_B$	2.9112	3.1135	4.0211
$Shape_C$	3.0119	2.5143	5.6285
$Shape_M$	3.8125	2.3571	4.4653

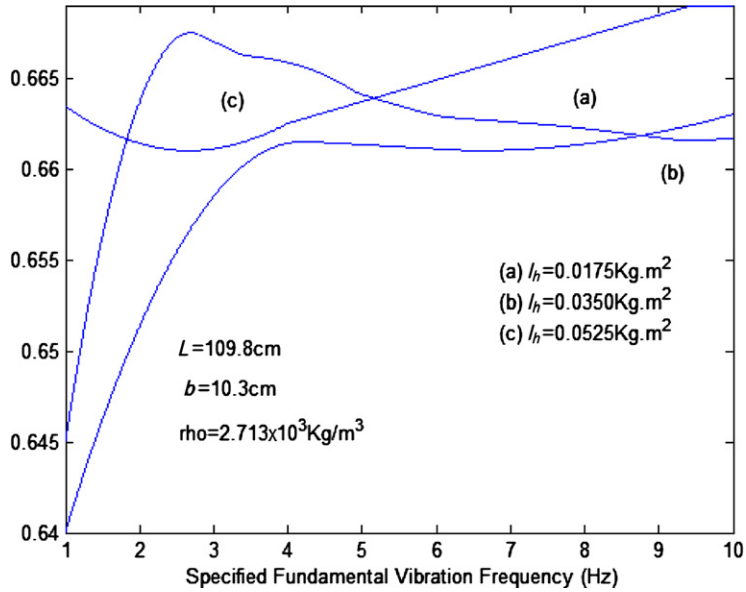

Figure 5.31: Weight Ratio of Optimum and Uniform Arms: $p = 3$.

For optimal fundamental frequency λ, from Eqs (5.116) and (5.117), variation of λ due to small changes in η, μ, ζ, and κ can expressed as

$$\frac{\delta\lambda}{\lambda} = -S_\eta \frac{\delta\eta}{\eta} - S_\mu \frac{\delta\mu}{\mu} - S_{\mu\zeta} \frac{\delta(\mu\zeta)}{\mu\zeta} - S_\kappa \frac{\delta\kappa}{\kappa} \tag{5.154}$$

where sensitivity indices are calculated accordingly (see (5.153) above).

Note that although $\delta\eta$, $\delta\mu$, $\delta\zeta$, and $\delta\kappa$ cause the corresponding variations δv and $\delta\alpha$ in v and α respectively, these variations will not affect the value of λ when small terms of order 2 or higher are ignored, since λ reaches one of its stationary values at v and α. This is why we do not need to consider the variations of v and α in the above sensitivity analysis.

It should be pointed out that sensitivity indices can also be formally defined as follows:

$$S_\chi = -\frac{\%\text{ change in }\lambda}{\%\text{ change in }\chi} = -\frac{\delta\lambda/\lambda}{\delta\chi/\chi} = -\frac{\chi}{\lambda}\frac{\delta\lambda}{\delta\chi} \tag{5.155}$$
$$\chi = \eta,\ \mu,\ \mu\zeta,\ \kappa$$

Clearly, $0 \le S_\chi \le 1$. Therefore, *the vibration frequency always decreases as system parameters increase in value*, a conclusion that agrees with intuition and that has been verified by numerical analysis [16].

Using Eqs (5.153) and (5.154), one can find the actual numerical values of sensitivity indices for any particular optimum shape design.

5.5 Minimum-Weight Design of Flexible Manipulators for a Specified Fundamental Frequency

The focus of this section is on the problem of designing a minimum-weight flexible manipulator for a given fundamental vibration frequency. As indicated in Figure 5.26, the fundamental vibration frequency of a flexible manipulator defines the range of operational speeds of the manipulators, since as the operational speed approaches the fundamental frequency, it may cause resonant vibration of the manipulator system. Therefore, to increase the operational speed of the manipulator, i.e. the productivity, one has to ensure that the manipulator has a large fundamental frequency. However, as we can see from Figure 5.27, a large fundamental frequency means that a manipulator must be heavier.

As pointed out by Asada et al. [27], the majority of flexible manipulators that have been studied in the literature have a simple structure consisting of beams with uniform mass and stiffness distribution. While the simplified beams permit analytical modeling and theoretical treatment, the arm construction is unrealistically primitive and its dynamic performance is severely limited. In our previous work [11,12,28,33], the problem of optimum mass and stiffness distribution of flexible manipulators under a given total weight constraint has been investigated using the variational formulation.

Under the constraint that a flexible arm must have a specified fundamental frequency, we will show here that the same method can be used to find an optimum mass and stiffness distribution such that the arm will have a minimum weight. For space applications, where flexible manipulators have been generally recognized as an ideal tool for material handling and space-structure construction, minimum-weight manipulators are of special interest due to the strict weight constraint imposed by the loading capacity of landers [18].

5.5.1 Basic Equations

A one-link flexible manipulator is modeled as a beam mounted on a hub with rotational inertia I_H in the horizontal plane. The minimum weight design of flexible manipulators will involve only the fundamental frequencies. Although rotary inertia and shear deformation of the beam are very important for higher order vibration frequencies, a previous study [11] has shown that their influence on the fundamental frequency is very small and can be neglected. Accordingly, the simple Euler–Bernoulli beam model without rotary inertia and shear deformation is valid for the study here and thus, for a specified fundamental frequency ω_s, the governing equation of harmonic vibration and the boundary conditions can be written as follows:

$$(EIv'')'' - \rho A \omega_s^2 v = 0 \tag{5.156}$$

$$v(0) = 0, \quad I_H \omega_s^2 v'(0) + EIv''(0) = 0 \tag{5.157}$$

$$EIv''(L) = 0, \quad \left(EIv''\right)'(L) = 0 \tag{5.158}$$

where v is the total displacement of the beam, EI is the bending rigidity, A the cross-sectional area, ρ the mass density per unit volume, and L the length of the beam. A prime indicates differentiation with respect to the coordinate x along the longitudinal axis of the beam.

For a flexible manipulator with a beam of uniform cross-section, it can be shown that the following relationship must be satisfied by the specified fundamental vibration frequency W_s, the total beam weight $W = \rho AL$, and the hub inertia I_H:

$$\left(\frac{W}{W_s}\right)^{1/4} = \theta_s(\eta), \quad W_s = \frac{EI}{\omega_s^2 L^3}, \quad \eta = \frac{I_H}{WL^2} \tag{5.159}$$

where θ_s is the minimum eigenvalue of the characteristic equation:

$$\sin\theta \cosh\theta - \cos\theta \sinh\theta + \eta\theta^3(1 + \cosh\theta \cos\theta) = 0$$

It is straightforward to show that θ_s increases monotonically as the hub inertia parameter decreases. The lower and upper bounds of θ_s can be found to be $1.8751 \leq \theta_s \leq 3.9266$, which are achieved at $\eta = \infty$ and $\eta = 0$ respectively. Similarly, $12.3623 \leq (W/W_s) \leq 237.7205$. Note that when $\eta = \infty$, Eq. (5.158) is reduced to the characteristic equation of a clamped cantilever, whereas when $\eta = \infty$, Eq. (5.158) is reduced to that of a hinged cantilever. Hence, for manipulators with beams of uniform cross-section, one can see from Eq. (5.158) that hub inertia can cause the total weight to vary over a wide range. For fixed hub inertia, Figure 5.27 shows that the total beam weight increases as the specified fundamental frequency increases.

For manipulators with beams of varying cross-section, however, simple equations such as Eq. (5.158) for the relationship between the fundamental frequency and the beam weight are no longer possible. In this case, the fundamental frequency is a nonlinear function of the shape function (or, equivalently, mass and stiffness distribution) of the cross-section. The objective of this work is to find the best possible tapering of a beam for a flexible manipulator, which for a specified fundamental frequency would generate the minimum beam weight.

Throughout this work we will assume the following relationship between the moment I and the area A of the beam's cross-section:

$$I(x) = \gamma A^p(x), \quad p \geq 1 \tag{5.160}$$

where γ is a constant.We are especially interested in three cases, namely $p = 1, 2, 3$, since they correspond to beams with rectangular cross-sections of given uniform height, geometrically similar cross-sections, and rectangular cross-sections of given uniform width respectively. The treatment in this section, however, is valid for all cases with $p \geq 1$.

5.5.2 Problem Formulation

In this section we use the variational method to establish the basic equations for solving the minimum-weight design problem. For this purpose, we transfer Eqs (5.156) and (5.157) into the following variational form using Rayleigh's principle:

$$\omega_s^2 = \min_v \frac{\int_0^L EIv''^2 \mathrm{d}x}{\int_0^L \rho A v^2 \mathrm{d}x + I_H v'(0)^2} \tag{5.161}$$

where v only needs to satisfy the geometric boundary condition $v(0) = 0$. The equivalence of (5.161) and Eqs (5.156) and (5.157) can be easily proved. The above equation can be rewritten in dimensionless form as follows:

$$\lambda_s = \min_v \frac{\int_0^1 \alpha^p v''^2 \mathrm{d}\varepsilon}{\int_0^1 \alpha v^2 \mathrm{d}\varepsilon + \eta v'(0)^2} \tag{5.162}$$

where a prime indicates differentiation with respect to the dimensionless coordinate $\xi = x/L$. The dimensionless eigenvalue λ_s, shape function α, and hub inertia parameter η are defined respectively as

$$\lambda_s = \frac{\rho^p L^{3+p}}{\gamma E W_0^{p-1}} \omega_s^2, \quad \alpha = \frac{\rho L A}{W_0}, \quad \eta = \frac{I_H}{W_0 L^2} \tag{5.163}$$

in which W_0 is a nominal weight.

To minimize the total weight of the beam, $\alpha(\xi)$ must be designed such that

$$\min_\alpha \int_0^1 \alpha \mathrm{d}\xi \tag{5.164}$$

subject to constraint (5.162).

Using the Lagrange multiplier method, it can be found from variational calculus that the minimum-weight design problem leads to the following set of differential equations:

$$(\alpha^p v'')'' - \lambda_s \alpha v = 0 \tag{5.165}$$

$$p\alpha^{p-1}(v'')^2 - \lambda_s v^2 = \lambda_s \sigma^2 \tag{5.166}$$

and the boundary conditions

$$v(0) = 0, \quad \alpha^p v''(0) + \lambda_s \eta v'(0) = 0, \quad \alpha^p v''(1) = 0, \quad (\alpha^p v'')'(1) = 0 \tag{5.167}$$

where σ is a Lagrange multiplier. These equations, together with constraint (5.162), form the complete set of basic equations of minimum-weight design for the one-link flexible manipulator.

Clearly, solution of Eqs (5.165)–(5.167) is not unique, since if $(v,\sigma^2,\alpha,\lambda_s)$ is a solution of (5.165)–(5.167), then $(cv,c^2\sigma^2,\alpha,\lambda_s)$ is another solution for any nonzero constant c. At first glance, the non-uniqueness of a solution may seem to create problems in numerical computation, but it actually offers us a way to completely remove the Lagrangian multiplier from Eq. (5.166) by selecting $c = 1/\sigma$. In other words, we only need to find the unknown function v/σ, instead of v and σ^2 individually, in order to solve the optimization problem. Therefore, we will assume Lagrange multiplier $\sigma = 1$. As for the optimum design of vibrating cantilevers [5,7], this observation has simplified the problem substantially.

It follows from Eq. (5.166) that for $p > 1$:

$$\alpha(\xi) = \frac{\phi_v(\xi)}{\beta} \tag{5.168}$$

where

$$\phi_v(\xi) = \left[\frac{v^2(\xi) + 1}{v''^2(\xi)}\right]^{\frac{1}{p-1}}, \quad \beta = \left(\frac{p}{\lambda_s}\right)^{\frac{1}{p-1}} \tag{5.169}$$

An important identity can be obtained by multiplying both sides of Eq. (5.165) by v and integrating over $0 \le \xi \le 1$. After integrating by parts and taking the boundary conditions (5.167) into account, we have, after applying Eq. (5.166):

$$\int_0^1 \alpha(\xi)\mathrm{d}\xi = (p-1)\int_0^1 \alpha(\xi)v(\xi)^2\mathrm{d}\xi + p\eta v'(0)^2 \tag{5.170}$$

5.5.3 Solution by Iterations

Since, in general, the solution of the nonlinear equations Eqs (5.165)–(5.167) cannot be obtained in closed form, a set of successive iteration schemes is developed to find the solutions numerically. The iteration schemes are based upon formal integration, with the introduction of one boundary condition at each integration. Care is taken to remove the singularity of solutions at singular points and to separate the differential operator of the highest order on the left-hand side at each step. This has been found necessary in order to make the numerical computation feasible and to obtain convergence by successive iteration.

The following two integral formulas are very useful in the formulation of iteration schemes:

$$\int_0^{\xi}\int_0^{x} G(s)\mathrm{d}s\mathrm{d}x = \xi^2 \int_0^1 (1-x)G(x\xi)\mathrm{d}x \tag{5.171}$$

$$\int_{\xi}^{1}\int_{x}^{1} G(s)\mathrm{d}s\mathrm{d}x = (1-\xi)^2 \int_0^1 xG[\xi + x(1-\xi)]\mathrm{d}x \tag{5.172}$$

Note that compared with double integration, single integration saves computation time and hence is preferred numerically.

Next we will present iteration schemes for the cases of $p = 1$ and $p > 1$.

Case where $p = 1$

For $p = 1$, function α drops out of Eq. (5.166) and we have a degenerate case. Then identity (5.170) becomes

$$\eta\, v'(0)^2 = \int_0^1 \alpha(\xi)\mathrm{d}\xi$$

To develop a successive iteration scheme, we formally integrate (5.165) and (5.166) with boundary conditions (5.167). Application of formulas in Eqs (5.170) and (5.171) leads to

$$v(\xi) = \xi v'(0) + \sqrt{\lambda_s}\xi^2 \int_0^1 (1-x)\sqrt{v^2(x\xi)+1}\,\mathrm{d}x \tag{5.173}$$

$$\alpha(\xi) = \frac{\sqrt{\lambda_s}(1-\xi)^2}{\sqrt{v^2(\xi)+1}} \int_0^1 x\alpha v[\xi + x(1-\xi)]\mathrm{d}x \tag{5.174}$$

$$v'(0) = -\frac{1}{\eta}\int_0^1 x\alpha(x)u(x)\mathrm{d}x \tag{5.175}$$

Based on these equations, the iteration scheme can be outlined as follows:

1. For a given λ, select initial $v_0'(0)$, $v_0(\xi)$, and $\alpha_0(\xi)$.
2. Update v_i according to

$$v_{i+1}(\xi) = \xi v_i'(0) + \sqrt{\lambda}\xi^2 \int_0^1 (1-x)\sqrt{v_i^2(x\xi)+1}\,\mathrm{d}x$$

3. Update α_i according to

$$\alpha_{i+1}(\xi) = \frac{\sqrt{\lambda_s}(1-\xi)^2}{\sqrt{v_{i+1}^2(\xi)+1}} \int_0^1 x\alpha_i v_{i+1}[\xi + x(1-\xi)]\mathrm{d}x$$

4. Update $v_i'(0)$ according to

$$v_{i+1}'(0) = -\frac{1}{\eta} \int_0^1 x\alpha_{i+1}(x)v_{i+1}(x)\mathrm{d}x$$

5. If a given accuracy is not satisfied, go back to Step 2.

Case where $p > 1$

For $p > 1$, by formal integration of (5.165) we find, after satisfying the boundary conditions at $\xi = 1$, substituting α from (5.168) into (5.165), and using (5.171) that

$$v''(\xi) = \frac{s[v^2(\xi)+1]^{\frac{p}{p+1}}}{M(v)^{\frac{p-1}{p+1}}} \tag{5.176}$$

where $M(v)$ and s are defined as

$$M(v) = p(1-\xi)^2 \int_0^1 x\phi_v[\xi + x(1-\xi)]v[\xi + x(1-\xi)]\mathrm{d}x$$

$$s = \mathrm{sign}\left[\int_0^1 x\phi_v[\xi + x(1-\xi)]v[\xi + x(1-\xi)]\mathrm{d}x\right]$$

It is easy to show that

$$v(\xi) = \xi v'(0) + \xi^2 \int_0^1 (1-x)v''(x\xi)\mathrm{d}x \tag{5.177}$$

$$v'(0) = -\frac{v''(0)}{\lambda_s \eta \beta \left|v''(0)\right|^{\frac{2p}{p-1}}} \tag{5.178}$$

Now the scheme for successive iterations can be specified as follows:

1. Select an initial $v_0''(\xi)$.
2. Update $v_i(\xi)$ according to (5.176) and (5.177).
3. Update $\phi_{vi}(\xi)$ according to (5.168).

4. Update $v_i''(\xi)$ according to (5.175).
5. If a given accuracy is not satisfied, go back to Step 2.

5.5.4 Numerical Examples

Several numerical examples have been considered based upon the successive iteration schemes described in the previous section. In this section we present some of the results for $p = 2$ and $p = 3$.

The successive iteration processes are controlled by the following accuracy criteria:

$$\frac{||v_{i+1} - v_i||}{||v_{i+1}||} + \frac{||\alpha_{i+1} - \alpha_i||}{||\alpha_{i+1}||} < \varepsilon$$

To simplify the numerical computation, we have approximated all functions using spline functions through interpolation over their values at $N + 1$ uniformly distributed discrete points in $0 \leq \xi \leq 1$. Throughout this section, $N = 10$ and $\varepsilon = 10^{-4}$ have been used in all computations. All numerical integrations in iterations are carried out by using the recursive Simpson formula.

The iteration for $v''(\xi)$ starts with $v_0''(\xi) = 1$. In this case, for large $\eta = 50$, convergence is achieved after 54 iterations for $p = 2$ and 39 for $p = 3$. For small η, say $0.5 \leq \eta \leq 1$, the speed of convergence becomes very slow (close to 1000 iterations are required for convergence), and for $\eta \leq 0.5$ the iterations do not converge at all with the initial guess $v_0''(\xi) = 1$. This problem can be overcome by using the converged $v''(\xi)$ of the previous value of η as the initial guess $v_0''(\xi)$ of the new η value, but the speed of convergence is still very slow and becomes extremely slow for $\eta \leq 1$.

For various values of specified fundamental frequencies $f_s(\omega_s = 2\pi f_s)$, Table 5.1 summarizes the ratio of the weights of the uniform beam and the optimum beam. More results are illustrated in Figures 5.28–5.31. Figure 5.32 illustrates the corresponding variation of linear dimension (i.e. radius of the cross-section) of the geometrically similar cross-section ($p = 2$) as a function of nondimensional coordinate ξ. Figure 5.33 gives the corresponding results for the rectangular cross-section of given uniform width ($p = 3$, i.e. linear dimension is the height of the cross-section).

5.6 Optimum Design of Flexible Manipulators: The Segmentized Solution

Our objective in this section is to address the control problem from a design perspective. The goal is to build a high-performance flexible manipulator such that the effect of its oscillation is reduced during normal operations. The finite rigidity of a flexible manipulator results in a finite fundamental frequency of vibration, while the infinite stiffness of a rigid arm implies

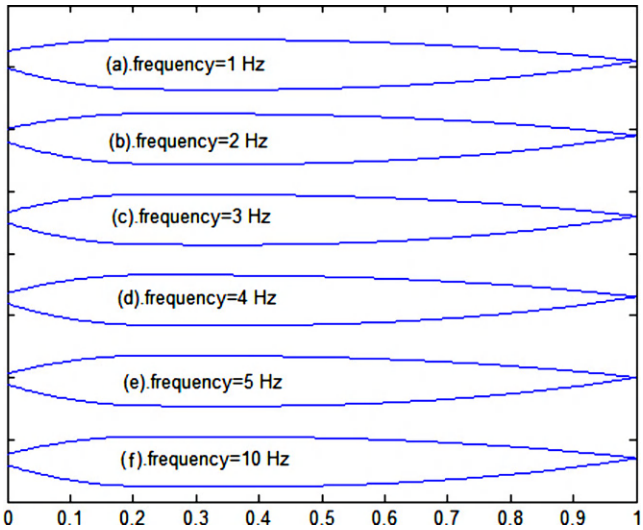

Figure 5.32: Optimum Tapering of Beam: $p = 2$.

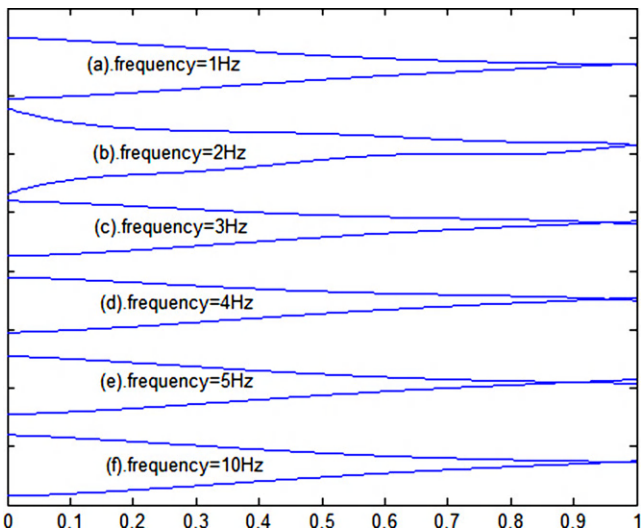

Figure 5.33: Optimum Tapering of Beam: $p = 3$.

an infinite value for the fundamental frequency. For any system with finite fundamental frequency, oscillation is unavoidable and becomes severe when the system operates near its fundamental frequency. Thus, to reduce the oscillation, one has to either operate the manipulator at low speeds or somehow increase its fundamental frequency. Since one of the major reasons for developing flexible manipulators is to obtain high-speed motion with less energy consumption, increasing the fundamental frequency is the only appropriate solution.

In previous work, we have solved the unconstrained design problems for both maximum speed and minimum mass formulations analytically using the variational method [11,33,38]. Theoretical and numerical analyses have indicated that the unconstrained formulations could result in unrealistic link designs such as zero-area cross-sections, which are not allowed in real applications. To overcome these situations, more constraints have been introduced in the design specification and nonlinear optimization techniques have been used to find the optimum solutions [28,33]. The major problem in these constrained design formulations is that the fundamental frequency is calculated approximately using the modal shape functions derived for manipulators with uniform cross-sections. This makes the task of verifying the results of optimum designs very difficult, and numerical examples have also indicated that the results are sensitive to the number of modal shape functions used.

To overcome these problems, an innovative design method based on the segmentized solution of vibration equations for flexible manipulators is developed here. The main advantage of this new method is that the design process is closely related to the actual process of manipulator construction, i.e. using many different, uniform segments to approximate a non-uniform link.

5.6.1 Basic Equations

This section presents the basic dynamic equations for a non-uniform flexible manipulator carrying a load at its end. We then solve these equations by approximating the link of the manipulator with a number of segments of uniform mass and bending rigidity distributions.

Our model consists of a flexible link of length L fixed on a rigid hub of inertia I_H. The harmonic vibration of this manipulator system is described by the amplitude of its pure link deflection ω and rigid hub rotation θ. Based on the Euler–Bernoulli bending theory [16], the vibration equation and the corresponding boundary conditions can be expressed in terms of the amplitude of its total link displacement, $u(x) = \omega(x) + x\theta$, as

$$(EIu'')'' - \rho A\omega^2 u = 0 \tag{5.179}$$

$$u(0) = 0, \quad I_H\omega^2 u'(0) + EIu''(0) = 0 \tag{5.180}$$

$$EIu''(L) - J_p\omega^2 u'(L) - a_c M_p\omega^2 u'(L) = 0 \tag{5.181}$$

$$(EIu'')'(L) + a_c M_p\omega^2 u'(L) + M_p\omega^2 u(L) = 0 \tag{5.182}$$

where $()' = \partial()/\partial x$, ω is the natural vibration frequency, EI is the bending rigidity, and ρA is the linear mass density. A tip load is characterized by its mass M_p, inertia J_p, and local x-coordinate a_c, of the center of mass. When a tip load is considered as a point, $a_c = 0$, Eqs (5.179)–(5.182) reduce to the form developed by Bellezze et al. [25].

For the purpose of optimum design, we will treat ω in Eqs (5.179)–(5.182) as the fundamental vibration frequency. Then, Eqs (5.179)–(5.182) can be reformulated into the following equivalent variational problem [28,33]:

$$\omega^2 = \min_{u(x)} \frac{\int_0^L EIu''^2 \mathrm{d}x}{\int_0^L \rho A u^2 \mathrm{d}x + I_H u'(0)^2 + G_L}$$

where $G_L = M_p u(L)^2 + 2a_c M_p u(L)u'(L) + J_p u'(L)^2$.

To reduce the number of symbols, we introduce the following dimensionless form of the above equation:

$$\lambda = \min_{\upsilon(\xi)} \frac{\int_0^1 \beta \upsilon''^2 \mathrm{d}\xi}{\int_0^1 \alpha \upsilon^2 \mathrm{d}\xi + \eta \upsilon'(0)^2 + R_1} \tag{5.183}$$

where $R_1 = \mu\upsilon(1)^2 + 2\chi\mu\upsilon(1)\upsilon'(1) + \kappa\upsilon'(1)^2$, $\xi = x/L$, $\upsilon(\xi) = u(x)/L$, and $()' = \partial()/\partial\xi$. Dimensionless frequency λ, linear mass distribution $\alpha(\xi)$, bending rigidity distribution $\beta(\xi)$, hub inertia parameter η, and tip load parameters μ, χ, κ are given by

$$\lambda = \frac{L^3 M_0}{D_0}\omega^2, \quad \alpha = \frac{\rho A L}{M_0}, \quad \beta = \frac{EI}{D_0}, \quad \eta = \frac{I_H}{M_0 L^2} \tag{5.184}$$

$$\mu = \frac{M_p}{M_0}, \quad \chi = \frac{a_c}{L}, \quad \kappa = \frac{J_p}{M_0 L^2} \tag{5.185}$$

where M_0 and D_0 are two arbitrary constants of mass and rigidity.

The total mass and its dimensionless form are

$$M = \int_0^L \rho A(x)\mathrm{d}x\ , \quad \gamma = \frac{M}{M_0} = \int_0^1 \alpha(\xi)\mathrm{d}\xi \tag{5.186}$$

5.6.2 Segmentized Solutions

To optimize mass and rigidity distributions, one needs to find the relationship between $\upsilon(\xi)$ and these distributions. This will lead to a set of equations similar to Eqs (5.179)– (5.182). Since Eq. (5.179) is a differential equation of varying coefficients, it cannot be solved easily. From the perspective of practical design, however, we can always approximate a non-uniform link with a link consisting of many uniform segments, each having a constant mass and

rigidity distribution. By increasing the number of segments, we can represent any link of practical interest as closely as we want.

Specifically, we divide the whole link $0 \le \xi \le 1$ into N segments, i.e. $0 = \xi_0 < \ldots < \xi_N = 1$. Segment i is of length $\Delta_i = \xi_i - \xi_{i-1}$ and is considered to be uniform with constant linear mass and bending rigidity α_i and β_i. For each segment, its total displacement can be found as

$$v_i(\xi) = S_i(\zeta)C_i \tag{5.187}$$

where $S_i = [\sin\lambda_i\zeta \ \sinh\lambda_i\zeta \ \ \cos\lambda_i\zeta \ \ \cosh\lambda_i\zeta]$, $\lambda_i^4 = \alpha_i\Delta_i^4\lambda/\beta_i$, $C_i \in R^4$ is a coefficient vector, and $0 \le \zeta = (\xi - \xi_{i-1})/\Delta_i \le 1$ is the local coordinate. Based on the considerations of deformation continuity and force balance at the interfacial cross-section of two segments, we can express C_{i+1} as a function of C_i by $C_{i+1} = \phi_i C_i$, and eventually every C_i as a function of $C = C_1$ by $C_i = \phi_{i-1} \ldots \phi_1 C$, where ϕ_i is a matrix whose elements are functions of mass and rigidity constants:

$$\phi_{\mathrm{i}} = \begin{bmatrix} c_i\sigma_{1i}cs_i & c_i\sigma_{2i}ch & -c_i\sigma_{1i}s_i & c_i\sigma_{2i}sh_i \\ c_i\sigma_{2i}cs_i & c_i\sigma_{1i}ch_i & -c_i\sigma_{2i}s_i & c_i\sigma_{1i}sh_i \\ \sigma_{1i}s_i & \sigma_{2i}sh_i & \sigma_{1i}cs_i & \sigma_{2i}ch_i \\ \sigma_{2i}s_i & \sigma_{1i}sh_i & \sigma_{2i}cs_i & \sigma_{1i}ch_i \end{bmatrix} \tag{5.188}$$

$$a_i = \frac{\alpha_i}{\alpha_{i+1}}, \quad b_i = \frac{\beta_i}{\beta_{i+1}}, \quad c_i = \left(\frac{a_i}{b_i}\right)^{1/4} \tag{5.189}$$

$$d_i = \frac{\Delta_i}{\Delta_{i+1}}, \quad \sigma_{1i} = 1 + b_i c_i^2, \quad \sigma_{2i} = 1 - b_i c_i^2 \tag{5.190}$$

where $cs_i = \cos\lambda_i$, $s_i = \sin\lambda_i$, $ch_i = \cosh\lambda_i$, and $sh_i = \sinh\lambda_i$. In other words, we are able to describe $v(\xi)$ over the whole link by a coefficient vector of four unknowns:

$$v(\xi) = S(\xi)C, \quad S = \sum_{i=1}^{N} v_i(\xi)\varepsilon(\xi;\xi_{i-1},\xi_i)\Phi_i \tag{5.191}$$

$$\Phi_1 = I_{4\times4}, \quad \Phi_{i+1} = \phi_i\Phi_i, \ \ i \le N-1 \tag{5.192}$$

where $\varepsilon(\xi;\xi_{i-1},\xi_i) = 1$ for $\xi_{i-1} \le \xi < \xi_i$ and $\varepsilon(\xi;\xi_{i-1},\xi_i) = 0$ otherwise.

By substituting Eq. (5.191) into the boundary conditions at the two ends, we obtain a homogeneous equation $QC = 0$ for C. Since C must be a nonzero vector, its coefficient matrix must be singular. Therefore, the characteristic equation for determining the natural vibration frequency can be specified as

$$\det Q = \sum(\lambda, X_\alpha, X_\beta, \Xi) = 0 \tag{5.193}$$

where $X_\alpha = (\alpha_1,\ldots,\alpha_N)$ and $X_\beta = (\beta_1,\ldots,\beta_N)$ are mass and rigidity distribution vectors, and $\Xi = (\eta,\mu,\chi,\kappa)$ represents hub inertia and tip load parameters. The fundamental frequency is

the smallest nonzero eigenvalue of the transcendental equation (5.193). Thus, Eq. (5.193) leads to the following expression for the fundamental frequency:

$$\lambda = f(X_\alpha, X_\beta; \Xi) \tag{5.194}$$

where both X_α and X_β are considered as design variables, while Ξ is treated as a design parameter vector.

The total mass of the flexible manipulator can be obtained by adding up the individual mass of each uniform segment:

$$\gamma = \alpha_1 \Delta_1 + \ldots + \alpha_N \Delta_N = X_\alpha \Delta^T \tag{5.195}$$

Equations (5.194) and (5.195), as well as Eq. (5.183), provide the basic expressions for the optimum design formulations discussed in the next section.

In Figure 5.34, it can be seen that the segmentized frequency rapidly approaches the optimum frequency, which is obtained using the analytical solution given in an earlier work [28].

Figure 5.35 compares the optimum analytical design to the four-segment optimum design. Note that with four segments the segmentized frequency is just 4% less than the analytical optimum. Other similar results have indicated that the optimum link can be approximated very accurately with only a few segments (usually eight or less for 5% accuracy).

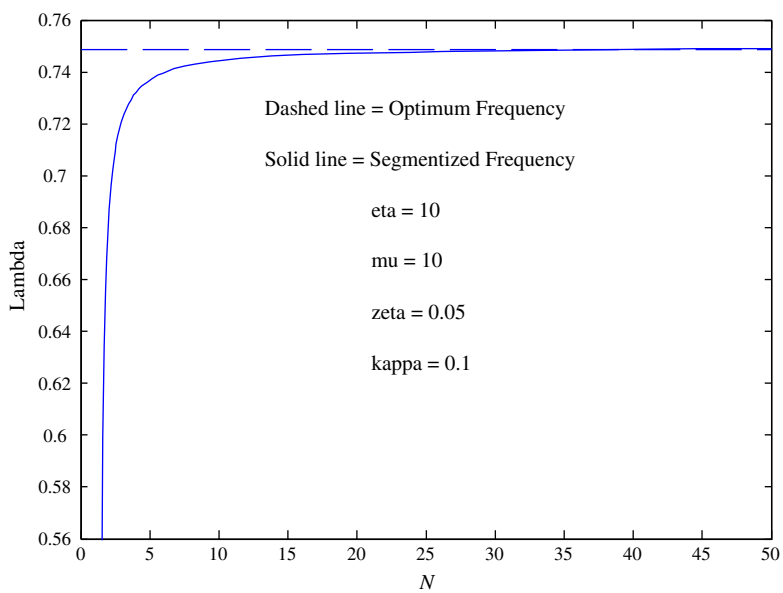

Figure 5.34: Frequency vs. Number of Segments.

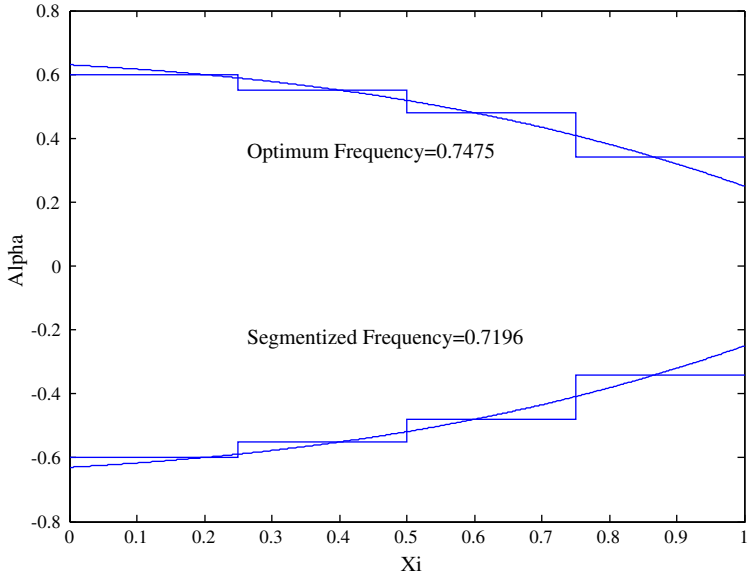

Figure 5.35: Analytic Optimum vs. Four-Segment Optimum.

5.6.3 Optimization Formulations for Linear Mass and Bending Rigidity Distributions

In this section, we investigate two optimum design problems for a flexible manipulator. The basic forms of these two problems can be stated as:

1. **Maximum speed design problem (MaxSDP).** For a given cross-section specification and a given total mass M_s, determine the optimum mass distribution (ρA) and rigidity distribution (EI) of a flexible manipulator with respect to a specified set of design constraints such that its fundamental vibration frequency ω is maximized.
2. **Minimum mass design problem (MinMDP).** For a given cross-section specification and a given fundamental vibration frequency ω_s, determine the optimum mass distribution (ρA) and rigidity distribution (EI) of a flexible manipulator with respect to a specified set of design constraints such that its total mass M is minimized.

The selection of direct design variables for optimization depends on the cross-section specification. For example, if a rectangular cross-section is specified then the direct design variables will be the thickness and width of the section. Here we only consider simple constraints such as the upper and lower bounds imposed on design variables, as well as on mass and rigidity distributions. This is sufficient in order to eliminate the possibility of generating unrealistic optimum designs, such as manipulators with zero-area cross-sections or with their mass/rigidity concentrated only at certain segments. More sophisticated constraints, such as maximum bending stress, strain, tip deflection, or feasibility of link construction, can also be included in design specifications. See Section 5.6.4 for a detailed discussion.

Maximum Speed Design Problem

For certain specific cross-sections, such as a solid circular cross-section, mass and rigidity distributions are not independent. In these cases, we can easily express both X_α and X_β as functions of some independent design variables, denoted as a vector Z. Therefore, we consider $X_\alpha = X_\alpha(Z)$ and $X_\beta = X_\beta(Z)$ in our optimization formulations.

Based on Eqs (5.194) and (5.195), the maximum speed design problem can be formulated as

$$\max_{Z} f(X_\alpha, X_\beta; \Xi) \tag{5.196}$$

$$\text{subject to} \quad X_\alpha \Delta^T = \gamma_s, \quad Z^L \le Z \le Z^U \tag{5.197}$$

$$X_\alpha^L \le X_\alpha \le X_\alpha^U, \quad X_\beta^L \le X_\beta \le X_\beta^U \tag{5.198}$$

where $\gamma_s = M_s/M_0$.

An adaptive random search algorithm has been developed to solve this problem.

Minimum Mass Design Problem

For the minimum mass design problem, we use Eqs (5.183) and (5.191) to calculate the fundamental frequency, instead of Eq. (5.194). This is because the fundamental frequency is given as a design constraint in this case. Therefore, the procedure for solving Eq. (5.194) will be invoked many times if Eq. (5.194) is to be used. Since Eq. (5.193) is transcendental, this will require significant computational time in optimization.

To avoid this computational problem, we substitute Eq. (5.191) into Eq. (5.183). It follows that

$$\lambda_s = \min_{C} \frac{C^T \psi(\lambda_s, X_\alpha, X_\beta; \Xi) C}{C^T \Omega(\lambda_s, X_\alpha, X_\beta; \Xi) C} \tag{5.199}$$

where $\lambda_s = L^3 M_0 \omega_s^2 / D_0$, and ψ and Ω are obtained by

$$\psi = \sum_{i=1}^{N} \beta_i \int_0^1 S''(\xi)^T S''(\xi) \mathrm{d}\zeta$$

$$\Omega = \sum_{i=1}^{N} \alpha_i \int_0^1 S(\xi)^T S(\xi) \mathrm{d}\zeta + Y_s$$

where $Y_s = \eta S'(0)^T S'(0) + \mu S(1)^T S(1) + 2x\mu S(1)^T S'(1) + k S'(1)^T S'(1)$, and $\lambda = \lambda_s$ is used in calculating displacement function $S(\xi = \xi_{i-1} + \zeta \Delta_i)$. Note that both ψ and Ω are positive definite matrices.

It is not difficult to see that, given X_α, X_β, and Ξ, the result of minimization in (5.199) is equal to the minimum eigenvalue of the generalized eigenvalue problem:

$$\det[\psi(\lambda_s, X_\alpha, X_\beta; \Xi) - \lambda\Omega(\lambda_s, X_\alpha, X_\beta; \Xi)] = 0 \tag{5.200}$$

Since Ω is nonsingular, this eigenvalue problem can be reduced to an ordinary eigenvalue problem, which can be easily solved. Thus, Eq. (5.200) provides a very efficient way to verify frequency constraint (5.199).

Based on Eqs (5.195) and (5.199), the minimum mass design problem can be formulated as

$$\min_Z X_\alpha \Delta^T \tag{5.201}$$

subject to $Z^L \le Z \le Z^U$, $X_\alpha^L \le X_\alpha \le X_\alpha^U$, $X_\beta^L \le X_\beta \le X_\beta^U$, and frequency constraint (5.199).

Design Formulations for Multiple Loads

In most cases, a flexible manipulator has to perform tasks in different situations, particularly with different tip loads. This is reflected by different values of vector Ξ. Results of numerical analyses have indicated that the fundamental vibration frequency [16] varies dramatically with tip load parameters. This naturally leads to the question of what is an "optimum" design for a manipulator dealing with multiple task situations. We consider the case of a finite number of task situations, i.e. $\Xi \in \{\Xi_1, \ldots, \Xi_n\}$.

The maximum speed design problem for multiple loads can be formulated as

$$\max_Z \sum_{k=1}^{n} w_k f(X_\alpha, X_\beta; \Xi_k) \tag{5.202}$$

$$\text{subject to} \quad X_\alpha \Delta^T = \gamma_s, \quad Z^L \le Z \le Z^U, \quad X_\alpha^L \le X_\alpha \le X_\alpha^U, \quad X_\beta^L \le X_\beta \le X_\beta^U \tag{5.203}$$

where $\Sigma_{k=1}^n w_k = 1,\ w_k \ge 0$, represents the weight assigned to situation i. In particular, if we choose $w_l = 1$ when $f(X_\alpha, X_\beta; \Xi_l) = \min_{1 \le k \le n} f(X_\alpha, X_\beta; \Xi_k)$and $w_k = 0$ when $k \ne l$, then Eqs (5.202) and (5.203) constitute the minimax design formulation, i.e. the objective is to maximize the worst-case fundamental frequency. This problem has been investigated in Refs [28,33], where the Pshenichnyi−Pironneau−Polak minimax algorithm with exact line search (PPP-ELS) [36,37] was used. The gradient information required by this algorithm, $\lambda_i^\delta = \partial\lambda/\partial x_i$, where $x_i = \alpha_i$ or β_i, can be obtained by using Eq. (5.200) since λ, which must be the smallest eigenvalue of (5.200), has already been found using Eq. (5.193). The result can be described as

$$\det\left[\psi_i^\delta - \lambda\Omega_i^\delta - \lambda_i^\delta \Omega\right] = 0 \tag{5.204}$$

where $\lambda_i^\delta$is the smallest eigenvalue, $\psi_i^\delta = \partial\psi/\partial > x_i$, and $\Omega_i^\delta = \partial\Omega/\partial x_i$. Equation (5.204) can easily be reduced to an ordinary eigenvalue problem because Ω is positive definite.

Similarly, the minimum mass design problem for multiple loads can be stated as

$$\min_{Z} \; X_n \Delta^T \tag{5.205}$$

$$\text{subject to} \quad \lambda_s \leq \sum_{k=1}^{n} w_k f(X_\alpha, X_\beta; \Xi_k), \quad Z^L \leq Z \leq Z^U, \quad X_\alpha^L \leq X_\alpha \leq X_\alpha^U, \quad X_\beta^L \leq X_\beta \leq X_\beta^U \tag{5.206}$$

where w_k has the same interpretation as in Eqs (5.202) and (5.203).

5.6.4 Practical Issues in Link Construction

In the previous section, simple design constraints were considered. However, the advantages of the optimum design would be nullified if the stress/strain distributions or displacement of the optimum manipulator were unacceptably large. To ensure the practicality of optimum designs, we investigate more complicated constraints related to the maximum strain/stress and deflection of a flexible manipulator.

Strain/Stress and Deflection Constraints

At each link cross-section the maximum strain $\varepsilon_{\max}$ and stress $\sigma_{\max}$ occur in the outermost fibers and are given by

$$\begin{aligned} \varepsilon_{\max}(\xi) &= h(\xi) v''(\xi) = h(\xi) S''(\xi) C \\ \sigma_{\max}(\xi) &= E \varepsilon_{\max}(\xi) \end{aligned} \tag{5.207}$$

where $h(\xi) = d_{\max}/L$; $d_{\max}$ is the maximum distance between the neutral axis and the outermost fibers of the cross-section. In many cases, $d_{\max}$ is half of the cross-section thickness, but it generally depends on the specific shape of the cross-section selected for a link.

From harmonic vibration, however, the exact value of $\varepsilon_{\max}$ or $\sigma_{\max}$ cannot be specified since vector C can only be determined up to an arbitrary constant. The simplest way to fix this problem is to normalize C, i.e. impose condition $\|C\| = 1$. In this case, strain/stress and deflection constraints can be specified as

$$\max_{\lambda \leq \lambda_p, 0 \leq \xi \leq 1} h(\xi) \|S''(\xi) C\| \leq \varepsilon_U, \quad \max_{\lambda \leq \lambda_p, 0 \leq \xi \leq 1} \|S(\xi) C\| \leq v_U \tag{5.208}$$

where λ_p, which must be less than the fundamental frequency, is the upper bound of operational frequency, ε_U and v_U are upper bounds imposed on link strain and displacement. Note that the value of ε_U is usually determined by the stress constraint. In actual computation, we only check strain and displacement at certain points, since the procedure to find the maximum strain or deflection is computationally intensive. For a uniform beam, we know from mechanics that the maximum strain occurs at the hub end ($\xi = 0$), while the maximum deflection occurs at the tip ($\xi = 1$).

Link Construction Constraints

Construction of an optimum link can be achieved by either using composite materials or structural design. Using composite materials, we can consider both Young's modulus E and mass density ρ as construction variables. With the structural design method, we can build a link segment using, say, trusses, to obtain the specific segment mass and rigidity required by the optimum design. But a simple method is to select the shape of cross-sections.

For certain cross-sectional shapes, however, we must impose additional constraints on design variables to ensure that an optimum link can be constructed.

For example, using a circular tunnel cross-section where design variables are $z = (r, t)$, and

$$A = \pi t(2r + t)/2, \quad I = \pi[(r + t)^4 - r^4]/8 - y_c^2 A, \quad d_{\max} = r + (1 - 4/\pi)t, \quad y_c = 4t/3\pi$$

the construction feasibility can be guaranteed by imposing the following constraints:

$$r_i + (1 - v_{1i})t_i \geq r_{i+1}, \quad r_i + v_{0i}t_i \leq r_{i+1} + t_{i+1}$$

where $0 \leq v_{0i}, v_{1i} \leq 1$. In other words, for any two adjacent segments, the inner radius of one segment must not exceed $(1 - v_{1i})$ thickness of another segment, and the outer radius must pass the inner radius by v_{0i}, the thickness of another segment.

Similarly, for a rectangular tunnel cross-section, we have $z = (a,b,t)$ and

$$I = [(b + 2t)(a + t)^3 - ba^3]/24 - y_c^2 A$$
$$A = t(2a + b + 2t), \quad d_{\max} = a + t/2, \quad y_c = t/2$$

The unfeasible situation can be prevented by adding the following constraints:

$$b_i + 2(1 - v_{1i})t_i \geq b_{i+1}, \quad a_i + (1 - v_{1i})t_i \geq a_{i+1}$$
$$b_i + 2v_{0i}t_i \leq b_{i+1} + 2t_{i+1}, \quad a_i + v_{0i}t_i \leq a_{i+1} + t_{i+1}$$
$$\text{for } 1 \leq i \leq N - 1$$

References

[1] B.L. Karihaloo, F.I. Niordson, Optimum design of vibrating cantilevers, Journal of Optimization Theory and Applications 11 (6) (1973) 638–654.

[2] P.R. Beesack, Isoperimetric inequalities for the non-homogeneous clamped rod and plate, Journal of Mathematics and Mechanics 8 (1959) 471–482.

[3] B. Schwarz, On the extremal of frequencies of nonhomogeneous strings with equimeasurable density, Journal of Mathematics and Mechanics 10 (1961) 401–422.

[4] B. Schwarz, Some results on the frequencies of non-homogeneous rods, Journal of Mathematical Analysis and Applications 5 (1962) 169–176.

[5] F.I. Niordson, On the optimal design of a vibrating beam, Quarterly of Applied Mathematics 23 (1965) 47–53.
[6] B.L. Karihaloo, F.I. Niordson, Optimum design of vibrating cantilevers, Journal of Optimization Theory and Applications 11 (1973) 638–654.
[7] R.M. Brach, On the extremal fundamental frequencies of vibrating beams, International Journal of Solids and Structures 4 (1968) 667–674.
[8] C.Y. Sheu, Elastic minimum-weight design for specified fundamental frequency, International Journal of Solids and Structures 4 (10) (1968) 953–958.
[9] W. Prager, J.E. Taylor, Problems of optimal structural design, Journal of Applied Mechanics 35 (1968) 102–106.
[10] N. Olhoff, S.H. Rasmussen, On single and bimodal optimum buckling loads of clamped columns, International Journal of Solids and Structures 13 (7) (1977) 605–614.
[11] F.Y. Wang, On the extremal fundamental frequencies of one-link flexible manipulators, International Journal of Robotics Research 13 (2) (1994) 162–170.
[12] F.Y. Wang, Optimum design of flexible manipulators: Integration of control and construction. Working Paper 40-91, SIE Department, University of Arizona, Tucson, 1991.
[13] L. Meirovitch, Computational Methods in Structural Dynamics, Sijthoff & Noordhoff, Rockville, IL, 1980.
[14] R.T. Haftka, Z. Gürdal, M.P. Kamat, Elements of Structural Optimization, second ed. Kluwer Academic, Boston, MA, 1990.
[15] A.H. Nayfeh, Perturbation Method, John Wiley, New York, 1973.
[16] F.Y. Wang, G.G. Guan, Influences of rotary inertia, shear deformation and tip load on vibrations of flexible manipulators, Journal of Sound and Vibrations 171 (4) (1994) 433–452.
[17] J.L. Russell, Optimization models for flexible manipulators. Ph.D. dissertation, Department of Systems and Industrial Engineering, University of Arizona, Tucson, 1995.
[18] S. Bailey, A Common Lunar Lander for the Space Exploration Initiative, NASA Johnson Space Center, Houston, TX, 1991.
[19] R.H. Cannon Jr., E. Schmitz, Precise control of flexible manipulators. Robotics Research: The First International Symposium, MA, MIT Press, Cambridge, 1984, pp. 841–861.
[20] W.J. Book, Recursive Lagrangian dynamics of flexible manipulator arms, International Journal of Robotic Research 3 (3) (1984) 87–101.
[21] P.K. Nguyen, R. Ravindran, R. Carr, D.M. Gossain, K.H. Doetsch, Structural Flexibility of the Shuttle Remote Manipulator System Mechanical Arm, SPAR AeroSpace Ltd., Tech. Info. AIAA, 1982.
[22] T. Sakawa, F. Matsuno, S. Fukushima, Modeling and feedback control of a flexible arm, Journal of Robotic Systems 2 (1985) 453–472.
[23] F. Khorrami, U. Ozguner, Perturbation method in control of flexible link manipulators, IEEE International Conference on Robotics and Automation 1 (1988) 310–315.
[24] G.B. Yang, M. Donath, Dynamic model of a one link manipulator with both structural and joint flexibility, IEEE International Conference on Robotics and Automation 6 (3) (1988) 454–461.
[25] F. Bellezze, L. Lanari, G. Ulivi, Exact modeling of the flexible slewing link. IEEE, International Conference on Robotics and Automation 2 (1990) 734–739.
[26] F.Y. Wang, J.T. Wen, Nonlinear dynamical model and control for a flexible beam, CIRSSE Report No. 75, RPI, Tory, NY, 1990.
[27] H. Asada, J.-H. Park, S. Rai, A control-configured flexible arm: Integrated structure/control design, IEEE Conference on Robotics and Automation 3 (1991) 2356–2362.
[28] F.-Y. Wang, J.L. Russell, Optimum shape construction of flexible manipulators with tip loads, Proceedings of IEEE International Conference on Decision and Control 1 (1992) 311–316.
[29] S. Timoshenko, G.H. MacWang, Elements of Strength of Materials, third ed. D. Van Nostrand, New York, 1949.
[30] W.L. Winston, Introduction to Mathematical Programming, PWS-Kent, Boston, 1991.
[31] Z.B. Zabinsky, R.L. Smith, J.F. McDonald, H.E. Romeigh, D.E. Kaufman, Improving hit-and-run for global optimization, Journal of Global Optimization 3 (1993) 171–192.

[32] F.Y. Wang, Optimum design of vibrating cantilevers: A classical problem revisited. Journal of Optimization Theory and Applications, 84(3),(1995) 635-652.
[33] F.Y. Wang, J.L. Russell, Optimum shape construction of flexible manipulators with total weight constraint. IEEE Transactions on Systems, Man and Cybernetics 25 (4) (1995) 605−614.
[34] F.Y. Wang, Exact solutions of three dynamic models for one-link flexible manipulators. RAL Technical Report No. 9, Systems and Industrial Engineering Department, University of Arizona, Tucson, 1991. August.
[35] D.G. Luenberger, Linear and Nonlinear Programming, second ed. Addison-Wesley, 1984.
[36] E.P. Polak, Basics of minimax algorithms, Proceedings of the Summer School on Nonsmooth Optimization and Related Topics (1988). Erice, Italy.
[37] E.J. Wiest, E. Polak, On the rate of convergence of two minimax algorithms, Journal of Optimization Theory and Applications 71 (1) (1991) 1−30.
[38] F.Y. Wang, J.L. Russell, Minimum-weight robot arm for a specified fundamental frequency, Proceedings of the IEEE Conference on Robotics and Automation 1 (1993) 490−495. Atlanta, GA.

CHAPTER 6

Mechatronic Design of Flexible Manipulators*

Chapter Outline

6.1 Introduction 186

6.2 Overview of Mechatronics Design 187

6.2.1 Why Mechatronic Design? 187

Modeling Accuracy and Control Efficiency of Flexible Manipulators 187

Interrelation and Interdependency of Subsystems of Manipulator Systems 188

6.2.2 What is Mechatronic Design? 188

6.2.3 How Does Mechatronic Design Work? 189

6.3 Mechatronic Design of Flexible Manipulators Based on LQR with IHR Programming 190

6.3.1 Dynamics of Flexible Manipulator Systems 190

State-space Equations of Flexible Manipulators 190

Output Specifications 192

6.3.2 LQR Formula: Inner Loop Optimizations 193

LQR: Inner Loop Optimization 194

6.3.3 IHR Algorithm: Outer Loop Optimization 195

IHR: Outer Loop Optimization 195

6.3.4 Integrated Optimization Process 196

Integrated Optimization 196

6.3.5 Results and Discussion 196

6.4 Mechatronic Design of Flexible Manipulators-Based on H_∞ with IHR Algorithm 210

6.4.1 State-Space Formulas for H_∞ Control Problems 210

6.4.2 Generalized Plant of a Flexible Beam System 212

6.4.3 H_∞ Controller Design 215

6.4.4 Simulation Results 216

6.4.5 System Robustness Analysis 225

Sensitivity Analysis 225

Numerical Results of System Robustness 226

6.5 Closed-Loop Design of Flexible Robotic Links 229

6.5.1 Dynamics of Single-Link Flexible Manipulator Systems 230

Link Mechanics 230

Actuator Dynamics 230

---

* *Advanced studies of Flexible Robotic Manipulators*, Fei-Yue Wang and Yanqing Gao, Copyright © 2003, Reproduced with permission from World Scientific Publishing Co. Pte. Ltd.

Flexible Manipulators. DOI: 10.1016/B978-0-12-397036-7.00006-4

Copyright © 2012 Elsevier Inc. All rights reserved.

Control Algorithm 231
6.5.2 Transfer Functions of the Integrated Systems 231
6.5.3 Segmentized Solution for Transfer Functions 232
6.5.4 Optimization Formulations for Mechatronic Design 234
Pole Location Optimization 236
Tracking Error Optimization 236
Reference Model Optimization 236
Minmax Optimization 237
6.6 Concurrent Design 237
6.6.1 General Concepts 238
6.6.2 Existing Representation of Special Concurrent Designs 239
6.6.3 Problems 240
System Analysis 240
Global Optimization 240
6.7 Concurrent Design of a Single-Link Flexible Manipulator Based on PID Controller 241
6.7.1 Dynamics of Single-Link Flexible Manipulator Systems 241
6.7.2 Implementation of Concurrent Design 243
6.7.3 Simulation Results 245
References 248

6.1 Introduction

A manipulator becomes flexible when its link deformation cannot be ignored in the analysis of its performance. A manipulator that has large dimensions is lightweight, fast, or handles a heavy load with flexibility. Flexible manipulators utilize less energy due to their light weight and higher productivity achieved through fast motion. They are safer to operate due to good damping behavior and less pronounced interconnections between the different segments for multiple-link manipulators. These manipulators are found in space exploration (NASA Mars Exploration Mission STS95, 1998) because of the constraints on arm length, weight, and "gravity loss"; in mining applications (robotic excavators) because of their heavy payload; in construction applications (robotic crane systems) because of the length and heavy tip load; and where dexterous manipulators are required, such as in medical operations or chip placement pick-and-place manipulators in electronic assembly manufacture. The NASA Remote Manipulator System has very low natural frequencies and consequently has to move slowly (0.5°/s) in order to avoid vibrations because of its beam mass (450 kg) and its heavy payload (27,200 kg).

In the last decades, research on flexible manipulators has increased dramatically. From the perspective of control, recent research has been carried out by Doyle and Glover [1,2], Francis [3], Gutierrez et al. [4], Jnifene [5], Zabinsky et al. [6] and references therein [7–9]. These studies performed control-intensive work to improve beam performance, but they

ignored the impact of the beam's mechanical properties. The resulting system was only locally optimal. At the same time, another goal was to find a better beam shape so as to move faster but with less vibration. One of the first papers on an optimal shape for flexible manipulators was by Karihaloo and Niordson [10]. Extensive studies on optimal shape design have been conducted by Wang [11], who simplified the scheme substantially. In 1991, this group examined the external fundamental frequencies and developed an iterative scheme, producing the first one-link optimum manipulator shape. It was shown that, by proper selection of the hub, the optimal link could improve the first natural frequency by 600%. A minimum weight design of flexible manipulators was developed by Wang and Russell [12,13]. In 1995, they also investigated a new approach, the segmentized scheme of optimal design, which treats the flexible beam as a collection of small lengths of rigid beam constrained by each other's interfacial conditions [14]. The new technique converts the optimal shape design problem into a matrix determinant problem. In 1996, a new computing method for optimum mass and rigidity distribution was formulated by Wang et al. [15] and Zhou [16] for a flexible manipulator with a tip load. The robustness with respect to design specification and appropriate constraints was considered. Practical issues were also addressed. These studies focused on open-loop design. They only concerned the beam's mechanical construction; that is, a proper design of the flexible beam shape that can make it suffer less vibration. However, in reality, all manipulators must be in a closed loop to obtain high performance. The couplings between the controller and the construction were not largely considered in these designs.

6.2 Overview of Mechatronics Design

6.2.1 Why Mechatronic Design?

Modeling Accuracy and Control Efficiency of Flexible Manipulators

Flexible manipulators are distributed systems described by partial differential equations. Therefore, their dynamic behavior has infinite degrees of freedom. From the perspective of control theory, it is impossible to design an infinite dimensional controller. The controlled plant must have a finite dimension, thereby requiring less significant constituents of the model to be omitted. This causes model uncertainties, since those constituents are generally time variable and system dependent. The boundary conditions set by tip load, hub inertia, friction, rotary inertia, and shear force also affect beam dynamics, which makes model implementation more complicated for the purpose of real-time control. However, the model must be accurate enough to take control into account. The efficiency of modeling and the precision of the control of flexible manipulators are contradictory factors and a compromise between the two for real-time implementation is inevitable.

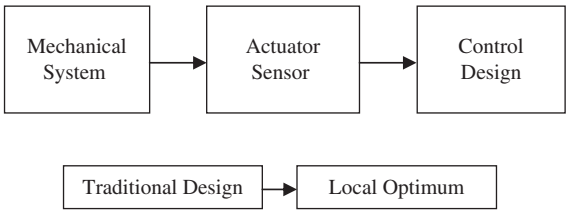

Figure 6.1: Traditional Design Procedure.

Interrelation and Interdependency of Subsystems of Manipulator Systems

The complexity of manipulator systems is also due to the interrelation and interdependency of their subsystems. A manipulator system consists of different subsystems:

- A kinematic system, mainly related to the beam structure
- A control system
- A driver system, or actuator
- A measuring system, or sensors.

Some subsystems exert influence over others, whereas some subsystems are only influenced by others. In traditional design, a manipulator link is designed first, followed by a driver system, measuring system, and then a control system, as shown in Figure 6.1. As a result, this traditional design scheme leads to a locally optimal solution, since these coupling effects have not been considered in the design process.

If a flexible manipulator system can be designed taking the interrelationships between subsystems into account while avoiding control-intensive or model-intensive work, the control and modeling problems will no longer be critical, thus improving productivity and reducing energy consumption. The mechatronic design method (MDM) fits these requirements exactly.

6.2.2 What is Mechatronic Design?

For applications in manipulator systems, the MDM is a system optimization through the integration of actuator, controller, system dynamics, and sensor specifications, as shown in Figure 6.2. Compared with traditional design, the following features can be identified for mechatronic design:

- **Different methodology.** MDM treats the mechanical, electrical, and control components of a flexible manipulator concurrently, instead of sequentially, from the very start of the design process. The coupling effects are automatically taken into account. This in turn results in global optimal objective functions in the system.

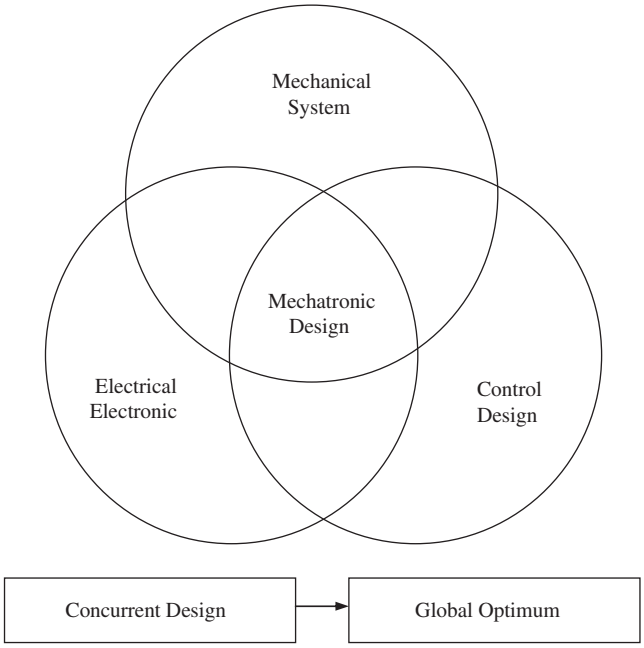

Figure 6.2: Mechatronic Design Procedure.

- **Different direction.** MDM focuses on the system's overall design instead of modeling or control. That is, the objective is to design a better manipulator system so its control problems and dynamic accuracy will not be critical to its performance. In other words, the result of this mechatronic design is better than what is obtained from model-intensive work or control-intensive work.

6.2.3 How Does Mechatronic Design Work?

Let (A,B,C) represent a flexible manipulator system, which is comprised of beam shape, sensor specification, actuator selection, and u the controller. J is the performance index. Assume that Ω is the space of all feasible manipulator systems and Λ is the feasible control space from the actuator. In traditional design

$$J = \inf_{u \in \Lambda} J(u; A, B, C) \tag{6.1}$$

and the objective is to find the optimal control for a system given by (A,B,C) only. But the mechatronic design goes further to find J^* by choosing different (A,B,C) values, by choosing a different beam shape, different sensor and actuator. Then the objective is to minimize the performance index J with respect to link construction, actuator selection, sensor specification, and control design, i.e.

$$J^* = \inf_{(A,B,C)\in\Omega, u\in\Lambda} J(u;A,B,C) = \inf_{(A,B,C)\in\Omega, u\in\Lambda} [\inf J(u;A,B,C)] \tag{6.2}$$

Accordingly, the global optimization can be carried out in two steps. The first step (the inner $\inf_{u\in\Lambda}$ loop) is to find the optimal control structure and its associated optimal value of the performance index based on a given plant (A,B,C), which is exactly the traditional optimal control design problem. The second step (the outer $\inf_{(A,B,C)\in\Omega}$ loop) is to find the optimal feasible plant that will further minimize the performance index obtained by the optimal controller. In this chapter, assuming that the DC motor and sensors are given, the outer loop is only searching the beam shape distribution.

6.3 Mechatronic Design of Flexible Manipulators Based on LQR with IHR Programming

6.3.1 Dynamics of Flexible Manipulator Systems

The dynamics of a flexible manipulator system are described by an infinite-dimensional mathematical model, since the model consists of partial differential equations. But to design a finite-dimensional controller, a finite-dimensional system model is needed. To achieve this goal, a finite-dimensional approximation needs to be used to model a flexible manipulator, retaining a finite number of modes and eliminating the other less significant modes based on the requirements of the controller. The N-mode expansion for the beam displacement $\omega(x,t)$ is given by

$$\omega(x,t) = \sum_{i=1}^{N} \varphi_i(x) q_i(t) \tag{6.3}$$

The separability in this case refers to describing the displacement as a series of terms that are products of two separate functions, each of which is a function of a single variable, a spatial variable x and time t respectively. φ_i is the ith modal shape, or eigenfunction. q_i is the corresponding generalized modal coordinate describing the flexible deformation.

The scheme for developing a mathematical model is to use the Lagrangian method or Hamilton's principle for the total kinetic energy, total potential energy, and virtual work done by the torque actuated to the joint. This method will not introduce extra errors into the system and will be used to obtain the state-space model for a flexible manipulator suggested in this chapter [16].

State-space Equations of Flexible Manipulators

In Section 3.5.2, dynamic equations of a one-link flexible manipulator in matrix form were obtained as

$$M\ddot{x} + Kx = b\tau \tag{6.4}$$

where

$$x = [\theta, q_1, q_2, q_3, \ldots, q_N]^T_{(N+1,1)}, \quad b = [1, \psi_1'(0), \psi_2'(0), \ldots, \psi_N'(0)]^T_{(N+1,1)}$$

$$M = \begin{bmatrix} \Omega_1 & \Omega_2(1) & \Omega_2(2) & \cdot & \Omega_2(N) \\ \Omega_2(1) & \Omega_3(1,1) & \Omega_3(1,2) & \cdot & \Omega_3(1,N) \\ \cdot & \cdot & \cdot & \cdot & \cdot \\ \Omega_2(N) & \Omega_3(N,1) & \Omega_3(N,2) & \cdot & \Omega_3(N,N) \end{bmatrix} \tag{6.5}$$

$$K = \begin{bmatrix} 0 & 0 & 0 & \cdot & 0 \\ 0 & k(1,1) & k(1,2) & \cdot & k(1,N) \\ \cdot & \cdot & \cdot & \cdot & \cdot \\ 0 & k(N,1) & k(N,2) & \cdot & k(N,N) \end{bmatrix}$$

As has been shown, $\Omega_3(i,j) = \Omega_3(j,i)$, $k(i,j) = k(j,i)$, and thus the matrices M, K are symmetric and are called the mass and rigidity matrices respectively.

Next, the actuator dynamics need to be incorporated into the link system. It is assumed that the arm is driven by a permanent magnet DC motor. Therefore, the actuator dynamics can be described as

$$-J_m\ddot{\theta} - \left(B_m + \frac{K_b K_m}{R}\right)\dot{\theta} + \frac{K_m}{R}v_c = \tau \tag{6.6}$$

where J_m is the actuator inertia, B_m the friction coefficient, K_m the torque constant, K_b the back e.m.f. constant, R the armature resistance, and θ, v_c the hub rotation and armature voltage respectively. In general, all motor circuit parameters can be considered as design variables. The overall state variable is defined as

$$q = \begin{bmatrix} x \\ \dot{x} \end{bmatrix} \tag{6.7}$$

Combining Eq. (6.4) with Eq. (6.5), we present the overall system state-space equations as

$$\dot{q} = Aq + Bu, \quad u = v_c \tag{6.8}$$

where

$$A = \begin{bmatrix} 0 & I \\ -M^{-1}K & -M^{-1}\overline{B} \end{bmatrix}, \quad B = \begin{bmatrix} 0 \\ M^{-1}\overline{D} \end{bmatrix}$$

$$\overline{M} = (M + J_m b\underline{e}_1)^{-1}, \quad \overline{B} = \left(B_m + \frac{K_b K_m}{R}\right) b\underline{e}_1, \tag{6.9}$$

$$\overline{D} = b\frac{K_m}{R}, \quad \underline{e}_1 = [1 \quad 0 \quad \ldots \quad 0]_{1\times n}$$

A is the function of beam construction. Thus, any changes in the beam's mechanical shape will result in a different A, which provides the basis for simultaneous optimal construction and control based on the mechatronic formulation discussed earlier.

Output Specifications

As can be seen from the system state-space equations, the state vector consists of θ, the generalized modal coordinates q_i and their first-order derivatives. So all controllers based on the state feedback are indirect, which means that the states need to be predicted. This will mean a trade-off with computation time and introduces a further inaccuracy into closed-loop, cutoff bandwidth. This presents hindrances to real-time processing and high motion speed. Output feedback takes precedence over state-space feedback as far as the mechatronic approach and the objectives of this chapter are concerned.

Tip deflection output is

$$y = w(L,t) = \sum_{i=1}^{N} \psi_i(L) q_i = [0 \quad \psi_1(L) \quad \psi_2(L) \quad \dots \quad \psi_N(L) \quad \overline{0}]q \tag{6.10}$$

where ψ_i is the ith eigenfunction and $\overline{0}_{1\times(n+1)}$ is the zero vector. A CCD camera clipped on the hub can be used to measure the output.

The tip position output is

$$y = v(L,t) = L\theta + \sum_{i=1}^{N} \psi_i(L) q_i = [L \quad \psi_1(L) \quad \psi_2(L) \quad \dots \quad \psi_N(L) \quad \overline{0}]q \tag{6.11}$$

and the hub tangent angle output is

$$y = \Theta = \theta + \sum_{i=1}^{N} \psi_i'(0) q_i = [L \quad \psi_1'(0) \quad \psi_2'(0) \quad \dots \quad \psi_N'(0) \quad \overline{0}]q \tag{6.12}$$

A potentiometer may be used to measure Θ.

In this mechatronic design, output feedback may be one of the above outputs or a mixture, such as

$$\begin{aligned} y &= Cq = \begin{bmatrix} w(L,t) \\ v'(L,t) \end{bmatrix} q \\ C &= \begin{bmatrix} 0 & \psi_1(L) & \psi_2(L) & \dots & \psi_N(L) & \overline{0} \\ 1 & \psi_1'(0) & \psi_2'(0) & \dots & \psi_N'(0) & \overline{0} \end{bmatrix} \end{aligned} \tag{6.13}$$

The corresponding state-variable equations are

$$\dot{q} = Aq + bu, \quad y = Cq \tag{6.14}$$

These output feedbacks will be used in control design in the later sections to show the improvement in the suggested mechatronic approach and to make a comparison between them.

As stated, mechatronic design is a global optimization of the overall system. For a flexible manipulator, the overall system consists of the integration of link dynamics, DC motor equation, measuring sensors, and the selected controller. The optimization process will result in an optimal link geometric distribution, an optimal controller structure subject to the performance requirement. To demonstrate this approach and also due to the computational complexity, the following restrictions are applied here. A rectangular beam is considered and divided into N equal segments along with the beam spatial coordinate. Each segment is uniform. In each segment, the width is the only variable to be optimized for the link geometry.

It was pointed out that output feedback instead of state-space feedback is a feasible choice. It is also possible that the optimum system performance index may not matter in the selection of the controller to a large degree, since the resulting index is the result of the overall system optimization. Due to this factor, the linear quadratic regulator (LQR) is admissible as the selected controller.

Mechatronic design based on the LQR formula is discussed here. The LQR feedback is outlined in Ref. [17] as an inner loop followed by an adaptive iterative algorithm (IHR) as an outer loop searching for the beam width distribution. The mechatronic design procedure is addressed by detailing the integration of the inner loop with the outer loop.

6.3.2 LQR Formula: Inner Loop Optimizations

For the flexible manipulator system given by Eq. (6.14), the LQR controller will be a linear output feedback of the form:

$$u = \Re y \tag{6.15}$$

where $\Re$ is a matrix of constant feedback coefficients to be determined. If the quadratic performance index (PI) is

$$J(u) = \frac{1}{2}\int_{t_0}^{\infty} (q^T(t)Qq(t) + u^T(t)Ru(t))\mathrm{d}t \tag{6.16}$$

where the Q, R are symmetric positive semi-definite weighting matrices, and after substituting the feedback controller Eq. (6.15) into Eq. (6.16), also assuming that the system is asymptotically stable so the $q(t)$ vanishes with time:

$$\lim_{t\to\infty} q^T(t)Pq(t) = 0 \tag{6.17}$$

where P can be solved by the Lyapunov equation:

$$A_c^T P + PA_c + C^T \Re^T R \Re C + Q = 0, \quad (A - B\Re C) = A_c \tag{6.18}$$

Then:

$$J = \frac{1}{2} q^T(0) P q(0) = \frac{1}{2} tr(PX) \tag{6.19}$$

where the $n \times n$ symmetric matrix X is defined by $q(0)q^T(0)$.

Following the substitution process in Ref. [17], two additional equations are described as

$$\begin{aligned} &A_c S + SA_c^T + X = 0 \\ &\Re = R^{-1} B^T P S C^T (CSC^T)^{-1} \end{aligned} \tag{6.20}$$

where $X = q(0)q^T(0)$ and S is a symmetric matrix of Lagrange multipliers.

It is now clear that the problem of selecting $\Re$ to minimize J subject to the dynamic constraint of Eq. (6.14) on the states is equivalent to the algebraic problem of selecting $\Re$ to minimize Eq. (6.20) subject to the constraint of Eq. (6.18) on the auxiliary matrix P. To solve this modified problem, we use the Lagrange multiplier method.

The equations for P, S, and $\Re$ are coupled among these nonlinear matrix equations. Therefore, some trial-and-error iterative design methods have to be used to find $\Re$. The process to find the feedback matrix $\Re$ is described as follows for a given set of A, B, C.

LQR: Inner Loop Optimization

1. Initialize:
   $i = 0$, select an initial $\Re_0$ so that A_c is asymptotically stable; set system initial state values $X = q(0)q^T(0)$ and the Stop criterion $\wp$.
2. ith iteration:
   Set $A_i = A - B\Re_i C$.
   Use *lyap.m* in the Control Toolbox of Matlab to solve the equations
   $A_i^T P + PA_i + C1 = 0$, where $C1 = C^T \Re R \Re_i C + Q$ and $A_i S + SA_i^T = 0$ for P_i and S_i.
   Set $J = ½tr(P_i X)$.
3. Updating:
   Gain updating direction: $\Delta\Re = R^{-1} B^T P_i S_i C^T (CS_i C^T)^{-1} - \Re_i$.
   Update gain: $\Re_{i+1} = \Re_i + \alpha \Delta\Re$
   where α is chosen so that $A - B\Re_{i+1} C$ is asymptotically stable.
   Check the eigenvalues of the new A; if unstable go to Step 5.
4. Criteria:

$$J_{i+1} = \frac{1}{2} tr(P_{i+1} X) \le J_i$$

If $(J_{i+1} - J_i) \leq \wp$, the given criterion, go to 5. Otherwise set $i = i + 1$ and go to Step 2.

5. Stop:
   Set $\Re = \Re_{i+1}$, $J = J_{i+1}$.
   If index $= 0$, go to Step 2.

This process will converge to J, the minimum performance index for the set of A, B, C, by searching proper feedback matrix $\Re$. In the next section, the outer loop searching the optimal beam shape will be discussed.

6.3.3 IHR Algorithm: Outer Loop Optimization

It was established that the components in the matrices of the state equations are related to a given link shape, meaning that matrices A, B, C are functions of the beam geometric distribution. Here, a procedure to find the link geometrics based on the adaptive Iterative Hit and Run (IHR) algorithm [9] is outlined. Some restrictions should be made clear from the perspective of the mechatronic design. Firstly, the beam weight remains constant, which, in terms of beam volume, means that the whole volume is constant. The only variable for the beam geometric is the width of the cross-section for each segment. However, the sum of these width variables must remain constant in order to keep the total volume constant based on an N segment solution. Another consideration, realistically, is that minimum stress on the beam is required, which, in terms of beam width, is its minimum width. These restrictions are applied to modify the IHR algorithm. The iterative procedure of the modified IHR can be specified as follows.

IHR: Outer Loop Optimization

1. Set uniform area A_0, minimum and maximum area constraints, $A_{\min}$ and $A_{\max}$, according to the beam strength requirement. Set $j = 1$. Set beam material parameters.
2. Calculate the uniform beam PI as the starting value.
3. Initialize loop vectors, loop factors, direction vector D, and stop criteria.
4. Select changing positions: randomly select $N/2$ of the N segments and mark them with 1s in vector D_j of length N. Mark the remaining $N/2$ segments with -1s. If N is odd, one randomly selected area will remain constant and will be marked by a 0.
5. Set direction vector: get $N/2$ samples from an $N(0,1)$ normal distribution and place them in each position of D_j where there is a 1. Place the negatives of this same sample in each position of D_j where there is a -1. This arrangement will ensure a constant volume during optimization. Here, D_j is called the direction vector.
6. Implement direction: generate a step size, S, uniformly from L_j the set of feasible step sizes in the direction D_j, where $L_j = \{S \in \Re : A_{\min} < A_j + SD_j < A_{\max}\}$. If $L_j = 0$, go to Step 4.
7. Set $S = S * \text{MUL}$, while $0 < \text{MUL} < 1$.
8. Update the area vector A_j:

$$A_{j+1} = A_j + SD_j$$

6.3.4 Integrated Optimization Process

Mechatronic design is about choosing the best plant and finding the associated controller for the performance requirement. It is an overall optimization process. This can be done by the integration of the inner loop optimization with the outer loop optimization as follows.

Integrated Optimization

1. Set design vector $\Xi = [I_H, M_p, a_c, J_p, L, B, E]$ and number of segments N. Set step multiplier MUL to 1 and FACTOR to an appropriate constant.
2. Set weighting matrices Q and R.
3. Load precalculated coefficients for modal shapes.
4. Calculate A_0 (uniform shape radius or width), set initial $index = 0$ and call LQR to get the corresponding J_0.
5. Update the area vector A_j.
   a. Call IHR to find A_j.
   b. Based on mode shape coefficients and current link geometry, calculate mass matrix M, potential matrix K, vectors B, C, and state equations after integration with motor dynamics.
   c. Call LQR to find J. If J is improving, set $J_{J+1} = J(A_{J+1})$. If J is improved, store it in an array and save this A_j. Update all loop variables and factors.
6. If all the differences between two J values in the array are smaller than the stopping criteria, stop. Otherwise, go to Step 5.
7. Stop. Output optimal feedback matrix $\Re^*$, optimal performance index J^*, and optimal flexible link structure A^*.

6.3.5 Results and Discussion

In order to verify the mechatronic method presented in this chapter, a rectangular aluminum flexible link is used for simulation. The mechatronic algorithm is intended to find the beam's geometric shape, or the width distribution, so that the PI reaches a minimum.

To meet the minimum stress requirement pointed out earlier, the maximum width $H_{\max}$ and the minimum width $H_{\min}$ are set at twice, and a quarter of, the uniform width separately. For the IHR algorithm, all other criteria were set to 0.000001.

To fully test this mechatronic design algorithm, the different output feedback combined with various state weighting matrix Q and the number of segments N, but with $R = I$ (identity), were used. Three sets of feedback were considered. They were the hub tangent angle $\{\Theta(0,t)\}$ feedback (Eq. (6.12)), the hub tangent angle with tip deflection $\{\Theta(0,t),\omega(L,t)\}$ (Eqs (6.10) and (6.12)), and the hub tangent angle with tip position $\{\Theta(0,t),v(L,t)\}$ (Eqs (6.8) and (6.10)). These sets of feedback have very clear physical meanings and are detectable. The initial state

set is $q_1(0) = [\sqrt{10}, 0, \ldots, 0]^T$. The scenario ({*feedback list*},*number of segments*,Q) was used, meaning that the feedback strategy is as {*feedback list*}, that the beam is divided into a *number of segments*, and that the value Q in LQR is Q. These notations are applied in the following figures and tables.

Note that it was necessary to show the PIs with a different number of segments. To do that, a performance index was set with $q = q_1(0)$, $Q = 100 \times I$, and with various $n = 4$, 6, 12, and one of these three sets of feedback. For uniform and associated optimal shapes, performance indices were obtained with different feedback and a different number of segments, as in Table 6.1. Column 1 is the type of feedback, while columns 2, 3, and 4 are for the different numbers of segments respectively. The performance indices of the optimal shape are improved over that of the associated uniform shape. For example, when $n = 4$ and $\{\Theta(0,t),\omega)\}$ feedback is applied, the PI for uniform shape is 3789.143, while the result for the mechatronic design is smaller, 3591.341. However, the performance indices show only a slight dependence on the number of segments. The associated feedback constants are listed in Table 6.2.

The related optimal shapes are illustrated as follows. In all figures, the solid outline is the optimal shape and the dotted one is for the uniform shape. The horizontal axis is the link spatial coordinate, the vertical axis is the beam width.

Table 6.1: Performance index with $Q = 100 \times I$

Feedback List	$n = 4$	$n = 6$	$n = 12$
$\{\Theta(0,t)\}$ feedback—uniform shape	4665.504	4665.504	4665.504
$\{\Theta(0,t)\}$ feedback—optimal shape	4647.230	4646.571	4643.038
$\{\Theta(0,t),w\}$ feedback—uniform shape	3789.143	3789.143	3789.143
$\{\Theta(0,t),w\}$ feedback—optimal shape	3591.341	3585.945	3580.064
$\{\Theta(0,t),v\}$ feedback—uniform shape	4342.569	4342.569	4342.569
$\{\Theta(0,t),v\}$ feedback—optimal shape	4180.548	4178.569	4176.437

Table 6.2: Optimal feedback constants with $Q = 100 \times I$

Feedback List	$n = 4$	$n = 6$	$n = 12$
$\{\Theta(0,t)\}$ feedback—uniform	3.674	3.674	3.674
$\{\Theta(0,t)\}$ feedback—optimal	3.686	3.677	3.675
$\{\Theta(0,t),w\}$ feedback—uniform	(2.7599−422.398)	(2.7599−422.398)	(2.7599−422.398)
$\{\Theta(0,t),w\}$ feedback—optimal	(2.498−337.071)	(2.539−380.396)	(2.423−378.554)
$\{\Theta(0,t),v\}$ feedback—uniform	(2502.705−2499.521)	(2502.705−2499.521)	(2502.705 −2499.521)
$\{\Theta(0,t),v\}$ feedback—optimal	(1768.423−1765.672)	(1732.346−1747.358)	(1746.276−1764.428)

Figures 6.3–6.5 show $\Theta(0,t)$ feedback (hub tangent angle) with $Q = 100 \times I$ and $n = 4, 6, 12$ respectively. All three optimal shapes have one common feature, with a large size at the hub end and a small size at the tip end.

Figures 6.6–6.8 illustrate $(\Theta(0,t)\omega(L,t))$ feedback (hub tangent angle, tip deflection) with $Q = 100 \times I$ and $n = 4, 6, 12$ respectively. In the same way, the best performance indices are

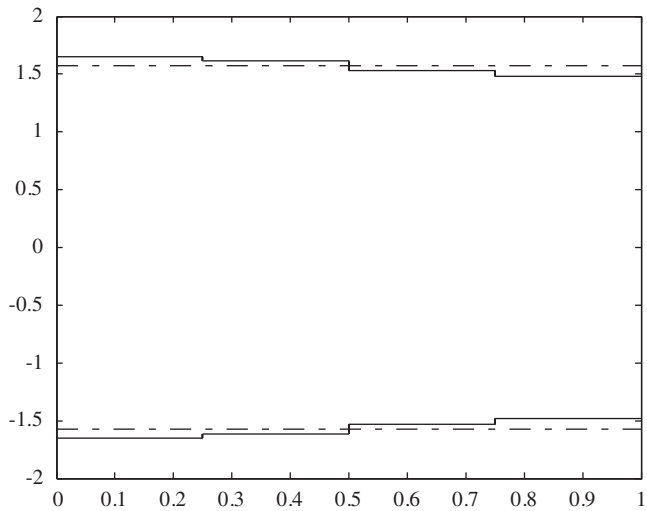

Figure 6.3: Optimal Shape for ({Θ(0,*t*)},4,100).

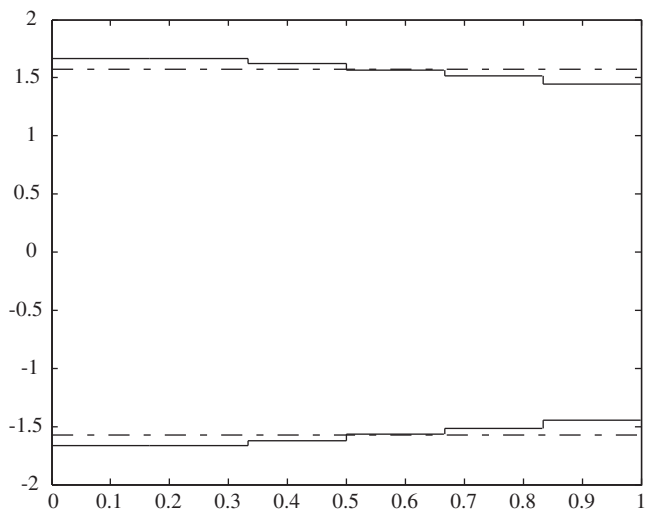

Figure 6.4: Optimal Shape for ({Θ(0,*t*)},6,100).

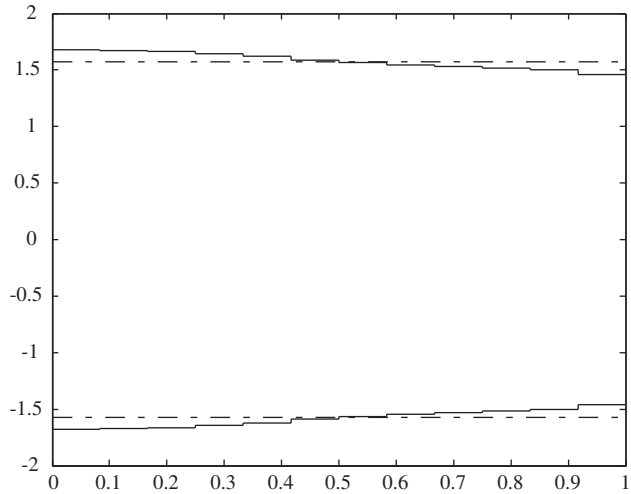

Figure 6.5: Optimal Shape for ({Θ(0,*t*)},12,100).

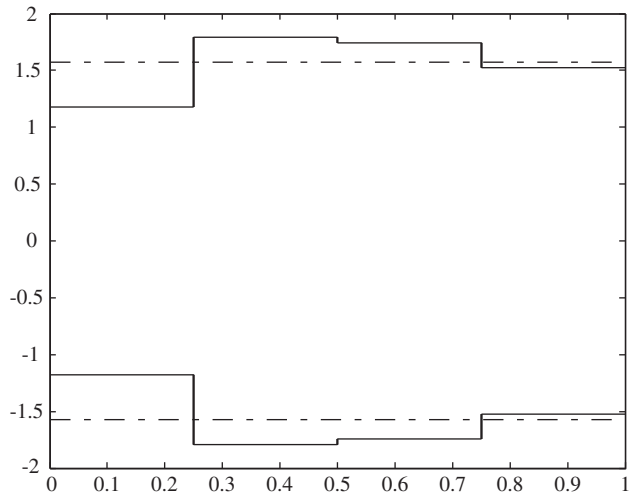

Figure 6.6: Optimal Shape for ({Θ(0,*t*),*w*},4,100).

almost the same for a different number of segments. A common feature of these three optimal shapes is a large beam size in the middle and a relatively small size at both ends.

Figures 6.9–6.11 show $(\Theta(0,t)v(L,t))$ feedback (hub tangent angle, tip position) with $Q = 100 \times I$ and $n = 4$, 6, 12 respectively. As before, the best performance indices are almost the same for different numbers of segments. A common feature of these three

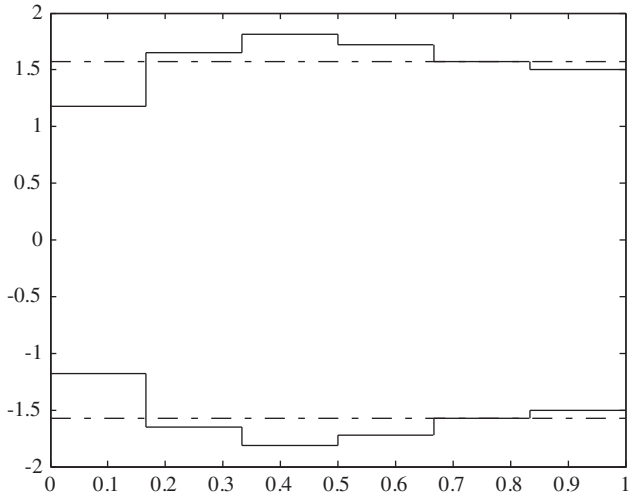

Figure 6.7: Optimal Shape for ({Θ(0,*t*),*w*},6,100).

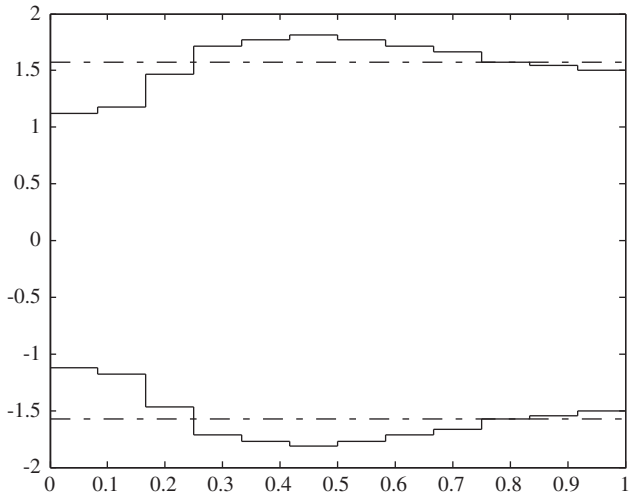

Figure 6.8: Optimal Shape for ({Θ(0,*t*),*w*},12,100).

optimal shapes is a relatively small beam dimension in the middle and a large dimension at the ends.

As shown in these figures, the geometric shapes of these optimal shapes are influenced significantly by the type of feedback, and not very much by the number of segments. Next, this mechatronic approach was applied to different weighting matrix Q with these types of feedback. The number of segments was fixed as 4 since the number of segments play a less

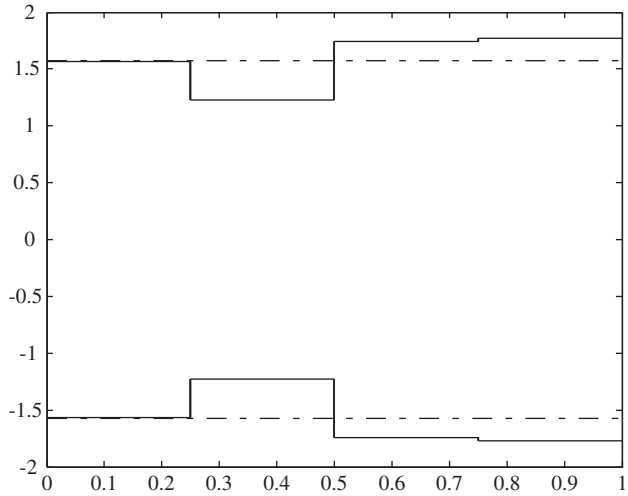

Figure 6.9: Optimal Shape for ({Θ(0,*t*),*v*},4,100).

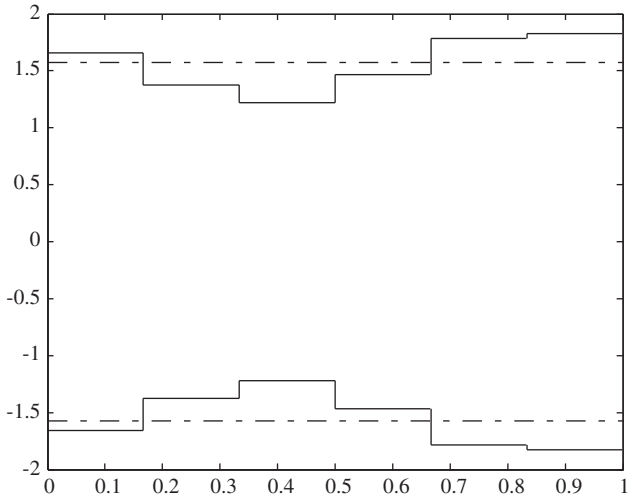

Figure 6.10: Optimal Shape for ({Θ(0,*t*),*v*},6,100).

important role here. Q was taken as $50 \times I$ and $10 \times I$. The performance indices are listed in Table 6.3, where the columns denote different types of feedback, and the rows different values of Q. The associated feedback constants are listed in Table 6.4.

Figures 6.12 and 6.13 show $\Theta(0,t)$ feedback (hub tangent angle) with different weighting matrix Q. As before, the optimal shapes have relatively large dimensions on the hub side.

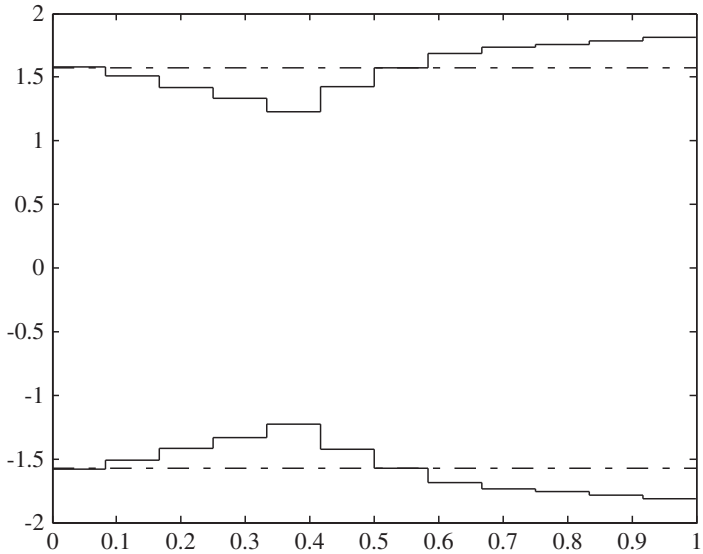

Figure 6.11: Optimal Shape for ({Θ(0,*t*),*v*},12,100).

Table 6.3: Performance index with different $Q = 100 \times I$, $50 \times I$, $10 \times I$

Beam Shape	{Θ(0,*t*)}	{Θ(0,*t*),*w*}	{Θ(0,*t*),*v*}
$Q = 100 \times I$—uniform shape	4665.504	3781.547	4342.763
$Q = 100 \times I$—optimal shape	4647.230	3591.538	4180.546
$Q = 50 \times I$—uniform shape	2611.373	2174.499	2421.595
$Q = 50 \times I$—optimal shape	2540.470	2098.374	2388.850
$Q = 10 \times I$—uniform shape	679.856	630.266	670.482
$Q = 10 \times I$—optimal shape	663.834	621.442	638.356

Table 6.4: Optimal feedback constants with different $Q = 100 \times I$, $50 \times I$, $10 \times I$

Beam Shape	{Θ(0,*t*)}	{Θ(0,*t*),*w*}	{Θ(0,*t*),*v*}
$Q = 100 \times I$—uniform shape	3.674	(2.7599−422.398)	(2502.705−2499.521)
$Q = 100 \times I$—optimal shape	3.686	(2.498−337.071)	(1768.423−1765.672)
$Q = 50 \times I$—uniform shape	(2.7599−422.398)	(2.279−395.458)	(2.7599−422.398)
$Q = 50 \times I$—optimal shape	(2.759−422.398)	(2.096−335.370)	(2.423−378.554)
$Q = 10 \times I$—uniform shape	1.659	(1.604−167.576)	(1138.098−1194.508)
$Q = 10 \times I$—optimal shape	1.653	(1.386−166.142)	(1045.568−1065.754)

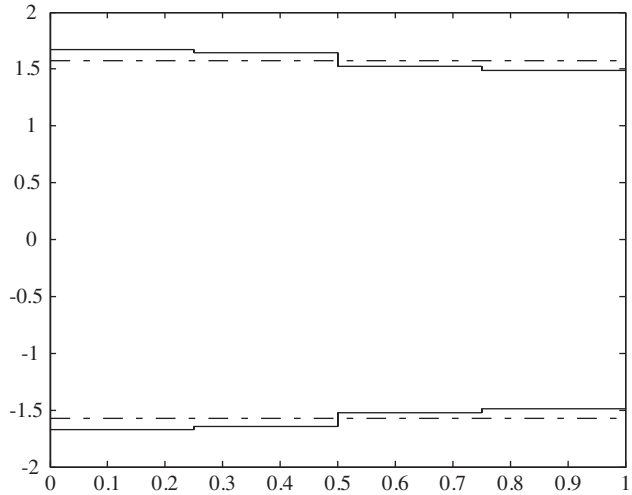

Figure 6.12: Optimal Shape for ({Θ(0,*t*)},4,50).

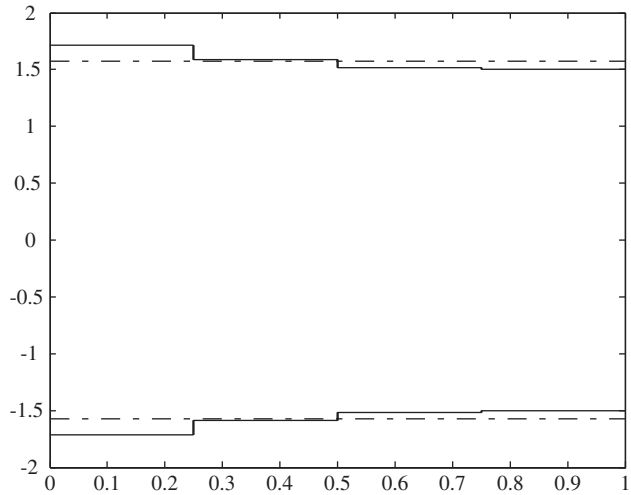

Figure 6.13: Optimal Shape for ({Θ(0,*t*)},4,10).

Figures 6.14 and 6.15 illustrate ($\Theta(0,t)\omega(L,t)$) feedback (hub tangent angle, tip deflection) with a different weighting matrix Q. The optimal shapes have a relatively large dimension in the middle.

Figures 6.16 and 6.17 show ($\Theta(0,t)v(L,t)$) feedback (hub tangent angle, tip position) with different weighting matrix Q. The optimal shapes have relatively small dimensions in the middle.

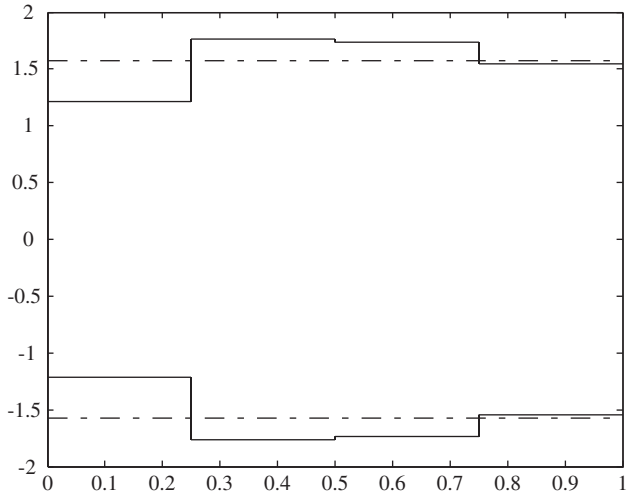

Figure 6.14: Optimal Shape for ({Θ(0,*t*),*w*},4,50).

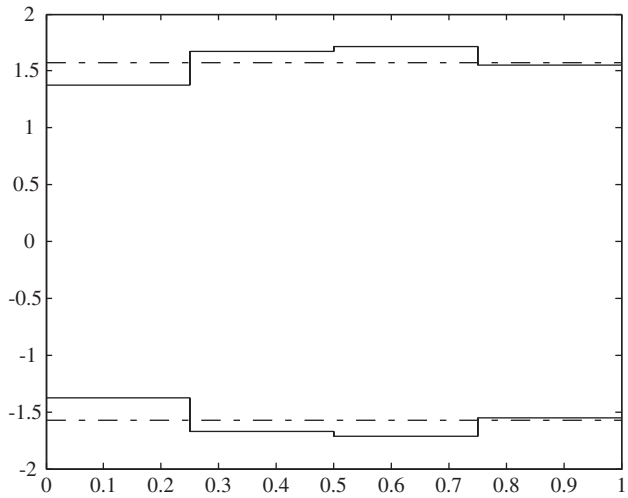

Figure 6.15: Optimal Shape for ({Θ(0,*t*),*w*},4,10).

Figures 6.18 and 6.19 illustrate hub tangent angle responses to initial state $q_1(0)$ for $\Theta(0,t)$ (hub tangent angle) and $(\Theta(0,t)w(L,t))$ (hub tangent angle, tip deflection) feedback respectively.

Figures 6.20 and 6.21 show the hub tangent angle responses to step input for $\Theta(0,t)$ (hub tangent angle) and $(\Theta(0,t)w(L,t))$ (hub tangent angle, tip deflection) feedback respectively.

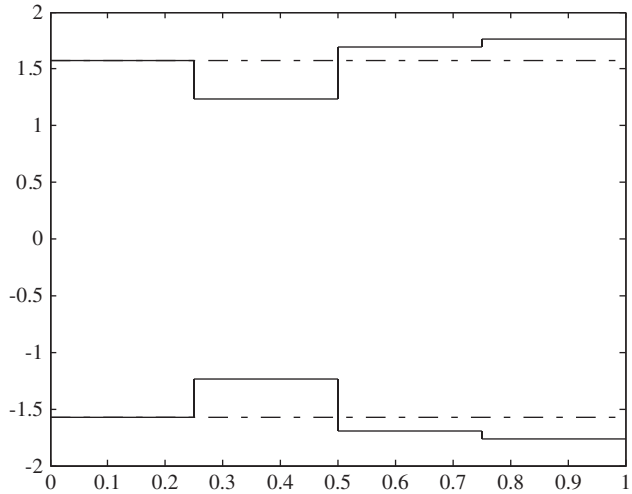

Figure 6.16: Optimal Shape for ({Θ(0,*t*),*v*},4,50).

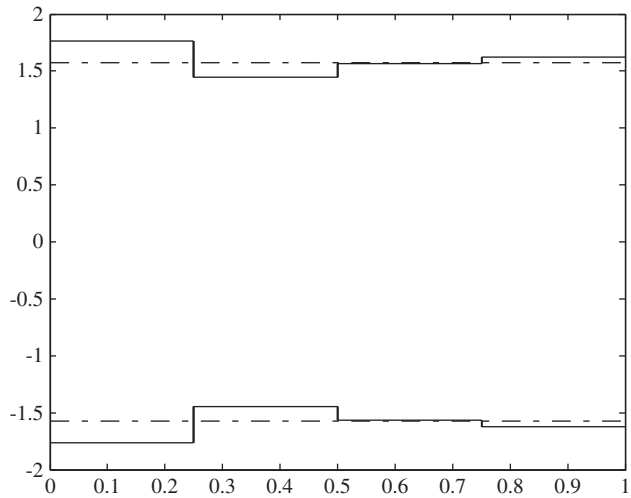

Figure 6.17: Optimal Shape for ({Θ(0,*t*),*v*},4,10).

Figures 6.22 and 6.23 illustrate the tip deflection responses to initial $q_1(0)$ for $\Theta(0,t)$ (hub tangent angle) and $(\Theta(0,t)w(L,t))$ (hub tangent angle, tip deflection) feedback respectively.

Figures 6.24 and 6.25 show the tip deflection step input responses for $\Theta(0,t)$ (hub tangent angle) and $(\Theta(0,t)w(L,t))$ (hub tangent angle, tip deflection) feedback respectively.

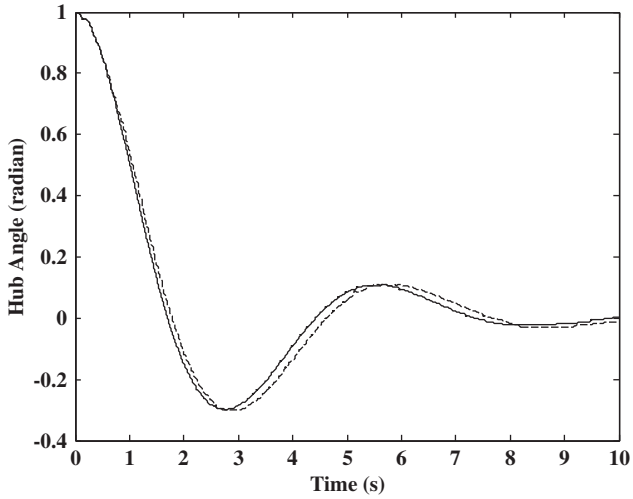

Figure 6.18: Hub Tangent Angle Initial Response for ({Θ(0,*t*)},4,100).

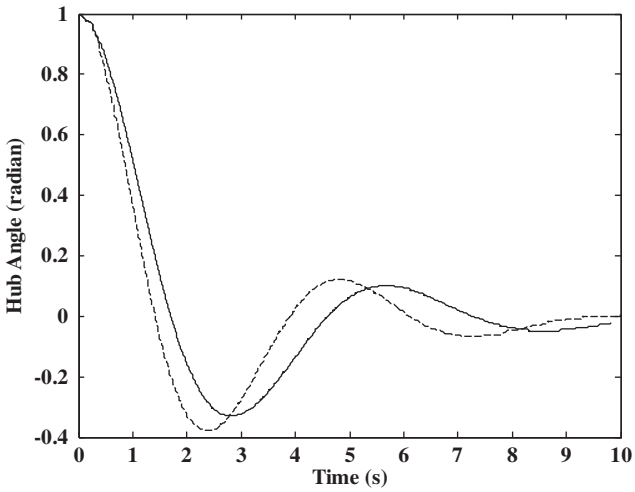

Figure 6.19: Hub Tangent Angle Initial Response for ({Θ(0,*t*),*w*(*L*,*t*)},4,100).

These results show that the performance index shows only a slight dependence on the number of segments, because according to this mechatronic algorithm, the final shape converges to its optimal shape. A system with two output feedbacks has a relatively lower performance index than one with only one output feedback, since the former has a higher degree of freedom to work with. The optimal shape for $\Theta(0,t)$ feedback is always larger on the hub side

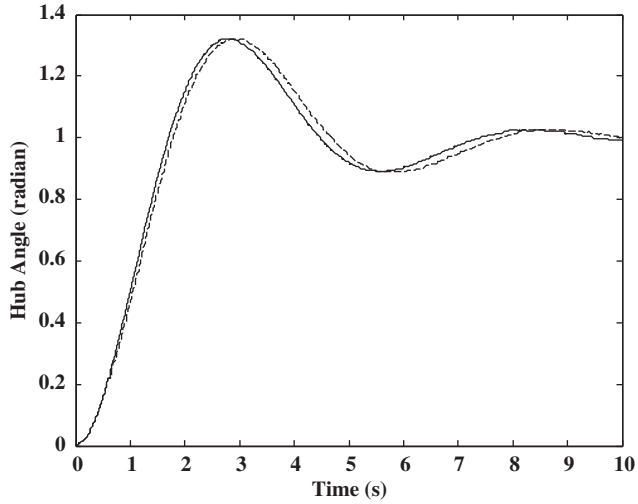

Figure 6.20: Hub Tangent Angle Step Input Response for ({Θ(0,*t*)},4,100).

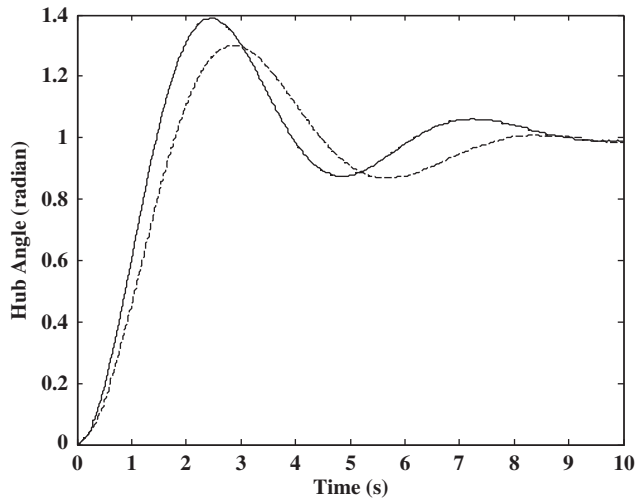

Figure 6.21: Hub Tangent Angle Step Input Response for ({Θ(0,*t*),*w*(*L*,*t*)},4,100).

and smaller at the tip end. The optimal shape for ($\Theta(0,t)w(L,t)$) has smaller dimensions at the ends, while the optimal shape for $\{\Theta(0,t)v(L,t)\}$ is smaller in the middle. For optimal shapes, the initial responses have less vibration and fast convergence. The step input response of the hub tangent angle for the optimal shape has a smaller rising time and the tip deflection converges much faster than those of uniform shapes.

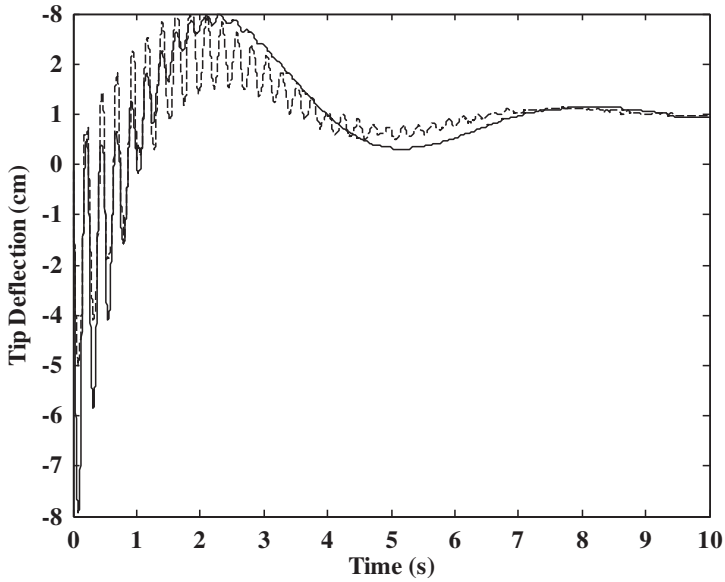

Figure 6.22: Tip Deflection Initial Response for ({Θ(0,*t*)},4,100).

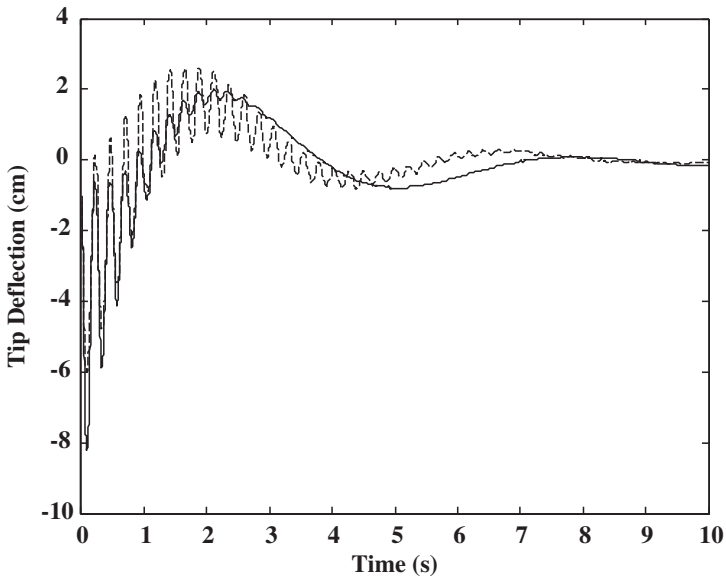

Figure 6.23: Tip Deflection Initial Response for ({Θ(0,*t*),*w*(*L*,*t*)},4,100).

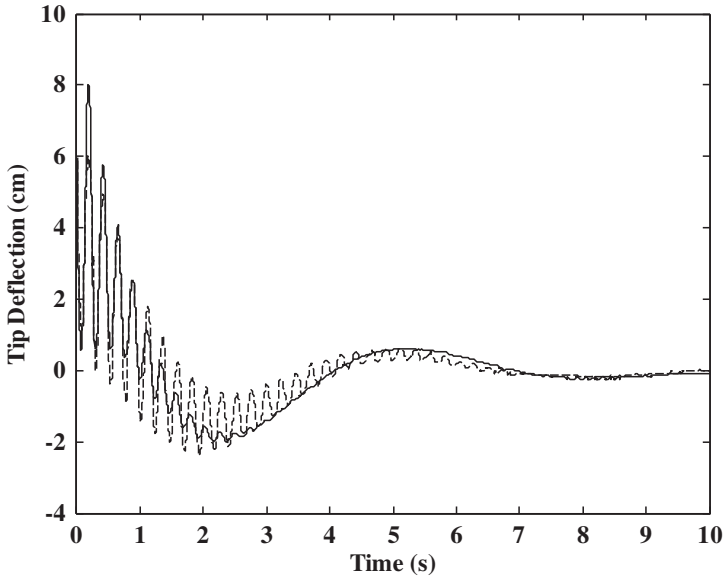

Figure 6.24: Tip Deflection Step Input Response for ({Θ(0,*t*)},4,100).

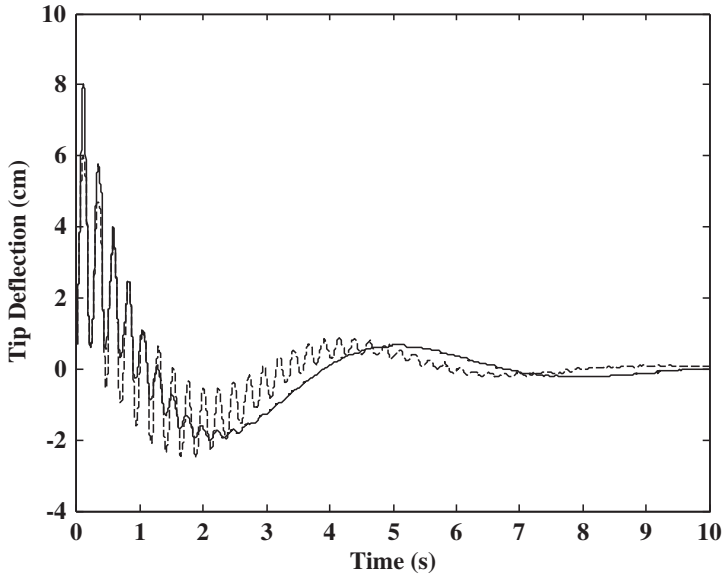

Figure 6.25: Tip Deflection Step Input Response for ({Θ(0,*t*),*w*(*L*,*t*)},4,100).

6.4 Mechatronic Design of Flexible Manipulators-Based on H_∞ with IHR Algorithm

6.4.1 State-Space Formulas for H_∞ Control Problems

A basic block diagram used in the state-space H_∞ controller [18,19] is where $G(s)$ is a generalized plant that includes what is usually called plant and all weighting functions, and K is the controller. They are all real, rational, and proper. All external inputs such as disturbances, measurement noise, model uncertainties, and unmodeled high-order vibrational dynamics are characterized as d. Signal z is the error output, u is the control input, and y is the measured variable (see Figure 6.26).

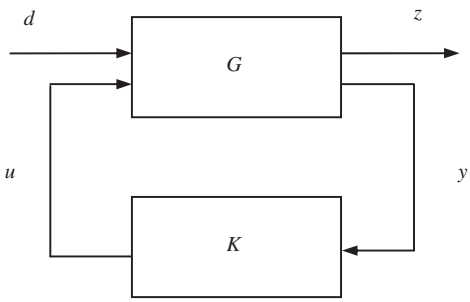

Figure 6.26: H_∞ Control Problem Configuration.

If the state-space equations in Ref. [20] are referred to, the linear system

$$\dot{x}(t) = A\,x(t) + B_1\,d(t) + B_2\,u(t) \tag{6.21a}$$

$$z(t) = C_1\,x(t) + D_{11}\,d(t) + D_{12}\,u(t) \tag{6.21b}$$

$$y(t) = C_2\,x(t) + D_{21}\,d(t) + D_{22}\,u(t) \tag{6.21c}$$

is obtained. Then the transfer function $G(s)$ is denoted as

$$G(s) = \begin{bmatrix} G_{11}(s) & G_{12}(s) \\ G_{21}(s) & G_{22}(s) \end{bmatrix}$$

$$= \begin{bmatrix} C_1 \\ C_2 \end{bmatrix} (sI - A)^{-1} [B_1 \;\; B_2] + \begin{bmatrix} D_{11} & D_{12} \\ D_{21} & D_{22} \end{bmatrix} = \begin{bmatrix} A & B_1 & B_2 \\ C_1 & D_{11} & D_{12} \\ C_2 & D_{21} & D_{22} \end{bmatrix} = \begin{bmatrix} A & B \\ C & D \end{bmatrix}$$

The transfer function from d to z is

$$T_{dz}(G,\, k) = G_{11} + G_{12}K(I - G_{22})^{-1}G_{21}$$

Then the H_∞ control problem is to design the controller $K(s)$ so that:

1. The system is internally stable, meaning the states of $G(s)$ and $K(s)$ tend to zero from all initial values when $d = 0$.
2. $\min \|T_{dz}\|_\infty = \min \sup_\omega \overline{\Delta}(T_{dz}(j\omega))$, where $\overline{\Delta}()$ denotes the maximum singular value.

If A, R, Q are $n \times n$ matrices and with symmetric R, Q, the Hamiltonian matrix is defined as

$$H = \begin{bmatrix} A & R \\ -Q & -A' \end{bmatrix}$$

Then there exists a symmetric $x := Ric(H)$, which satisfies the Riccati equation:

$$A\dot{x} + xA' + xRx + Q = 0$$

Two Hamiltonian matrices are involved in the H_∞ control problem:

$$H_\infty = \begin{bmatrix} A & r^{-2}B_1B_1' - B_2B_2' \\ -C_1'C_1 & -A' \end{bmatrix}$$

$$J_\infty = \begin{bmatrix} A' & r^{-2}C_1C_1' - C_2C_2' \\ -B_1'B_1 & -A \end{bmatrix}$$

For $\|T_{dz}\|_\infty \leq r$, a performance index for noise attenuation from input d to output z, an admissible H_∞ controller [18] exists if:

1. $X_\infty = Ric(H_\infty) \geq 0$.
2. $Y_\infty = Ric(J_\infty) \geq 0$.
3. $\rho(X_\infty Y_\infty) \leq r^2$, where $\rho(\ )$ is the maximum singular value.

One such controller is

$$K(s) = \begin{bmatrix} A_\infty & -Z_\infty L_\infty \\ F_\infty & 0 \end{bmatrix}$$

where

$$\begin{aligned} A_\infty &= A + r^{-2}B_1B_1'X_\infty + B_2F_\infty + Z_\infty L_\infty C_2 \\ F_\infty &= -B_2'X_\infty \\ L_\infty &= -Y_\infty C_2' \\ Z_\infty &= (I - r^{-2}Y_\infty X_\infty)^{-1} \end{aligned}$$

As seen from the above formulas, $K(s)$ is coupled with r. In this case, an attempt is made to find a minimum r to which the above three conditions still hold and $K(s)$ exits, so that the attenuation from error input d to error output z reaches the maximum degree.

6.4.2 Generalized Plant of a Flexible Beam System

In Eq. (3.86), the omitted high-order terms in the kinetics of the tip load are considered to be $\frac{1}{2} M_p\dot{\theta}^2 w(L,t)^2 + M_p(\dot{\theta} + \dot{w}(L,t))w(L,t)\dot{\theta}b_c$, then Eq. (3.87) becomes

$$\begin{aligned} T_{p\text{new}} = T_p &+ \frac{1}{2}M_p\dot{\theta}^2 \sum_{i=1}^{N}\sum_{j=1}^{N} q_i q_j \psi_i(L)\psi_j(L) \\ &+ M_p b_c \dot{\theta}^2 \sum_{i=1}^{N} q_i \psi_i(L) + M_p b_c \dot{\theta}^2 \sum_{i=1}^{N}\sum_{j=1}^{N} q_i \dot{q}_j \psi_i(L)\psi_j(L) \end{aligned} \tag{6.21}$$

In the same way, if the term $\frac{1}{2}\int_0^L (w\dot{\theta})^2 \rho \mathrm{d}x$ in Eq. (3.88) is considered, then the link kinetics is

$$T_{b\text{new}} = T_b + \frac{1}{2}\dot{\theta}\sum_{i=1}^{N}\sum_{j=1}^{N} q_i q_j \int_0^L \psi_i \psi_j \rho \mathrm{d}x \tag{6.22}$$

After going through all the derivative processes,

$$M\ddot{x} + Kx = b_{\text{new}} \tag{6.23}$$

is obtained, where

$$b_{\text{new}} = b\tau + b_0 \tag{6.24}$$

$$b_0 = \begin{bmatrix} -\sum_{i=1}^{N}\sum_{j=1}^{N}(\dot{\theta}q_i q_j)\Omega_4(i,j) - 2\sum_{i=1}^{N}(\dot{\theta}q_i)\Omega_5(i) - \sum_{i=1}^{N}\sum_{j=1}^{N}(q_i\dot{q}_j)\Omega_6(i,j) \\ \dot{\theta}^2\Omega_5(1) + \dot{\theta}^2\sum_{i=1}^{N} q_i\Omega_4(1,i) + \Omega_6(1,i) \\ \dot{\theta}^2\Omega_5(j) + \dot{\theta}^2\sum_{i=1}^{N} q_i\Omega_4(j,i) + \Omega_6(j,i) \\ \dot{\theta}^2\Omega_5(N) + \dot{\theta}^2\sum_{i=1}^{N} q_i\Omega_4(N,i) + \Omega_6(N,i) \end{bmatrix} \tag{6.25}$$

$$\Omega_4(i,j) = M_p\psi_i(L)\psi_j(L) + \int_0^L \psi_i\psi_j\rho\mathrm{d}x$$

$$\Omega_5(i) = M_p b_c \psi_i(L)$$

$$\Omega_6(i,j) = M_p b_c \psi_i(L)\psi_j(L)$$

Then Eq. (6.14) becomes

$$\dot{q} = Aq + Bu + v_0 \tag{6.26}$$

where

$$v_0 = \begin{bmatrix} 0 \\ \overline{M}^{-1} b_0 \end{bmatrix} \tag{6.27}$$

In this model, v_0 is a time-varying term, acting like a system disturbance but originating from model uncertainties. To describe these uncertainties, a frequency weighting function in the form of

$$v_0(s) = w_1(s)v(s) \tag{6.28}$$

is introduced, where

$$w_1(s) = C_{w1}(sI - A_{w_1})^{-1}B_{w_1} + D_{w_1} \tag{6.29}$$

$w_1(s)$ will be specified later.

If the fact that measured output y is affected by measurement noise and higher frequency model uncertainties are considered, then the system state-space model in Eq. (6.8) becomes

$$\dot{q} = A_g q + Bu + D_g v_0 \tag{6.30}$$

$$y = Cq + w_0 \tag{6.31}$$

where $q = [\theta \quad q_1 \quad q_2 \quad \ldots \quad \dot{q}_1 \quad \dot{q}_1 \quad \ldots]'_{n\times n}$ and D_g is an identity matrix with the same dimension of q.

Following the same pattern, to describe w_0

$$w_0(s) = W_2(s)w(s) \tag{6.32}$$

is introduced, where $w_2(s) = C_{w2}(sI - A_{w2})^{-1}B_{w2} + D_{w2}$. These coefficients will be specified in the next section.

Naturally, beam system stability is the main concern and therefore the regulated variables are chosen as

$$z_g = q = H_g x \tag{6.33}$$

where H_g is an identity matrix. The error vector is

$$z = \begin{bmatrix} z_1 \\ z_2 \end{bmatrix} = \begin{bmatrix} \Theta z_g \\ ru \end{bmatrix} \tag{6.34}$$

where $\Theta = \mathrm{diag}(\Theta_1 \quad \Theta_2 \quad \ldots \quad \Theta_n)$ is the weighting matrix on variable z_g, and r is the scalar factor. All states and the control variables are in the "error vector", and the states are

expected to be eliminated to stabilize the closed loop under the regulation of K, while the control variable will also become zero, thus saving energy consumption.

Let the state variable vector be

$$x = \begin{bmatrix} q \\ x_{w1} \\ x_{w2} \end{bmatrix}, \quad d = \begin{bmatrix} v \\ w \end{bmatrix} \tag{6.35}$$

where x_{w_1} and x_{w_2} are the states of the frequency weighting functions $w_1(s)$ and $w_2(s)$ respectively.

After some manipulations, Fujita et al [17] is referred the state-space representations in Eqs (6.21a)–(6.21c) are

$$A = \begin{bmatrix} A_g & D_g C_{w1} & 0 \\ 0 & A_{w1} & 0 \\ 0 & 0 & A_{w2} \end{bmatrix}, \quad B_1 = \begin{bmatrix} D_g D_{w1} & 0 \\ B_{w1} & 0 \\ 0 & B_{w2} \end{bmatrix}, \quad B_2 = \begin{bmatrix} B \\ 0 \\ 0 \end{bmatrix}$$

$$C_1 = \begin{bmatrix} \Theta H_g & 0 & 0 \\ 0 & 0 & 0 \end{bmatrix}, \quad D_{11} = \begin{bmatrix} 0 & 0 \\ 0 & 0 \end{bmatrix}, \quad D_{12} = \begin{bmatrix} 0 \\ rI \end{bmatrix} \tag{6.36}$$

$$C_2 = [\, C \quad 0 \quad C_{w2} \,], \quad D_{21} = [\, 0 \quad D_{w2} \,], \quad D_{22} = [0]$$

After substituting $u(s) = -F(s)y(s)$, the transfer functions

$$T_{z_1 v} = \Theta H_g \phi (I + BFC\phi)^{-1} D_g W_1 \tag{6.37}$$

$$T_{z_2 v} = -rFC\phi (I + BFC\phi)^{-1} D_g W_1 \tag{6.38}$$

$$T_{z_1 w} = -\Theta H_g \phi BF (I + G_g F)^{-1} W_2 \tag{6.39}$$

$$T_{z_2 w} = -rF (I + G_g F)^{-1} W_2 \tag{6.40}$$

are obtained, where

$$\phi = (sI - A_g)^{-1}, \quad G_g = C(sI - A_g)^{-1} B \tag{6.41}$$

From the above equations, the H_∞ control problem now is to design $F(s)$ to internally stabilize the system but satisfy

$$\left\| \begin{matrix} T_{z1v} & T_{z1w} \\ T_{z2v} & T_{z12} \end{matrix} \right\|_\infty \leq r \tag{6.42}$$

One such controller is

$$k(s) := \begin{bmatrix} A_\infty & -Z_\infty L_\infty \\ F_\infty & 0 \end{bmatrix} \tag{6.43}$$

where

$$\begin{aligned} A_\infty &= A + r^{-2}B_1B_1'X_\infty + B_2F_\infty + Z_\infty L_\infty G_2 \\ F_\infty &= B_2'X_\infty \\ L_\infty &= -Y_\infty C_2' \\ Z_\infty &= (T - r^{-2}Y_\infty X_\infty)^{-1} \end{aligned} \tag{6.44}$$

and X_∞, Y_∞ are the solutions of two Hamiltonian matrices involved in the H_∞ control problem:

$$H_\infty = \begin{bmatrix} A & r^{-2}B_1B_1' - B_2B_2' \\ & -C_1C_1' \quad -A' \end{bmatrix} \tag{6.45}$$

$$J_\infty = \begin{bmatrix} A' & r^{-2}C_1C_1' - C_2C_2' \\ & -B_1B_1' \quad -A \end{bmatrix} \tag{6.46}$$

The purpose of the H_∞ controller here is to find the minimum r, thus attenuating z to the maximum degree while still holding the necessary and sufficient stable conditions discussed in section 6.4.1. The implementation algorithm is presented in the next section.

6.4.3 H_∞ Controller Design

To design the H_∞ controller discussed in the previous section, the weighting functions and factors need to be specified. Because v_0 is in a relatively low frequency range for low-frequency model uncertainties, $w_1(s)$ with a "cutting frequency" around 250 Hz is chosen. So $w_1(s)$ is given as

$$w_1(s) = \frac{9.79 \times 10^3}{(1 + s/(1.72\pi))(1 + s/(2.0\pi))} \tag{6.47}$$

$w_2(s)$ assures robustness for high-frequency noise:

$$w_2(s) = \frac{5.21 \times 10^{-7}(1 + s/(0.02\pi))(1 + s/(0.1\pi))(1 + s/(200.0\pi))}{(1 + s/(6.0\pi))(1 + s/(20.0\pi))(1 + s/(160.0\pi))} \tag{6.48}$$

The parameters Θ and r are adjusted by the cost:

$$J(u, (v, w)) = \int_{-\infty}^{\infty} [z_g^T Q z_g + u^T R u - (v^T v + w^T w)]\mathrm{d}t \tag{6.49}$$

where $Q = \Theta^T\Theta$ and $R = r^2$. H_∞ can be interpreted to reduce this cost. Based on the observations in Fujita et al. [17] and our simulations, the weighting matrix Θ for our beam system with 10 states is

$$\Theta = \mathrm{diag}(60.0 \quad 80.36 \quad 15.91 \quad 10.7 \quad 5.1 \quad 15.1 \quad 2.1 \quad 6.2 \quad 5.2 \quad 5.1) \tag{6.50}$$

and the scalar factor $r = 5 \times 10^{-5}$. The output feedback used here is as in Eq. (6.12).

In order to search the minimum value r, and since it is not known in which region such an index r constitutes a controller, an adequate number of random r values (usually $r \leq 1$) are tested. All the r values for which such a controller exists are saved, and the minimum r represents the cost function for its beam shape. The loop in the H_∞ controller is

1. For a given beam construction distribution, calculate beam system dynamics A_g, B, C.
2. Calculate generalized plant matrices:
   a. Get the state-space matrices for frequency weighting functions.
   b. $A_{w_1}, B_{w_1}, C_{w_1}, D_{w_1}$;$A_{w_2}, B_{w_2}, C_{w_2}, D_{w_2}$.
   c. Get weighting factor Θ and scalar factor r.
   d. Generate $A, B_1, B_2, C_1, C_2, D_{11}, D_{12}, D_{21}, D_{22}$.
3. Search for minimum index r loop for a beam shape distribution:
   a. Randomly pick an r value.
   b. Check X_∞, Y_∞, ρ conditions.
   c. Decide to save this r in a vector or discard it.
   d. Choose the next r, which is smaller than the last valid r, then go to Step b.
   e. After a certain number of iterations, single out the minimum r from the vector to represent this shape. Save this r and its shape.
4. Check stop criteria. If the differences between the three smallest r values in this r vector meet the criteria, stop here. Otherwise, go back to Step 3 for another routine.
5. Calculate F_∞, L_∞, Z_∞, A_∞ to get the controller $K(s)$ based on the minimum r and A_g, B, C.

6.4.4 Simulation Results

There are two blocks in the searching loop, the H_∞ controller block and the IHR algorithm block. The former is used to find the best controller that has a minimum index r based on the input of beam geometric shape as specified in the previous chapter. The latter is used to generate a feasible beam shape distribution. This loop stops until the index vector meets the criteria described in the previous chapter.

For a given beam shape, one such admissible H_∞ controller associated with an index r is shown in Eq. (6.33), which conforms to all the required conditions. The beam consists of four

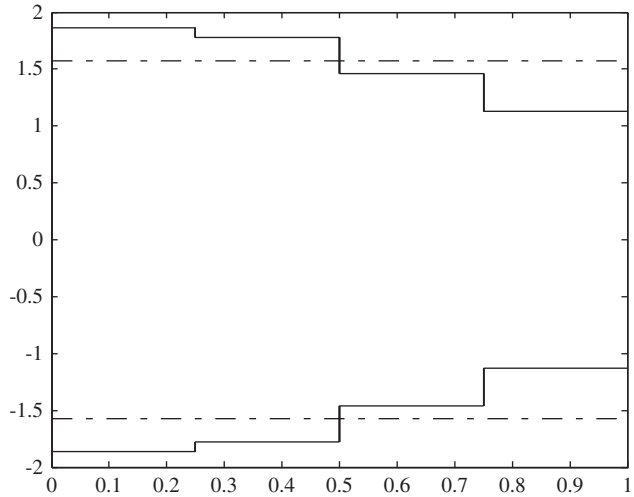

Figure 6.27: Optimal Shapes for H_∞ Controller.

segments, and the number of degrees of its mechanical dynamics is set to 10 (the first four modal shapes are used here).

For a Θ feedback controller as in Eq. (6.6), Figure 6.27 is one of the best shapes, having a minimum index of $r = 0.832$.

The admissible H_∞ controller associated with the shape and this r is

$$-F(s) = 2.158 \times 10^3 \frac{(s+50.2655)(s+31.4159)(s+6.1133+18.8706i)}{(s+50.2577)(s+31.4219)(s+5.7432+18.5868i)}$$

$$\frac{(s+6.1133-18.8706i)(s+18.8496)(s+17.4371)(s+13.1358+11.0675i)}{(s+5.7432-18.5868i)(s+13.2079+11.0351i)(s+13.2079-11.0351i)(s+17.1713)}$$

$$\frac{(s+13.1358-11.0675i)(s+0.2660+9.2176i)(s+0.2660-9.2176i)}{(s+0.4437+9.9505i)(s+0.4437-9.9505i)(s+3.9752)(s+0.0376+5.0332i)}$$

$$\frac{(s+0.4664+3.9814i)(s+0.4664-3.9814i)(s+0.1299)(s+3.9720)}{(s+0.0376-5.0332i)(s+0.0658+2.4910i)(s+0.0658-2.4910i)(s+018.8489)}$$

This controller has 15 degrees of freedom, 10 of them having been contributed by the beam dynamics, two from the frequency weighting function $w_1(s)$, and the rest originating from frequency weighting function $w_2(s)$.

This controller is tested with the same initial state as in Section 6.3, $q_1(0) = [\sqrt{10}, 0, \ldots, 0]^T$. As before, the dashed curve is for the uniform beam and the solid one is the response of the optimal beam shape. For Θ feedback, the initial response of the hub tangent angle is shown

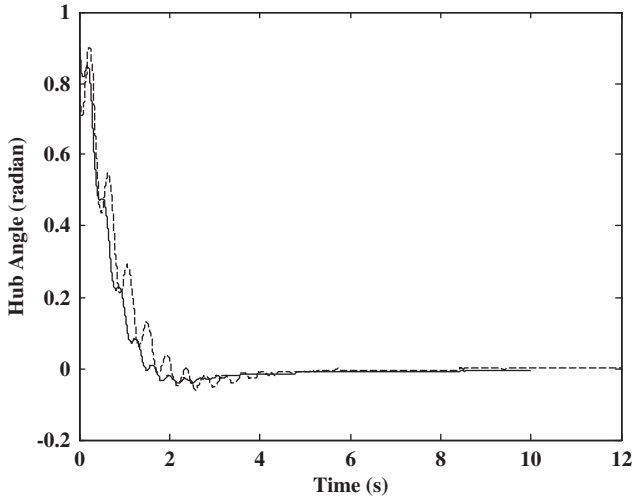

Figure 6.28: Hub Tangent Angle Initial Response for $\Theta(H_\infty)$ Feedback.

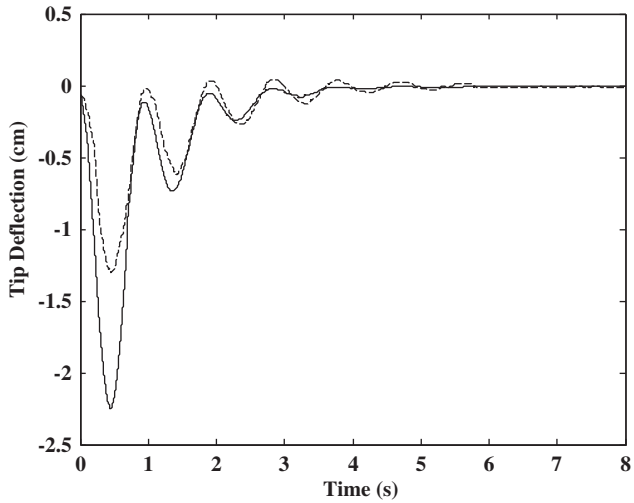

Figure 6.29: Tip Deflection Initial Response for $\Theta(H_\infty)$ Feedback.

in Figure 6.28. It has a small overshoot, but nevertheless steadily converges to the equilibrium point with several pulses. The optimal shape has faster convergence than the uniform shape. Figure 6.29 shows the associated initial responses of the tip deflection. It has a significant first deflective pulse and is larger than that of the uniform beam, but this decreases quickly, almost at the same speed as that of the hub tangent angle.

Figure 6.30 shows the step response of the hub tangent angle for the uniform and associated optimal beams respectively. They both have an overshoot after crossing the given input

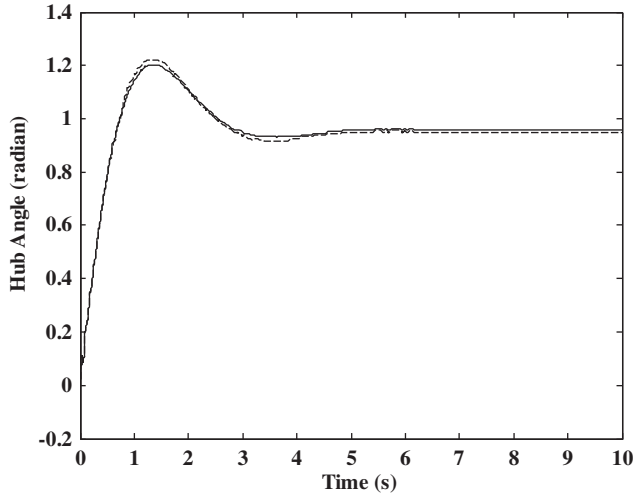

Figure 6.30: Step Response of Hub Angle for $\Theta(H_\infty)$ Feedback.

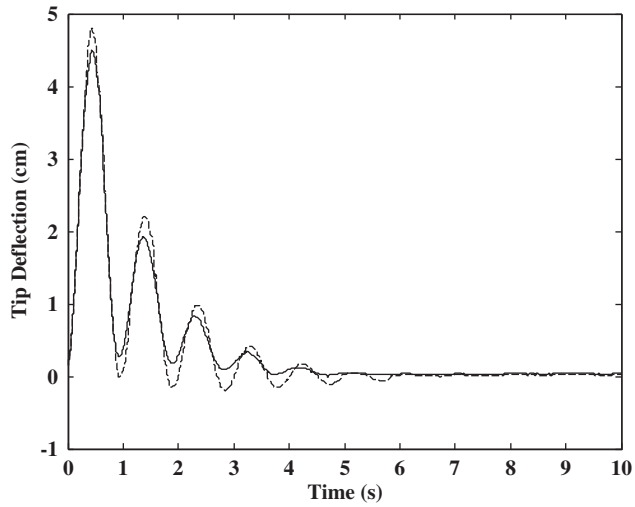

Figure 6.31: Step Response of Tip Deflection for $\Theta(H_\infty)$ Feedback.

reference, but this fades away gradually. Figure 6.31 illustrates the step response of tip deflection. Both responses progress through several cyclic oscillations and each transition lasts slightly longer than that of the hub tangent angle. The deflection of the optimal beam is smaller and converges faster. The step-type disturbance is added as disturbance v for the stable test. As derived earlier, v is assumed to describe the system uncertainties. The results are shown in Figures 6.32 and 6.33. A notable deflective pulse is seen, but this quickly recovers to the equilibrium point.

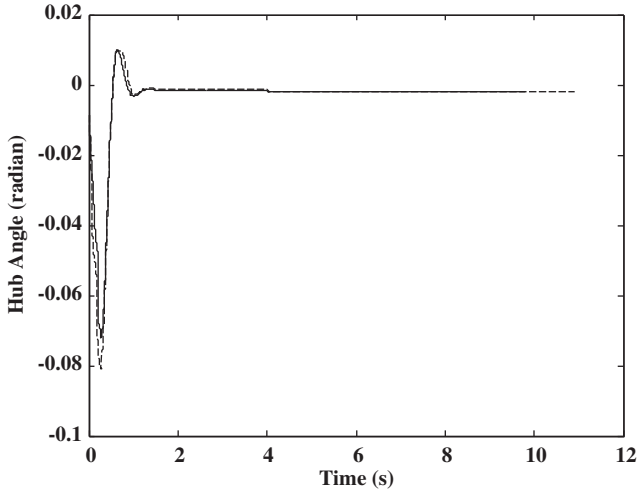

Figure 6.32: Step-Type Disturbance Response of Hub Angle for $\Theta(H_\infty)$ Feedback.

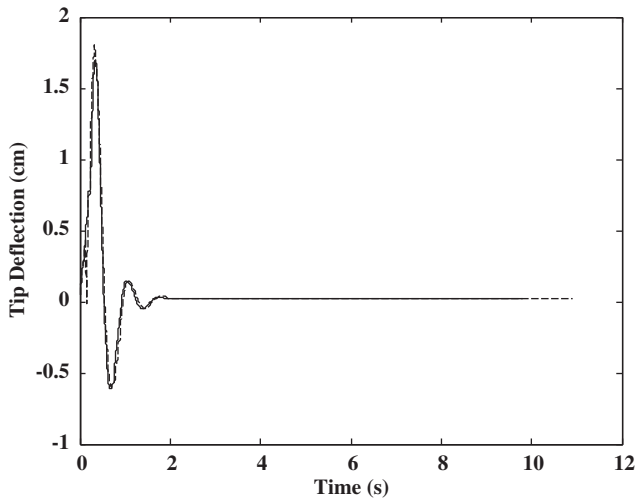

Figure 6.33: Step-Type Disturbance Response of Tip Deflection for $\Theta(H_\infty)$ Feedback.

For tip deflection w feedback, $M\ddot{x} + Kx = b\tau$, the optimal shape is shown in Figure 6.34 with $r = 0.952$. The initial responses of the hub tangent angle are illustrated in Figure 6.35. The response of the optimal beam has a smaller vibration then the uniform beam, but both have higher frequency vibration than the responses of Θ feedback. Figure 6.36 shows the associated initial responses of the tip deflection. The optimal shape has a bigger first pulse, but decays faster for the whole transient.

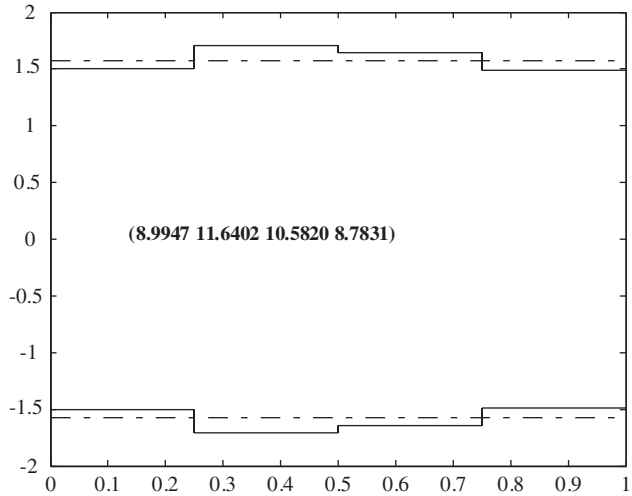

Figure 6.34: Optimal Shapes for $w(H_\infty)$ Feedback.

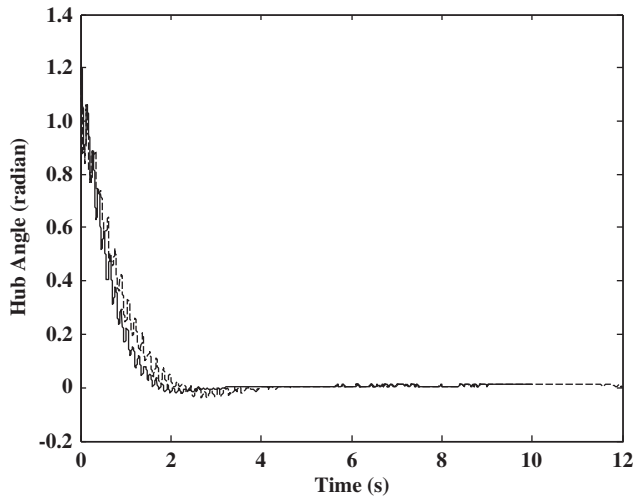

Figure 6.35: Hub Tangent Angle Initial Response for $w(H_\infty)$ Feedback.

Figure 6.37 shows the w feedback step response of the hub tangent angle for the uniform and associated optimal beams respectively. Figure 6.38 illustrates the step response of tip deflection.

For the tip position v feedback as in Eq. (6.5):

$$x = [\theta, q_1, q_2, q_3, \ldots, q_n]^T_{(N+1,1)}$$
$$b = [1, \psi'(0)_1, \psi'_2(0), \ldots, \psi'_N(0)]^T_{(N+1,1)}$$

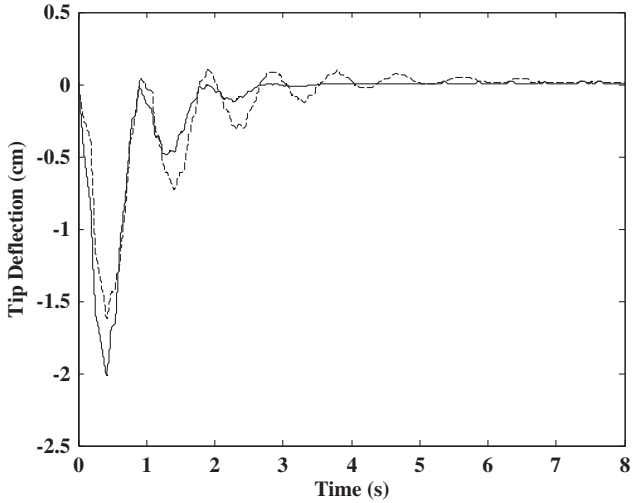

Figure 6.36: Tip Deflection Initial Response for $w(H_\infty)$ Feedback.

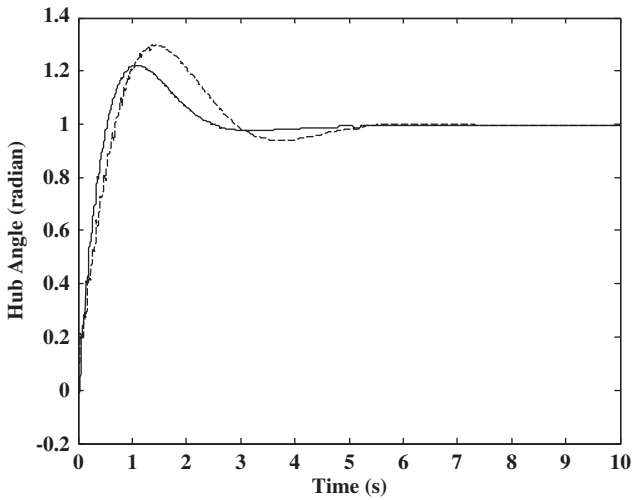

Figure 6.37: Step Response of Hub Angle for $w(H_\infty)$ Feedback.

The optimal shape is shown in Figure 6.39 with $r = 0.8162$. The initial response of the hub tangent angle is illustrated in Figure 6.40. Figure 6.41 presents the associated initial responses of the tip deflection. Figure 6.42 shows tip position feedback step responses of the hub tangent angle for uniform and associated optimal beams respectively. Figure 6.43 shows the step responses of tip deflection.

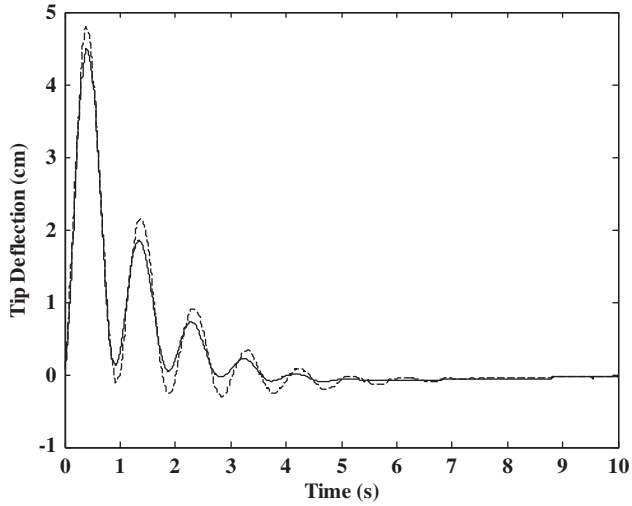

Figure 6.38: Step Response of Tip Deflection for $w(H_\infty)$ Feedback.

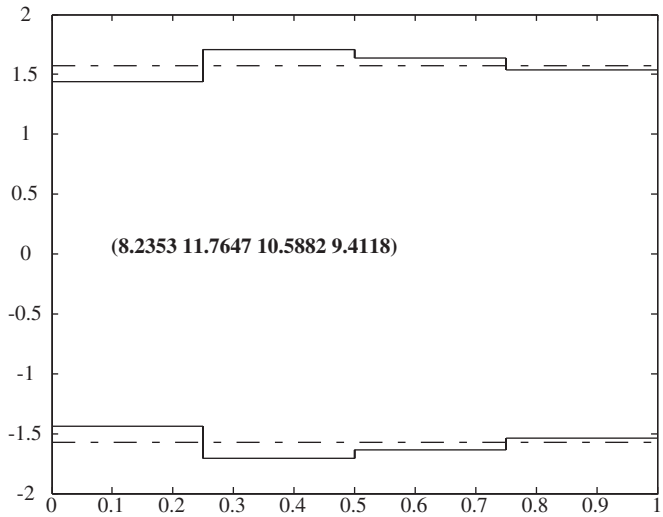

Figure 6.39: Optimal Shapes for $v(H_\infty)$ Feedback.

The optimal shape has faster responses and less vibration cycles than a uniform beam under the Θ feedback. In this chapter, both the generalized state-space model and model uncertainties are developed for the H_∞ controller to completely avoid the complexity of frequency-domain implementation. The design goal is to internally stabilize the closed loop, while minimizing the maximum singular value of the transfer function from characterized error inputs to error outputs, so that the effects of disturbances and system uncertainties are removed. All the results show that the H_∞ controller here is stable against system uncertainty and works robustly.

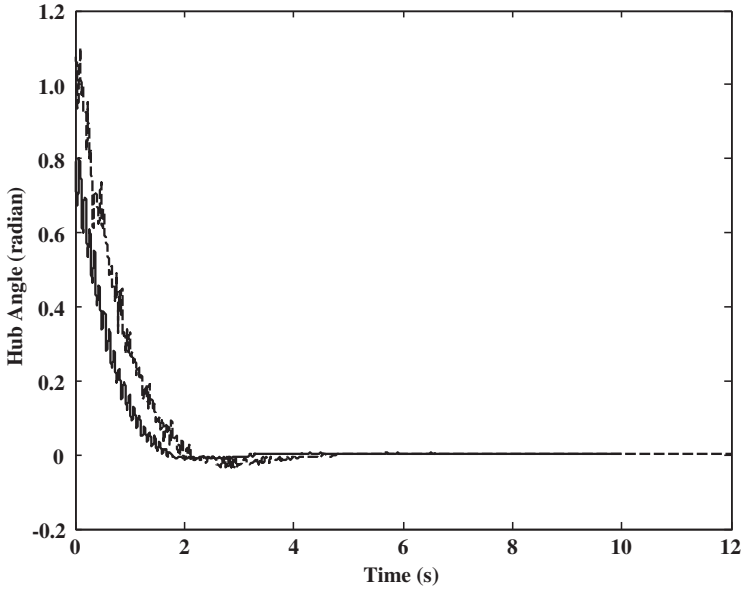

Figure 6.40: Hub Tangent Angle Initial Response for $v(H_\infty)$ Feedback.

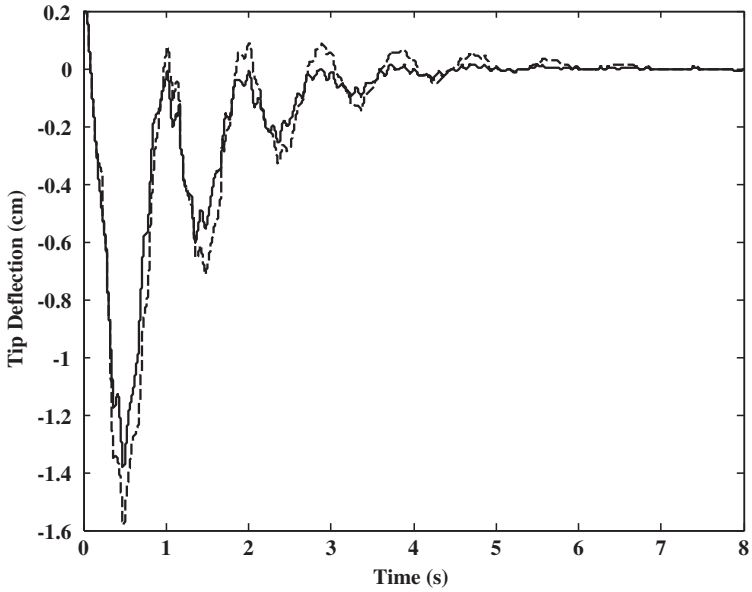

Figure 6.41: Tip Deflection Initial Response for $v(H_\infty)$ Feedback.

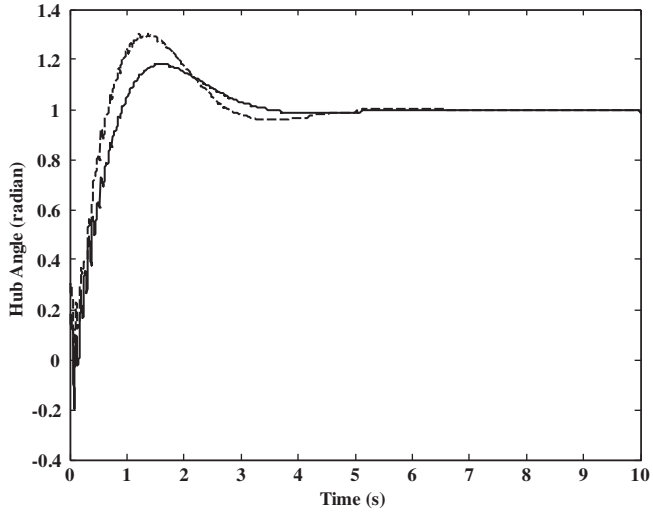

Figure 6.42: Step Response of Hub Angle for $v(H_\infty)$ Feedback.

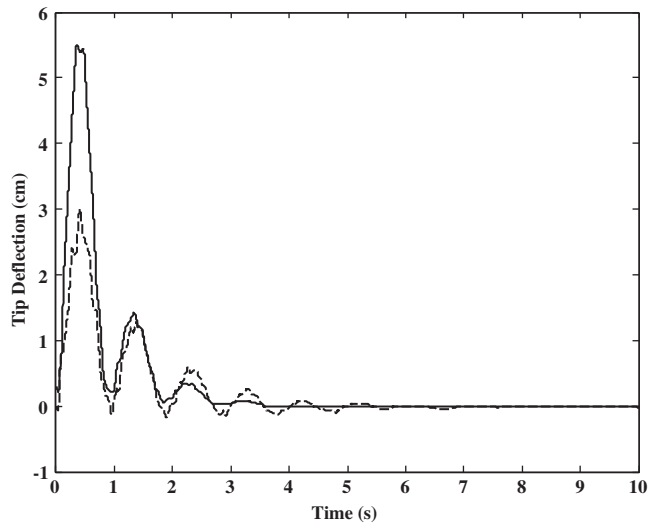

Figure 6.43: Step Response of Tip Deflection for $v(H_\infty)$ Feedback.

6.4.5 System Robustness Analysis

Sensitivity Analysis

In Chapter 3, less significant terms of the dynamic model were truncated to give the Euler–Bernoulli dynamic model with rotary inertia, but this generated a modeling error. It is critical to design a controller that has the ability to provide stability in spite of modeling

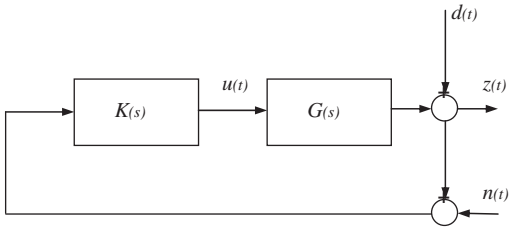

Figure 6.44: Standard LQR Feedback Configuration.

errors. Many papers have been published that address these problems. This section focuses on beam parameter variations due to beam manufacture accuracy and DC motor dynamics variations. After the DC motor equation and the beam dynamics are integrated into the system state equation, these two kinds of variations are treated as system disturbance $d(t)$. This is illustrated as the system configuration in Figure 6.44. The plant is $G(s)$ and the feedback compensator is $K(s)$, which can be designed by various techniques. The system output is $y(t)$, the system control input is $u(t)$. The sensitivity of the overall system depends on the technique employed in the design of the controller. In this case LQR and H_∞ were chosen to demonstrate the mechatronic methodology, since a system's robustness depends on the characteristics of these controllers. For systems with LQR, the classical analysis of robustness is measured in the frequency domain. The notions of singular value, multivariable loop gain, and Bode magnitude plot are either evaluated for the sensitivity analysis, or they are used directly as design tools. These methods are not addressed here. Instead, numerical results with these two kinds of parameter variations are presented to show the system's robustness.

Numerical Results of System Robustness

First the beam shape variations were tested. For a beam with one segment, the performance index differences with the three feedbacks are carried out for ± 0.1 width variations of the ith segment. The optimal LQR controller is unchanged at $Q = 50$. A_i is the width of the ith segment from the hub end. The results are given in Table 6.5. All data in the following tables show the PI difference due to the variation of the segment width or motor parameter.

Table 6.5: Robustness analysis with ($q_1(0)$,4,5)

	$\{\Theta\}$	$\{\Theta,\omega\}$	$\{\Theta,v\}$
Optimal shape (A_1 A_2 A_3 A_4)	(11.2031 10.7338 9.2351 8.8080)	(5.9555 12.4597 12.027 9.5578)	(9.8623 6.1054 11.4927 12.5595)
Optimal PI	2540.470	2098.374	2388.850
$A_1 \pm 0.1$	± 9.7	± 3.3	± 3.0
$A_2 \pm 0.1$	± 9.3	± 3.4	± 8.0
$A_3 \pm 0.1$	± 9.7	± 3.4	± 7.7
$A_4 \pm 0.1$	± 9.7	± 3.5	± 6.5

In order to explore the PI with different variations of each segment separately, a beam with four-segment feedback $\{\Theta,\omega\}$, $Q = 50$ is chosen. Table 6.6 summarizes the results.

From a beam with 12 segments, feedback $\{\Theta,\omega\}$, $Q = 50$ is chosen. Table 6.7 illustrates analyses with only one segment variation at a time.

For motor parameter uncertainties, J_m with -0.1 variation was attempted. The results are listed in Table 6.8.

The results in the above tables show that small beam geometric variation changes the associated PI slightly when compared with the original optimal PI. Note, however, that the larger the variation in the beam dimension, the larger the offset of the PI. Motor parameter J_m is shown to have a larger impact than PI.

For the H_∞ controller, the beam shape (13.8813, 12.6027, 8.4932, 4.5228) instead of the optimal shape (13.8813, 12.6027, 8.4932, 5.0228) was tested. Compared with the uniform beam with the first segment near the tip, the value was 9 instead of 10. The tip deflection response for the initial condition, step input, and step-type disturbance respectively is shown

Table 6.6: Robustness analysis with $(q_1(0),\{\Theta,\omega\},4,50)$

	$A_i - 0.3$	$A_i - 0.2$	$A_i - 0.1$	$A_i + 0.1$	$A_i + 0.2$	$A_i + 0.3$
A_1	−8.1	−2.8	−2.5	−3.3	9.9	16.5
A_2	9.7	−2.6	3.4	−2.5	−6.2	10.9
A_3	−10.0	6.8	−3.4	2.5	6.5	−10.6
A_4	10.1	−6.7	3.4	3.5	6.4	10.5

Table 6.7: Robustness analysis with $(q_1(0),\{\Theta,\omega\},12,50)$

$A_1 + 0.1$	$A_2 + 0.1$	$A_3 + 0.1$	$A_4 + 0.1$	$A_5 + 0.1$	$A_6 + 0.1$
−3.8	2.8	−5.3	−3.7	−1.1	0.5
$A_7 - 0.1$	$A_8 - 0.1$	$A_9 - 0.1$	$A_{10} - 0.1$	$A_{11} - 0.1$	$A_{12} - 0.1$
1.1	−0.7	0.8	1.2	−1.7	1.9

Table 6.8: Robustness analysis with motor coefficient J_m variations $(q_1(0),Q = 100 \times I,50 \times I,10 \times I)$

	$\{\Theta\}$	$\{\Theta,\omega\}$	$\{\Theta,v\}$
$Q = 100 \times I$	−23.0453	−54.3013	−15.1548
$Q = 50 \times I$	−5.4908	−14.3455	−5.7012
$Q = 10 \times I$	−2.3543	−9.6067	−5.4134

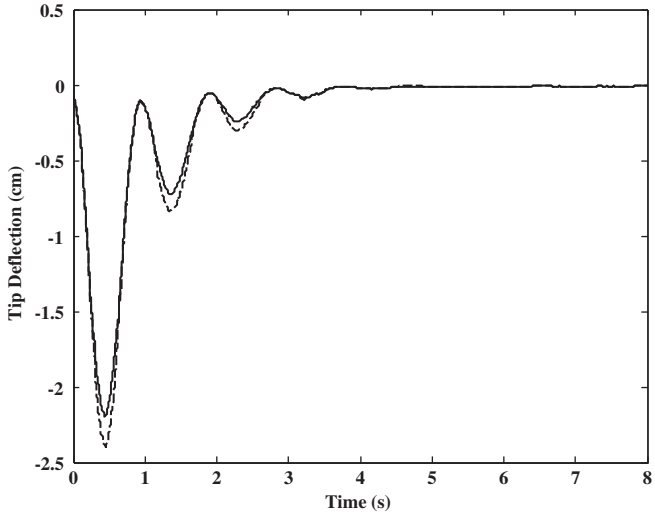

Figure 6.45: Initial Input Response (Tip Deflection) for H_∞.

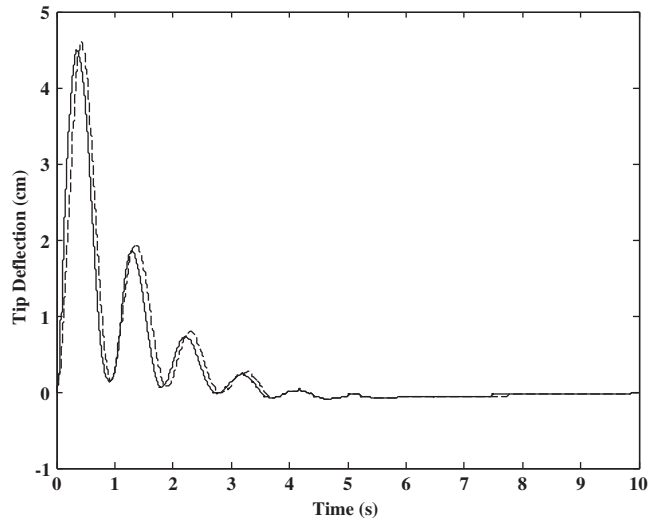

Figure 6.46: Step Input Response (Tip Deflection) for H_∞.

in Figures 6.45–6.47. There is not much difference between the optimal shape and the uniform beam.

As these results show, both LQR and H_∞ controllers for flexible manipulators have very good robustness in terms of parameter variation and disturbance. H_∞ has stronger stability against system uncertainties.

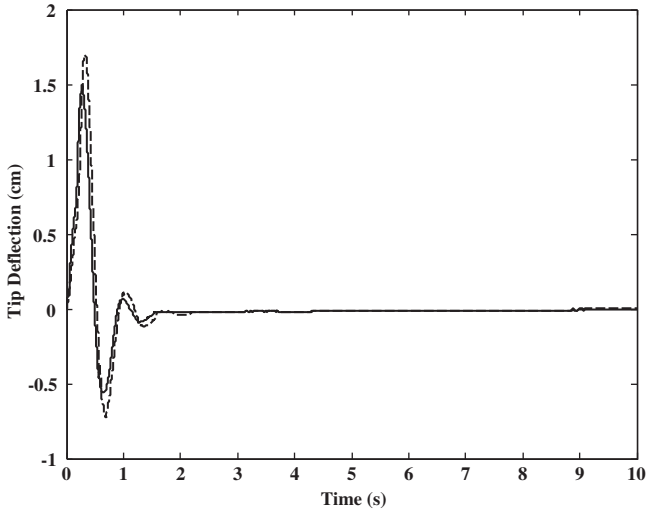

Figure 6.47: Step-Type Disturbance Response (Tip Deflection) for H_∞.

6.5 Closed-Loop Design of Flexible Robotic Links

In this section, the problem of the optimal design of a flexible manipulator link based on its closed-loop transfer function is formulated through the integration of actuator dynamics, control algorithm, sensor location, and the mechanics of arm construction.

The objective is to conduct a thorough investigation of the problem of optimal design of a flexible robotic link from the perspective of mechatronics. In other words, the focus of this section is on optimal design through the integration of actuator dynamics, control algorithm, sensor model, and link mechanics of flexible arm systems. Traditionally, these four areas have been analyzed and/or designed independently for a flexible arm system but, as we will see later in this section, these aspects are closely related in determining the dynamic performance of the flexible arm system and their integration in the design phase might lead to substantial improvement in dynamic response and energy consumption of the arm system. It is important to point out that our intention is to use flexible arms as a case study for the general methodology of integrated design based on mechatronic formulations.

By approximating a flexible link with N small uniform segments, we obtain analytical segmentized solutions for transfer functions for integrated arm systems. This enables us to formulate various optimization problems with explicit objective functions. Several optimization criteria are discussed in this section.

6.5.1 Dynamics of Single-Link Flexible Manipulator Systems

A single flexible robotic link is modeled as a beam fixed on a rigid hub driven by a DC motor. This section presents equations of link mechanics, actuator dynamics, and a control algorithm for a flexible link.

Link Mechanics

Let us consider transverse motions of a single-link flexible robotic arm carrying a load at its tip. The arm is modeled as a beam of length L fixed on a rigid hub with rotary inertia I_H. Shear deformations and rotary inertia of the beam are neglected. The Euler–Bernoulli dynamic equation and the boundary conditions of the arm can be written in the following form:

$$(Dv'')'' + \rho\ddot{v} = 0, \quad I_H\ddot{\theta} - Dv''(0,t) = \tau \tag{6.51}$$

$$v(0,t) = 0, \quad v'(0,t) = \theta \tag{6.52}$$

$$Dv''(L,t) + J_p\ddot{v}(L,t) + a_cM_p\ddot{v}(L,t) = 0 \tag{6.53}$$

$$(Dv'')'(L,t) - a_cM_p\ddot{v}'(L,t) - M_p\ddot{v}(L,t) = 0 \tag{6.54}$$

where $v = w(z, t) + x\theta(t)$ is the total deflection of the beam, w the pure flexible beam deflection, θ the rigid hub rotation, τ the torque applied on the hub, D the bending rigidity (product of Young's modulus and the moment of inertia of the cross-section), ρ the mass density per unit length (product of the mass density per unit volume and the area of the cross-section), M_p, J_p, and a_c the mass, moment of inertia, and x-coordinate of the center of mass of the tip load respectively. Primes indicate differentiation with respect to coordinate x. Here design variables from the link construction are rigidity and mass distributions along the length of the beam, as well as the hub inertia. Note that usually distributions D and ρ are coupled and are not independent of each other.

Actuator Dynamics

Let the arm be driven by a permanent magnet DC motor, then the actuator dynamics can be described as

$$J_m\ddot{\theta}_m + \left(B_m + \frac{K_bK_m}{R}\right)\dot{\theta}_m = \frac{K_m}{R}v_c - r\tau, \theta = r\theta_m \tag{6.55}$$

where J_m is the actuator inertia, B_m the friction coefficient, K_m the torque constant, K_b the back e.m.f. constant, R the armature resistance, r the gear ratio, and θ_{m}, θ, and v_c are the rotor rotation, hub rotation and armature voltage respectively. In general, all motor circuit parameters can be considered as design variables.

Control Algorithm

The general form of linear control laws based on the feedback of the hub rotation and beam deformation can be represented as

$$v_c = u - h_{c\theta}(\theta) - \sum_{i=1}^{n_v}[h_{v0}^i(v(l_i,t) + h_{v1}^i(v'(l_i,t)) + h_{v2}^i(v''(l_i,t))] \tag{6.56}$$

where u is input command, $h_{c\theta}$, h_{v0}^i, h_{v1}^i, and h_{v2}^i are linear time differential or integral operators that specify the feedback control law and l_i locations on the link where deformation information (displacements, rotations, and strains) is collected. Design variables are gain parameters associated with the linear operators. For example, a PD control law using hub rotation, tip deflection, and strain at the hub end can be specified as

$$v_c = u - K_{\theta_m}\theta_m - K_{\dot{\theta}_m}\dot{\theta}_m - -K_v^1 v''(0,t) - K_{\dot{v}}{}^1\dot{v}''(0,t) - K_v^2 v(L,t) - K_{\dot{v}}^2\dot{v}''(L,t) \tag{6.57}$$

Here u gives the desired final hub position. More sophisticated control laws may also be considered in integrated design formulations.

6.5.2 Transfer Functions of the Integrated Systems

Procedures for optimum design of the integrated flexible arm system will be carried out in the frequency domain. To this end we have to find the closed-loop transfer functions from the input command to the hub rotation and the beam deflection by combining the link mechanics, actuator dynamics, and control algorithm. Applying the Laplace transform to Eqs (6.51)–(6.56), we obtain the following equations for the frequency domain:

$$(DV'')'' + \rho s^2 V = 0 \tag{6.58}$$

$$V(0,s) = 0, \quad s^2 I_H V'(0,s) - DV''(0,s) = T \tag{6.59}$$

$$DV''(L,s) + s^2[J_p V'(L,s) + a_c M_p V(L,s)] = 0 \tag{6.60}$$

$$(DV'')'(L,s) - s^2 M_p[a_c V'(L,s) + v(L,s)] = 0 \tag{6.61}$$

$$T(s) = -H_{a\tau}(s)V'(0,s) + KV_c(s) \tag{6.62}$$

$$V_c(s) = U(s) - H_{c\theta}(s)V'(0,s) - \sum_{i=1}^{n_v}[H_{v0}^i(s)V(l_i,s) + H_{v1}^i(s)V'(l_i,s) + H_{v2}^i(s)V''(l_i,s)] \tag{6.63}$$

where

$$H_{a\tau}(s) = \frac{J_m}{r^2}s^2 + \left(\frac{B_m}{r^2} + \frac{K_b K_m}{r^2 R}\right)s, \quad K = \frac{K_m}{r^2 R}$$

and transfer functions $H_{c\theta}$, H^i_{v0}, H^i_{v1}, and H^i_{v2} are obtained from the corresponding time-domain operators by replacing differential and integral operations with s and $1/s$ respectively. Note that we have eliminated the Laplace transform of hub rotation θ from these equations using the relationship

$$\Theta(s) = V'(0, s) \tag{6.64}$$

Using Eqs (6.62) and (6.63), the second boundary condition in Eq. (6.59) can be reformulated as

$$\begin{aligned}&(s^2 I_H + H_{a\tau} + KH_{c\theta})V'(0, s) + K\sum_{i=1}^{n_v}[H^i_{v0}(s)V(l_i, s) + H^i_{v1}(s)V'(l_i, s) + H^i_{v2}(s)V''(l_i, s)]\\ &\quad -DV''(0, s) = KU(s)\end{aligned} \tag{6.65}$$

which involves only deflection terms. Now the combination of Eqs (6.58), (6.61), (6.65), and $V(0,s) = 0$ gives a complete set of equations for solving the Laplace transform of the deflection function.

The three transfer functions to be used in optimum design are defined as

$$H(x, s) = \frac{V(x, s)}{U(s)}, \quad H_\theta(s) = \frac{\Theta(s)}{U(s)} = H'(0, s) \tag{6.66}$$

$$H_w(x, s) = \frac{W(x, s)}{U(s)} = H(x, s) - xH_\theta(s) \tag{6.67}$$

Clearly, $H(x,s)$ can be found by choosing $U(s) = 1$.

Transfer functions $H(x,s)$ and $H_\theta(s)$ are related to mass and rigidity distributions ρ and D and other design variables implicitly through differential equations. The major remaining task to achieve analytical optimization formulations is to find the explicit relationship between the transfer functions and the design variables. A piecewise-uniform-link approximation has been used in the next section to solve this problem.

6.5.3 Segmentized Solution for Transfer Functions

For general unknown varying mass and rigidity distributions, it is very difficult, if not impossible, to solve differential Eq. (6.58) and its boundary conditions. In order to obtain the relationship between the transfer functions and the design variables, some approximation must be made. For numerical solutions, one may use the finite element or finite difference equation methods. However, numerical solutions are not efficient for our purpose of optimum design. Thus, in this section we present an analytical solution using the piecewise-uniform-link approximation.

Let us consider that the flexible link can be approximated by N small uniform segments. Each segment has uniform mass and rigidity distributions. In other words,

$$\rho(x) = \sum_{i=1}^{N} \rho_i \delta(x; x_{i-1}, x_i), \quad D(x) = \sum_{i=1}^{N} D_i \delta(x; x_{i-1}, x_i) \tag{6.68}$$

where ρ_i and D_i are positive numbers and

$$\delta(x; x_{i-1}, x_i) = \begin{cases} 1 & \text{for } x_{i-1} \le x < x_i \\ 0 & \text{otherwise} \end{cases}$$

Accordingly, the deflection function can be expressed as

$$V(x, s) = \sum_{i=1}^{N} V_i(x, s) \delta(x; x_{i-1}, x_i) \tag{6.69}$$

where V_i is the deflection on the ith segment.

Substituting Eqs (6.67) and (6.68) into Eq. (6.58) and applying the conditions of continuity of deflection, rotation, bending moment, and shear force at both ends of each segment, we can arrive at the following equations after quite long and tedious calculations:

$$\begin{gathered} V_i = S_i(\xi, s)\Phi_i C \\ \Phi_i = I_{4\times 4}, \quad \Phi_{i+1} = \Phi_i \phi_i, \quad 1 \le i \le N-1 \end{gathered} \tag{6.70}$$

where

$$\begin{aligned} S_i &= [\sin \lambda_i \xi \quad \sinh \lambda_i \xi \quad \cos \lambda_i \xi \quad \cosh \lambda_i \xi] \\ \xi &= \frac{x - x_{i-1}}{\Delta_i}, \quad \Delta_i = x_i - x_{i-1} \\ \phi_i &= \begin{bmatrix} \frac{\gamma_i}{\delta_i}\psi_{1i} & -\frac{\gamma_i}{\delta_i}\psi_{2i} \\ \psi_{2i} & \psi_{1i} \end{bmatrix} \\ \psi_{1i} &= \begin{bmatrix} \Sigma_{1i} \cos \lambda_i & \Sigma_{2i} \cosh \lambda_i \\ \Sigma_{2i} \cos \lambda_i & \Sigma_{1i} \cosh \lambda_i \end{bmatrix} \\ \psi_{2i} &= \begin{bmatrix} \Sigma_{1i} \sin \lambda_i & \Sigma_{2i} \sinh \lambda_i \\ \Sigma_{2i} \sin \lambda_i & \Sigma_{1i} \sinh \lambda_i \end{bmatrix} \\ \Sigma_{1i} &= 1 + \frac{d_i \gamma_i}{\delta_i}, \quad \Sigma_{2i} = 1 - \frac{d_i \gamma_i}{\delta_i} \\ \lambda_i^4 &= -\frac{\rho_i \Delta_i^4}{D_i} s^2 \end{aligned} \tag{6.71}$$

$$\delta_i = \frac{\Delta_i}{\Delta_{i+1}}, \quad d_i = \frac{D_i}{D_{i+1}}, \quad \gamma_i = \frac{\lambda_i}{\lambda_{i+1}} = \delta_i \left(\frac{\rho_i}{\rho_{i+1}} \frac{D_{i+1}}{D_i} \right)^{1/4} \tag{6.72}$$

and C is determined by

$$\begin{aligned} BC &= K\Delta_1 [0 \quad U(s) \quad 0 \quad 0]^T \\ B &= [B_1^T \quad B_2^T \quad B_3^T \quad B_4^T]^T \end{aligned} \tag{6.73}$$

Here B_i is found from the boundary conditions

$$\begin{aligned} B_1 &= S_1(0) \\ B_2 &= (s^2 I_H + K H_{c\theta} + H_{a\tau}) S_1'(0) - \frac{D_1}{\Delta_1} S_1''(0) + \Delta_1 \sum_{i=1}^{n_v} [H_{v0}^i S_k(\xi_i, s) + H_{v1}^i S_k'(\xi_i, s)] \, \Phi_k \\ & x_{k_i - 1} \le l_i \le x_{k_i}, \quad \xi_i = \frac{l_i - x_{k_i - 1}}{\Delta_{k_i}} \end{aligned} \tag{6.74}$$

$$B_3 = \frac{S_N''(1)}{\lambda_N^2} - \frac{\lambda_N^2}{\rho_N \Delta_N^2} \left[J_p \frac{S_N'(1)}{\Delta_N} + a_c M_p S_N(1) \right] \tag{6.75}$$

$$B_4 = \frac{S_N'''(1)}{\lambda_N^3} + \frac{\lambda_N M_p}{\rho_N \Delta_N} \left[a_c \frac{S_N'(1)}{\Delta_N} + S_N(1) \right] \tag{6.76}$$

Let

$$B^{-1} = [B^1 \quad G(s) \quad B^3 \quad B^4]$$

Then the deflection transfer function can be found as

$$H(x, s) = K\Delta_1 \sum_{i=1}^{N} S_i(\xi, s) \delta(x; x_{i-1}, x_i) \Phi_i G(s) \tag{6.77}$$

Thus, we obtain an explicit expression for the deflection transfer function in terms of mass and rigidity distribution. The poles of the integrated arm system can be obtained from

$$\det B(s) = 0 \tag{6.78}$$

which is a transcendental equation.

6.5.4 Optimization Formulations for Mechatronic Design

Traditionally, mechanical, electrical, and control systems for a robotic manipulator have been designed individually and, as a consequence, the coupling effects of these systems

with each other as well as their influence on performance have been largely ignored. For example, a link of a flexible arm is usually constructed without considering its effects on the arm control system, and the control algorithm is developed after the link has already been built. However, as indicated by the analysis in the previous section, the mass and rigidity distributions of the link have a strong influence on transfer functions and, therefore, on control performance of the integrated arm system. The idea of combining mechanical, electrical, and control aspects in the design phase for better system performance is the major motivation for mechatronic research. In this section we present several optimization formulations for flexible arm design through the integration of link mechanics, actuator dynamics, and the control algorithm.

Frequency responses of hub rotation error and pure beam deflection are found as

$$\begin{aligned} E_\theta &= \frac{\Theta(jw) - \Theta_d(jw)}{U(jw)} = 1 - H'(0,jw) \\ H_w(x,jw) &= \frac{W(x,jw)}{U(jw)} = \frac{V(x,jw) - x\Theta(jw)}{U(jw)} = H(x,jw) - xH'(0,jw) \end{aligned} \tag{6.79}$$

In order to suppress the overall beam deflection, we introduce the following weighted measure:

$$E_w(w) = \int_0^L p(x)\|E_w(x,jw)\|\mathrm{d}x \tag{6.80}$$

where $p(x)$ is a non-negative weight function. To consider the deflection at a particular location, e.g. at tip $x = L$, one can set $p(x)$ to be a δ function. For normal operations, stresses produced along the beam must be under the elastic stress limit of the beam material. The maximum bending stress along the beam and the corresponding transfer function are given by [3]

$$\sigma_x(x,t) = \frac{h(x)}{2}E''_w(x,t), \quad \Sigma_x(x,t) = \frac{h(x)}{2}EH''_w(x,t) \tag{6.81}$$

where E is Young's modulus and h is the height of the beam.

For certain specific cross-sections, such as a solid circular cross-section, mass and rigidity distributions are not independent. In these cases, we can easily express both ρ_i and D_i as functions of some independent design variables, denoted as a vector X_b, i.e. we consider $\rho = \rho(X_b)$ and $D = D(X_b)$ in our optimization formulations. We also introduce two vectors X_a and X_c to represent design variables of the actuator and controller respectively.

Pole Location Optimization

For a given set of constraints, let us find the optimal mass and stiffness distributions, actuator, control and sensor parameters, such that the first M poles of the transfer function H are located as closely as possible to a set of specified positions. This can be expressed as

$$\begin{aligned} &\min_X (P_n(x;d) - P_d)^H W_n (P_n(x;d) - P_d) \\ &X = (X_a, X_b, X_c) \end{aligned} \tag{6.82}$$

subject to

$$\begin{aligned} &X_{aL} \le X_a \le X_{aU}, \quad X_{bL} \le X_b \le X_{bU}, \quad X_{cL} \le X_c \le X_{cU} \\ &\sum_{i=1}^{N} \rho_i(X_b) = W_b, \quad \max_{0 \le \omega \le \omega_0} E_w(\omega) \le \delta_w \end{aligned} \tag{6.83}$$

$$\max_{0 \le \omega \le \omega_0} \|\Sigma_x(j\omega)\| \le \delta_\sigma \tag{6.84}$$

$$\max_{0 \le \omega \le \omega_0} \|E_\theta(j\omega)\| \le \delta_\theta \tag{6.85}$$

where P_d is the set of specified pole positions, $d = (I_H, M_p, a_c, J_p)$, $(X_{aL}, X_{aU}, X_{bt}, X_{bU}, X_{cL}, X_{cU})$ are the lower and upper bounds for design vectors, W_b is the specified total mass of the beam, and $(\delta_w, \delta_\sigma, \delta_\theta)$ are the corresponding upper bounds of tip deflection, beam stress, and rotation error over the frequency range $[0, w_0]$.

Tracking Error Optimization

For a given set of constraints, Eqs (6.83)–(6.85), we find the optimal mass and stiffness distributions, actuator, control, and sensor parameters, such that

$$\min_X \int_0^{\omega_0} f(\omega) \|E_\theta(j\omega)\| \mathrm{d}\omega \tag{6.86}$$

where ω_0 is a cut-off frequency and $f(\omega)$ a weight function.

Reference Model Optimization

For a given set of constraints, Eq. (6.83)–(6.85), we find the optimal mass and stiffness distributions, actuator, control, and sensor parameters, such that

$$\min_X \int_0^{\omega_0} f(\omega) \|H_d(j\omega) - H(j\omega)\| \mathrm{d}\omega \tag{6.87}$$

where H_d is a desired transfer function, e.g. the transfer function of a rigid arm,

$$H_d(s) = \frac{\omega_n^2}{s^2 + 2\zeta\omega_n + \omega_n^2}$$

Minmax Optimization

Generally, an arm has to perform tasks under different situations, e.g. moving with different tip loads or driven by different control algorithms. This is reflected by different values of design parameter vector d. A reasonable criterion for optimum design in this case is to *maximize the worst-case bandwidth of the flexible arm*. Specifically, let $D = \{d_1,\ldots,d_n\}$ be a set of possible values of parameter vector d, then the problem of optimum design in this case can be formulated as a standard minimax problem:

$$\max_X \min_{1\le i\le d} \{f(X; d_i)\}$$

subject to the same constraints as in (6.83)–(6.85). Several minimax algorithms can be used for this problem.

6.6 Concurrent Design

Great progress has been made in aspects of modeling, optimal design, and control of flexible manipulators over the past few decades [21]. Various approaches have been developed for modeling of flexible manipulators and a variety of control strategies for the control of flexible manipulator systems can be found in recent research papers. These studies paid more attention to control-intensive work but ignored the impact when applied to flexible beams' mechanical shape. On the other hand, studies of optimal beam shape design to improve the properties of flexible manipulators have been carried out by some researchers and further studies were performed by Wang and his research group, who developed an iterative scheme that produced the first single-link optimum manipulator shape, a minimum-weight design of a flexible manipulator, and a new computing method for optimal mass and rigidity distributions for a flexible manipulator with a tip payload [13,22,23]. However, these studies focused either on control strategies or proper shape design of a flexible beam, and coupling effects between controllers and construction were less considered. Asada et al. [24] studied the methodology of structure and control integrated design (SCID), which focused on the fusion of an object's structure and control, and applied SCID in the design of a robotic system, flexible arm system, and even an intelligent air-conditioning system.

Wang and colleagues [15,25–27] proposed the mechatronic design method (MDM) for global optimization of an overall mechatronic system, such as a flexible manipulator system that takes the interrelationships between the subsystems into account while avoiding control-intensive or model-intensive work.

6.6.1 General Concepts

Concurrent design is an integrated design methodology. As for tasks involving engineering systems design, it may contain many subsystems, several design process stages, constraints, and requirements, involving multiple disciplines. The designer should use various methods, technologies, and strategies to meet these requirements. Traditional sequential design follows a serial, subsystem-independent route, which leads to a locally optimal solution at best. However, in concurrent design, the designer concurrently considers the interactions and coupling effects among different subsystems and takes the interactions and trade-offs among different or even conflicting requirements into account in the design process. It therefore tends to lead to a global optimal design result that must simultaneously meet requirements such as quality, cost, performance or even market requirements, as well as meeting constraints such as manufacturing, etc.

In a broad sense, concurrent design is a cross-domain design methodology that provides guidance in engineering design and project implementation. From this point of view, concurrent design is similar to the theories of multidisciplinary design optimization (MDO) and concurrent engineering (CE). They all focus on the optimization and distribution of the resources in the design and development process, and explore and exploit synergistic effects of coupling between various interacting disciplines/phenomena, to ensure an effective and efficient product development process and balance product performance considerations with manufacturing, economics, and life-cycle issues.

In a narrow sense, we can take a mechatronic system as an example. It is generally composed of several subsystems: a mechanical system, driving, sensor, and control system, etc. In traditional sequential design, each subsystem is always designed sequentially, locally, and separately, with few interactions between each of these subsystems, while in concurrent design the subsystems are treated concurrently rather than sequentially, so any coupling effects are automatically taken into account. The primary goal is to construct a global optimal mechatronic system at the system level instead of an optimal mechanical system or an optimal control system. From this viewpoint, concurrent design is equivalent to MDM, SCID, etc. to some degree.

In fact, a multidisciplinary system made up of all the local-optimal-designed subsystems is not always a global optimal system. According to the function and scope of application, concurrent design can be classified into broad-sense and narrow-sense concurrent design [28−30], as shown in Figure 6.48.

In an engineering design, broad-sense concurrent design deals with both top-level issues, such as conceptual design, architecture, organization and management of the development process, etc., and lower level issues such as materials, technology, mechanical structure, controllers, optimization, etc. However, it attaches heavier weight to the former. From the viewpoint of knowledge, broad-sense concurrent design involves nontechnical disciplines

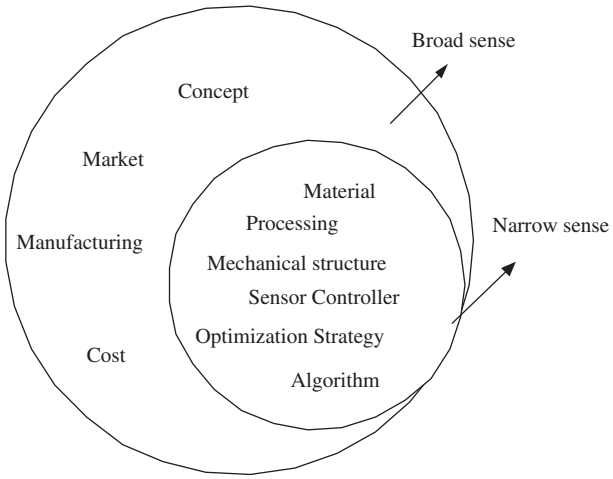

Figure 6.48: Broad-Sense and Narrow-Sense Concurrent Design.

like manufacturing, marketing, cost, life cycle, etc.; technical disciplines such as controls and sensors, mechanical structures, optimization strategies and algorithms, materials, etc.; and the coupling between them. In general, broad-sense concurrent design tends to integrate all the subsystems and disciplines, to manage the whole process of design with optimization strategies, considering the coupling effects among the subsystems and disciplines. As a result, it leads to a global optimal design solution that meets both technical and nontechnical requirements. As Finger et al. [20] pointed out, in creating a concurrent design system, the goal is to infuse knowledge of downstream activities into the design process so that designs can be generated rapidly and correctly. Therefore, the ultimate goal is to effectively and concurrently design a complex system and make the product more competitive.

6.6.2 Existing Representation of Special Concurrent Designs

When applied to a specific system (a mechatronic system in this context), concurrent design can be viewed as narrow-sense concurrent design, without considering those top-level issues or nontechnical disciplines. As mentioned in a previous section, a mechatronic system generally contains various subsystems: mechanical and structural systems, sensor and control systems, materials, etc. Thus, the design variable set contains the variables from these subsystems. According to design requirements and the constraints that need to be satisfied, the design objective is transformed into an optimization objective function (or functions) and constraint equations. The optimal design problem is thus transformed into a simultaneous optimization problem with multiple variables from each subsystem. Although it may be a complicated multi-objective optimization problem subject to multiple constraints, this design method guarantees

attainment of a globally optimal design solution or a suboptimal solution with a higher probability, if the optimization problem is properly solved by mathematics.

In narrow-sense concurrent design, globally simultaneous optimization can be expressed in the following mathematical form:

$$\begin{aligned} & X = [X_S,\ X_M,\ X_C,\ X_O] \\ \text{Min} \quad & f(X) = f([X_S,\ X_M,\ X_C,\ X_O]) \\ \text{S.t.} \quad & h_i(X) = 0 \ \ (i = 1, 2, \ldots, n) \\ & g_j(X) \leq 0 \ \ (i = 1, 2, \ldots, m) \end{aligned} \tag{6.88}$$

where X is a set of design variables; X_S, X_M, X_C, X_O represent sets of mechanical and structural variables, material variables, control and sensor variables, and other variables respectively. f denotes optimization objective functions, and $h_i(X)$, $g_j(X)$ represent equality constraints and inequality constraints.

Narrow-sense concurrent design shares a similar concept with the methodology of structure and control integrated design (SCID), control structural design, and the mechatronic design method (MDM) proposed by Wang et al. [22,25]. They all focus on the coupling, fusion, and simultaneous optimization of the subsystems of the mechanical structure, control, material, etc., and attempt to overcome the conflicts and waste of resources in the sequential design of those subsystems.

6.6.3 Problems

There are some problems to be faced due to the complexity involved.

System Analysis

Since a mechatronic system generally involves multiple disciplines that may have coupling effects, the complexity of searching for a global optimal solution increases dramatically with the growth in design variables and constraints. Properly constructing objective optimization functions, the selection of design variables and definition of their scope are important and are subject not only to design requirements and constraints, but also to the mathematical solvability of the optimization problem. Reducing complexity (especially computational complexity) by properly and skillfully dealing with constraints is also important. Measures to plan and simplify how to deal with constraints can be taken, such as using an algorithm for finding coupled constraints and for creating a solution plan that minimizes the need for simultaneous solution, and using algorithms like that proposed by Navinchandra and Rinderle [31], for example.

Global Optimization

Global optimization of a multi-objective function subject to nonlinear constraints is very difficult, or even unsolvable, especially for a nonlinear and nonconvex objective function. The situation varies from case to case, so there is no universal method to guarantee a global optimal

solution. In multidisciplinary design optimization (MDO), an effective strategy is to divide the design system into a hierarchical system and a nonhierarchical system according to the relationships between subsystems, and then use different optimization strategies and algorithms [32]. Constraint deletion and searching for a tighter limit for the design space can be considered. Interval methods [33] have been used to solve the global optimization problem, which subdivide the constraint-based design space to a part of the serial space that gradually satisfies all the constraints. Smith et al. [34] proposed a step and iterative method to optimize structures and controllers. Wang and colleagues [22,25] proposed LQR output feedback-based global optimization strategies for optimal construction and control of flexible manipulator systems.

The choice of algorithm is also critical in global optimization. Most traditional nonlinear programming techniques or gradient-based algorithms are local methods that are prone to become bogged down with local processes. Some intelligent optimization algorithms are good choices in tackling this problem, such as evolutionary computation algorithms (a genetic algorithm, simulated annealing algorithm and taboo search algorithm), evolutionary programming and strategies, etc.

6.7 Concurrent Design of a Single-Link Flexible Manipulator Based on PID Controller

In this section, a narrow-sense concurrent design method is introduced in the optimization control and design of a single-link flexible manipulator system to achieve good performance at high speed, good vibration suppression, etc. The system includes a single-link flexible arm, driving motor, sensor, controller, etc.

6.7.1 Dynamics of Single-Link Flexible Manipulator Systems

The flexible manipulator considered here is a single-link flexible arm mounted in the horizontal plane with a tip-mass payload. It consists of a beam of length L fixed on a rigid hub as shown in Figure 6.49, where X_0OY_0 and X_1OY_1 represent the stationary and moving

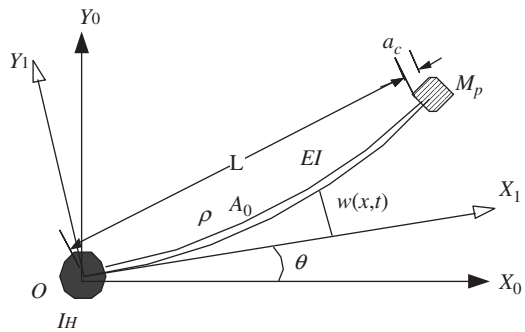

Figure 6.49: A Single-Link Flexible Manipulator.

coordinates respectively. E, I, ρ, A_0, M_p, a_c, and I_H are Young's modulus, the rotary inertia of the cross-sectional area, beam density, cross-sectional area of the beam, payload mass, the distance of the tip center of mass to the end of the beam along the X_0 axis, and hub rotary inertia respectively.

The motion of the flexible manipulator is described by the rigid rotation angle θ of the hub and the flexible displacement w of the beam. Thus, the total displacement y of a point along the manipulator at a distance x from the hub is

$$y = x\,\theta(t) + w(x,\ t) \tag{6.89}$$

We use the Euler–Bernoulli model, where rotary and shear deformation of the beam are neglected, to describe the dynamic behavior of the flexible manipulator [28]. Then the governing equations of beam deformation and hub rotation are

$$EI(x)\left(\frac{\partial^4 y}{\partial x^4}\right) + \rho A_0(x)\frac{\partial^2 y}{\partial t^2} = 0 \tag{6.90}$$

$$I_H\ddot{\theta} - EI(x)\left(\frac{\partial^2 y}{\partial x^2}\right)_{x=0} = \tau_{\text{in}} \tag{6.91}$$

$$y_{x=0} = 0, \quad y'_{x=0} = \theta \tag{6.92}$$

$$EI(x)\left(\frac{\partial^2 y}{\partial x^2}\right)_{x=L} + J_p\left(\frac{\partial \ddot{y}}{\partial x}\right)_{x=L} + a_c M_p \ddot{y} = 0 \tag{6.93}$$

where a prime (y') donates spatial derivative $\partial y/\partial x$, and a dot ($\dot{y}$) donates time derivative $\partial y/\partial t$. For a non-uniform beam, bending rigidity $EI(x)$ and cross-sectional area $A_0(x)$ are functions of x, while for a uniform beam they are constant.

Suppose the arm is equally divided into n segments each with a length of $\Delta x = L/n$. We define

$$x_i = i \bullet \Delta x, y_i = y(i\Delta x, t) \tag{6.94}$$

Using the finite difference method (see Section 3.5.3), the desired dynamic equations of motion of the system can be written as

$$[M]\ddot{y} + [K]y = [B]\tau_{\text{in}} \tag{6.95}$$

where M, K, and B are mass, stiffness, and input matrices of the flexible manipulator respectively [28]. τ_{in} represents control torque at the hub.

The manipulator is driven by a DC motor connected to the hub through a speed reducer, where a velocity-measuring dynamo is used for speed negative feedback of the motor output shaft. Dynamics of the DC motor and reducer are

$$(J_m + J_L)\ddot{\theta} + \left(B_m + \frac{K_\tau\,(K_e + K_W \bullet K_1)}{R}\right)\dot{\theta} = \frac{K_\tau K_\theta}{R}V_c - r\ \tau_{\text{in}} \tag{6.96}$$

where J_m, J_L, B_m, K_r, K_e, K_w, K_1, R, and r are rotary inertia of motor rotors, rotary inertia on the speed reducer side, damping ratio, torque constant, back e.m.f. constant, feedback factor, feedback gain, armature resistance, reduction ratio, and angular displacement of the motor respectively.

We define

$$q_0 = [\theta\ \ y_1\ \ y_2 \cdots\ \ y_n]^T \tag{6.97}$$

The overall state variable is defined as

$$q = \begin{bmatrix} q_0 \\ \dot{q}_0 \end{bmatrix} \tag{6.98}$$

Combination of Eqs (6.95) and (6.96) yields the state-space equations of the system, which include flexible manipulator, driving motor, and speed reducer. Special decoupling treatments are taken to avoid round-up errors of matrix M inversion in the transformation from Eq. (6.95) to first-order differential equations [28]. The state-space equations are

$$\begin{aligned} \dot{q} &= Aq + Bu \\ Z &= Cq \end{aligned} \tag{6.99}$$

where

$$A = \begin{bmatrix} A_{11} & A_{12} \\ A_{21} & A_{22} \end{bmatrix}, \quad B = \left[\underbrace{\frac{rK_\tau K_\theta}{R} \quad 0 \quad \cdots \quad 0}_{2n+2}\right]^T, \quad C = \left[\underbrace{0 \quad \cdots \quad 0 \quad 1}_{n+1}, \underbrace{0 \quad \cdots \quad 0}_{n+1}\right]$$

$$A_{11} = [0]_{(n+1)\times(n+1)}, \quad A_{12} = I_{(n+1)\times(n+1)}, \quad A_{22} = [0]_{(n+1)\times(n+1)}$$

A_{21} refers to the literature [28,29].

6.7.2 Implementation of Concurrent Design

Narrow-sense concurrent design of a mechatronic system is a globally simultaneous optimization process of the overall system, including the subsystems of mechanical structure, sensor and controls, materials, etc. As a study example, the overall system of a single-link flexible manipulator is the integration of flexible manipulator, driving motor and reducer, measuring sensors, controller, etc. The optimization is very complex unless some simplifications are made, so the following restrictions are applied here. The flexible beam is equally divided into n segments. Each segment is uniform and the width (b_i, $i = 1,2,\ldots,n$) of

each segment is the only variable to be optimized for link geometrics. With an increase in segment number n, the number of state variables increases greatly to $2n + 2$, which consequently increases the burden of optimization. In this section, a PID controller is chosen as a case study. In fact, any admissible controllers proposed in the literature can be used in the optimization if computational complexity and feasibility are not considered. According to Wang and Gao [22], the system optimum performance index may not be of utmost importance in the selection of the controller. It is preferable to attain an optimal result with a simple controller and an optimally designed structure through concurrent consideration and optimization of the subsystems.

For simulation, a conventional PID controller after Laplace transformation is expressed as

$$H(s) = K_p\left(1 + \frac{1}{T_i s} + \frac{sT_d}{1 + sT_d/N}\right)E(s) \tag{6.100}$$

where K_p, T_i, and T_d represent proportional gain, integral time constant, and derivative time constant. $E(s)$ is the transfer function of tip position error between reference and actual output. N is a large number.

The overall system model that includes mechanical variables of flexible manipulator structure, sensor and controller variables can be written as

$$\sum_T = \sum_0 (A, B, C) \sum_1 (K_p,\ T_i, T_d) \tag{6.101}$$

where $\Sigma_0(A,B,C)$ and $\Sigma_1(K_p,T_i,T_d)$ represent the manipulator system model and PID controller respectively.

Then the design variables are chosen as

$$X = [\, b_1,\ \ b_2, \ldots,\ \ b_n,\ K_p,\ T_i,\ T_d, K_1] \tag{6.102}$$

Some criteria for evaluating PID tuning, such as IAE, ISE, ITAE and ITSE, can be chosen as the optimum performance index for the global optimization, which can be transformed into the optimization objective function. One of the evolutionary algorithms, the genetic algorithm (GA), is employed in the design optimization, which has been proven to provide a robust search in complex spaces to find nearly global optima. Thus, the optimization approach will lead to an optimal shaped beam (link geometric distribution) and an optimal controller subject to the performance requirements.

An example of the framework of concurrent design of a single-link flexible manipulator system with PID controller is illustrated in Figure 6.50.

Three constraints need to be satisfied in the optimization problem, including beam rigidity, control system stability, and keeping the total mass of the flexible beam constant. They are treated as follows [28,29].

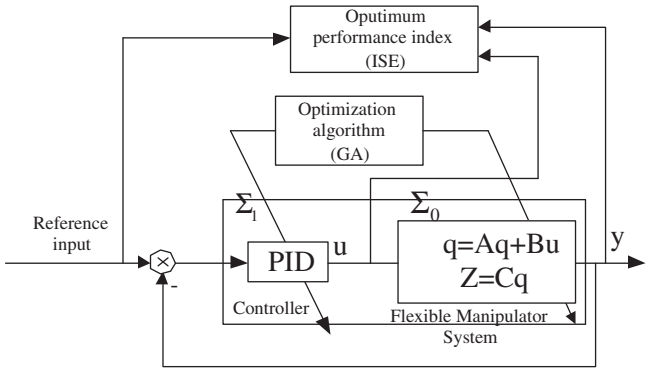

Figure 6.50: Framework of Concurrent Design.

According to rigidity checks before the optimization process, beam width b_i is simply restricted to a conservative range, $[b_{\min}, b_{\max}]$, which is then brought within the design variable range during GA optimization.

Control system stability is an implicit constraint condition, which is treated as the method of discarding infeasible solutions. Stability is verified after each set of solutions is generated in the GA operations and then the infeasible solutions are discarded.

Keeping the total mass of the flexible beam constant, we have $\Sigma_{i=1}^{n} b_i = n \cdot b$. We define $g(b_i) = |\Sigma_{i=1}^{n} b_i - n \cdot b|$. The penalty function method is adopted to transform the equality constrained optimization problem into an unconstrained one.

6.7.3 Simulation Results

In this section, some results from computer-based simulation are presented. The simulation has been developed using the Mathworks Inc. MATLAB® software. The main physical parameters of the flexible manipulator system are as follows:

$$\begin{aligned}
&\text{beam average width}\\
&b = 0.0064\ \text{m}, \quad L = 0.947\ \text{m}, \quad E = 7.0 \times 10^{10}\ \text{N/m}^2,\\
&I_H = 2.3 \times 10^{-4}\ \text{kgm}^2, \quad M_p = 0.033\text{kg}, \quad a_c = 0.035\text{m},\\
&J_p = 1.5 \times 10^{-4}\ \text{kgm}, \quad J_m = 0.01384 \times 10^{-4}\ \text{kgm},\\
&K_w = 0.0669\ \text{V/(rad/s)}, \quad K_e = 0.24\ \text{Nm/A}, \quad r = 1/50,\\
&R = 1.38\Omega, \quad b_i \in [0.8b, 1.2b], \quad n = 5 \sim 8
\end{aligned}$$

An improved real-code GA is adopted in the optimization. The ISE criterion is chosen as optimum performance index, then the fitness function is constructed as $f = f_{\max} - \Phi(X)$, where $\Phi(X)$ is a penalty function including quality constraint and ISE criterion equation, and $f_{\max}$ is

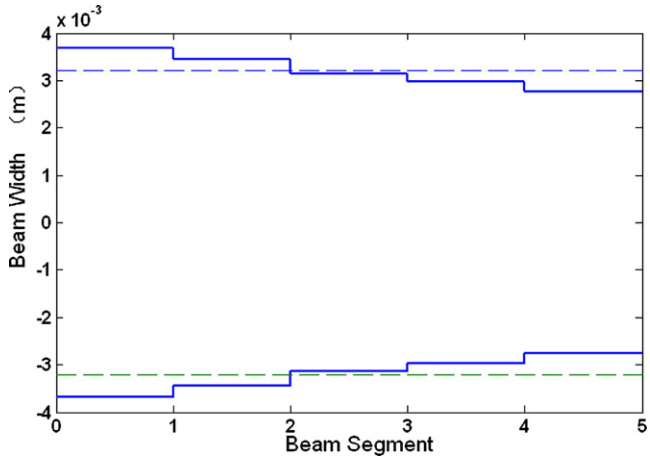

Figure 6.51: Optimal Shape (Beam Width Distribution) for $n = 5$.

a large number to keep f positive. A number of simulation exercises have been carried out. Figure 6.51 shows the optimal shape (width distribution) of the flexible beam with segment number $n = 5$. Figure 6.52 illustrates the GA optimization progress. Figure 6.53 shows the unit step response of the optimally designed manipulator system with PID controller.
The step response curve (dotted) of a common uniform shape flexible manipulator control system and the step response curve (solid) of an optimized flexible manipulator control system using this method are illustrated in Figure 6.53. This figure shows that the tip vibration of the flexible beam is suppressed to some degree.

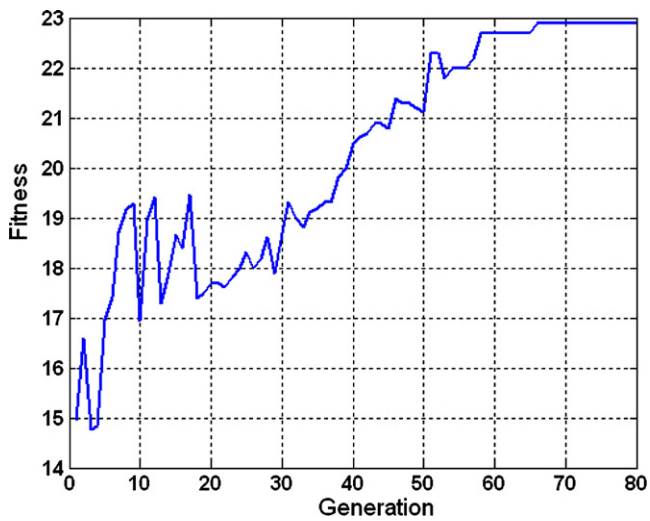

Figure 6.52: GA Optimization Progress for $n = 5$.

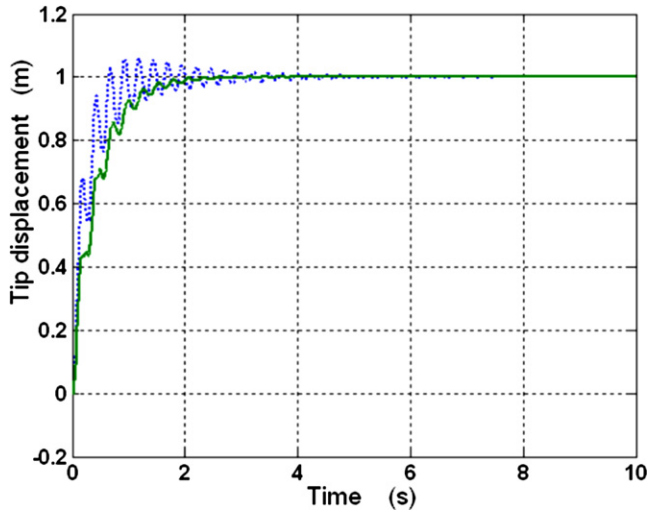

Figure 6.53: Step Responses of Common and Optimized Flexible Manipulator System with PID Controller.

Figure 6.54 shows the optimal shape (width distribution) of the flexible beam with segment number $n = 8$. As illustrated in the figures, the optimal shapes of the beam are not much affected by the segment numbers.

In this chapter, the mechatronic design of flexible manipulators is presented. This design approach emphasizes a global optimal system design by taking coupling effects into account automatically, including concurrent optimization of the geometric shape of the

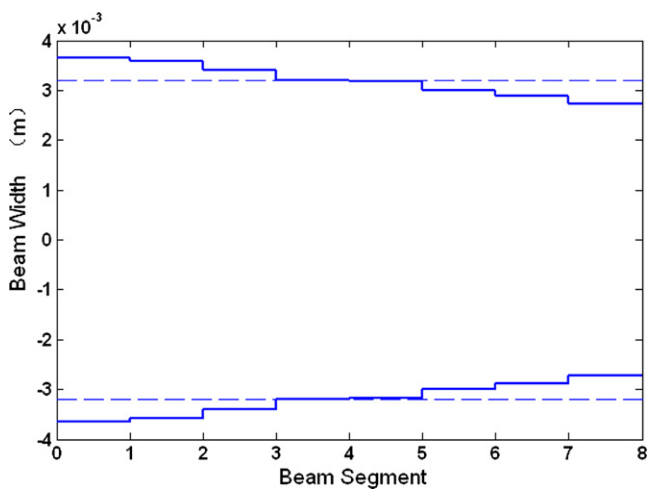

Figure 6.54: Optimal Shape (Beam Width Distribution) for $n = 8$.

flexible link and selection of parameters for the controller. Using this method, the flexible link can improve the performance index compared to its uniform shape. This approach can theoretically be applied to other systems' control problems by choosing different objective functions as required. This chapter presents some investigations of concurrent design methodology, especially in the optimal design of a mechatronic system. In the application considered, an optimization design of a single-link flexible manipulator system is achieved, simultaneously integrating the design variables from mechanical, driving, sensor, and control subsystems. The desired performance has been demonstrated by simulation results. The use of a simple PID controller is based on two considerations: reducing the complexity of the optimization, and evaluating the efficiency of the methodology with control reduction. The concurrent design of a flexible manipulator system with other control strategies, such as a robust controller and a different optimum performance index, has been carried out, and this research will meet the higher requirements of optimal systems design.

References

[1] J. Doyle, K. Glover, State-space solution to standard H_2 and H_∞ control problem, IEEE AC 34 (8) (1989) 831–847.

[2] K. Glover, J. Doyle, State-space formulae for all stabilizing controllers that satisfy an H_∞-norm bound and relations to risk sensitivity, Journal of Systems and Control Letters 11 (1988) 167–172.

[3] B. Francis, A. Course, in: H_∞ Control Theory, Springer-Verlag, Berlin, 1998.

[4] L.B. Gutierrez, F.L. Lewis, J.A. Lowe, Implementation of a neural network tracking controller for a single flexible link: Comparison with PD and PID controller, IEEE Transactions on Industrial Electronics 45 (2) (1998) 307–318.

[5] A. Jnifene, A. Fahim, A computed torque/time delay approach to the end-point control of a one-link flexible manipulator, Dynamics and Control 7 (1997) 177–189.

[6] Z.B. Zabinsky, R.L. Smith, J.F. McDonald, H.E. Romeigh, D.E. Kaufman, Improving hit-and-run for global optimization, Journal of Global Optimization 3 (1993) 171–192.

[7] A.A. Amsden, F.H. Harlow, The SMAC method: A numerical technique for calculating incompressible fluid flows, Los Alamos Scientific Laboratory Report No. LA-4370, 1970.

[8] K. Lezn, H. Ozbay, et al., Frequency domain analysis and robust control design for an ideal flexible beam, Automatica 27 (1991) 947–961.

[9] F.-Y. Wang, On the extermal fundamental frequencies of one-link flexible manipulators, International Journal of Robotics Research 13 (2) (1994) 162–170.

[10] B.L. Karihaloo, F.I. Niordson, Optimum design of vibrating cantilevers, Journal of Optimization Theory and Applications 11 (1973) 638–654.

[11] F.Y. Wang, Optimum design of flexible manipulators: Integration of control and construction. Working Paper 40–91, SIE Department, University of Arizona, Tucson, 1991.

[12] F.Y. Wang, J.L. Russell, Minimum-weight robot arm for a specified fundamental frequency, Proceedings of the IEEE Conference on Robotics and Automation, Atlanta, GA, 1 (1993) 490–495.

[13] F.-Y. Wang, J.L. Russell, Optimum shape construction of flexible manipulators with tip loads, Proceedings of IEEE International Conference on Decision and Control, 1, (1992) 311–316.

[14] F.Y. Wang, Optimum design of vibrating cantilevers: A classical problem revisited, Journal of Optimization Theory and Applications 84 (3) (1995) 635–652.

[15] F.-Y. Wang, P.X. Zhou, P. Lever, Dynamic effects of rotatory inertia and shear deformation on flexible manipulators, Proceedings of IEEE International Conference on Systems, Man, and Cybernetics, Beijing, China, (1996) 2315–2320.
[16] P. Zhou, Mechatronic design of flexible manipulators. Ph.D. dissertation, Department of Systems and Industrial Engineering, University of Arizona, Tucson, 1999.
[17] M. Fujita, F. Matsumura, K. Uchida, Experimental evaluation of H_∞ control for a flexible beam magnetic suspension system: Robust control, Lecture Notes in Control and Information Sciences 183 (1992) 122–129.
[18] G. Zhu, T. Lee, S. Ge, Tip tracking control of a single-link flexible robot: A backstepping approach, Dynamics and Control 7 (4) (1997) 341–360.
[19] F.Y. Wang, G.G. Guan, Influences of rotary inertia, shear deformation and tip load on vibrations of flexible manipulators, Journal of Sound and Vibrations 171 (4) (1994) 433–452.
[20] S. Finger, M.S. Fox, F.B. Prinz, J.R. Rinderle, Concurrent design, Applied Artificial Intelligence 6 (3) (1992) 257–283.
[21] S. Timoshenko, G.H. MacCullough, Elements of Strength of Materials, third ed., D. Van Nostrand, New York, 1949.
[22] F.-Y. Wang, Y. Gao, Advanced Studies of Flexible Robotic Manipulators, Modeling, Design, Control and Applications, World Scientific, Singapore, 2003.
[23] F.Y. Wang, J.L. Russell, Optimum shape construction of flexible manipulators with total weight constraint, IEEE Transactions on Systems, Man, and Cybernetics 25 (4) (1995) 605–614.
[24] H. Asada, J.-H. Park, S. Rai, A control-configured flexible arm: Integrated structure/control design, IEEE Conference on Robotics and Automation 3 (1991) 2356–2362. Sacramento, CA.
[25] P. Zhou, F.-Y. Wang, W. Chen, P. Lever, Optimal construction and control of flexible manipulators: A case study based on LQR output feedback, Mechatronics 11 (1) (2001) 59–77.
[26] P. Zhou, F.-Y. Wang, Mechatronic-based integrated construction and control of flexible manipulators, 14th IFAC World Congress, Beijing, China, 1999. 5–9 July.
[27] F.-Y. Wang, Optimum design of lightweight and flexible robot arms: A mechatronic approach, Proceedings of the 1st Chinese World Congress on ICIA, Beijing, China, (1993) 1160–1165.
[28] Z.-Q. Xiao, Flexible manipulator system modeling and control optimization based on concurrent design. Ph.D. dissertation, Institute of Automation, Chinese Academy of Sciences, Beijing, 2004.
[29] Z.-Q. Xiao, L. Cui, GA based concurrent optimization and design of flexible manipulator system, Robot 26 (2) (2004) 170–176.
[30] Z. Xiao, Concurrent design of flexible manipulator system. Proceedings of the 26th Chinese Control Conference, Zhangjiajie, Hunan 4 (2007) 744–749.
[31] D. Navinchandra, J.R. Rinderle, Interval approaches for concurrent evaluation of design constraints. Proceedings of Concurrent Product and Process Design, ASME, San Francisco, CA, 1990. 364–367.
[32] Y.X. Qing, D.Y. Liang, Multidisciplinary design optimization: A survey of its algorithms and application to aircraft design, Acta Aeronautica et Astronautica Sinica 21 (1) (2000) 1–6.
[33] H. Ratschek, J. Rokne, New Computer Methods for Global Optimization, Ellis Horwood, Chichester, UK, 1998.
[34] M.J. Smith, K.M. Grigoriadis, R.E. Skeelton, Optimal mix of passive and active control in structures. Journal of Guidance, Control and Dynamics 15 (4) (1992) 912–919.

CHAPTER 7

Conclusions and Future Research

We have presented a unified and systematic approach to deal with the modeling, analysis, optimization, and mechatronic design of flexible manipulators. This approach will enable us to deal with various issues in the design and operation of flexible manipulators so that both analytical and numerical procedures, especially new methods in optimization in the field of computational intelligence, can be applied. Based on this approach, we have developed a mechatronic methodology for the design of flexible manipulators that combines their mechanical, electrical, sensing, and control components concurrently instead of sequentially, from the very beginning of the design process. Theoretically, this method is capable of finding global optimal design solutions and results in a better design outcome.

The mechatronic approach as a significant and valid design for the global optimization of a flexible manipulator is the highlight of this research. The critical point of this design is global integration and optimization, which treats all the subsystems in a system as a whole and covers the full searching space for system parameters, including the beam parameters (material and geometric), coefficients in motor dynamics and controller parameters, and controller structure. Compared to traditional optimal design, which relies on a local optimization by assigning a controller to a given plant, the mechatronic mechanism achieves a better solution by regarding the plant and the controller concurrently. Each parameter in the system equation or their combination can be the optimized variable. From this perspective, the boundaries of mechatronic design expansion into other fields are limited only by the imagination. The LQR standard output feedback is the only option considered here to illustrate this basic idea. H_∞ control is used to obtain a more robust system resistant to disturbances.

In this research, the search space is limited only with regard to the beam's physical dimension; all other parameters are considered to be constant. There are two options for mechatronic simulation, the first being that addressed in this book. From a uniform link, the most significant modes and associated natural frequencies were calculated and these modes were used as the universal space base. Thus, all elements in those coefficients of the state-space equation are the only functions of the geometric link. Since the mechatronic method as outlined in Chapter 6 searches the beam's geometric distribution through the whole space to find an optimal solution, this "base" approach can save a considerable amount of computation time.

Flexible Manipulators. DOI: 10.1016/B978-0-12-397036-7.00007-6
Copyright © 2012 Elsevier Inc. All rights reserved.

The other option for mechatronic simulation is what is called the "segmentized method". Based on segmentized beams, and their interfacial conditions, a set of constraints is established. To solve these equations with beam boundary conditions, the most significant natural frequencies from the determinant equal to zero were obtained. Furthermore, a series of eigenfunctions for each segment was found. In this approach, even if one segment of the beam shape changes, all these frequencies and eigenfunctions will be changed. Because of the searching process in the mechatronic design, this approach will take longer to reach the optimal point. So the first option is prefereable for mechatronic design, which is why it was employed in this research.

The simulation results show that in all cases the performance index (PI) improved to various degrees. It was found that the PI does not change very much with varying numbers of segments. The results are better for two-output feedback than that for single feedback. If the motor parameters are added into the search space, better performance is obtained.

The results obtained here show that the H_∞ controller gives better performance, but this is a tradeoff for slower computation time because the H_∞ controller is much more complicated than the LQR controller and needs more calculation. The robustness analysis was also conducted numerically. As was pointed out, the controller provides robust features for parameter uncertainties or variations, as well as disturbance. The numerical responses to different kinds of parameter variations were illustrated, showing that the system designed by the mechatronic method displays good robustness against parameter variations.

Based on the results obtained in this book, we believe that computational intelligence methods, in particular evolutionary computing, such as genetic algorithms, should be investigated in the ongoing research on flexible manipulators.

Intelligent Systems Series

Editor-in-Chief

Fei-Yue Wang: Chinese Academy of Sciences
Contact information: feiyue@ieee.org

Editorial Board Members

Jim Hendler: Rensselaer Polytechnic Institute

William T. Scherer: University of Virginia

Hsinchun Chen: University of Arizona

Kathleen Carley: Carnegie Mellon University

Ruiwei Dai: Chinese Academy of Sciences

Youxian Sun: Zhejiang University

Chelsea (Chip) C White: Georgia Tech

Petros Ioannou: University of Southern California

Frank Lewis: University of Texas at Arlington

Bruno Sicilianos: Università degli Studi di Napoli Federico II

Wendy Hall: University of Southampton

Flexible Manipulators

Modeling, Analysis, and Optimum Design

Yanqing Gao
The University of Arizona

Fei-Yue Wang
Chinese Academy of Sciences

Zhi-Quan Xiao
Wuhan Textile University

ZHEJIANG UNIVERSITY PRESS
浙江大学出版社

ELSEVIER

AMSTERDAM • BOSTON • HEIDELBERG • LONDON
NEW YORK • OXFORD • PARIS • SAN DIEGO
SAN FRANCISCO • SINGAPORE • SYDNEY • TOKYO
Academic Press is an imprint of Elsevier

Academic Press is an imprint of Elsevier
The Boulevard, Langford Lane, Kidlington, Oxford OX5 1GB, UK
225 Wyman Street, Waltham, MA 02451, USA

First edition 2012

Copyright © 2012 Elsevier Inc. All rights reserved.

No part of this publication may be reproduced, stored in a retrieval system or transmitted in any form or by any means electronic, mechanical, photocopying, recording or otherwise without the prior written permission of the publisher

Permissions may be sought directly from Elsevier's Science & Technology Rights Department in Oxford, UK: phone (+44) (0) 1865 843830; fax (+44) (0) 1865 853333; email: permissions@elsevier.com. Alternatively you can submit your request online by visiting the Elsevier web site at http://elsevier.com/locate/permissions, and selecting *Obtaining permission to use Elsevier material*

Notice
No responsibility is assumed by the publisher for any injury and/or damage to persons or property as a matter of products liability, negligence or otherwise, or from any use or operation of any methods, products, instructions or ideas contained in the material herein. Because of rapid advances in the medical sciences, in particular, independent verification of diagnoses and drug dosages should be made

British Library Cataloguing in Publication Data
A catalogue record for this book is available from the British Library

Library of Congress Cataloging-in-Publication Data
A catalog record for this book is availabe from the Library of Congress

ISBN−13: 978-0-12-397036-7

For information on all Academic Press publications visit our web site at books.elsevier.com

Printed and bound in the UK

12 13 14 15 16 10 9 8 7 6 5 4 3 2 1

Working together to grow libraries in developing countries
www.elsevier.com | www.bookaid.org | www.sabre.org
ELSEVIER BOOK AID International Sabre Foundation

Preface

Flexible robotic manipulators, consisting of mainly lightweight or large dimension robotic manipulators, exhibit many advantages over conventional rigid robotic manipulators. For example, flexible manipulators require less material and smaller actuators, consume less power and cost less, and provide fast motion, high force to mass ratio, more maneuverability and transportability,. Therefore, the use of flexible manipulators could lead to reduced energy consumption, increased productivity, and enhanced payload capacity. Over the past few decades, flexible manipulators have been deployed widely in many fields, such as space exploration, manufacturing automation, construction, mining, and hazardous operations.

However, the flexible nature of flexible manipulators has brought up many challenging problems in their construction and operation for design, modeling, analysis, and control. For example, due to link deformation, the dynamics of manipulators is significantly complicated and distributed parameter model should be applied for precise description. The model complexity also leads to the non-minimum phase characteristics of flexible manipulators that prevent the direct use of many conventional and effective control algorithms for the operation of flexible manipulators. Finding an effective control mechanism that would account for the need of both accurate positioning and elastic motion has motivated a great deal of research effort over the past two decades.

Although significant progresses have been made in many aspects over the last two decades, many issues are not resolved yet, simple and effective, as well as reliable controls of flexible manipulators still remain an open quest. Clearly, further efforts and results in this area would contribute significantly to robotics, and in particular, automation, as well as its application and education in general control engineering. To accelerate this process, this book summaries the main results of our studies in design, modeling, control and applications of flexible manipulators over the past two decades.

In the past, research work has been focused on modeling of link deformation, dynamics, and development of independent motion control algorithms and systems. Very few studies with quantitative results have been reported in the literature on the effect of size, shape, mass distribution, tip load, sensing location, coupling of control algorithms and link construction, and other factors on the dynamics and operational performance of flexible manipulators. However, such analyses are critical to the effectiveness of any model for optimization and control

purposes. The objective of this book is to provide a unified approach that will consider all factors in mechanical simultaneously, electrical, sensing, and control components to address design, modeling, analysis, optimization, and control of flexible manipulators. To this end, a systematic study of various models and comparison between pros and cons with respect to specific design and control problems are developed here. Many critical factors in construction and operation of flexible manipulators are addressed with systematic but specific numerical investigations based on the current available dynamic models. In many cases, analytical procedures developed for flexible manipulators in previous studies seem no longer applicable in our investigation. New methods for optimal design problems with meaningful constraints are explored and established.

The complexity of a manipulator system is due to the interrelation and interdependency of its subsystems, for example, its kinematic units, control units, driver units, and measuring or sensing units. In traditional design, a manipulator's link structure is designed first, followed by its driver system, then a measuring system, and finally its control system. This leads to a sequential design process and a local optimal solution at the best, and therefore the potential of the flexible manipulator, that is, the global optimality of the manipulator, is rarely realized in full. To overcome this problem, a concurrent design procedure that integrates all subsystems must be under taken. In other words, a mechatronic approach must be considered in the design, construction, and operation of flexible manipulators. The establishment of a computational framework and related methods, and procedures for mechatronic design, construction, and operation of flexible manipulators is the main objective and the unique feature of our book.

We would like to thank our former associates and graduate students at the Program for Advanced Research in Complex Systems (PARCS), the University of Arizona, Tucson, Arizona, USA, and the Key Laboratory for Complex Systems and Intelligence Science, Chinese Academy of Sciences, Beijing, China, and our colleague in the National Laboratory of Management and Control for Complex Systems, Beijing, China for their significant contributions and great assistance to the completion of this book. This project is supported in part by the Grant to the Outstanding Group for Research Innovation in Intelligent Control and Computational Intelligence, from the National Natural Science Foundation of China.

Yanqing Gao
The University of Arizona
Tucson, Arizona, USA

Fei-Yue Wang
Chinese Academy of Sciences
Beijing, China

Zhi-Quan Xiao
Wuhan Textile University
Wuhan, Hubei, China.

Index

Note: Page numbers followed by *f* indicate figures, *t* indicate tables.

A

Acceleration feedback, 8–9
  see also Feedback
Actuator dynamics, of single flexible robotic link, 230
Adaptive controller, 8–9, 60
  see also Controller
Admissible functions, 37–38, 126–127, 149–150

B

Beam
  deformation, 231, 242
  dynamic model, linearization of, 34–37
  kinetic energy of, 18–19
  model *see* Euler–Bernoulli beam model; Timoshenko beam mode

C

Cantilever(s)
  beam, 101–102, 107, 111, 113, 167
  vibrating, 100–102, 106, 122, 126, 152, 169
Centrifugal forces, 92–94
Closed-loop design, of flexible robotic links, 229–237
  optimization formulations for, 234–237
    minimax, 237
    pole location, 236
    reference model, 236–237
    tracking error, 236
  single-link
    actuator dynamics of, 230
    control algorithm, 231
    mechanics of, 230
    transfer functions
      of integrated systems, 231–232
      segmentized solution for, 232–234
Composite material designs, 103, 119–120
Computed torque/delayed deflection approach, 7
Concurrent design(s), 237–241
  broad sense, 238–239, 239f
  defined, 238
  existing representation of, 239–240
  global optimization of, 240–241
  narrow sense, 238, 239f, 240
  of single-link flexible manipulator systems based on PID controller, 241–248
    dynamics of, 241–243, 241f
    framework of, 245f
    implementation of, 243–245
    simulation results, 245–248, 246f–247f
  system analysis for, 240
Constrained optimum shape design, 156–159
  with multiple tip loads, 158–159
  numerical examples, 162–163
  with single tip load, 157–158
Control algorithm, of single flexible robotic link, 231
Control analysis, 91–97
Controller
  adaptive, 8–9, 60
  fractional order, 9–10
  H_∞, 7, 210–228, 210f, 251–252
  linear quadratic Gaussian, 6–7
  neural network tracking, 7
  PID, 241–248, 241f, 245f–246f, 247f
Coriolis forces, 92–94
Coulomb friction, 8–9, 39
Cross-sectional designs
  uniform tunnel, 116–118, 118f
  variable tunnel, 118–119, 119f

D

Damping, 6–7, 60–61, 95–96
  matrix, 56–57
  Rayleigh, 56–57
Degrees of freedom (DOF), 1
Design model, of flexible manipulators, 122–124, 123f
Disturbance rejection, 8–9
Dynamic programming (DP) algorithm, segmentized optimization approach, 137–138

E

End-effectors, 60, 118–119, 122–123
Equations of motion
  for Euler–Bernoulli beam model, 26–27
  of flexible arms, 21–34
  nonlinear dynamic, 91
    discretization of, 92–94
Error
  hub rotation, 235
  optimization, tracking, 236
  tip position, 244
  truncation, 48
Euler–Bernoulli beam model, 16–18, 148–149, 166–167
  derivation of, 22–26
  with dimensionless variables, 36

Euler–Bernoulli beam model (*Continued*)
dynamic
asymptotic behavior of, 71
characteristic equations for, 65–66
natural frequencies, 80–83
transverse section, motion of, 62, 62f
equations of motion for, 26–27
finite element, 52
finite-dimensional, 41–47
after linearization, 35
with rotary inertia, 82f
asymptotic behavior of, 71
characteristic equations for, 66–67
one-link flexible manipulators, 63
with tip load
asymptotic behavior of, 72
characteristic equations for, 69–70
one-link flexible manipulators, 64
Euler–Bernoulli equations, 122–125
design model, 122–124, 123f
vibration equations, 124–125
Experimental verification, of flexible manipulators, 72–79
External forces, work done by, 21

F

Feedback
acceleration, 8–9
flatness-based estimated state, 8–9
hub tangent angle, 197, 197t, 198f, 199f, 201, 202t, 203f, 217–218, 218f–225f
output, 7, 192–194, 196–197, 206–207, 215–216, 240–241, 251
Finite difference model, 47–51
Finite element model, 16, 51–57
Finite-dimensional modeling
of Euler–Bernoulli beam, 41–47
of flexible manipulators, 37–57
determinants, 37–39
frequencies and shapes, 39–41, 39t–40t, 40f–44f
Flatness-based estimated state feedback control, 8–9
Flexible arms
equations of motion of, 21–34
fuzzy control for, 9
integrated, transfer functions of, 231–232
vibration control of, 8–9
Flexible manipulator(s)
analysis of, 2
comparison with rigid robotic manipulators, 1
distinguished from rigid manipulator, 1
earlier research on, 5–6, 16, 186–187
equations of motion, 18, 91–94
finite-dimensional modeling of *see* Finite-dimensional modeling
mechatronic design of *see* Mechatronic design method
modeling of, 2, 15–58
one-link *see* One-link flexible manipulators
optimization of, 2, 99–184
recent work on, 6–11
two-link, 143–146, 145f, 147f
uniform, 37–39
Flexible robotic links, closed-loop design of, 229–237
optimization formulations for, 234–237
minimax, 237
pole location, 236
reference model, 236–237
tracking error, 236
single-link
actuator dynamics of, 230
control algorithm, 231
mechanics of, 230
transfer functions
of integrated systems, 231–232
segmentized solution for, 232–234
Fractional order controller, 9–10
see also Controller
Friction
compensation, 10
Coulomb, 8–9, 39
Future research, 251–252

G

Genetic algorithm (GA), 244–246, 246f
Geometrically constrained optimum designs, 116–119, 117f
maximum radius constraints, 116
minimum radius constraints, 116
uniform tunnel cross-sectional designs, 116–118, 118f
variable tunnel cross-sectional designs, 118–119, 119f

H

H_∞ controller design, 7, 210f, 215–216, 251–252
flexible beam system, generalized plant of, 212–215
with IHR algorithm, 210–228
simulation results, 216–223
state-space formulas for, 210–211
system robustness analysis, 225–228
see also Controller
Hamiltonian matrix, 211
Hamilton's principle, 18, 21–33, 43, 91, 190
Hub
inertia, 18–19, 131, 134, 146–147, 150–151, 153, 159–160, 164, 167–168, 174–175
rigid, 17, 17f, 148–149
rotation, 148–149, 191–192, 231
tangent angle
feedback, 197, 197t, 198f–199f, 201, 202t, 203f, 217–218, 218f–225f
with tip deflection, 198, 199f–200f, 203–205, 204f, 206f–209f, 218f–220f, 222f–225f
with tip position, 199–200, 201f–202f, 203, 205f
torque applied at, 21, 47–48, 122–123, 230, 242

I

Identity matrix, 213–214
IHR algorithm
H_∞ control problem configuration with, 210–228, 210f

designing of, 215–216
flexible beam system, generalized plant of, 212–215
simulation results, 216–223
state-space formulas for, 210–211
system robustness analysis, 225–228
LQR formula with, 195
segmentized optimization approach, 138–140
Input–output inversion, 6–7
Integrated flexible arm system, transfer functions of, 231–232
Integro-partial difference equations, 5, 91, 122
Interior-point-based method, 9

K

Kalman filter, 6–7
Kinetic energy
of beam, 18–19, 22–30, 45–46
inertia matrix, of driving end, 54
of moving flexible manipulator, 53
rotational, 53
of tip load, 18–21
total, 54

L

Lagrange multiplier technique, 6, 43, 51–52, 100–103, 108–109, 127–128, 151, 168–169, 194
Lightweight arms, 16
Linear quadratic Gaussian (LQG) controller, 6–7
see also Controller
Linear quadratic regulator (LQR), 251
inner loop optimizations, 193–195
iterative algorithm, 195
standard feedback configuration, 226f
Link construction constraints, segmentized solutions for, 182
Lump-modeled flexible robots, 10
Lyapunov energy function method, 91, 94–95

M

Mass matrix, 53, 55–56, 92–93
Maximum radius constraints, optimum designs with, 116
Maximum speed design problem (maxSDP), 178–179
Mechatronic design method (MDM), 2–3, 185–252, 188f
accuracy of, 187
closed-loop design, of flexible robotic links *see* Closed-loop design, of flexible robotic links
concurrent design *see* Concurrent design
control efficiency of, 187
defined, 188–189
dynamics of, 190–193
output specifications, 192–193
state-space equations, 190–192
functionality of, 189–190
H_∞ control problem configuration with IHR algorithm, 210–228, 210f
designing of, 215–216
flexible beam system, generalized plant of, 212–215
simulation results, 216–223
state-space formulas for, 210–211
system robustness analysis, 225–228
LQR formula
inner loop optimizations, 193–195
integrated optimization process, 196
iterative algorithm, 195
results, 196–207
overview of, 187–190
reasons for, 187–188
subsystems, interrelation and interdependency of, 188
Minimax design method, 158–159
numerical examples, 164
optimization of, 142–143, 144f, 237
Minimum mass design problem (minMDP), 178–180
Minimum radius constraints, optimum designs with, 116
Minimum-weight design, of flexible manipulators, 166–172
basic equations, 166–167
numerical examples, 172
problem formulation, 168–169
solution by iterations, 169–172
Modeling, of flexible manipulators, 2, 15–58
external forces, work done by, 21
finite difference model, 47–51
finite element model, 51–57
finite-dimensional *see* Finite-dimensional modeling
kinetic energy
of beam, 18–19
of tip load, 18–21
tip load, 17–19, 17f–18f
total potential energy, 21
Multidisciplinary design optimization (MDO), 238, 240–241
Multiple loads, design formulations for, 180–181

N

NASA
Center for Intelligent Robotic Systems for Space Exploration (CIRSSE), 72
Mars Exploration Mission, 186
Remote Manipulator System, 1–2, 186
operational problems in, 2
Neural network tracking controller, 7
see also Controller
Neuro-fuzzy state-space modeling, 9
Nonlinear programming method, 157–158

O

One-link flexible manipulators, 10, 47–48, 52
-based on PID controller, concurrent design of, 241–248
dynamics of, 241–243, 241f
framework of, 245f
implementation of, 243–245
simulation results, 245–248, 246f–247f
coordinate systems for, 61, 61f
dynamic models for, 61–64
Euler–Bernoulli dynamic model for
with rotary inertia, 63
with tip load, 64
transverse section, motion of, 62, 62f

One-link flexible manipulators (*Continued*)
parameters of, 73t
robotic link, 229–237
state-space equations of, 190–192
Timoshenko dynamic model
with rotary inertia, 63–64
with shear deformation, 63–64
Optimization, of flexible manipulator, 2, 99–184
composite material designs, 103, 119–120
geometrically constrained optimum designs, 116–119, 117f
maximum radius constraints, 116
minimum radius constraints, 116
uniform tunnel cross-sectional designs, 116–118, 118f
variable tunnel cross-sectional designs, 118–119, 119f
mechatronic design, 234–237
minimax, 237
pole location, 236
reference model, 236–237
tracking error, 236
minimum-weight design, 166–172
basic equations, 166–167
numerical examples, 172
problem formulation, 168–169
solution by iterations, 169–172
new iteration approach
basic equations, 102–104
$p = 1$, 106–108, 111, 111t, 112f–113f
$p = 2$, 112–116, 113t, 114f–115f
$p = 3$, 112–116, 113t, 114f
$p > 1$ and $q = 0$, 108–109
$p > 1$ and $q \neq 0$, 109–110
$q = 0$, 105
$q \neq 0$, 105
segmentized solutions, 172–182
basic equations, 174–175
design formulation with multiple loads, 180–181
link construction constraints, 182
maximum speed design problem, 178–179
minimum mass design problem, 178–180
stress/strain and deflection constraints, 181
shape construction with tip weight constraint, 148–165
basic equations, 148–151
constrained shape design, 156–159
numerical examples, 159–164
sensitivity analysis, 164–165
unconstrained shape design, analytical approach to, 151–155
variation formulation, 150–151
shape design with tip loads, 120–147
analytical solutions, 125–133
Euler–Bernoulli equations, 122–125
minimax optimum design, 142–143, 144f
problem setup, 120–122
segmentized optimization approach, 133–142
sensitivity analysis, 146–147, 148f
two-link optimum design, 143–146, 145f, 147f
Output feedback, 7, 192–194, 196–197, 206–207, 215–216, 240–241, 251
see also Feedback
Output specification, 192–193

P

Passivity analysis, 91–97
Payload, tip-mass, 20, 52–54, 237, 241–242
Perturbation method, 5, 7, 16, 106–107, 113, 122
Photosensors, 7
PID controller, single-link flexible manipulator systems based on, 241–248
dynamics of, 241–243, 241f
framework of, 245f
implementation of, 243–245
simulation results, 245–248, 246f–247f
see also Controller
Pole location optimization, for mechatronic design, 236
Port-based modeling, 7–8
Potential energy
of beam, 22–32, 45–46, 53–55
of tip load, 18
total, 21, 45–46, 55
Pshenichnyi–Pironneau–Polak minimax algorithm with exact line search (PPP-ELS), 180

R

Rayleigh damping, 56–57
see also Damping
Recursive Lagrangian formulation, 5
Reference model optimization, for mechatronic design, 236–237
Rigid manipulator(s)
distinguished from flexible manipulator, 1
robotic, comparison with flexible manipulators, 1
Rigidity matrix, 56
Robotic crane systems, 1
Robotic excavators, 1
Robotic manipulators
flexible, 16
rigid, comparison with flexible manipulators, 1
Rotary inertia
Euler–Bernoulli dynamic model with, 63
asymptotic behavior of, 71
characteristic equations for, 65–66
influence on vibration frequencies, 73–74, 74f–75f
Timoshenko dynamic model with, 63–64

S

Segmentized optimization approach, 133–142
formulation, 133–137, 135f
numerical results, 140–142
solutions, 137–140, 172–182, 252
basic equations, 174–175
design formulation with multiple loads, 180–181
link construction constraints, 182

maximum speed design problem, 178–179
minimum mass design problem, 178–180
stress/strain and deflection constraints, 181
Sensitivity analysis
of flexible manipulators-based on H_∞ with IHR algorithm, 225–226
of optimum shape design
with tip loads, 146–147, 148f
with tip weight constraint, 164–165
Shear deformation
influence on vibration frequencies, 74–75, 75f
Timoshenko dynamic model with, 63–64
Single-link flexible manipulators *see* One-link flexible manipulators
Stability analysis, of nonlinear dynamic model, 94–97
State-space equations, of flexible manipulators, 190–192
H_∞ control problems, 190–192
Stiffness matrix, 53, 55–56
Stokes–Dirac structure, 7–8
Structure and control integrated design (SCID), 237, 240
System robustness analysis, 225–228
numerical results of, 226–228, 226t–227t, 228f–229f

T

Timoshenko beam model, 18
derivation of, 27–33
with dimensionless variables, 36–37
dynamic
asymptotic behavior of, 71
characteristic equations for, 67–69
natural frequencies, 83–88
transverse section, motion of, 62f, 63–64
equations of motion for, 33–34
after linearization, 35
with rotary inertia, 87f
one-link flexible manipulators, 63–64
with shear deformation, 87f
Tip deflection, 7, 121, 131, 192, 228f–229f, 231
hub tangent angle with, 198, 199f–200f, 203–205, 204f, 206f–209f, 218f–220f, 222f–225f
output, 192
Tip inertia, influence on vibration frequencies, 79f
Tip length, influence on vibration frequencies, 77f–78f
Tip load, 17–19, 17f–18f, 186–187
Euler–Bernoulli dynamic model with, 64
asymptotic behavior of, 72
characteristic equations for, 69–70
influence on vibration frequencies, 76–79, 76f–77f
kinetic energy of, 18–21
optimum shape design with, 120–147
analytical solutions, 125–133
Euler–Bernoulli equations, 122–125
minimax optimum design, 142–143, 144f
problem setup, 120–122
segmentized optimization approach, 133–142
sensitivity analysis, 146–147, 148f
two-link optimum design, 143–146, 145f, 147f
Tip position, 9–10
hub tangent angle with, 199–200, 201f–202f, 203, 205f
output, 192
Tip weight constraint, optimum shape construction with, 148–165
basic equations, 148–151
constrained shape design, 156–159
numerical examples, 159–164
sensitivity analysis, 164–165
unconstrained shape design, analytical approach to, 151–155
variation formulation, 150–151
Torque transmission, 5
Tracking error optimization, for mechatronic design, 236
Transfer function(s), 7
closed-loop
of integrated systems, 231–232
segmentized solution for, 232–234
Two-link optimum design model, 143–146, 145f, 147f

U

Unconstrained optimum shape design, analytical approach to, 151–155
numerical examples, 159–161
Uniform tunnel cross-sectional designs, 116–118, 118f *see also* Cross-sectional designs

V

Variable tunnel cross-sectional designs, 118–119, 119f *see also* Cross-sectional designs
Vibration equations, 124–125
Vibrations of flexible manipulators, dynamic analysis of
asymptotic behavior, 70–72
characteristic equations, 64–70
experimental verification and numerical analysis, 72–79
natural frequencies and modal shape functions, 80–88
one-link flexible manipulators, 61–64
step responses and general solutions, 88–91
Vision-based flexible tip point control, 8

W

Wave-based control analysis, 10